Interfacial design strategies for selective electrocatalytic CO_2 reduction through control of proton coupled electron transfer

Xinlei Zhang

Doctor of Philosophy

University of York

Department of Chemistry

March 2024

Abstract

The aim of this project was to construct and study a novel copper-based electrocatalyst embedded in a microenvironment with well-defined hydrophobicity to control proton activity and improve CO_2 mass transport to modify the selectivity of the CO_2 reduction reaction (CO_2RR). Specifically, anodized aluminium oxide (AAO) membranes were used to grow and confine Cu nanowires (CuNWs) and the hydrophobicity of the CuNW-AAO composite electrode was increased by reaction with various silane molecules. Uniformly distributed CuNWs were successfully prepared in a commercial AAO porous membrane by square-wave pulsed electrodeposition. The length and width of CuNWs can be controlled by adjusting deposition time and applied current density. Analysis of the electrochemical behaviour of the composite CuNW-AAO electrode using capacitance measurements and a methylviologen redox probe, shows that the electrochemical surface area (ECSA) and roughness factor are reflective of electrolyte penetration throughout the CuNW-AAO electrode, supporting electrocatalysis along the length of the CuNW's surrounded by AAO. Next, the hydrophobicity of the CuNW-AAO electrode was increased by reaction with various silane molecules. Contact angle measurements were used to quantify hydrophobicity as a function of silane and study the stability of the silane coating to electrolyte and under electrochemical conditions. Analysis showed that silane modified CuNW-AAO electrodes maintain large ECSA and roughness factor, and that addition of the silane coating etches the CuNWs surface, presumably via generation of HCl, increasing the electrode surface roughness. Control experiments using Cu foil electrodes exposed to silane, show that Cu can also be directly modified with silane. CO_2RR reactions of silane modified Cu foil electrodes, show promotion of CO_2 to C_{2+} product. Contact angle measurements after reaction showed a reduction in hydrophobicity due to partial loss of the silane coating. CO_2RR using silane modified and unmodified CuNW-AAO electrodes resulted in mechanical instability due to hydrogen bubble formation behind the AAO membrane.

Table of Contents

List of Figures

List of Schemes

List of Tables

Acknowledgements

I would like to express gratitude to my supervisor Dr Richard E. Douthwaite for his helpful guidance, great support on my PhD research works. I would also like to thank my IPM Professor Alison Parkin for her guidance with my TAP meetings.

My thanks to Joy, at the start of my PhD, Joy helped me a lot with my experimental skills and electrochemistry basic knowledge development. I would like to thank Dr Alexander Heyam for NMR training, Dr Jon Barnard for SEM training at the nanocentre, Dr Scott Hicks for GC technical support and to Charan Panesar's help for providing evaporator at Department of Electronics. I would also like to thank Mr Stuart Murray and Mr Mark Roper for CO_2RR reactor manufacture. I would like to acknowledge the assistance of Mr Niall Donaldson for daily lab work support.

My sincere thanks to RED group labmates for their kind help and support during my PhD. Finally, I really thank my parents, my husband and my family for their great support and encouragement to me.

Covid-19 Statement

My PhD project started in October 2019. Covid lockdowns occurred from March 2020 to June 2020 preventing any laboratory work. An underpinning element of the project relies on access to metal evaporation equipment in Physics and Electronics. This facility had limited access during June 2020 – March 2021 due to covid restrictions and refurbishment of the room containing the equipment. The final phase of the project requires testing of the electrochemical performance of electrodes using a reactor built by Chemistry workshops. This faced delays between summer 2021 – summer 2022 due to workshop capacity, exacerbated by reduction in personnel. Troubleshooting of the final design was also required during autumn of 2022 which was also met with workshop delays.

Declaration

I declare that the work in this thesis is based on my own research conducted at the Department of Chemistry, University of York (UK), from year 2019 to 2024. This thesis has not been submitted for any other degree qualification or been presented somewhere else. All the work in this paper was carried out by me independently, except: 1. XPS analyses and the data fitting were performed by Harwell XPS facility. 2. The CO_2RR reactor was manufactured by workshop at Department of Chemistry, University of York. 3.Some comparative reference data were cited in this article.

Xinlei Zhang

1. Introduction

1.1. General considerations

In recent years, industrial development and population growth have led to the excessive consumption of fossil fuels, including coal, petroleum and natural gas.[1,2] As the final product of carbon combustion, CO_2 has continued to accumulate in the atmosphere in large quantities, causing many serious environmental problems, such as the global greenhouse effect.[3] Therefore, people are committed to the development of clean energy, such as using solar energy, wind energy to obtain renewable electricity resources.[4,5] Sustainable energy sources such as wind, solar and tidal energy generate electricity in nature. In contrast, electrochemical carbon dioxide reduction is emerging as an environmentally-friendly and controllable energy conversion technology and is used as a potential solution to solve the carbon cycle problem of human society.[6–8]

Aqueous electrocatalytic conversion of CO_2 (CO_2RR) into high-energy-density C_{2+} chemicals provides an energy vector for the storage of renewable electricity and reduction in CO_2 emissions. However, rate and selectivity are limited by CO_2 solubility in water and parasitic hydrogen evolution. Strategies have been developed to overcome solubility using gas diffusion electrodes and modify proton activity using catalyst surface treatments. In this project we describe a new strategy to control the environment at the electrode surface by embedding the catalyst in a partially hydrophobic environment to control proton activity. A modified commercial alumina membrane (AAO) with an ordered porous structure was used to template the growth of copper nanowires (CuNWs) of predictable morphology. After growth, the membrane was functionalized with various chlorosilanes with variable hydrophobicity, which exhibit good chemical stability, with the aim to control the surface wetting ability and proton activity within the membrane. This methodology is hoped to provide a platform for mechanically stabilizing nanowire catalysts and controlling proton activity that are key to CO_2RR selectivity and stability.

1.2. Motivation of carbon dioxide recycle

The rapid development of global industry over the last century, has sharply increased energy demand and the consumption of fossil fuels with the direct consequence of increased emissions in particular CO_2. During the period 1960-2021, the CO_2 emissions of most countries and regions has shown an overall upward trend

as shown in Figure 1.1, and the current global anthropogenic CO_2 emissions are about 37 Gtons CO_2 per year.[9,10] The increasing concentration of CO_2 in the atmosphere is the main cause of the greenhouse effect and sea level rise and urgent action is required.[11–13] Ideally strategies to eliminate emissions or even reduce atmospheric CO_2 are required but even mitigation methods would be of benefit if waste CO_2 destined for emission could be reused. One potential option is to use electrochemical reduction for carbon dioxide utilization (CDU) by converting CO_2 into products with high added value such as platform chemicals or fuels,[14] or alternatively to produce storable liquids for carbon dioxide storage (CDS) which would arguably have the greatest potential impact.[15] In this project, the focus is the reduction reaction of CO_2 gas (CO_2RR) through an electrocatalytic system into useful or storable hydrocarbons and/or oxygenates.

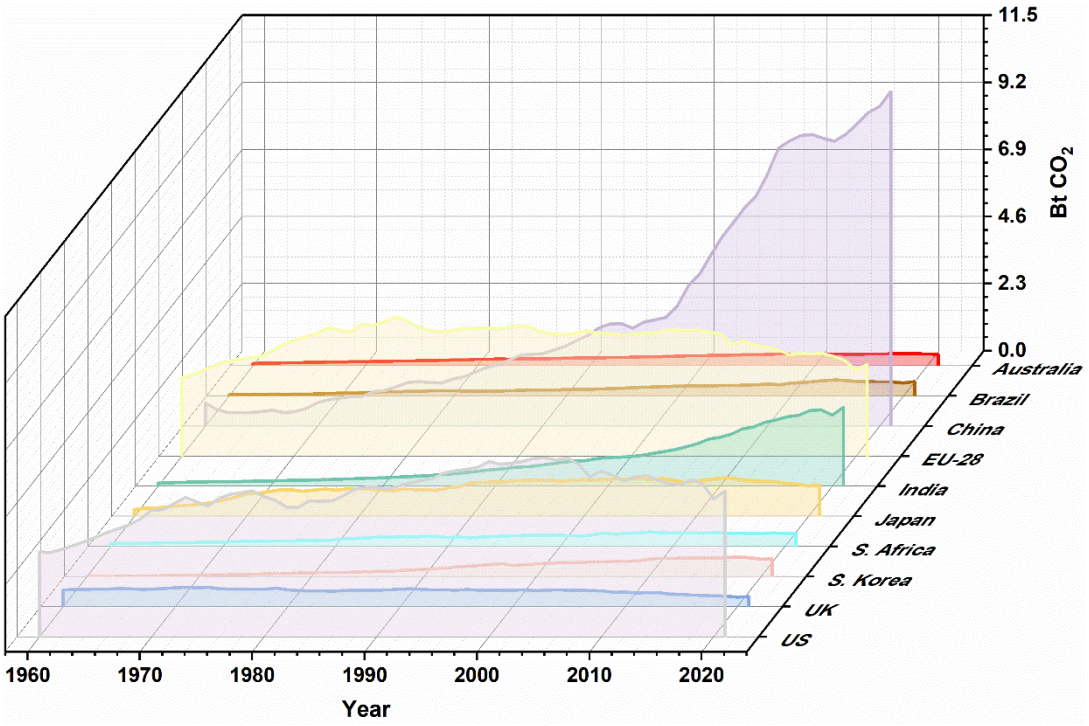

Figure 1.1: Global carbon dioxide emissions, 1960-2021. Data in chart is originated from P. Friedlingstein, et al., Earth Syst. Sci. Data, 2022, 14, 4811–4900. (essd.copernicus.org)

Since Hori[16] first used electroreduction to achieve CO_2 fixation and quantified both gaseous and liquid products in 1985, understanding of the carbon dioxide reduction reaction (CO_2RR) has developed significantly particularly as global warming has accelerated and abundant cheap renewable electricity appears to becoming a reality. The traditional thermal catalysis of CO_2 hydrogenation has reached industrial

scale. However, due to the large amount of H_2 involved in the reaction, this process is not an immediate solution to reducing CO_2 emissions. Compared with catalytic hydrogenation, CO_2 electrochemical reduction has milder reaction conditions and a wider range of valuable products using water as a proton and electron source. Consequently, research on CO_2 electrochemical reduction has been extensively investigated in the laboratory, and is considered to be a potentially viable future method. Converting CO_2 into chemical energy can be considered a technology that completes the recycling of CO_2 by simulating the principle of photosynthesis in natural ecosystems.[17–19] In this process, the existing large amounts of CO_2 as chemical feedstock can be reduced into fuels with high energy density which has financial and environmental benefits also available for human use to complete the carbon neutral cycle. Formally, in the CO_2RR process, a large negative potential (-1.90 V vs.RHE, pH=7) is required to form $*CO_2^-$ radical ($*$ denotes an adsorption site), which is adsorbed and stabilized on the electrocatalyst surface:[20,21]

$$* + \mathrm{CO_2} + \mathrm{e^-} \rightarrow * \mathrm{CO_2^-}$$

However, this large overpotential is circumvented in practical CO_2RR by coupling with proton transfer (Table 1.1). Although the formation of products (such as methane) from CO_2 is thermodynamically more advantageous than the formation of CO, however, the feasibility of the process can be limited due to the difficulty of transferring multiple electrons to the reduction sites. Therefore, nH^+/ne^- reduction products (such as HCOOH and CO) are usually obtained in the reaction. Here products and intermediates are produced at low overpotential but via kinetically complex proton coupled electron transfer pathways to give species including carbon monoxide (CO), formate ($HCOO^-$)/formic acid (HCOOH), methanol (CH_3OH), methane (CH_4), ethylene (C_2H_4), ethanol (CH_3CH_2OH) by combining with multiple electrons (e^-) and protons (H^+) transfer which are listed in Table 1.1. Furthermore, the electrochemical CO_2RR in an aqueous solution is usually accompanied by the occurrence of the hydrogen evolution side reaction (HER). Because the reaction potentials of H_2 evolution and CO_2 reduction are very similar, which will result in two competitive reactions. The high hydrogen production rate greatly suppresses the selectivity to high value-added carbon-containing products and the applied energy is also wasted instead of reducing CO_2. Therefore, the ideal electrocatalyst for high-activity CO_2RR should have high current density, high selectivity (while suppressing HER) and good stability.

Table 1.1: Electrochemical CO_2 reduction reactions with different electron pathway and equilibrium potentials.

Reaction	$E°\ (V\ vs.\ RHE)$
$CO_2 + 2H^+ + 2e^- \rightarrow CO\ (g) + H_2O$	-0.11
$CO_2 + 2H^+ + 2e^- \rightarrow HCOOH\ (l)$	-0.21
$CO_2 + 4H^+ + 4e^- \rightarrow HCHO\ (l) + H_2O$	-0.07
$CO_2 + 6H^+ + 6e^- \rightarrow CH_3OH\ (l) + H_2O$	0.03
$CO_2 + 8H^+ + 8e^- \rightarrow CH_4\ (g) + 2H_2O$	0.17
$2CO_2 + 12H^+ + 12e^- \rightarrow C_2H_4\ (g) + 4H_2O$	0.08
$2CO_2 + 12H^+ + 12e^- \rightarrow C_2H_5OH\ (l) + 3H_2O$	0.09
$2CO_2 + 14H^+ + 14e^- \rightarrow C_2H_6\ (g) + 4H_2O$	0.14
$3CO_2 + 18H^+ + 18e^- \rightarrow C_3H_7OH\ (l) + 5H_2O$	0.10

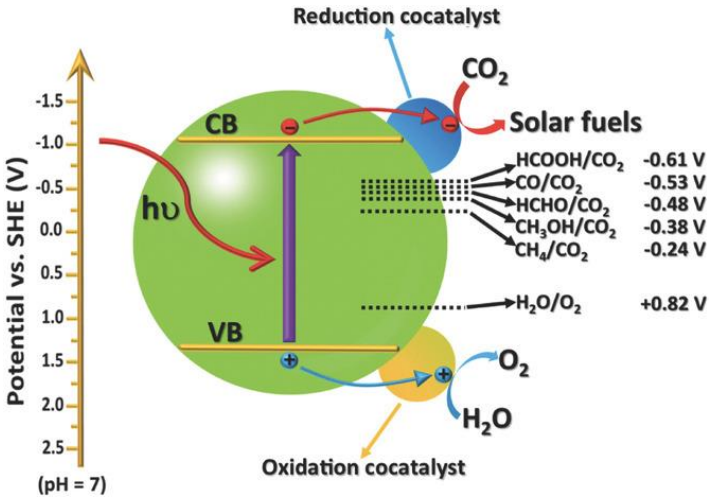

Figure 1.2: Scheme of photocatalytic CO_2RR on a semiconductor photocatalyst with reduction and oxidation cocatalysts for solar fuel production.[22] Image is originated from J. Ran, M. Jaroniec and S.-Z. Qiao, Adv. Mater., 2018, 30, 1704649.

In recent years, in the research literature of CO_2RR, many newly-developing catalyst materials have attracted the attention of researchers to improve catalytic activity and stability. According to different reaction characteristics, the mainstream catalyst materials can be divided into three categories: photocatalysts, biocatalysts and the most widely applied electrocatalysts.[23–25] For photocatalytic CO_2 reduction a reaction mechanism is shown in Figure 1.2, where the reaction is usually carried out in a gas or liquid phase environment, and involves carbon dioxide reduction and complementary water oxidation. Most of the research revolves around the

development of oxide, phosphide, sulfide and metal-organic framework catalyst materials.[22,26] Common reduction products are CO, CH_4 and CH_3OH, however, most photocatalysts are still limited to promoting the formation of single carbon products. Considering that the system needs to be operated under sunlight in practical applications, the catalyst should show long-term stability and high photon to product conversion efficiency. At the same time, it is necessary to reduce the occurrence of side reactions such as the hydrogen evolution reaction (HER) in aqueous systems where water is the electron and proton supply.[27] Current researches have made progress either improving the reactivity by adding cocatalyst, reducing electron-hole recombination by nanostructuring, and improved reactor design, etc.[28,29] The introduction of specific nanostructures can help accelerate charge separation and transfer efficiency and enhance molecular adsorption and activation capabilities. Unfortunately, photocatalysts with the ability to resolve all the above challenges simultaneously for photocatalytic CO_2 reduction applications in the real world have not been realized.

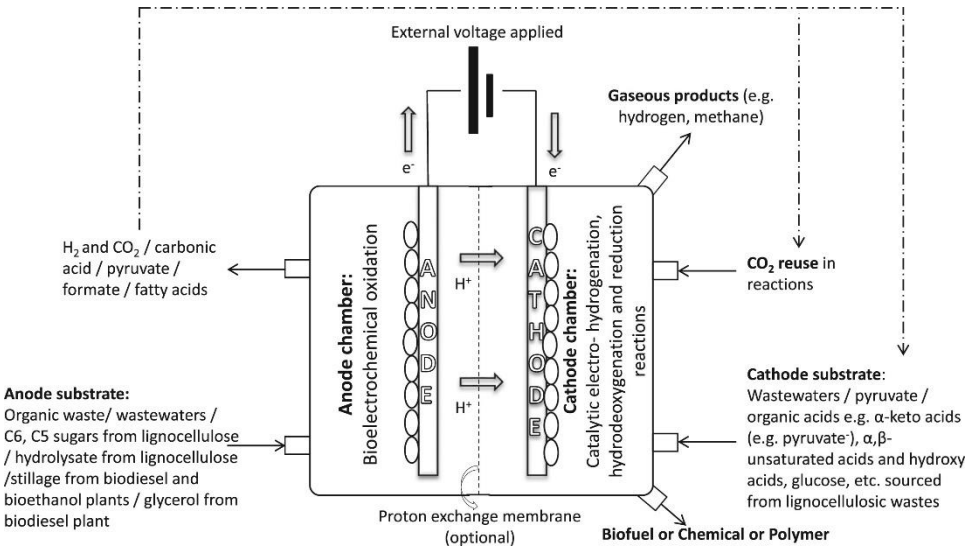

Figure 1.3: Scheme of bioelectrolysis processes with anode and cathode substrates that can be sourced from waste biomass.[30] Image is originated from J. Sadhukhan, J. R. Lloyd, K. Scott, G. C. Premier, E. H. Yu, T. Curtis and I. M. Head, Renew. Sustain. Energy Rev., 2016, 56, 116–132.

For biocatalytic CO_2 reduction (a system is shown in Figure 1.3), researchers have found some biocatalysts that can reduce CO_2 gas to specific molecules under specific ambient temperature, pressure and pH conditions.[31] Because of the presence of biomass, it can reduce the energy (overpotential) required to activate CO_2 reduction

to a certain extent due to the introduction of more active sites.[32] The most common reaction configurations are enzyme (electrode) reduction of CO_2 and cell (microbial electrode) reduction of CO_2.[33] The former system is mainly through electrochemical devices combined with formate dehydrogenase (FDH, which can promote formate/CO_2 conversion at low redox potential), or carbon monoxide dehydrogenase (CODH, which promotes CO/CO_2 conversion), or formate dehydrogenase (FDH)-formaldehyde dehydrogenase (FLDH)-ethanol dehydrogenase (ADH) synergistic effect (which promotes the production of methanol from CO_2 through a multi-enzyme cascade), or nitrogenase (which has catalytic activity of reducing CO_2 to formates, CO and hydrocarbons) to achieve CO_2 conversion.[33–36] However, due to the influence of membrane structure, enzyme kinetic factors, the electron transfer and energy transmission between the electrode and the enzyme can be limited, which is not conducive to mass transfer in reactions. Hardly any report has clearly pointed out the exact electron utilization rate during the reaction process, and the catalytic mechanism of many reactions is still unclear. Simultaneously, the expensive enzyme purification technology greatly increases the cost of achieving large-scale applications. In contrast, some recent systems are based on the presence of electron transfer in living cells with the electrode surface.[30] So far, only a very small number of strains have the ability for CO_2 catalytic reduction, and the products are only limited to methane and acetic acid (relying on the biological characteristics of the strains), the distribution of reaction products is not currently diverse.[37] Furthermore, due to the formation of gaseous products and the presence of HER, the microbes tend to detach from the electrode surface.[38] Overall, biocatalysis technologies are still in the early stages of development, and the technology is not yet mature enough to be used for large-scale batch reactions.[39,40]

In contrast, the electrocatalytic reduction of CO_2 using inorganic electrocatalysts which has been studied for many years is considered to a promising future technology for scale-up.[41–43] Electrocatalytic reduction of CO_2 can proceed under homogeneous or heterogeneous conditions and is usually carried out under mild conditions of room temperature and atmospheric pressure (Figure 1.4). An aqueous medium usually provides the proton source for CO_2RR, and the distribution of reaction products can be diverse. According to existing literature reports,[44–47] more than twenty gaseous and liquid phase products from CO_2RR have been found (The standard electrode potentials of each product for CO_2RR half-reactions are listed in in Appendix 1, Table A 1.1). As an important intermediate for the formation of many reduction products, the formal generation of $* CO_2^-$ is the first stage of CO_2RR, usually a rate-limited stage ($* CO_2^-$ has a high energy barrier, (-2.20 V vs.SCE), and is a key

step in determining the direction of the reaction (formation of formates or $* CO$ intermediates)[48,49] Subsequent reduction processes occur more easily.

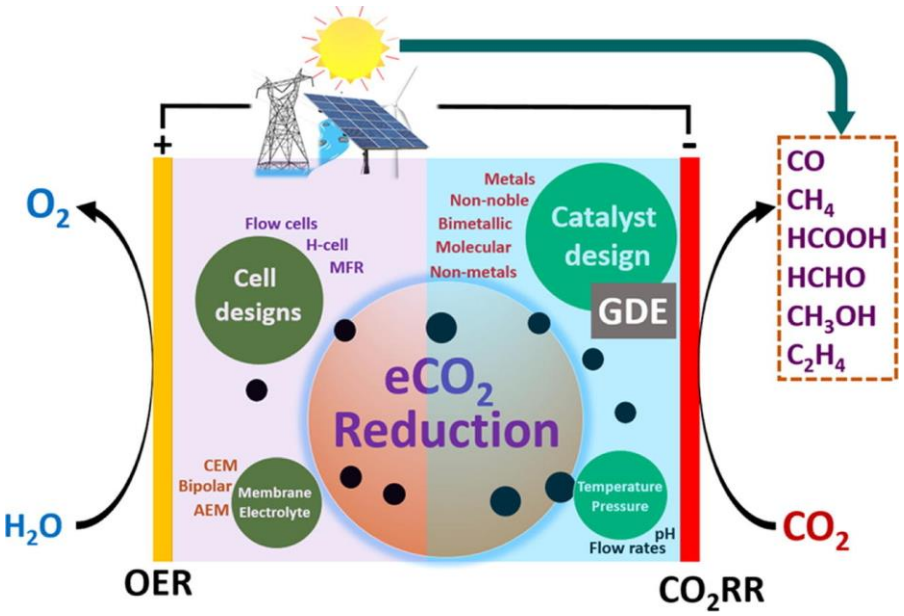

Figure 1.4: Scheme of electrocatalytic CO_2RR with cathodic reduction and anodic oxidation processes for carbon product formation.[50] Image is originated from R. A. Tufa, D. Chanda, M. Ma, D. Aili, T. B. Demissie, J. Vaes, Q. Li, S. Liu and D. Pant, Appl. Energ., 2020, 277, 115557.

Metal CO_2RR electrocatalysts can be divided into four categories according to the binding properties of the catalyst electrodes for key hydrogen and carbon monoxide intermediates ($* H$ and $* CO$) as shown in Figure 1.5: *a)* catalysts such as Hg, Ti, Cd, Zn, Pb, Sn do not form surface hydrides and weakly bind CO to give formate or formic acid, usually via an outer sphere mechanism.[51–54] *b)* catalysts such as Fe, Ni, Ir, Ru, Rh, Pd, Pt strongly bind CO and H leading to preferential H_2 formation because the concentration of water is much greater than CO_2.[55–58] *c)* catalysts such as Au, Ag, Zn, Ga have very weak hydride adsorption and weakly bind CO primarily generating CO and water.[59–61] *d)* Cu, can bind CO and hydrides with intermediate bond strength promoting reaction and supporting surface mobile intermediates that can couple to give a range of hydrocarbon and oxygenate products including C_{2+} from C-C coupling.[62,63] Meanwhile, the exchange current density of HER on metals in acidic media has been reported in a large number of experimental studies. Plotting current density values against the metal hydrogen bond strength shows a characteristic behavior known as the “volcano” curve (Figure 1.5 (b)) and is based on the Sabatier principle: the HER activity increases up to a peak obtained

when medium bond strengths (Pt, Rh, Ir) are reached and then decreases again towards higher bond strengths, from which it can be seen that the bond strength of Cu-H is moderate. Moreover, using an earth abundant metal with low-cost such as copper can benefit to support potential large-scale industrial application.[64–68] However, even though the technologies of CO_2RR have gradually matured, there remain major challenges, such as: ***a) Low solubility of CO_2 in aqueous solutions***, which limits mass transfer to the electrode surface ***b) Low product selectivity*** (especially for multi-carbon products with high added value). ***c) The catalytic activity***, which is directly affected by the geometric area, active sites and adsorption properties of catalyst electrodes, ***d) Low stability***, due to morphological changes and coking which poisons the surface. For catalysts that have been extensively studied, HER remains the most difficult problem to overcome in CO_2RR, especially for metal electrodes. In essence, the low selectivity of CO_2RR for specific products on many metal electrodes is mainly due to HER occurring at high overpotential, rather than inherent low catalytic activity. Therefore, finding suitable metal electrodes and improving electrode performance are still urgent challenges in this field.

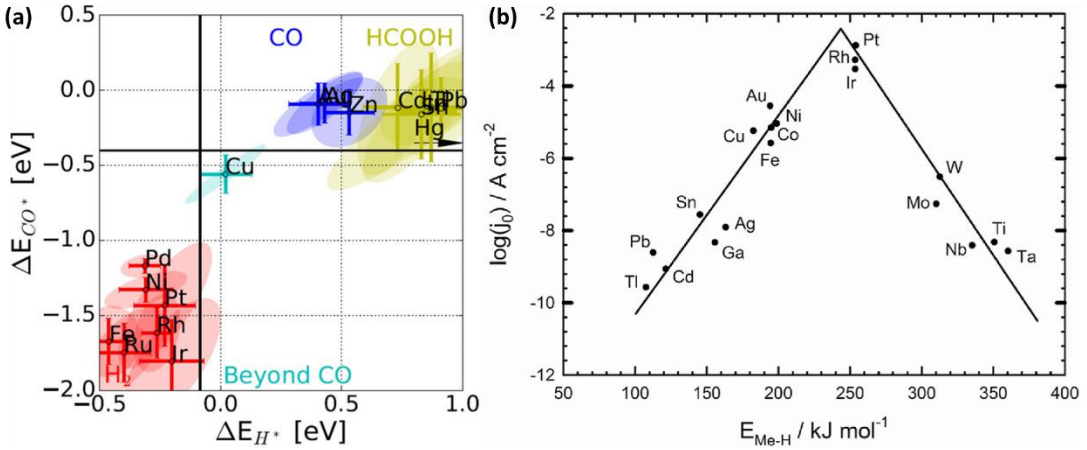

Figure 1.5: Metal catalyst classification for CO_2 reduction based on the binding energies of intermediates to CO ($\triangle E_{CO^*}$) and to H_2 ($\triangle E_{^*H}$).[51] (b) A volcano plot for the HER derived from the experimental current density and the DFT-calculated metal-hydrogen bond strength. Pt is near the apex of the plot, meaning it has nearly the optimal catalytic activity.[69] Image is originated from A. Bagger, W. Ju, A. S. Varela, P. Strasser and J. Rossmeisl, ChemPhysChem, 2017, 18, 3266–3273 and S. M. Stratton, S. Zhang and M. M. Montemore, Surf. Sci. Rep., 2023, 78, 100597.

1.3. Electrochemical CO_2 reduction reaction based on copper catalysts and proton-coupled electron transfer process

1.3.1. Copper-based catalysts

Some transition metals such as Au,[70–73] Ag[74–77] and Zn[78–81] have a catalytic activity for CO_2RR, but Cu is the only metal catalyst that can directly convert CO_2 into a variety of hydrocarbons and alcohol compounds, especially the commercially valuable C_{2+} products due to the combination of $*H$ and $*CO$ intermediates.[82,83] For copper-based electrocatalysts, the product selectivity is affected by the morphology, microstructure and near surface composition of the copper. For example monocrystal copper, Cu(111) is favorable for the formation of CH_4, while Cu(100) is more favorable for the C-C coupling to promote the generation of C_2H_4.[84,85] In addition, the electrocatalytic reduction of CO_2 normally needs to be carried out at a relatively negative potential resulting in a competitive HER side reaction in a solution with proton source, which negatively affects Faraday efficiency (FE). Normally, at 1 atmosphere pressure, the ratio of CO_2 to H_2O molecules in the aqueous solution is ~1: 1300.[86] Although protons (H^+) can be easily obtained in aqueous solutions by water electrolysis, the supply of CO_2 is limited by its low concentration and mass transfer to the catalyst surface.

1.3.1.1. Challenges of Cu-based catalysts

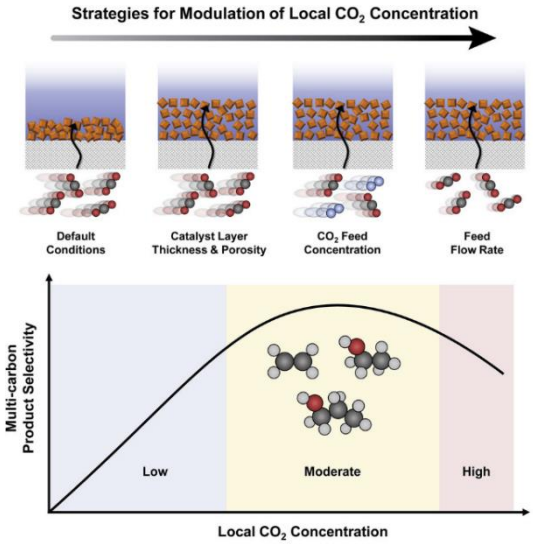

Figure 1.6: Schematic illustration of the strategies to modulate local CO_2: controlling catalyst layer structure or CO_2 feed concentration/feed flow rate in a gas-diffusion electrodes (GDE) system. Gray, red, and blue balls represent C, O, and N atoms, respectively.[87] Image is originated from Y. C. Tan, K. B. Lee, H. Song and J. Oh, Joule, 2020, 4, 1104–1120.

The following factors greatly affect CO_2RR using Cu-based electrocatalysts and also represent challenges for use at scale: ***(i) Local CO_2 concentration at the electrode surface***. The solubility of CO_2 gas in aqueous solution is very low, which is not conducive to fast CO_2RR. However, Tan et al.[87] demonstrated that excessively high local CO_2 concentration is not conducive to the formation of desirable multi-carbon products as shown in Figure 1.6. Therefore, it is essential to control the local CO_2 concentration if C_{2+} products are the target. Control of catalyst morphology is one strategy, for example, three-dimensional structures conducive to the capture and storage of CO_2 gas, which is significantly better than that of flat Cu foil.[88] Also surface engineering strategies have been adopted to change the surface properties of Cu-based electrodes, to enhance the binding capacity with CO_2 by molecular compounds, or to enhance the hydrophobicity of electrode surface to capture more CO_2 gas.[89,90] ***(ii) Kinetics and mass transfer***. Increasing the rate of CO_2RR suppresses the HER side reaction. The surface of Cu-based electrodes can be modified by compounds to make the electrode have a stronger binding capacity for CO_2. Simultaneously, the modified surface can be used to increase the diffusion gradient to enhance the CO_2 mass transfer kinetics and further improve the selectivity of catalysts. Reactor engineering is also important for mass transfer which is considered later in section x ***(iii) Surface area and active sites***. The number of active sites directly affects the electrocatalytic performance. The most common strategies to effectively increase the density of catalytic active sites is to increase the surface area. The surface morphological structure of Cu-based catalysts, especially nanostructured three-dimensional electrodes, is conducive to increasing the electrode surface area.[91] In addition, chemical changes to the electrode surface will also affect the distribution and type of active sites and modify the electrolyte-gas-electrode interface potentially increasing activity and selectivity.[92,93] ***(iv) Electrode stability***. Electrodes should have good stability and reproducible performance during long-term operation and the intermediate products generated during reaction should not cause poisoning or deactivation of electrodes. The surface of Cu based electrodes is known to undergo structural changes during CO_2RR making it difficult correlate structure with function and stability. Surface engineering strategies can stabilise the electrode surface structure extending lifespan and improving stability.[94]

1.3.1.2. Metrics for comparing CO_2RR Cu-based catalysts

The key metric of CO_2RR is the partial current density (rate of product formation per geometric surface area or active site), which should be measured as a

function of applied potential. However, there are no agreed standards for reporting CO_2RR data which can be presented in numerous ways most often as a Faradaic efficiency at a particular potential. The accurate determination of the number of electrochemically active sites is also extremely difficult. This limits the insight available to determine the role of often interdependent factors for CO_2RR rate and selectivity. A key consideration is the *area of the electrode*, which can be defined in multiple ways to obtain a current density and is often approximated by determining the electrochemical active surface area (ECSA) and roughness factor (R_f) of the electrode. However, these measurements are not defined with respect to CO_2RR and the number of active sites is not be determined directly. The applied *potential* can be measured accurately and the mechanisms of PCET and CO_2RR are potential dependent. Product selectivity reported as Faradaic efficiency as a function of potential has less meaning without knowledge of the number of active sites (or pragmatically, the active surface area) to determine the preferred metric of partial current density. The *mass transfer rate* can be measured as an average bulk value using a flow meter and sufficient CO_2 needs to diffuse to the cathode surface during reaction. The mass transfer of CO_2 in water is difficult due to low solubility and often limits the current requiring careful cell and reactor design. In typical H-cells the concentration of CO_2 on the cathode surface is low, which is not conducive to increasing the rate of CO_2RR and has led to the development of gas diffusion electrodes based on fuel cell technology. The *pH* during the reaction varies and OH^- will be generated on the surface of the cathode, resulting in a large increase in local pH value. Like the preceding effect of CO_2 concentration, changes in pH will also affect the concentration of CO_2 on the cathode surface via equilibria with HCO_3^- and CO_3^{2-} species which cannot be reduced, and affecting the PCET rate. Theoretical models are available to estimate the pH during CO_2RR.[95,96]

1.3.2. Proton-coupled electron transfer process during CO_2RR

1.3.2.1. Mechanism of CO_2RR via PCET process

Proton-coupled electron transfer process usually play an important role in catalytic reactions in water where the transfer of each electron is coupled with protonation to reduce the activation energy (overpotential) of reduction by minimising electron-electron repulsion.[97] The exact mechanism and order of events can vary dependent on the system. For an electrocatalytic reaction on a metal electrode such

as Cu in an aqueous solution, the protons in solution can be transferred to the electrode surface and reduced forming a metal-hydrogen (hydride) bond.

During the CO_2RR process, CO_2 in the solution will diffuse to the cathode surface for PCET to obtain the key reaction intermediates, which are further converted into the final C_1 and C_{2+} products via further PCET processes with protonation occurring via the electrode or surface. The limiting step of CO_2RR could be the mass transfer of CO_2 on to the cathode surface, the electron transfer to CO_2, and the process of PCET of CO_2 and any reaction intermediates.[98–100] For Cu electrodes, these limitations can result in low adsorption of CO_2 on the copper surface, low product selectivity, and high over-potential. Generally, there is an electric double-layer region of 5-10 nm on the surface of the cathode catalyst. By adjusting the surface of the catalyst, this may help to improve the adsorption capacity of CO_2 and the reaction rate of PCET.[101] In addition, continuous CO_2 consumption and hydroxide (OH^-) ion generation will occur on the cathode surface during the reaction, which will cause changes in the cathode surface environment. Interface design strategies could help to stabilize the electrode surface environment and control the PCET rate by the interaction between the modifying surface groups, electrolyte and CO_2 gas.

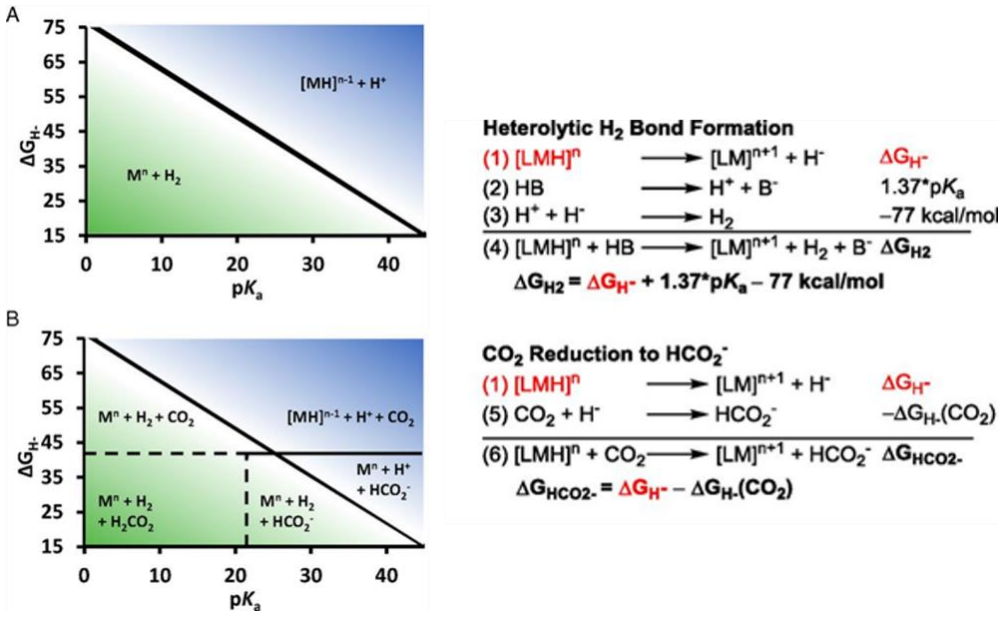

Figure 1.7: Free energy calculations for H_2 and HCO_2^- generation from metal hydrides and aqueous thermodynamic product diagrams (A without CO_2 and B with CO_2).[102] Image is originated from B. M. Ceballos and J. Y. Yang, PNAI, 2018, 115, 12686–12691.

Regulating the rate and selectivity of the CO_2RR by means of control of PCET is a key principle of this project. Figure 1.7 shows the thermodynamic products as a function of hydricity (ΔG_{H^-}, thermodynamic requirement for CO_2 reduction) of the metal hydride intermediate versus proton activity (pK_a).[102] In the green area, the HER side reaction is thermodynamically favourable indicating that HER is favoured compared to C_1 product (formic acid in Figure 1.7) under many initial reaction conditions. However, under polarization the conditions are very different at the electrode surface where H^+ is consumed and the pH is much higher than in the bulk. Only at lower ΔG_{H^-} and higher pK_a (lower right blue triangle of figure B) is CO_2 reaction to HCO_2^- thermodynamically favourable compared to HER. In multiple PCET processes, the catalyst can lower the activation barrier by forming a surface bound intermediate, which is different from the high energy requirements of solution processes. Therefore, multiple PCET process can kinetically compete with HER, and improve the selectivity of products from CO_2RR processes. The formation of CH_4 on Cu(100) following the PCET mechanism has been confirmed.[103] Not only limited to copper electrodes, for sputtered Ag thin film electrodes, when the applied potential is -1.40 V to -1.55 V (vs.Ag/AgCl), CO_2 reduction mechanism in KCl electrolyte also follows the PCET mechanism.[104] However, the standardized evaluation of PCET rate in other reaction process under different experimental conditions is still limited.

1.3.2.2. The effect of PCET process on the C_{2+} product selectivity of CO_2RR

Recently, more research has focussed on acquiring valuable C_{2+} products through Cu-based electrocatalysis. During CO_2RR on Cu-based catalysts, the primary intermediate $*CO$ is able to couple multiple PCET steps to form C-C intermediates, as shown in Figure 1.8.[105] The limiting steps (marked in red in Figure 1.8) usually occur at the solid-liquid-gas three-phase interface which greatly affects the catalytic reactivity. Generally, products are produced though three stages: (i) CO_2 gas is adsorbed on the surface of Cu electrodes and combined with the catalysts in the Helmholtz layer and protons and electrons to form the primary intermediate $*CO$. (ii) multistage PCET and C-C coupling to form multiple reaction intermediates. (iii) Small carbon-containing molecules obtained by electrocatalytic reduction will be desorbed from the catalyst surface and diffused into the electrolyte.[106,107]

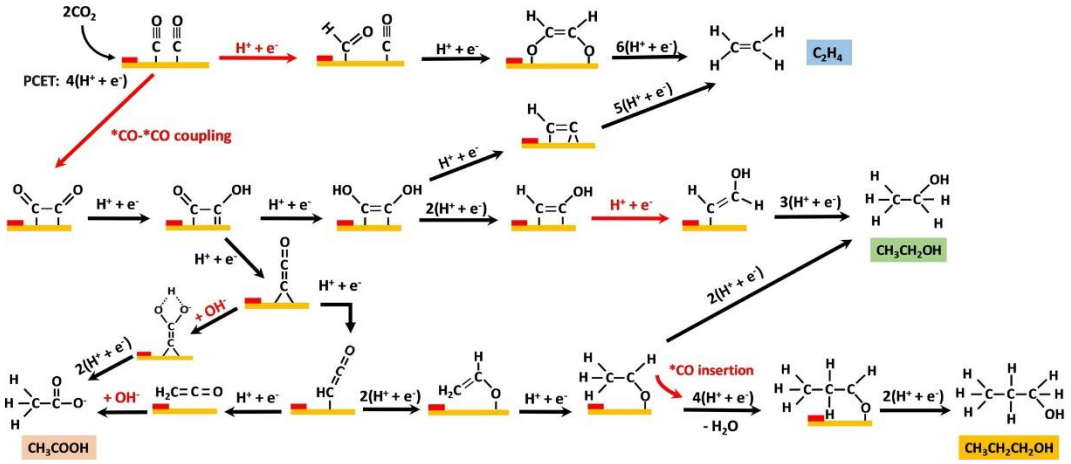

Figure 1.8: Reaction mechanisms of CO_2RR to C_{2+} products (the rate determining steps are marked in red).[105] Image is originated from W. Zheng, X. Yang, Z. Li, B. Yang, Q. Zhang, L. Lei and Y. Hou, Angew. Chem. Int. Edit., 2023, 62, e202307283.

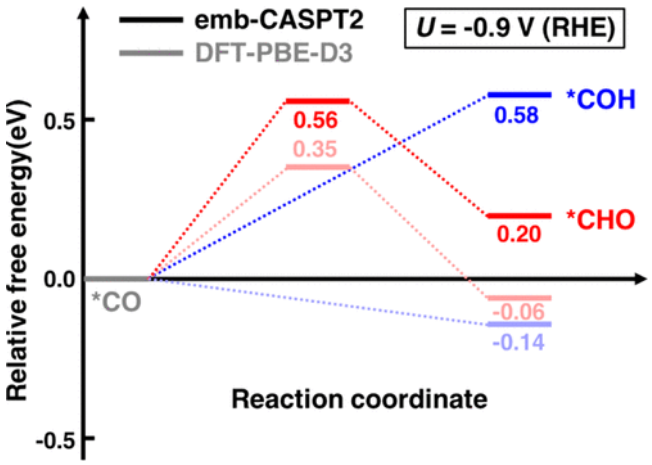

Figure 1.9: Energetic differences of the CO reduction reaction on Cu(111) to form *CHO (red lines) and *COH (blue lines) via a PCET path predicted between emb-CASPT2 and DFT-PBE-D3 on planar Cu(111)—an ECW correction.[108] Image is originated from Q. Zhao, J. M. P. Martirez and E. A. Carter, J. Am. Chem. Soc., 2021, 143, 6152–6164.

The sufficient adsorption strength of the primary intermediate $*CO$ on the Cu-based catalyst surface (to the active sites) is a key factor affecting the C-C coupling and multistage PCET steps to improve the selectivity of C_{2+} products. Much research has been focussed on ensuring that enough $*CO$ can be adsorbed on the surface of Cu-based catalysts to promote coupling by further designing and improving the morphology, structure, surface environment and three-phase interface of Cu-based catalysts.[109–114] Simultaneously, since $*H$ and $*CO$ adsorbed on the surface of Cu-based catalysts compete to bind to the surface active sites, the proportional

relationship between adsorption energy of $*H/*CO$ intermediates will also affect the yield of C_{2+} products. In response to this, several multi-component catalysts have been developed to improve the surface adsorption rate of $*CO$.[115,116] In addition, density functional theory (DFT) has also been applied to calculate the adsorption rate of $*CO$ and the kinetics of the C-C coupling reactions.[117–119] For example, Zhao et al.[108] compared PCET and *H transport paths in CO_2RR using embedded correlation wave function (ECW), and found that more $*CO$ can be reduced to $*COH$ intermediates on Cu(111) when a potential of −0.9 V was applied and with the increase of potential, the trend of generating intermediates gradually changes from $*COH$ to $*CHO$ (as shown in Figure 1.9).[108] Zhang et al. designed a layered precursor derived $CuAl_2O_4$/CuO catalyst.[120] Through DFT combined with in-situ spectroscopy, it has been found that $CuAl_2O_4$ in the catalyst regulated the $*H$ coverage rate by promoting the dissociation of H_2O, and high $*H$ coverage rate was conducive to the formation of hydrogenated $*HCCHOH$ intermediate, which is beneficial to ethanol production (as shown in Figure 1.10).

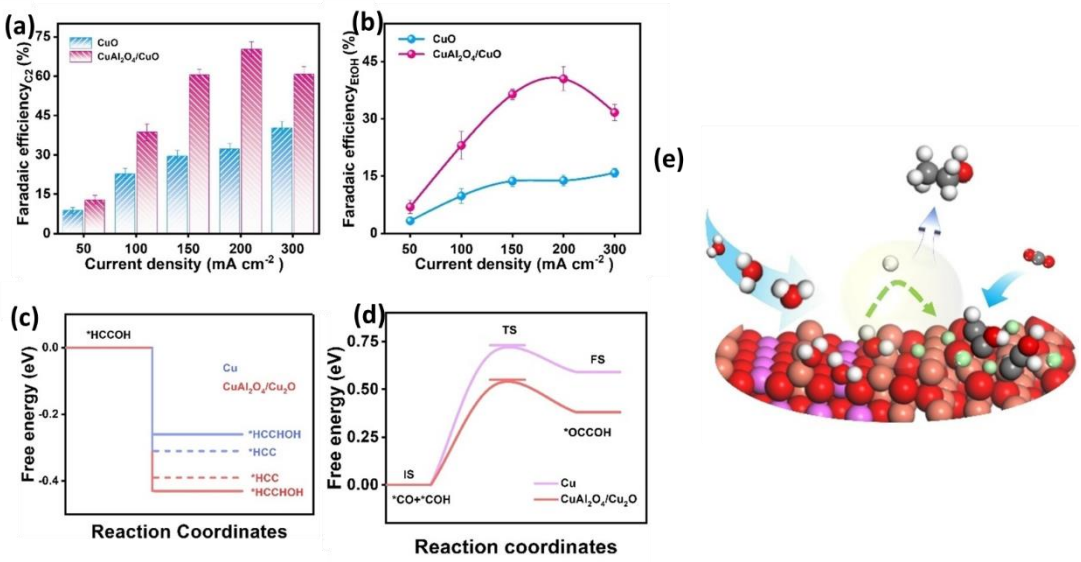

Figure 1.10: CO_2RR performance evaluation: (a) FE values of C_2 products on CuO and $CuAl_2O_4$/CuO catalysts at increasing current densities. (b) FE values of ethanol product on CuO and $CuAl_2O_4$/CuO catalysts at increasing current densities. (c) Free energy diagram for the hydrogenation (*HCCOH to *HCCHOH) and dehydroxylation (*HCCOH to *HCC) steps on Cu(111) and $CuAl_2O_4$/CuO(004)/Cu_2O(111) model. (d) Energy profiles for initial state (IS), transition state (TS), and final state (FS) of C-C coupling on Cu(111) and $CuAl_2O_4$/CuO(004)/Cu_2O(111) model. (e) Schematic of CO_2RR to ethanol on $CuAl_2O_4$/CuO/Cu_2O catalyst. Red, white, gray, orange and purple balls stand for oxygen, hydrogen, carbon, copper and aluminum, respectively, and green balls stand for adsorbed *H.[120] Image is originated from T. Zhang, B. Yuan, W. Wang, J. He and X. Xiang, Angew. Chem. Int. Edit., 2023, 62, e202302096.

1.4. Microenvironment and interface design strategies of Cu-based catalysts for CO_2RR

In view of the challenges still faced by Cu-based catalysts, in addition to the regulation of catalyst composition, the design and improvement of the surface microenvironment and three-phase interface of Cu-based catalysts also have an important impact on the CO_2 conversion efficiency, catalyst activity and stability. The reaction microenvironment usually includes the solid-liquid-gas three-phase interface on the catalyst surface, which impacts the reaction kinetics and thermodynamics. The interface design strategies can adjust the surface properties of the copper-based catalyst, such as hydrophobicity and surface absorbability for CO_2, so that the surface environment of the catalyst tends to be stable, to increase the PCET rate in the reduction process, enhance the selectivity of the electrode for specific products, and improve the overall efficiency of CO_2RR. Different strategies can have complex effects on CO_2RR activity and selectivity, and until now research is mainly empirical using various reactor designs making it difficult to extract clear design and operating principles for a specific target product.

1.4.1. Catalytic microenvironment of Cu-based catalysts for CO_2RR

In general, the catalytic microenvironment of Cu-based catalysts refers to the intrinsic characteristics of the catalyst, which is mostly related to the morphology, surface structure and defects. In Figure 1.11, Cu-based catalysts with different crystal facets, defects and morphology are reported to show specific selectivity for different products in CO_2RR. Strategies to improve the selectivity of Cu-based catalysts for C_{2+} products will be discussed according to the different micro and macro morphologies.

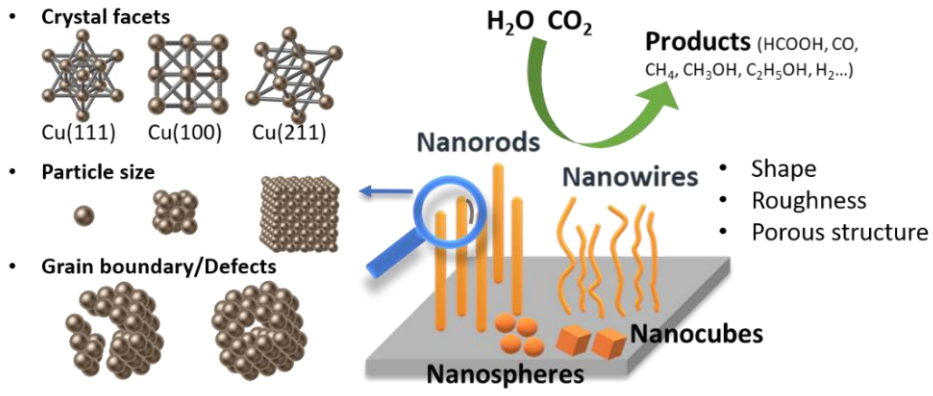

Figure 1.11: Different scales and influence of nano-copper catalysts in CO_2RR.

1.4.1.1. The microstructure and morphology of Cu-based catalysts for CO_2RR

Catalyst morphology can be affected at both micro and macro scale. Generally, the binding energy of reaction intermediates can be adjusted via changing the surface coordination number of Cu, which is dependent on the size of the catalyst particle or surface feature. The particle size effect of Cu nanoparticles has been reported that as the size of the nanoparticles decreases (less than 5 nm), the reduction ability to H_2 and CO will increase.[121] It is ascribed to low-coordinated number can cause more uncoordinated sites to strengthen the adsorption of $*CO$ rather than the intermediates for hydrocarbon. As a part of surface structure tuning, the dominant crystal facets have specific product selectivity due to the different surface adsorption energy of products and intermediates. It has been found that Cu(100) is conducive to $*CO$ dimerization, which contributes to C_2H_4 formation,[122] Cu(110) and Cu(111) are favourable for CH_4.[17,123] In addition, defects such as oxygen vacancy or grain boundary can also be beneficial for $*CO$ chemisorption to promote C-C coupling.[124,125]

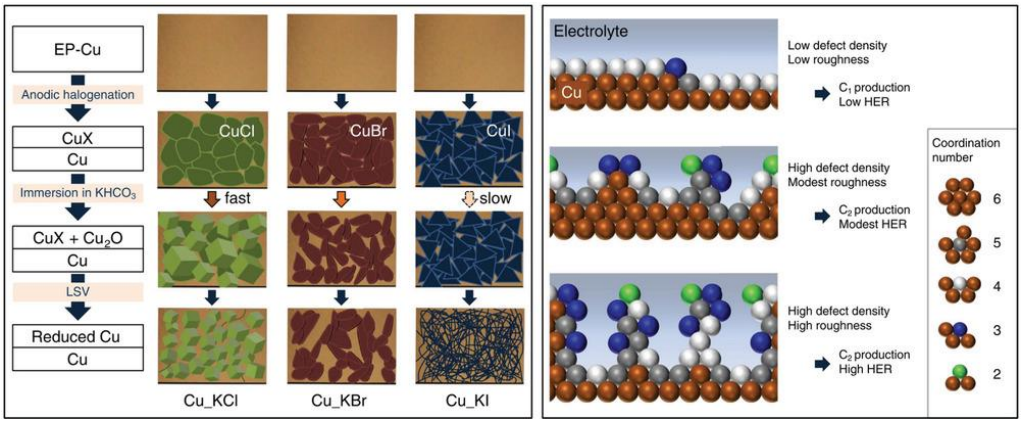

Figure 1.12: Schematics to show the morphology evolution of Cu catalysts prepared from different precursors, and defect structures-influenced electrochemical selectivity. The sphere with green, blue, light gray, dark gray, and brown color represents the Cu atom with the coordination number of 2, 3, 4, 5, and 6, respectively. (EP-Cu: electropolished Cu foil)[126] Image is originated from T. Kim and G. T. R. Palmore, Nat. Commun., 2020, 11, 3622.

It has been found that changing the electronic structure of Cu through defect engineering can enhance the ability of the catalyst surface active sites to bind electrons at the three-phase interface and increase CO_2RR activity.[127–129] Kim et al. used anodic halogenated surfaces of CuCl, CuBr and CuI foil electrodes, high density defects were constructed on the electrode surface by electrical reduction reconstruction as shown in Figure 1.12.[126] Then positron annihilation spectroscopy

(PAS) was used to characterize the defect sites and the Faradaic efficiency (FE) for C_{2+} products was 70.73%, 71.54%, and 72.58%, respectively. Moreover, C_2H_6 was selectively produced when the roughness of the electrode with defect sites was large, while C_2H_4 was selectively produced when the roughness decreased. Gu et al. applied a CO-rich environment to reconstruct stepped-site Cu with high coverages of $*CO$ intermediates.[130] The presence of the surface defects promoted the adsorption of more $*CO$ on the electrode surface, which made the electrode up to 67% FE for C_2H_5OH. However, it is well known that CO_2RR results in Cu surface reconstruction and preparing catalysts that can be reused or exhibit stability for more than a few hours remains a major challenge.

1.4.1.2. The macroscopic morphology of Cu-based catalysts for CO_2RR

The macroscopical roughness and porosity can increase the active surface of the catalyst to increase the overall current density and modify CO_2 mass transfer to increase the efficiency of CO_2RR.[131] Particularly, the introduction of nanostructures can bring better electrocatalytic performance for Cu-based catalysts. Different nanostructures have been widely developed and include Cu nanoparticle (CuNP),[132] Cu nanowire (CuNW),[133] Cu nanocubes (CuNC),[134] Cu needles,[135] Cu dendrites,[136] Cu with biomimetic nanostructures.[137]

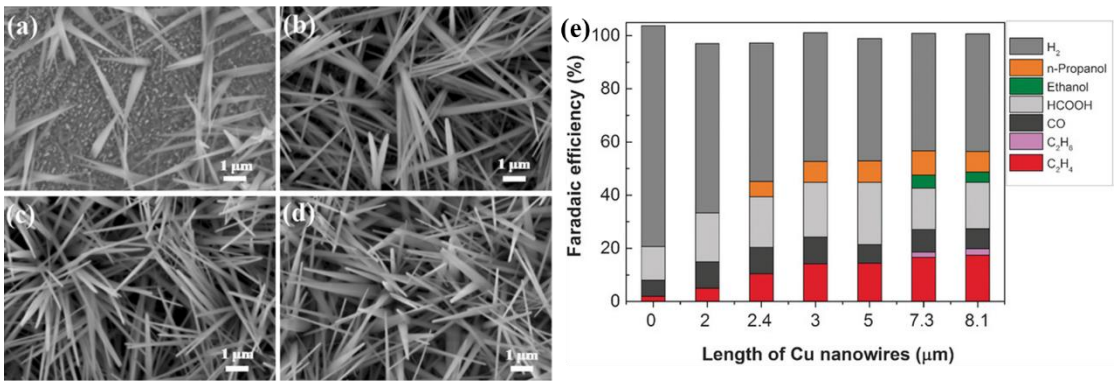

Figure 1.13: (a)-(d) SEM images of $Cu(OH)_2$ nanowires with synthesis time of 1, 3, 5, and 8 mins, respectively. (e) Faradic efficiency for C_2H_4, C_2H_6, CO, HCOOH, ethanol, n-propanol, and H_2 on Cu nanowire arrays with different lengths at −1.1 V vs.RHE in CO_2-saturated 0.1 M $KHCO_3$ electrolytes. (0 μm nanowire = Cu foil)[138] Image is originated from M. Ma, K. Djanashvili and W. A. Smith, Angew. Chem. Int. Edit., 2016, 55, 6680–6684.

Ma et al. prepared CuNW arrays by electrochemical reduction after two-step synthesis of CuO nanowire arrays on Cu foil shown in Figure 1.13.[138] They found that

CO, HCOOH, and C_{2+} products (n-propanol and C_2H_4) could be detected when the CuNW array length was ≥ 2.4±0.56 μm. Furthermore, C_2H_6 and C_2H_5OH can be detected when the length of the CuNW array was ≥ 7.3±1.3 μm. In addition, when the density of the CuNW array increased, the electrode exhibited high selectivity for C_2H_4, because the high-density arrays could cause the rising pH value due to the change of OH^- concentration in the electrolyte near to the electrode surface, which promoted the C-C coupling reaction, and then produced more C_2H_4. It provides a potential method for controlling the selectivity of C_{2+} products. However, in this study, the effect of the length and density changes of CuNW arrays on the specific surface area or electrochemical surface area (and the active sites) was not determined.

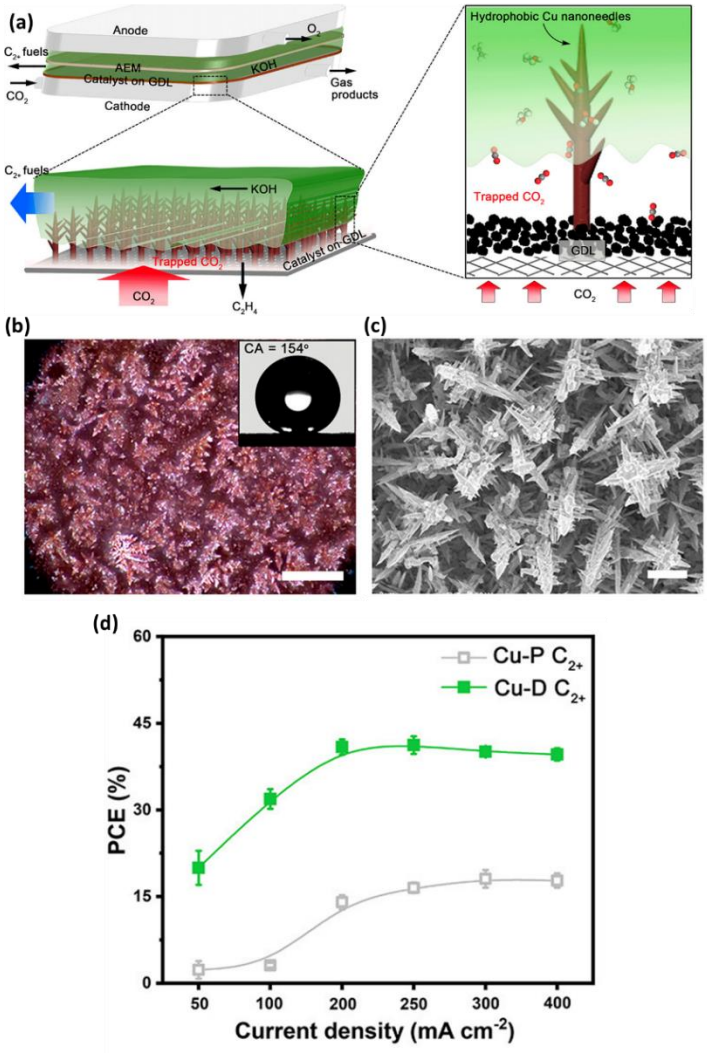

Figure 1.14: (a) Illustration of the microfluidic CO_2 flow cell (left) and the stable gas-liquid-solid triple-phase boundary enabled by the hierarchical electrode design (right). (b)-(c) Optical microscope photograph and SEM image of hierarchical Cu dendrites. Inset shows a water contact angle photograph of a Cu dendrite electrode. (d) Half-cell (cathodic) power conversion efficiency of C_{2+} products on Cu-D and Cu-P electrodes.[139] Image is originated from Z.-Z. Niu, F.-Y. Gao, X.-L. Zhang, P.-P. Yang, R. Liu, L.-P. Chi, Z.-Z. Wu, S. Qin, X. Yu and M.-R. Gao, J. Am. Chem. Soc., 2021, 143, 8011–8021.

Niu et al. constructed a kind of biomimetic copper nano catalysts on gas diffusion layers (GDLs) electrode, which have a layered structure like the Setaria's leaves shown in Figure 1.14.[139] The introduction of this unique structure improved the hydrophobicity of the Cu surface, which was conducive to the construction of a stable solid-liquid-gas three-phase interface, as is reported to significantly increased the concentration of CO_2 gas near the Cu electrode and further promoted mass transfer. The C_{2+} conversion rate on the hydrophobic biomimetic Cu nanoelectrode was as high as 64±1.4% and the Cu nano electrode also had good stability that operating at the industrially relevant current density of 300 $mA \cdot cm^{-2}$. The electrocatalytic properties and parameters of more Cu-based electrocatalysts with different nano-morphologies are listed in Table A1.2.

Therefore, further optimization of the nanostructure and morphology of Cu-based catalysts is of great significance to improve the selectivity of C_{2+} products in CO_2RR. In future studies, it is worth to combine the in-situ spectroscopy, DFT theoretical calculations and electrode electrochemical behaviour analysis to further reveal the influence of nanostructure and morphology on the reaction mechanism and product selectivity.

1.4.2. Modifying the local microenvironment of Cu-based catalysts for CO_2RR

Research on Cu electrocatalyst microstructure and morphology is relatively mature. However, there are still not many studies addressing the effect of local microenvironment near the catalyst surface and effect on product selectivity. Assuming optimization of the inherent properties of Cu-based catalysts it may be possible to gain further improvements by controlling the local microenvironment, so as to enhance the selectivity of certain products. Generally, the local microenvironment can be considered as the reaction environment near the electrode surface, which is embodied in the reaction gas-liquid-solid three-phase interface (shown in Figure 1.15) in most heterogeneous CO_2RR processes. These will also depend significantly on the reactor design. Problems such as competing HER, the low solubility of CO_2 gas in aqueous electrolyte and poor electrode stability, even if some active sites such as special morphology or crystal defects can be successfully constructed on Cu-based catalysts through microstructural regulation, they still show instability under the application of a reduction potential, resulting in the loss of the active sites in the most CO_2RR. Therefore, if the balance and stability of the three-phase interface can be further improved, the reaction activity and stability could be

greatly improved, and it will be more conducive to the C-C coupling process and acquisition of C_{2+} products.

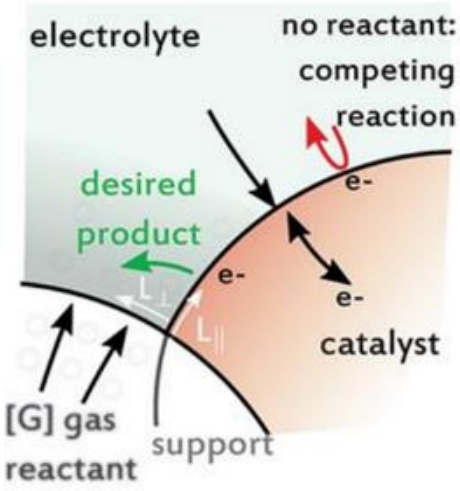

Figure 1.15: The volume in which gas reactants, active sites, and water and ions coexist determines the maximum available current for gas electrolysis. Catalyst regions with limited reactant concentration promote by-product reactions such as HER.[140] Image is originated from F. P. García de Arquer, C.-T. Dinh, A. Ozden, J. Wicks, C. McCallum, A. R. Kirmani, D.-H. Nam, C. Gabardo, A. Seifitokaldani, X. Wang, Y. C. Li, F. Li, J. Edwards, L. J. Richter, S. J. Thorpe, D. Sinton and E. H. Sargent, Science, 2020, 367, 661–666.

In CO_2RR, when the gas-liquid-solid interface is modified, the catalytic activity and catalyst stability will be directly affected. Recently, improving the hydrophobicity of Cu-based catalyst surfaces has been found to be an effective way to improve the stability of the three-phase interface, which can effectively avoid local pH changes caused by low CO_2 solubility or CO_2 rapid consumption near the catalyst surface.[141–144] Rational surface modification to improve the hydrophobicity of Cu-based catalysts is a hot topic in CO_2RR. For example, Wakerley et al[145] modified copper dendrites with 1-octadecanethiol to obtain a superhydrophobic surface (contact angle ≥ 153°), which increased the FE of C_2H_4 (56%), but resulted in a sharp decrease in reaction activity on the blocked electrode surface. Therefore, when selecting coatings or molecules to improve the hydrophobicity on the surface of Cu-based catalysts, consideration should be given to whether the electrochemical surface area and the reactive sites will be blocked by the coatings, or if the introduction of a coating may involve other chemical reactions that poison the electrode.

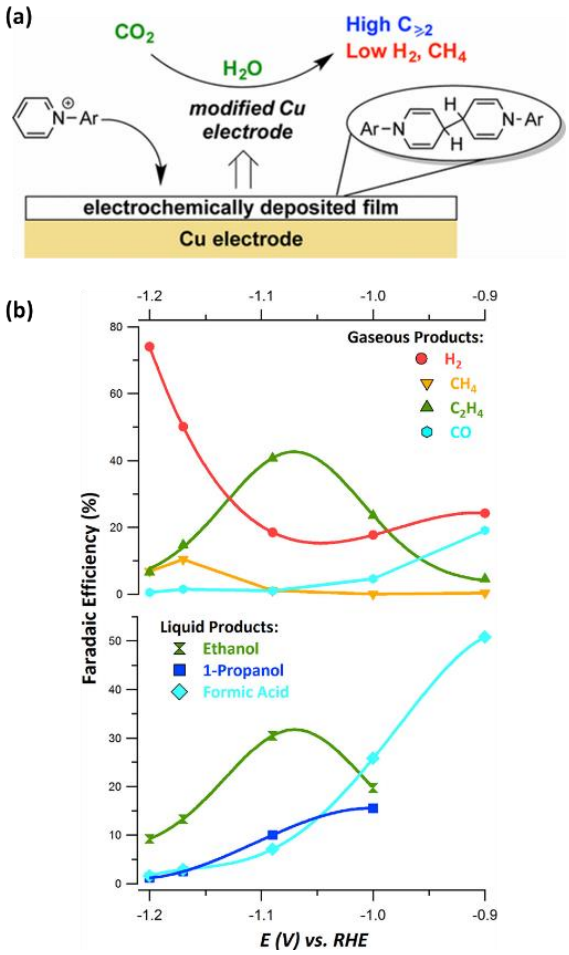

Figure 1.16: (a) The reaction pathway of CO_2RR on polycrystalline copper with N-substituted pyridinium additives. (b) Faradaic efficiency toward products produced during CO_2 reduction on a polycrystalline copper electrode in a CO_2 saturated 0.1 M $KHCO_3$ electrolyte with 10 mM N-tolylpyridinium chloride at different applied potentials.[146] Image is originated from Z. Han, R. Kortlever, H.-Y. Chen, J. C. Peters and T. Agapie, ACS Cent. Sci., 2017, 3, 853–859.

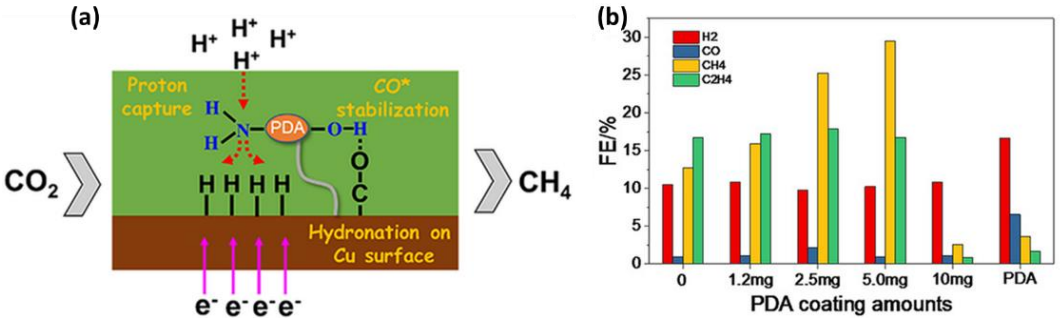

Figure 1.17: (a) The proposed reaction pathway of enhancement of methane formation promoted by polydopamine (PDA) on CuNWs surface. (b) The relationship of products selectivity and PDA coating thickness.[147] Image is originated from H. Liu, K. Xiang, Y. Liu, F. Zhu, M. Zou, X. Yan and L. Chai, ChemElectroChem, 2018, 5, 3991–3999.

Han et al. made the N-tolylpyridinium deposition on the surface of polycrystalline Cu as a film, and some N-heterocycle additives used to suppress CH_4 to obtain C_{2+} products (shown in Figure 1.16).[146] The FE of the modified electrode for C_{2+} were higher than 75%. They used several N-arylpyridinium additives to adjust the ratio of FE for C_{2+} and inhibited the FE of CH_4 and H_2. Liu et al. used polydopamine (PDA) to functionalize Cu nanowires (CuNWs) to enhance the selectivity to CH_4 and verified that the $–NH_2$ group in PDA can help capture H^+ in electrolyte in Figure 1.17.[147] In this way, it will provide a local source of $*H$ for $*CO$ intermediates on the electrode surface, while phenolic hydroxyl groups are conducive reported to enhance the stability of the $*CO$ intermediates on the surface. The selectivity to CH_4 of functionalized CuNWs was higher than that of nonfunctional CuNWs (~2.3 times), while maintaining a stable catalytic operation for more than 14 h. Arquer et al. constructed an ionomer bulk heterojunction (CIBH) architecture, which contains a metal and a superfine ionomer layer with hydrophobic and hydrophilic functionalities.[140] It can transmit gas and ions from tens of nanometres to the micron scale. Through this modification strategy, the CO_2 electrolytic reduction of C_2H_4 on Cu could be realized (45% cathode energy efficiency) at a current density (14.3 $A \cdot cm^{-2}$) in 7 M KOH.

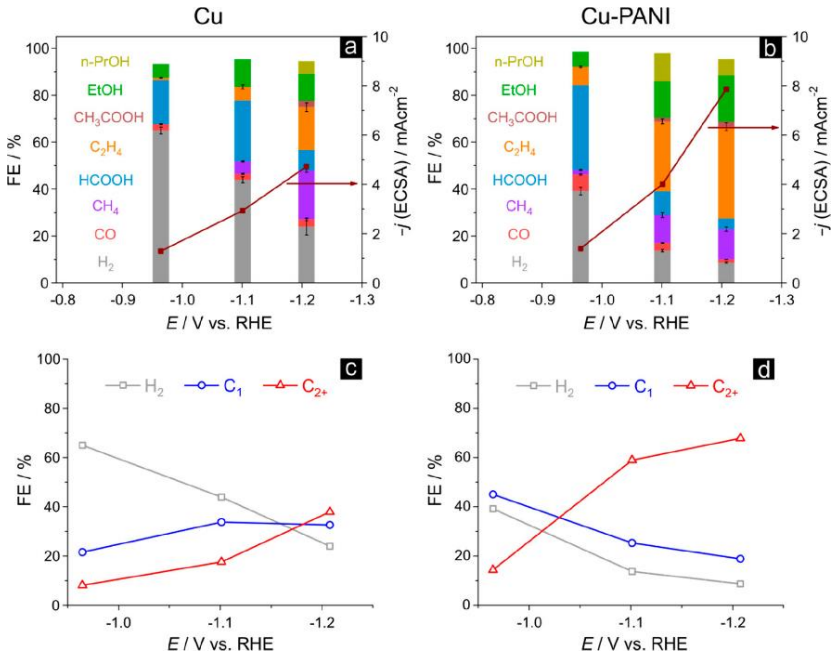

Figure 1.18: Catalytic selectivity of the Cu/PANI interface: (a)-(b) Comparison of the Faradaic efficiency (FE) of every product, as well as the ECSA-normalized current density, for the Cu and Cu–PANI electrode, respectively. (c)-(d) Summary of the FE of H_2, C_1 and C_{2+} production for the Cu and Cu–PANI electrode, respectively.[148] Image is originated from X. Wei, Z. Yin, K. Lyu, Z. Li, J. Gong, G. Wang, L. Xiao, J. Lu and L. Zhuang, ACS Catal., 2020, 10, 4103–4111.

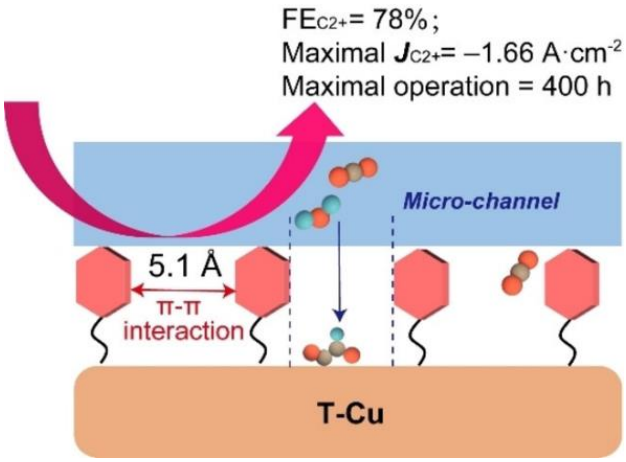

Figure 1.19: Toluene-modified Cu (T-Cu) presents a suitable intermolecular spacing for enriching CO_2 and retarding water transport, as well as forming a hydrophobic interface to inhibit cathodic corrosion, thus leading to high activity and enhanced electrochemical stability.[149] Image is originated from Z. Liu, X. Lv, S. Kong, M. Liu, K. Liu, J. Zhang, B. Wu, Q. Zhang, Y. Tang, L. Qian, L. Zhang and G. Zheng, Angew. Chem. Int. Edit., 2023, 62, e202309319.

As can be seen from the above research, the improvement of interfacial water transport and adsorption of intermediates by adjusting the hydrophobicity of Cu-based catalyst surface is a crucial factor for the realization of efficient C_{2+} production. However, the above research does not clearly identify the influence of the modified coating on Cu-based catalysts on the surface-active sites or even the long-term stability of the electrode operation. Wei et al. introduced a 50 nm thick polyaniline (PANI) film on Cu surface to enhance the hydrophobicity of Cu surface and inhibit HER.[148] At the same time, through the interaction between the –NH– group on the PANI and the CO_2 molecule, CO_2 was enriched on the electrode surface so that the CO intermediate is much easier to be controlled (while promoting the CO–CO coupling). The FE of C_{2+} products increased from 15% (on the original Cu) to more than 60% (on the Cu-PANI) in Figure 1.18, and the CO_2RR can be stably performed on the Cu-PANI electrode for 20 h. At the same time, it has been pointed out that the double-layer capacitance of Cu-PANI electrode was slightly decreased (compared to a Cu electrode), but most of the electrochemical contact on the electrode surface was still not blocked. Considering that when the catalyst surface is modified by some long chain alkyls or polymers to inhibit HER in CO_2RR, the hydrophobic molecules will tend to form a dense hydrophobic layer on the catalyst surface, which may block the mass transfer of CO_2 gas. Liu et al. used toluene to modify a Cu electrode surface and ensured that the distance between benzyloxy group could remain at 5.1 Å, which was able to maintain continuous CO_2 transmission (as shown in Figure 1.19) and the high concentration of CO_2 on the catalyst surface can promote the conversion to C_{2+} (FE

up to 78%) while maintaining reaction stability.[149] This toluene modified Cu electrode is capable of maintaining high stability for up to 400 hours.

More performance comparisons of modified Cu electrodes are listed in Table A1.3. Based on the research results of the modified hydrophobic Cu-based catalysts, the rational design of a Cu surface with molecular modification is a crucial method to control the local microenvironment of catalysts, which can effectively overcome the limitations of mass transfer in CO_2RR, stabilize the reaction three-phase interface, and have the potential to promote the reaction product distribution to C_{2+}.

1.5. Reactor design

Developing and improving reactors is a critical aspect of enhancing mass transfer and CO_2 conversion for CO_2RR and arguably has had the greatest impact on improving CO_2RR activity and selectivity. Reactor size, design, reactor and membrane materials and experimental parameters will affect the current density, selectivity and stability. Common reactor types include H-cell,[150] polymer electrolyte membrane flow cell,[151] microfluidic flow cell,[152] solid oxide electrolysis cell[153] and DEMS cell.[154] An ideal reactor should be conducive to overcoming the CO_2 mass transport limitation, achieve high current density, have good operating stability, and be more capable of realizing commercial-scale CO_2RR applications.

1.5.1. H-cell

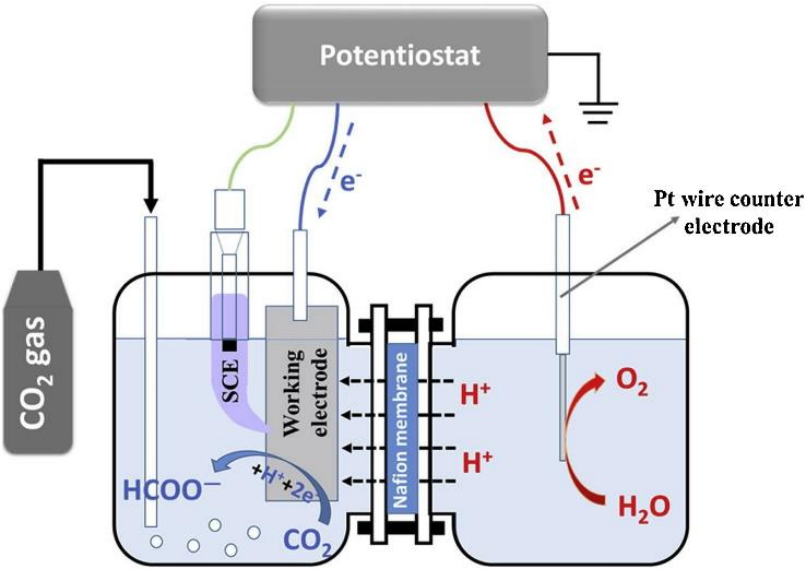

Figure 1.20: A schematic diagram of the conventional H-type electrochemical cell.[155] Image is originated from C. Zhao and J. Wang, Chem. Eng. J., 2016, 293, 161–170.

The H-cell is still the most widely used reactor in CO_2RR because of its relative ease of use. The reactor is mainly composed of a cathode chamber (equipped with a working electrode and a reference electrode) and an anode chamber (equipped with a counter electrode), which are separated by an ion exchange membrane (to prevent re-oxidation of intermediates during the reaction). The overall structure is shown in Figure 1.20. Usually in the electrolysis process, CO_2 gas will be continuously pumped into the cathode chamber and reacts on the catalyst surface to produce products, which are then analyzed using gas chromatography (GC). After the reaction is complete, liquid samples are collected from the cathode chamber to detect liquid products by proton nuclear magnetic resonance (NMR) or high-performance liquid chromatography (HPLC) analysis. Finally, FE of CO_2RR can be calculated through the analysis results. To reduce the errors of product FE, it is necessary to ensure the system is gas tight. The volume of the cathode and anode chambers need to be as small as possible to keep the distance between the electrodes as small as possible to reduce the electrode and solution resistance and increase the concentration of products to be above the detection limit of gas or liquid product analysis.

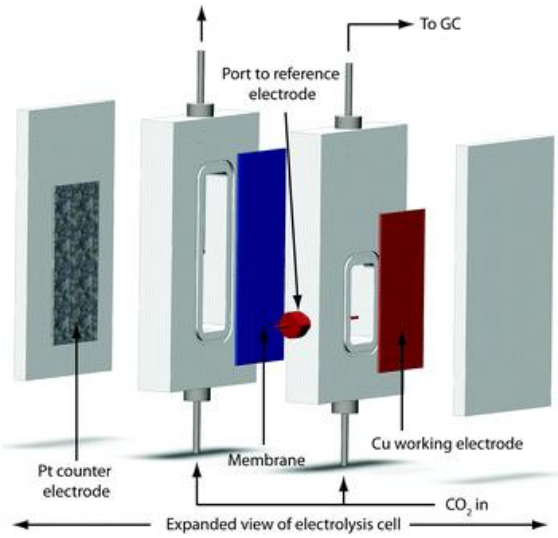

Figure 1.21: A schematic of the modified H-type electrochemical cell for CO_2RR.[156] Image is originated from K. P. Kuhl, E. R. Cave, D. N. Abram and T. F. Jaramillo, Energy Environ. Sci., 2012, 5, 7050–7059.

Many studies on the improvement of H-cell structure have been carried out.[157–159] Kuhl et al designed an H-cell with a larger electrode area (1.5 cm x 3 cm) and a smaller electrolyte volume (8 mL).[160] As shown in Figure 1.21, the structure can effectively reduce the distance between electrodes, which is conducive to improving

the CO_2RR current density and product concentration and sixteen different products from CO_2RR can be detected by using this self-designed reactor. However, H-cell still faces the problem of limited mass transfer, which is mainly manifested in the decrease of CO_2 concentration on the electrode surface with reaction time, which is not conducive to the adsorption and dimerization of $*CO$ on the electrode surface, and the ability of the catalyst to produce C_{2+} products will be reduced as well.

1.5.2. Gas diffusion electrodes and polymer electrolyte membranes in microfluidic flow cells (MFC)

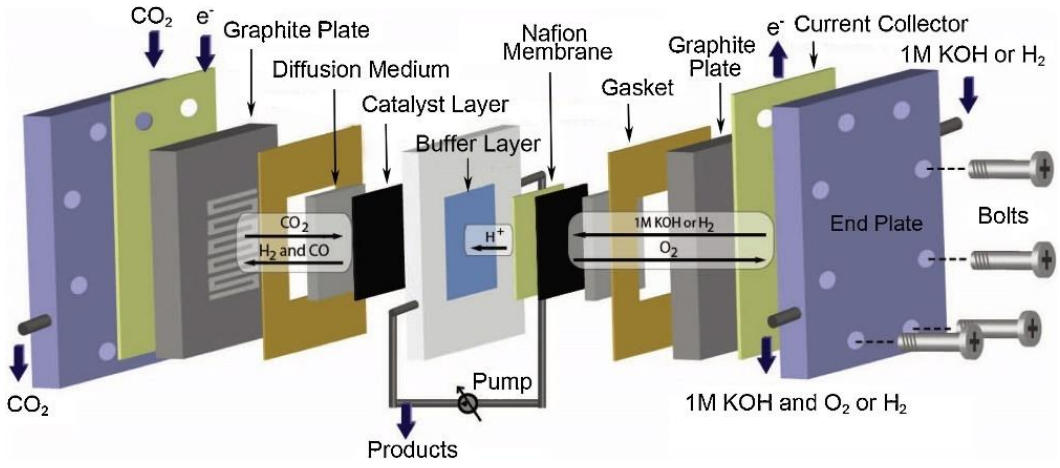

Figure 1.22: A schematic diagram of the polymer electrolyte membrane flow cell featuring a buffer layer of circulating liquid-phase electrolyte.[161] Image is originated from J. Wu, F. G. Risalvato, P. P. Sharma, P. J. Pellechia, F. S. Ke and X. D. Zhou, J. Electrochem. Soc., 2013, 160, F953.

Microfluidic flow cells have similar two compartment electrode design separated by a membrane as H-cells, but contain porous channelled electrodes with reactants and products flowed behind the electrode. This fuel cell inspired design allows the CO_2 concentration in the cathode chamber to be maintained and the mass transfer restriction can be overcome to maintain a high CO_2 concentration on the catalyst surface which is conducive to the generation of C_{2+} products. However, this design is more complex to operate to achieve an optimum three-phase gas-liquid-catalyst interface and electrolyte can flood the electrode channels. Among the many microfluidic flow cells that have been designed, the polymer electrolyte membrane

flow cell (PEMFC, the cell structure is shown in Figure 1.22) has shown significant advantages in increasing the reaction current density.[161,162]

In general, MFC has great potential to become a large-scale reactor that can be used industrially because of its structural characteristics and excellent performance. However, when MFC is used in heterogeneous reaction, it usually involves different factors such as electrode material and polymer electrolyte membrane type, so the complexity of reaction conditions will be increased, and it is difficult to simply use a single index to evaluate the performance of the electrolytic cell. In this project, we used a combination of traditional H-cell with flow cell because the electrode design does not allow reactants and products to pass through the rear of the electrode to contact the liquid electrolyte.

Aim

This project aims to construct and investigate new Cu-based electrocatalysts based on Cu nanowires (CuNW) embedded in a hydrophobic anodized aluminium oxide membrane for the CO_2 reduction reaction:

1- Uniform CuNW will be prepared by a square-wave pulsed electrodeposition using porous anodized aluminium oxide membranes (AAO) as a template. The length and diameter of CuNW will be controlled by adjusting deposition time and current density.

2- The electrochemical surface area (ECSA) and roughness (R_f) of the CuNW-AAO electrode will be measured by double-layer capacitance measurements, and a redox couple used to probe electrochemical access of the CuNW embedded in the AAO.

3- The surface of the CuNW-AAO electrode will be modified with silane molecules to increase hydrophobicity and stability and change the local chemical microenvironment of the Cu electrode surface specifically to reduce proton activity to increase C-C coupling and reduce parasitic hydrogen evolution.

4- The effects of silane coating on ECSA and R_f of electrode surface will be studied by double-layer capacitance measurement and redox probe, and the effects of different types and concentrations of silane coating on the mass transfer mechanism of electrode surface will be analysed by EIS to probe electrochemical access of the CuNW embedded in modified AAO.

5- The electroreduction of CO_2 will be studied using Cu-based electrodes and silanes modified Cu-based electrodes to determine if selectivity can be controlled, particularly for C_{2+} products.

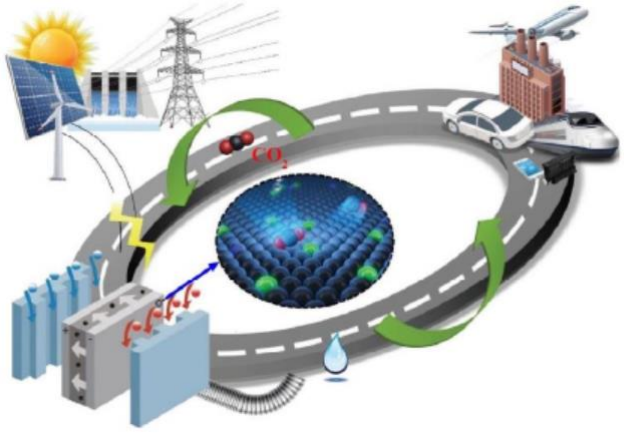

2. Experimental

In this chapter, the procedures for CuNW electrode preparation, catalyst surface modification and CO_2 reduction experiments will be described including the bespoke experimental equipment, and characterization methods of the electrodes and the challenges encountered.

2.1. Materials

All the chemical reagents were analytical grade. All aqueous solutions were prepared using Millipore water (18.2 MΩ.cm). Anodized aluminium oxide membranes (AAO, diam. 25 mm) were purchased from Whatman®. Copper foils (0.55 mm thickness, 99.98% trace metals basis) were purchased from Goodfellow. Gold wire (0.5 mm dia. 99.99% pure) was purchased from Testbourne, Ltd. $KHCO_3$, $CuSO_4 \cdot 5H_2O$, H_3BO_3 and NaOH were purchased from Fisher and Acros Chemicals. Methylviologen, Methyltrichlorosilane, trichloro(phenyl)silane, (3-aminopropyl) triethoxysilane, deuterium oxide (D_2O), dimethylsulfoxide (DMSO), n-hexane, Na_2SO_4, H_2SO_4 were purchased from Sigma Aldrich. Dodecyltrichlorosilane was purchased from Tokyo Chemical Industry, Ltd. Silver conductive paint was purchased from SCP, Ltd. Nafion-117 membrane was purchased from Fuel Cell Store. Copper tape (AT526) was from RS, Ltd. Gas cylinders (CO_2 and standard mixture gas cylinders) were purchased from BOC, Ltd.

Before using Nafion membrane for CO_2RR, in order to ensure the participation of ion exchange in the electrolyte, the Nafion membrane needs to be reactivated, which includes: 1) the Nafion membrane needs to be boiled in a 3% H_2O_2 solution for 1 hour to remove impurities on surface (including some cations that may adsorb). 2) the Nafion membrane needs to be boiled in deionized water for 1 hour to remove remaining impurities and H_2O_2 on surface. 3) the Nafion membrane needs to be protonated by boiled in 0.5 M H_2SO_4 solution for 1 hour. 4) the Nafion membrane needs to be cleaned and kept in deionized water.

2.2. Physical characterization

The morphology of AAO membranes and CuNWs were characterized by scanning electron microscopy (SEM, JEOL 7800F Prime) at an accelerating voltage of 15 keV equipped with EDX chemical microanalysis (Oxford Instruments). The working distance from the objective lens to sample surface was usually 10 mm.

Powder X-ray diffraction (PXRD) was performed by using a Bruker D8 powder diffractometer equipped with a Cu K_α source (40 kV, 40 mA, 0.02° step). X-ray photoelectron spectroscopy (XPS) spectrum (Kratos Axis Supra spectrometer with a monochromated Al K_α = 1486.9 eV) were performed in the EPSRC National Facility (HarwellXPS). The contact angle measurements were obtained on the Ossila contact angle goniometer, using a liquid drop of 0.1 M $KHCO_3$ same as the electrolyte for CO_2RR (at least five test points on each sample surface). NMR spectra were obtained using a Bruker (^{1}H NMR AVIIIHD 600 Widebore) spectrometer.

2.2.1. The preparation of SEM samples

2.2.1.1. AAO membrane sample preparation for SEM

Figure 2.1: Photo of commercial AAO membrane.

The commercial AAO membranes (in Figure 2.1) were soaked in acetone for 10 minutes to remove impurities from surfaces and pores. After the samples were completely dried, the samples were cut into small pieces and fixed on the SEM sample holder with carbon conductive adhesive. The normal horizontal sample holder table was used to observe the plan view morphology, and the 90° sample holder table was used to observe the cross-section morphology. Then a thin carbon layer was covered on the sample surfaces by using carbon coater to improve the conductivity, so as to observe the surface morphology and pore size of AAO membranes.

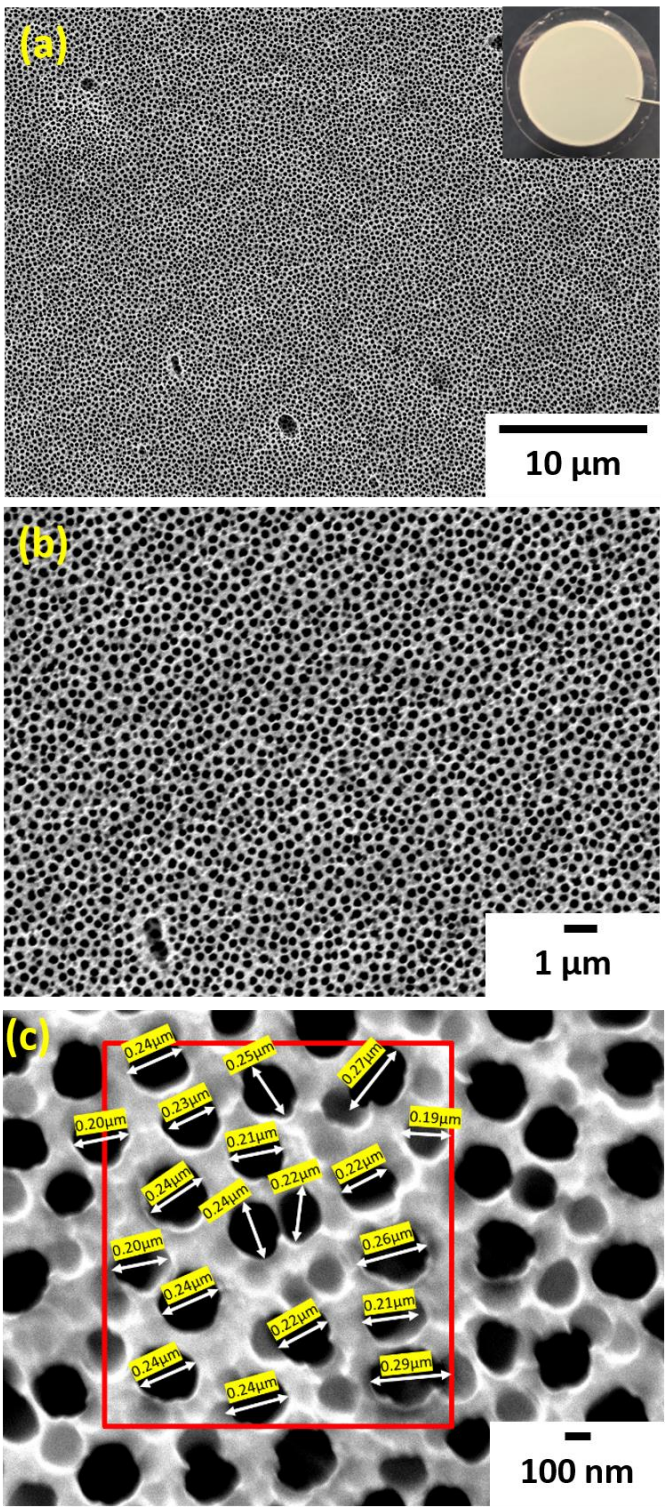

Figure 2.2: SEM images of the commercial AAO membrane surface morphology: (a) x 2 700, (b) x 6 000, (c) x 45 000 (plan view).

In Figure 2.2 (a)-(b), the surface morphology of AAO membrane samples can be clearly observed by SEM, showing a uniform and ordered porous structure, and a few defects exist in very few areas, which may be caused by mechanical damage

during manufacture. In Figure 2.2 (c), at high magnification, it can be clearly observed that the pore size distribution of AAO membranes is relatively uniform, about 0.20-0.30 μm, which is suitable for serving as a template for CuNWs deposition.

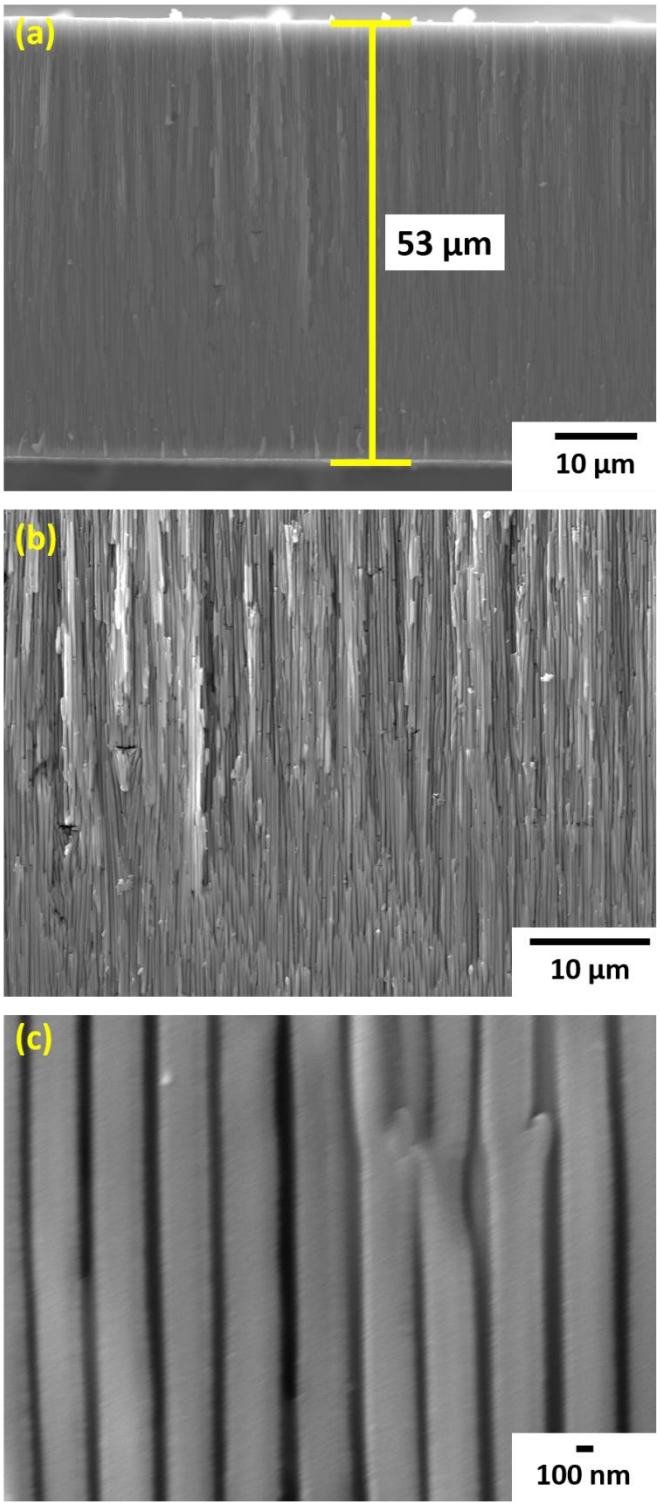

Figure 2.3: SEM images of the commercial AAO membrane channel morphology: (a) x 1 500, (b) x 2 200, (c) x 30 000 (cross-section view).

In Figure 2.3 (a)-(b), the pore morphology of AAO membrane can be observed from the cross-section SEM images. Firstly, it can be seen that the thickness of the entire membrane template is about 53 µm, which will be conducive to controlling the overall length of CuNWs during deposition. Then, it can be clearly seen in Figure 2.3 (c) that the distribution of pore diameter is quite uniform, which will help to control a highly uniform diameter distribution of the deposited CuNWs.

2.2.1.2. CuNW-AAO electrode sample preparation for SEM

Similar to the AAO template sample preparations for SEM, the CuNW-AAO electrode samples were cut into small pieces and fixed on the SEM sample holder with carbon conductive adhesive. These samples have a thermally evaporated gold layer at the back used as an ohmic contact for CuNW deposition, and carbon can be deposited on top to minimise charging. For observing the dispersity of CuNWs morphology, a NaOH solution was used to etch away the AAO template and then a thin carbon layer deposited.

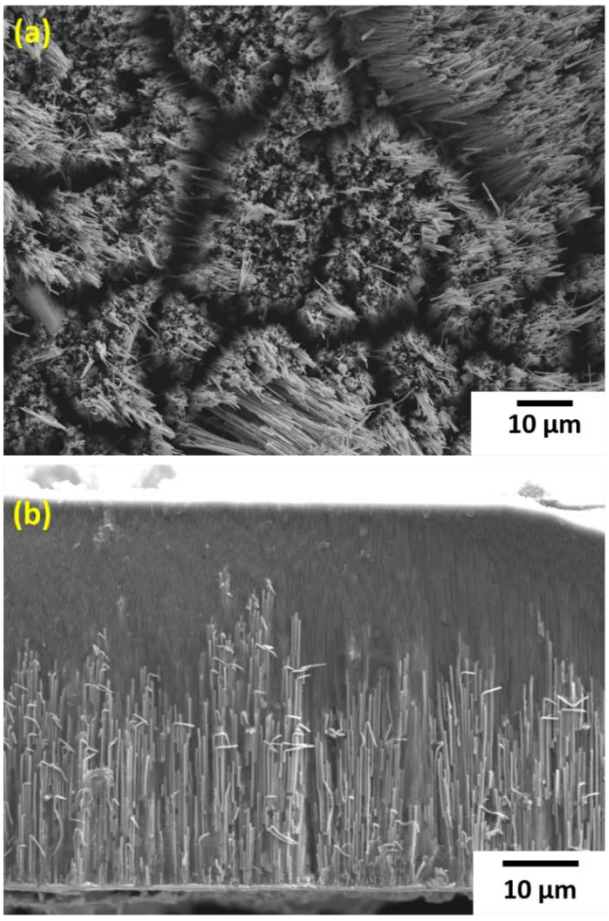

Figure 2.4: SEM images of the CuNW-AAO electrode morphology: (a) x 1 100 (plan view), (b) x 1 500 (cross-section view).

Figure 2.4 (a) is the plan view of CuNWs after removing part of the AAO template, and Figure 2.4 (b) is the cross-section view of CuNWs existing in the pores of the AAO template, indicating that different morphology characteristics of CuNWs can be clearly observed in SEM images through the aforementioned sample preparation processes.

2.3. CuNW electrochemical deposition

The CuNW was grown in an Au deposited AAO membrane fixed on the Al discs. The electrodeposition of CuNW was performed on the Versa Studio Parstat 3000 potentiostat in a three-electrode reactor using the Au deposited AAO membrane as working electrode (WE), a platinum mesh as the counter electrode (CE) and a standard Ag/AgCl electrode as the reference electrode (RE, $E^{\ominus}$ = + 0.197V vs.RHE). Cyclic voltammetric and electrochemical impedance experiments were carried out using a Biologic (SP-150) potentiostat connected to a three-electrode setup. The WE was the Cu-based electrodes, the platinum mesh and standard Ag/AgCl electrode worked as CE and RE, respectively. For the double-layer capacitance measurements, the supporting electrolyte was 0.1 M Na_2SO_4 saturated with N_2, and the 10 mM methylviologen in 0.1 M Na_2SO_4 saturated with N_2 electrolyte was used for redox probe measurements. EIS was performed on the Biologic (SP-150) potentiostat in a frequency range of 0.1 Hz-100 kHz with an amplitude of 10 mV.

The electrochemical CO_2 reduction experiments were conducted in a home-made flow cell with the two chambers separated by a Nafion-117 membrane. The supporting electrolyte was 0.1 M $KHCO_3$ saturated with CO_2 (pH=6.8). The three-electrode system consisting of a platinum foil (CE), a leak-free Ag/AgCl (RE, consisting of a plastic body to prevents the potassium, chloride and other ions leakage into the solution), and Cu-based electrode (WE) was connected to the Versa Studio Parstat 3000 potentiostat. The gas products were analysed on a GC online analysis (Shimadzu GC-2014) fitted with a thermal conductivity detector (TCD) was used for H_2 analysis, and a flame ionization detector (FID, connected to a Restek methanizer) for carbonaceous products analysis. The gas products were analysed on ^{1}H NMR (Bruker AVIIIHD 600 Widebore).

2.3.1. Preparations of Au layer on AAO membrane by thermal evaporation

The commercial AAO membranes with porous structure were used as the templates for CuNWs growth. First, the AAO membranes were soaked in the acetone and ethanol for 5-10 minutes to clean the surface and remove impurities. After drying, as shown in Figure 2.5 (a)-(b), the cleaned AAO membranes were fixed on the glass sheet by Kapton tape and set on the sample holder in the chamber of the gold evaporator. In a vacuum environment of 10^{-6} mbar, a gold layer with a thickness of 300 nm was thermally evaporated on one side of the AAO membranes. In the software (designed by department of Physics, York) connected with the sensors, the physical property parameters of the target metal (Au) need to be set in advance (shown in Figure 2.6), and the thickness of the evaporated gold layer can be controlled by monitoring the data displayed by the sensors. The gold layer on AAO membranes can be used as the working electrode for CuNWs deposition and to provide an ohmic contact for the subsequent catalytic reactions.

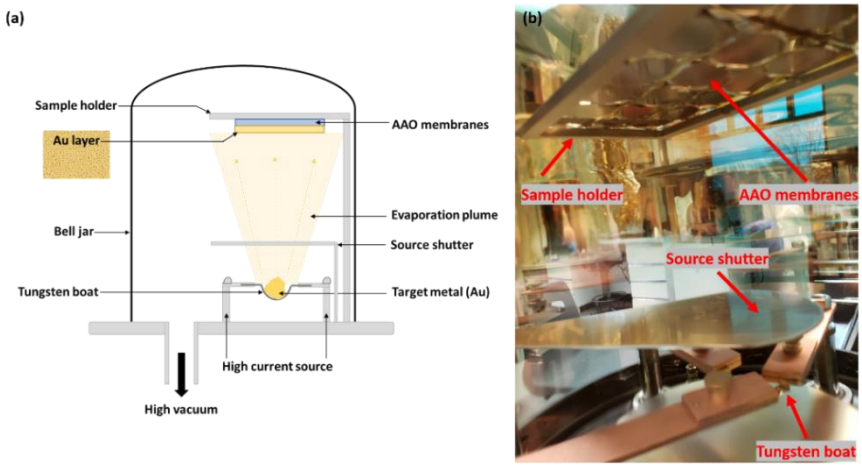

Figure 2.5: (a) Structure diagram of the thermal evaporator designed by department of Physics. (b) Photo of the samples inside the bell jar chamber.

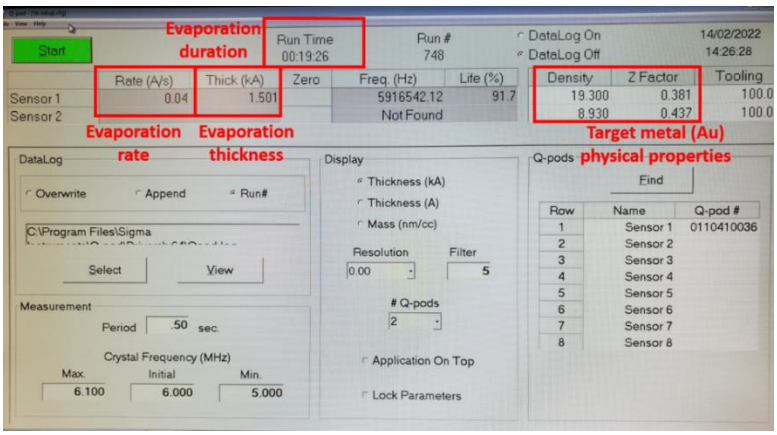

Figure 2.6: Software interface connected with the sensors monitoring evaporation parameters.

The Au evaporated AAO membranes are usually stored in a desiccator and can be used as a template for the growth of CuNWs by electrodeposition after annealing at 770 °C for 10 min.

2.3.2. Preparations of CuNW-AAO electrodes by electrodeposition

First, the Au deposited AAO membranes were fixed on the Al discs with conductive silver paint, and a section of Cu tape was fixed on the back of the Al disc (as shown in Figure 2.7). Then, lacquer was used to seal the entire electrode (to prevent contact with the electrodeposition solution), and only a window of about 1 cm^2 was kept as the effective area for electrodeposition. Finally, Teflon tape was used to cover the lacquer covered area, only the window area was exposed. Millipore water was used to prepare the electrodeposition solution composed of 0.2 M $CuSO_4 \cdot 5H_2O$ and 0.1 M H_3BO_3, and 0.5 M H_2SO_4 solution was used to adjust the pH value of electrodeposition solution to 3. The electrode covered with Teflon tape was immersed in the electrodeposition solution for 1 hour, so that the solution could be fully in contact with the Au layer through the pores of the AAO membranes. Next, the electrodeposition was performed at room temperature in a three-electrode reactor using a platinum mesh as the working electrode and a standard Ag/AgCl electrode as the reference electrode ($E^{\ominus}$ = +0.197 V vs.RHE). The pulsed constant current method was applied to deposit CuNWs, the deposition procedures are shown in Figure 2.8. Based on literature reports,[163] compared with triangular and trapezoidal waves, the square waves are more conducive to maintaining good uniformity of CuNWs (in Table 2.1 (a)-(b)). The electrodeposition was performed in pulsed mode with $time_{on}$ = 1 s and $time_{off}$ = 10 s on the Versa Studio Parstat 3000 potentiostat, the deposition parameter settings for each procedure are listed in Table 2.2. The pulsed polarization can be employed to replenish the double-layer by inverting the polarity of current. In order to obtain the uniform CuNWs, the growth rate and dimension of CuNWs can be controlled by varying parameters such as current density, time of deposition, on/off cycles, and the optimum electrodeposition condition of growing CuNWs will be explored in Chapter 3.

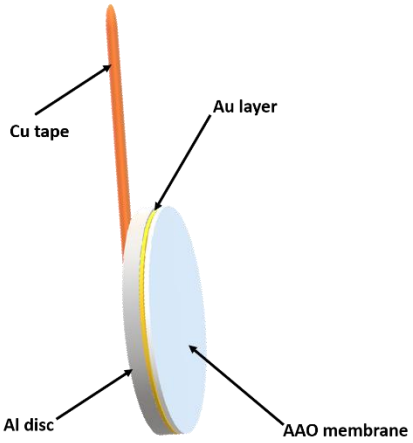

Figure 2.7: The configuration of AAO membrane on Al disc used for CuNW electrodeposition.

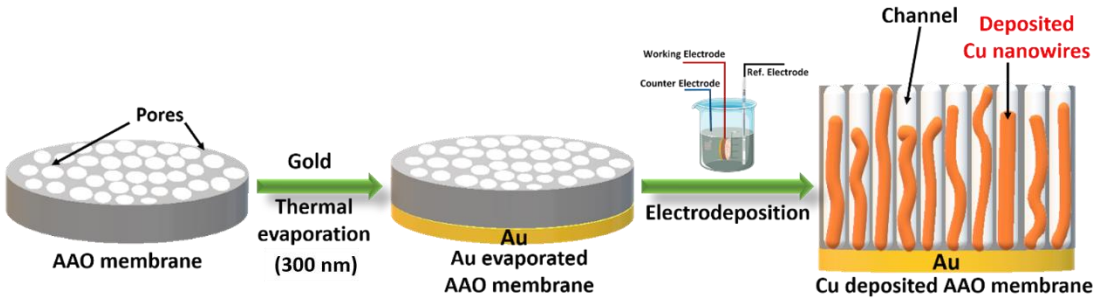

Figure 2.8: The preparation process of CuNWs via electrodeposition method.

Table 2.1: Parameters of the pulsed waves employed for electrodeposition of CuNWs: (a) Square wave mode, (b) triangular wave mode.

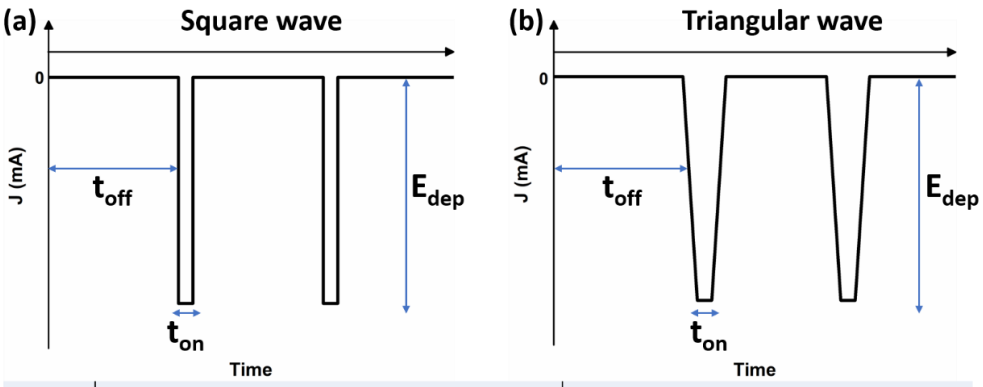

t_{off}	10 s	10 s
Scan	step	1 V s^{-1}
t_{on}	1 s	1 s

Table 2.2: Deposition parameter settings on Parstat 3000 potentiostat.

Electrodeposition procedure	*Parameter setting*
Number of cycles	$\frac{Total\ time\ (s)}{Time\ of\ per\ cycle\ (11\ s)}$
Pulsed time off (10 s per cycle) (chronopotentiometry)	No current applied
Pulsed time on (1 s per cycle) (chronopotentiometry)	Expected current value applied
Loop termination	

The potential (V)-time(t) curves and the charge passed during the electrodeposition process can be measured on Versa Studio Parstat 3000 potentiostat, so that the mass of deposited metallic Cu can be calculated within a certain period of deposition time:

$$Q_{total}\ (C, A \cdot s) = \int_{t_i}^{t_f} i\ (A) dt(s) \qquad \text{Eq. 2-1}$$

$$M_{Cu}(g) = K_{Cu}\left(\frac{g}{C}\right) Q_{total}(C) \qquad \text{Eq. 2-2}$$

As the expressions, Q_{Cu} is the total charges (C) passed during CuNW deposition, i is the applied deposition current (A), t is the total deposition time (s) of the Cu, M_{Cu} is the deposited Cu mass (g), K_{Cu} is the electrochemical equivalent (0.0003292 g·C^{-1}) of Cu.

2.3.3. Preparations of Cu foil electrodes

The smooth flat Cu foil electrodes were used as references to compare the electrochemical performance of CuNW-AAO electrodes. First, a 25 mm diameter Cu foil disc was soaked in acetone and ethanol for 5-10 minutes to clean the surface and remove impurities. After drying, the Cu foil was electropolished by applying 3.0 V provided by a power supply in 85% phosphoric acid for 5 minutes. Then the fresh Cu foil electrode was cleaned by Millipore water and ready for use.

2.3.4. Electrochemical measurements of CuNW-AAO electrodes

2.3.4.1. Double-layer capacitance (DLC) measurements

In general, to compare the electrochemical behaviour of different catalysts, the electrocatalytic activity of the electrodes can be evaluated based on the current density normalized to the geometric area [164]. For smooth planar electrodes, the electrochemical area of the electrode is approximately the geometric area of the electrodes. The introduction of porous or nanostructures will increase the specific surface area of the electrodes, potentially resulting in an increase in the number of active sites. Therefore, comparing the normalized electrochemical surface areas of different electrodes will help to evaluate the electrocatalytic activity of different electrodes.

The electrochemical surface area can reflect the active surface area on the catalysts. The electrochemical surface area of an electrode can be calculated from the Helmholtz double-layer capacitance (DLC), which can usually be determined by the ratio of the differential capacitance to the standard smooth surface capacitance to give a roughness factor [165]. The differential capacitances with different scan rates in a narrow potential range can be used for DLC calculations. When the cyclic voltammetry is obtained in a non-Faradaic range, the differential capacitance equals the double-layer capacitance, which can be defined as the roughness factor (RF):

$$C_{dl} = \frac{d(\Delta J)}{2dv} \qquad \text{Eq. 2-3}$$

$$Roughness\ Factor\ (R_f) = \frac{C_{dl\ of\ sample}}{C_{dl\ of\ smooth\ Cu\ foil}} \qquad \text{Eq. 2-4}$$

ECSA is directly proportional to the double-layer capacitance and geometric surface area of catalyst:

$$ECSA = R_f \cdot S \qquad \text{Eq. 2-5}$$

As the expressions, ΔJ is the difference between the anodic and cathodic current density, C_{dl} is the measured double-layer capacitance, v is the scan rate (mV·s^{-1}), S is the geometric surface area of the electrode. All the cyclic voltammetric measurements for ECSA were performed in N_2-saturated 0.1 M Na_2SO_4 electrolyte. CV measurements were performed using a Biologic (SP-150) potentiostat connected to a three-electrode system with CuNW-AAO or Cu foil as working electrode, a platinum mesh (1 cm^2) counter electrode and a Ag/AgCl reference electrode. An applied potential of -0.6 to -0.8 V vs.Ag/AgCl was used in a non-Faradic region to avoid involvement in unrelated redox reactions. All the CV measurements on the CuNW-AAO electrodes were performed after the CuNW-AAO electrodes were soaked in the electrolyte for 30 min to ensure an adequate contact between the electrolyte and the CuNW surface inside the AAO template.

2.3.4.2. Redox couple measurements

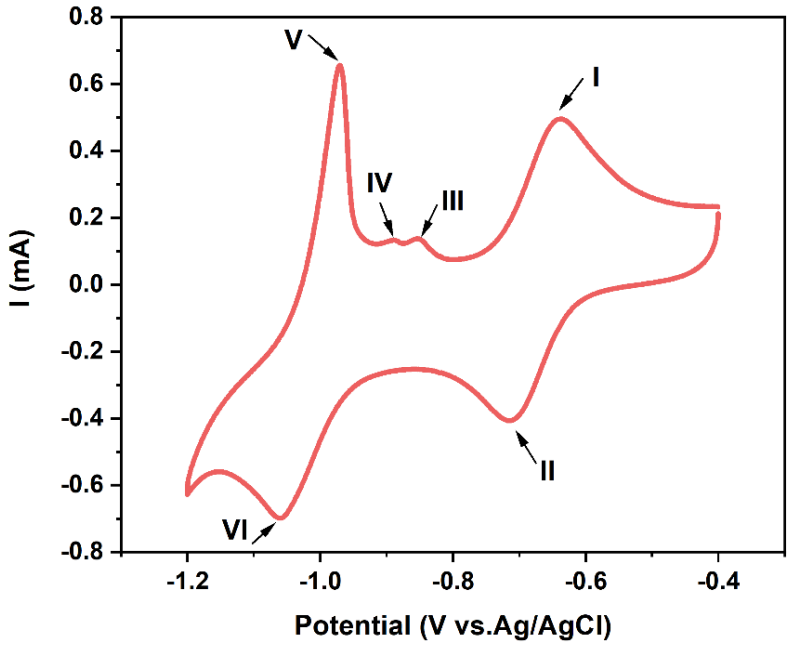

Figure 2.9: Cyclic voltammogram of 10 mM methylviologen and 0.1 M Na_2SO_4 at a Cu foil electrode, scan rate = 400 mV s^{-1}. (Peak I and II: redox couple of $MV^{2+} \leftrightarrow MV^{+}$, peak V and VI: redox couple of $MV^{+} \leftrightarrow MV^{0}$, peak III: $(MV)_2^{2+} \rightarrow MV^{2+}$, peak IV: $MV^{0} \rightarrow (MV)_2^{2+}$)

1,1'-Dimethyl-4,4'-bipyridinium dichloride (methylviologen) can be used as a probe to explore the cyclic voltammetric behaviour of Cu-based catalysts due to its redox chemistry [166,167]. The electrochemical redox reactions of methylviologen on the surface of copper catalysts mainly depend on the accessibility of the electrochemically active sites on the electrode surface.

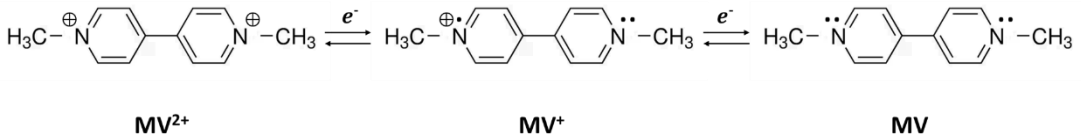

Scheme 2.1: Methylviologen molecules at different oxidation states.

As shown in Figure 2.9, there are two main redox peaks in the redox process of methylviologen corresponding to the three oxidation states in Scheme 2.1. Generally, during a CV scan on Cu electrodes, the two voltammetric peaks (peak I and peak II) at -0.64 V and -0.71 V vs.Ag/AgCl appear, corresponding to the redox couple formation [166]:

$$MV^{2+} + e^{-} \leftrightarrow MV^{+} \qquad \text{Eq. 2-6}$$

In this process, electron transfer occurs between the electrode and MV^{2+}/MV^{+}, and the reaction is controlled by diffusion, so the peak current will follow the Randles-Ševčík equation. According to the Nernst equation ($E = E^{O} - \frac{RT}{zF}\ln Q$, E: reduction potential, E^{O}: standard potential, R: universal gas constant, T: temperature in kelvin, z: ion charge (moles of electrons), F: Faraday constant, Q: reaction quotient), under the non-standard conditions, if ion concentration in the electrolysis changes, it will affect the electrode reduction potential, that is, the system can reach electrochemical equilibrium by controlling the applied potential or adjusting the concentration of each component in the electrolyte. The process is different from the kinetic reversibility, which is affected by the reactant state.

Two voltammetric peaks (peak V and peak VI) appear at -0.97 V and -1.06 V vs.Ag/AgCl represent the formation of neutral species [166]:

$$MV^{+} + e^{-} \leftrightarrow MV^{0} \qquad \text{Eq. 2-7}$$

Also, during an oxidation process, a voltammetric peak (III) at -0.85 V vs.Ag/AgCl arise from the electrode reaction [168]:

$$2MV^0 \rightarrow (MV)_2^{2+} + 2e^- \qquad \text{Eq. 2-8}$$

The peak (IV) at -0.89 V vs.Ag/AgCl appears, is due to the (two-electron) oxidation of the spin-paired radical-cation dimer [168]:

$$(MV)_2^{2+} \rightarrow 2MV^{2+} + 2e^- \qquad \text{Eq. 2-9}$$

The peak (IV) for dimer oxidation can only be seen at low scan rates because it usually takes some time to form the dimer. The analysis of these peaks according to the Randles-Ševčík equation shows that the peak currents of peaks I and II are linearly correlated with the square root of the scan rates. So ECSA can be evaluated according to the Randles-Ševčík equation [169]:

$$i_p = 0.4463\, n\, F A\, C\, (\frac{nFvD}{RT})^{\frac{1}{2}} \qquad \text{Eq. 2-10}$$

As the expressions, i_p is peak current, n is the number of electrons transferred in the redox (n =1), D is the diffusion coefficient of methylviologen ($D = 7.7 \times 10^{-6}\, cm^2 s^{-1}$), A is the electrochemical active surface area (cm^2), C is the bulk concentration of methylviologen, v is the scan rate, F is Faraday constant ($96485\ \mathrm{A} \cdot s \cdot mol^{-1}$), R is the gas constant ($8.314\, J \cdot K^{-1} \cdot mol^{-1}$), T is the temperature ($298.15\, K$). All the cyclic voltammetric measurements for ECSA were performed in N_2-saturated 0.1 M Na_2SO_4 electrolyte contained 10 mM methylviologen. CV measurements were performed using a Biologic (SP-150) potentiostat connected to a three-electrode system with CuNW-AAO or Cu foil as working electrodes, a platinum mesh (1 cm^2) counter electrode and an Ag/AgCl reference electrode. The applied potential window of -0.55 to -0.85 V vs.Ag/AgCl confirmed that measurements were performed in the region of $MV^{2+} \leftrightarrow MV^{+}$ redox reactions. All the CV measurements on the CuNW-AAO electrodes were performed after the CuNW-AAO

electrodes were soaked in the electrolyte for 30 min to ensure an adequate contact between the electrolyte and the CuNW surface inside the AAO template.

2.3.5. Electrochemical impedance of CuNW-AAO electrodes

In addition to measuring the electrochemical area of catalysts by DLC, electrochemical impedance spectroscopy (EIS) can also be applied to characterize the electrochemical area of catalysts. EIS were obtained on the Biologic (SP-150) potentiostat in a frequency range of 0.1 Hz-100 kHz with an amplitude of 10 mV. In Chapter 3 and Chapter 4, the EIS measurements on Cu-based electrodes were performed in N_2-saturated 0.1 M Na_2SO_4 at open circuit potential and -0.4 V (vs.RHE). The measurements were in a separate three-electrode cell with the Pt mesh as counter electrode and Ag/AgCl electrode as reference electrode. All the EIS measurements on the CuNW-AAO electrodes were performed after the CuNW-AAO electrodes were soaked in the electrolyte for 30 min to ensure an adequate contact between the electrolyte and the CuNW surface inside the AAO template.

2.4. Interfacial design strategies for CuNW-AAO electrodes

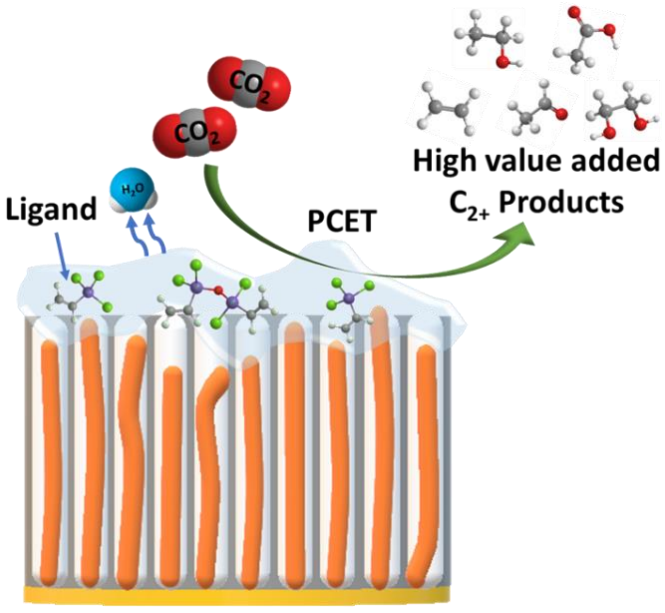

Figure 2.10: Scheme of surface functionalization on CuNWs in CO_2 reduction.

In the project, the main research objective is to control the local environment around the electrode surface to improve the selectivity and stability of the catalysts. To ensure sufficient catalytic active sites on the CuNW surface, rather than directly modify the Cu surface (which may limit the number of active sites), we are more concerned with retaining the AAO template as a support for local environmental regulation. So, some appropriate molecules will be used to functionalize the AAO template surface, to tune the hydrophobicity and stability of the electrodes, so that the surface wetting ability and proton activity can be controlled. The process is shown in Figure 2.10 and is akin to a macroscopic metalloenzyme containing channels for proton transport. The ordered structure should support predictable CO_2 and proton mass transfer when being used for CO_2RR, mechanically stabilize the CuNW structure and provide a platform for controlled modification of CO_2 reduction selectivity

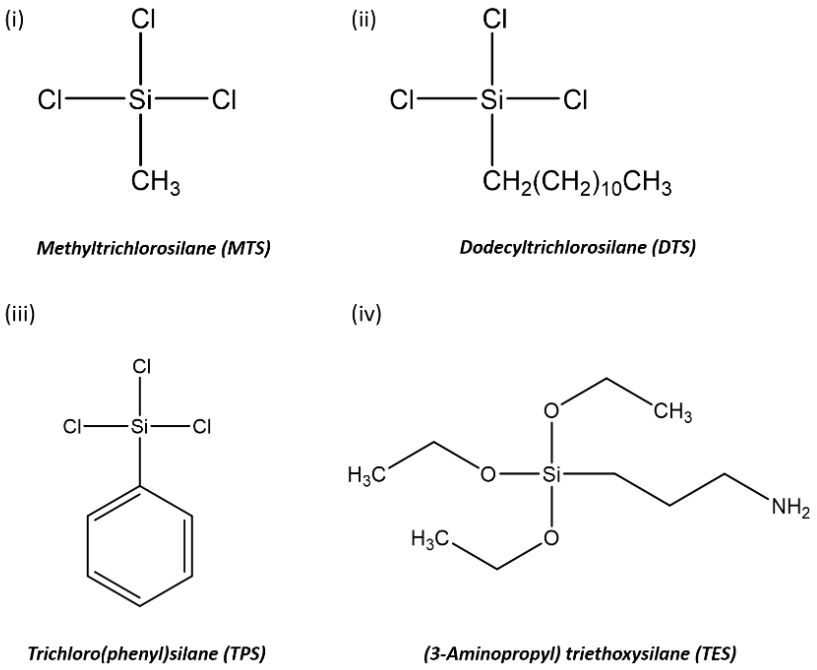

Scheme 2.2: MTS DTS TPS and TES molecules used to modify the electrodes.

The interfacial molecular structure of the coating modification will have a major effect on the hydrophobicity of the electrode surface. It has been revealed in some literature reports that, a certain coverage of silane molecular coatings can be grafted with the inner wall of AAO porous channels (that is, the hydrolyzable group of chlorosilanes will be coupled with the hydroxyl groups of the mesoporous inner wall)

to inhibit the infiltration of water into the porous channels of AAO membranes [170–174]. In this project, four kinds of silane coating with different chain lengths were selected: Methyltrichlorosilane (MTS), dodecyltrichlorosilane (DTS), trichloro(phenyl)silane (TPS) and (3-aminopropyl) triethoxysilane (TES) were used as molecular coatings (Scheme 2-2) on AAO membranes, CuNW-AAO electrodes, and directly on Cu foil electrodes modification to explore the effects of chlorosilane molecules on the electrochemical surface area and local chemical environment of catalysts.

2.4.1. Control sample AAO membrane modification

AAO membranes were cleaned in solution contains 10 mL ethanol and 10 mL acetone for 1 h, next the membranes were dried in oven at 70 °C for 1 h. Then, MTS DTS, TPS and TES molecular coatings were used to modify AAO, respectively. When modifying AAO membranes with the chlorosilane solutions, the treatment process is as shown in Table 2.3:

Table 2.3: MTS DTS TPS and TES molecular coatings modification treatment processes.

Molecule	***0.004 M silane solution***	***Processing procedure***
MTS	9 µL MTS in 20 mL hexane	Soaked in solution for 1h Dried in oven for 1h (100 °C)
DTS	24 µL DTS in 20 mL hexane	Soaked in solution for 1h Dried in oven for 1h (100 °C)
TPS	13 µL TPS in 20 mL hexane	Soaked in solution for 1h Dried in oven for 1h (100 °C)
TES	19 µL TES in 20 mL hexane	Soaked in solution for 1h Dried in oven for 1h (100 °C)

(The volume of the above solutions was measured using a PIPETMAN 10-100 µL pipette.)

2.4.2. Control Cu foil electrode modification

Fresh Cu foil electrodes after electropolishing were modified with 0.004 M chlorosilane solutions by using the same method as described in 2.4.1. Cu foil electrodes were also modified with higher concentration 0.1 M chlorosilane solutions to saturate modifiable surface using the process shown in Table 2.4.

Table 2.4: MTS DTS TPS and TES molecular coatings modification with high concentration treatment processes.

Molecule	*0.1 M silane solution*	*Processing procedure*
MTS	0.2 mL MTS in 20 mL hexane	Soaked in solution for 1h Dried in oven for 1h (100 °C)
DTS	0.6 mL DTS in 20 mL hexane	Soaked in solution for 1h Dried in oven for 1h (100 °C)
TPS	0.3 mL TPS in 20 mL hexane	Soaked in solution for 1h Dried in oven for 1h (100 °C)
TES	0.5 mL TES in 20 mL hexane	Soaked in solution for 1h Dried in oven for 1h (100 °C)

(The volume of reagents was measured using a PIPETMAN 10-100 µL pipette.)

2.4.3. CuNW-AAO foil surface modification

The prepared CuNW-AAO electrodes shown in Figure 2.7 were modified with 0.1 M chlorosilane solutions according to the treatment process shown in Table 2.4.

2.5. Electrochemical reduction of CO_2

All the electrochemical reduction measurements were performed at room temperature using a Versa Studio Parstat 3000 potentiostat in a bespoke three-electrode system described in detail in section 2.6. A platinum foil was used as the counter electrode, and an Ag/AgCl electrode (in a saturated-NaCl solution) was used as the reference electrode. The CO_2RR were performed in a home-made flow cell with CO_2 saturated (0.1 M) $KHCO_3$ as the electrolyte (pH=6.8), and a Nafion-117 membrane was used to separate the anodic and cathodic chambers, in order to avoid the re-oxidation of reduction products. The flow rate of CO_2 gas bubbling was 20 $mL{\cdot}min^{-1}$. The reactions were performed at constant potential. The response current can be recorded by chronoamperometry at different applied potentials. When recording curves, if the shape of the curve changes significantly when iR compensation is applied, which means compensation is required. The operation of iR compensation on potentiostat is shown in Appendix 2. Gas and liquid products were analysed by using gas chromatography (GC) and nuclear magnetic resonance (NMR) spectroscopy, respectively.

2.5.1. Quantification of gaseous products

GC online analyses were performed on a Shimadzu GC-2014 fitted with a ShinCarbon ST micropacked column. The automatic sample injection was applied every 20 min with a gas sampling loop (volume: 1.0 mL). The oven chamber temperature procedures were in three steps: 1. held at 40 °C for 4.5 min; 2. heated to 200 °C with a rate of 80 °C·min^{-1}; 3. held at 200 °C for 3.5 min. The procedures are shown in Figure 2.11. A thermal conductivity detector (TCD) was used for H_2 analysis, and a flame ionization detector (FID, connected to a Restek methanizer) for carbonaceous products analysis. The temperatures of the two detectors were kept at 200 °C. Argon was used as the carrier gas with a 30 mL·min^{-1} flow rate.

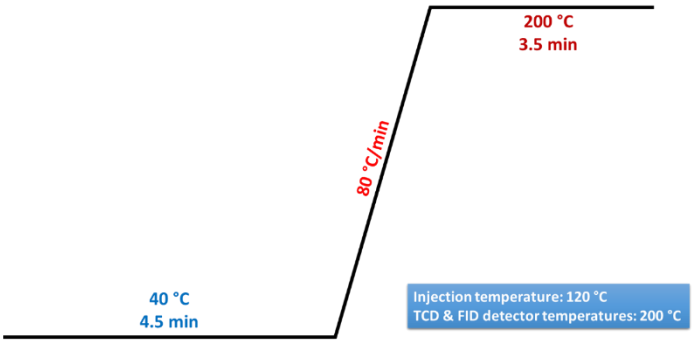

Figure 2.11: Temperature procedures of GC analysis.

The procedures in Figure 2.11 can be used to detect common gas products including: CO_2, CO, CH_4, C_2H_4, C_2H_6 and H_2. The retention times and peaks of each gas product are shown in Table 2.5 and Figure 2.12:

Table 2.5: Retention times of all gases on chromatograms with the volume ratios of standard gas mixture used for the GC calibration curves.

Gas product	*Formula*	*Volume (%)*	*Retention time (min)*	*Detector*
Argon	Ar	-	-	-
Hydrogen	H_2	2.380	0.70	TCD
Air	(mainly O_2/N_2)	-	1.26	FID
Carbon monoxide	CO	2.423	1.58	FID
Methane	CH_4	2.462	3.01	FID
Carbon dioxide	CO_2	87.725	5.63	FID
Ethylene	C_2H_4	2.435	8.21	FID
Ethane	C_2H_6	2.575	8.82	FID

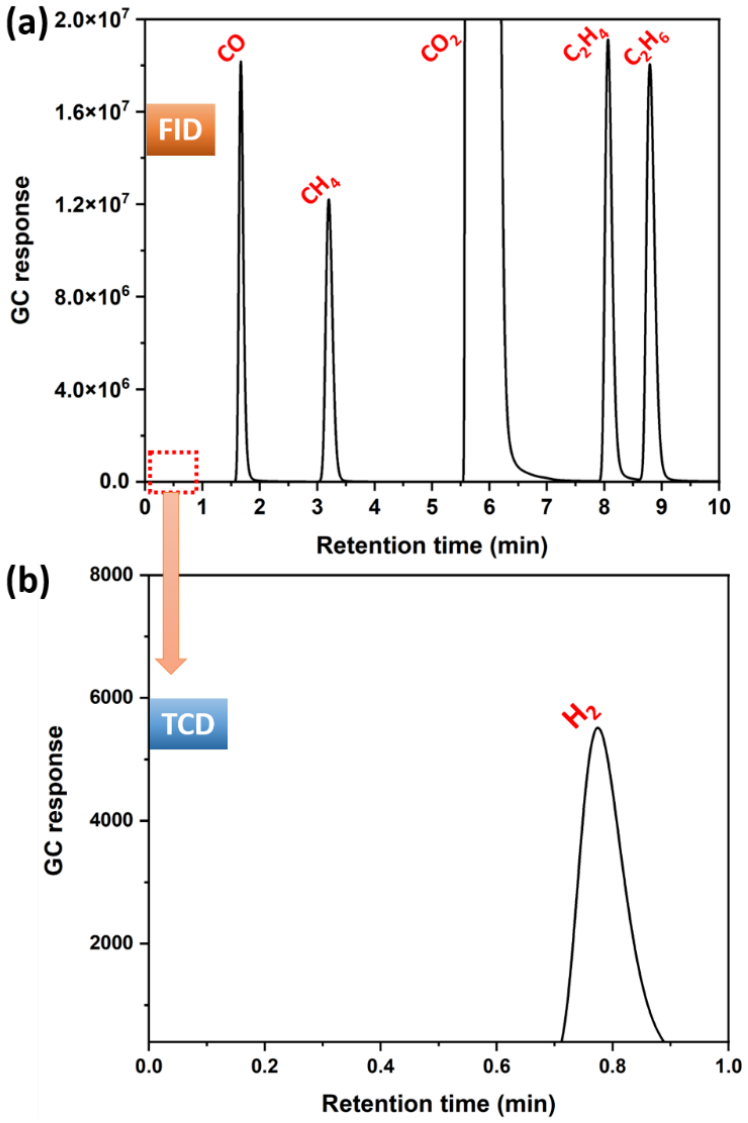

Figure 2.12: Typical chromatograms of gas products: (a) peaks from the FID detector, (b) peaks from TCD detector.

The standard gas mixture (BOC, Ltd.) was used to calibrate GC, the composition of which is shown in Table 2.5. The standard gas mixture and CO_2 gas (BOC, Ltd., CP Grade) were mixed and diluted in different proportions for determination. Calibration curves of H_2, CO, CH_4, C_2H_4 and C_2H_6 gas products were established according to the peak area (GC response) versus (vol %). The calibration curves of gas mixtures can be used to determine the amount of produced gas during chronoamperometry (CA), as shown in Figure 2.13:

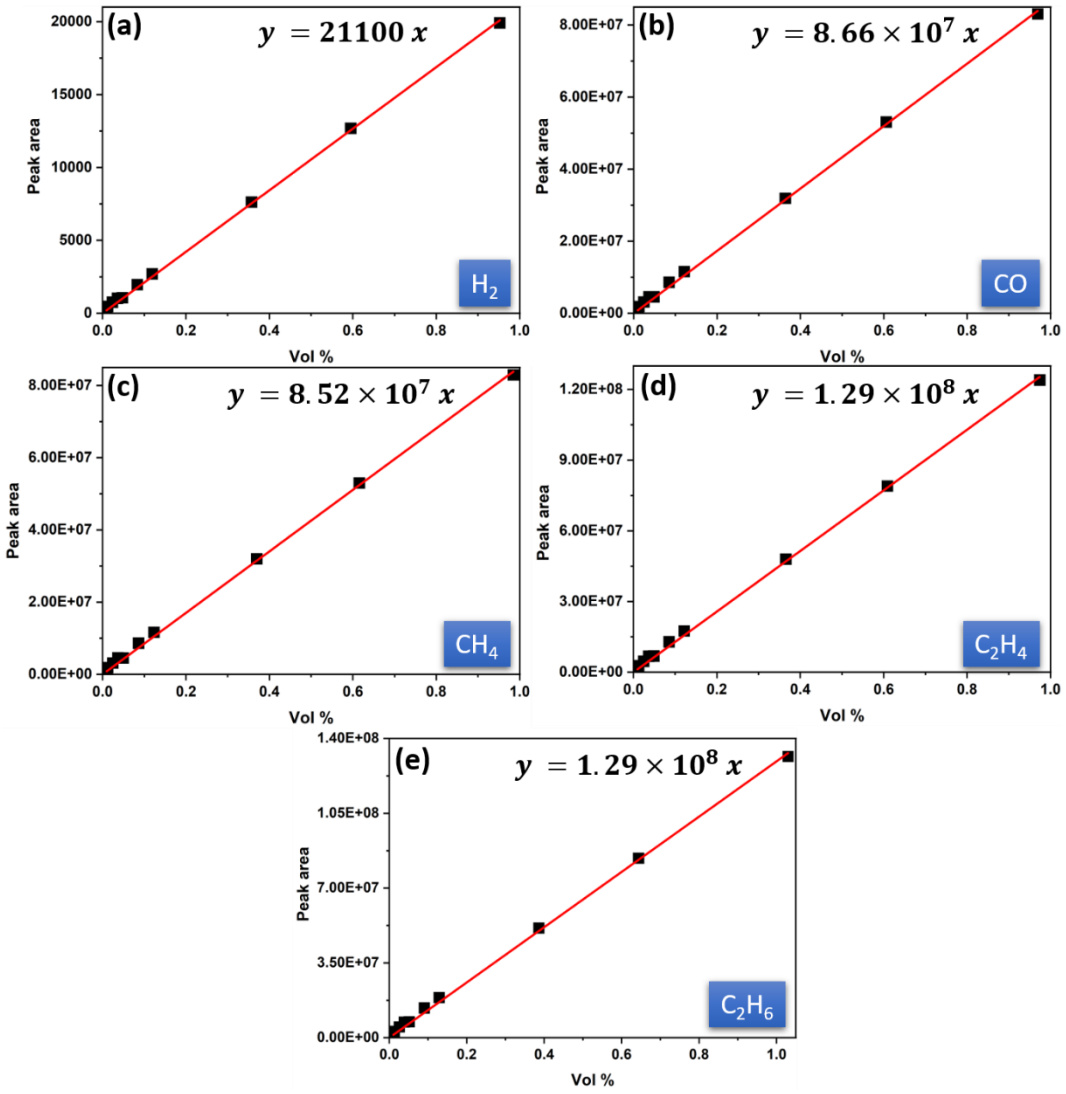

Figure 2.13: Gas calibration curves: (a) H_2, (b) CO, (c) CH_4, (d) C_2H_4 and (e) C_2H_6.

Based on the calibration curves, it shows a linear relationship ($y = ax + b$) between peak area and vol :

$$vol_{ratio} = \frac{Peak\ area}{Slope} \qquad \text{Eq. 2-11}$$

The average of the second and third GC measurements of triplicate runs were used to calculate the average Faraday efficiency (FE%) of each gas product to ensure the reaction was at equilibrium and stabile, and the electrolyte was saturated with CO_2 gas. The average current of each product can be calculated according to the following equations [175,176]:

Assuming ideal gas law ($PV = nRT$),

$$i_{product}\ (A)\ =\ \left(\frac{PV}{RT}\right) \times z_{e^-} \times F \qquad \text{Eq. 2-12}$$

$$i_{product}(mA)\ =\ \left(\frac{PV}{RT}\right) \times z_{e^-} \times F \times 1000 \qquad \text{Eq. 2-13}$$

As the expressions, R is the gas constant ($8.314\ J \cdot K^{-1} \cdot mol^{-1}$), P is the atmospheric pressure $= 101325\ Pa$, all experiments were proceeded at room temperature ($T\ = 298.15\ K$), the flow rate of CO_2 during the CO_2RR was 20 mL·min^{-1} and the Faraday constant (F) is $96485\ C \cdot mol^{-1}$. z_{e^-} is the number of the e^- transfer. For example, when calculating the $FE\%$ for the electrochemical reduction of CO according to the reaction ($CO_2 + 2H^+ + 2e^- \rightleftharpoons CO + H_2O$, $z = 2$):

$$i_{CO}\ (mA)\ =$$

$$\frac{101325\ (Pa) \times Vol_{ratio} \times 20\ (m^3/min)}{8.314\ (m^3 \cdot Pa/K \cdot mol) \times 298.15\ (K)} \times \frac{1}{60 \times 10^6} \times 2 \times 96485\ (C \cdot mol^{-1}) \times 1000 \qquad \text{Eq. 2-14}$$

$$J_{CO}\ (mA/cm^2)\ =\ \frac{i_{CO}\ (mA)}{Geometric\ surface\ area\ of\ the\ working\ electrode\ (cm^2)} \qquad \text{Eq. 2-15}$$

So, the percentage of the total current towards CO product:

$$Faradic\ efficiency\ (FE\%)\ =\ \frac{J_{CO}\ (mA/cm^2)}{J_{Total}\ (mA/cm^2)} \times 100 \qquad \text{Eq. 2-16}$$

2.5.2. Quantification of liquid products

All electrochemical experiments were performed using 18 mL (the volume of cell chamber 8 mL and Duran bottle 10 mL for catholyte connected with the pump) of catholyte flowed through the working electrode chamber. Liquid products were analyzed by ^{1}H NMR (Bruker AVIIIHD 600 Widebore) with water suppression (zgesgp) as shown in Figure 2.14. The analytical liquid sample consist of 540 µL

catholyte, 50 μL D_2O and 10 μL dimethyl sulfoxide (DMSO, 391 ppm (5 mM), as internal standard). The concentrations of liquid products can be calculated via the NMR peak area relative to the internal standard of DMSO using the following equations:

$$\frac{6 \times C_{ref(ppm)}}{(Peak\ area)_{ref}} = \frac{n \times C_{product(ppm)}}{(Peak\ area)_{product}} \quad \text{Eq. 2-17}$$

$$C_{product(mol/L)} = \frac{C_{product(ppm)} \times 10^{-3}}{Mwt_{(g/mol)}} \quad \text{Eq. 2-18}$$

$$Q_{total}\ (C) = \int_{t_i}^{t_f} i\ dt \quad \text{Eq. 2-19}$$

$$FE\% = \frac{C_{product\ (mol/L)} \times V_{catholyte} \times n \times F}{Q_{total}} \times 100 \quad \text{Eq. 2-20}$$

As the expressions, n is number of the corresponding protons in the expected product in Table A1.1 [177–180]. $C_{product}$ is the product concentration, $C_{ref(ppm)}$ is the concentration of diluted DMSO (6.51 ppm), and F is the Faraday constant ($96485\ C \cdot mol^{-1}$). The corresponding product peaks on ^{1}H NMR spectra are summarized in Table A1.1 [177–180].

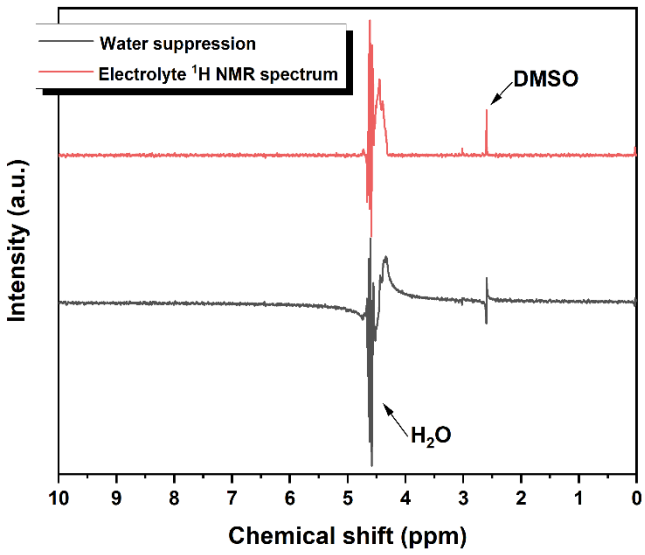

Figure 2.14: ^{1}H NMR spectrum of 0.1 M $KHCO_3$ electrolyte by water suppression method.

2.6. CO_2 reduction flow-cell design

The conventional H-cell is currently the most widely used reactor at the CO_2RR (laboratory scale) [181–184]. The main structure consists of a cathode chamber (including a working electrode and a reference electrode) and an anode chamber (including a counter electrode), which are connected by channels and separated by an ion exchange membrane (to prevent re-oxidation of the products), as shown in Figure 2.15 [182]. Because the concentration of CO_2RR product is generally low, the size of the reactor and the distance between the electrodes will have a great influence on the mass transfer process and product FE.

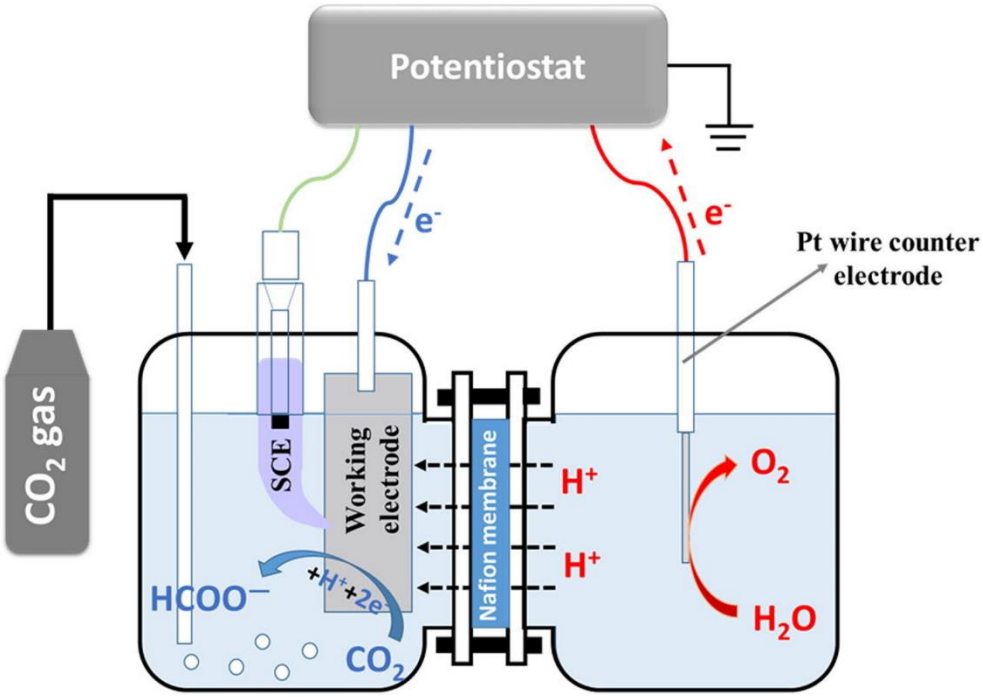

Figure 2.15: The structure of an H-type 3 electrode cell for the electrochemical reduction of CO_2 reaction [182] Image is originated from C. Zhao and J. Wang, Chem. Eng. J., 2016, 293, 161–170.

In recent years, flow-cell reactors [185–189] based on gas diffusion electrodes (GDE) have emerged, in which a polymer electrolyte membrane (PEM) separates the cathode from the anode, CO_2 gas is pumped directly to the back of cathode, and the electrolyte can be continuously circulated through a pump (in Figure 2.16 [189]). Compared with the traditional H-cell, it has higher thermodynamic and dynamic variability, and is more conducive to the mass transfer processes, but requires a porous electrode. Although reactor designs have been improved, there are still many

factors limiting the reaction, and further research is needed to explore the optimal design conditions to improve the mass transfer and product FE in the CO_2RR.

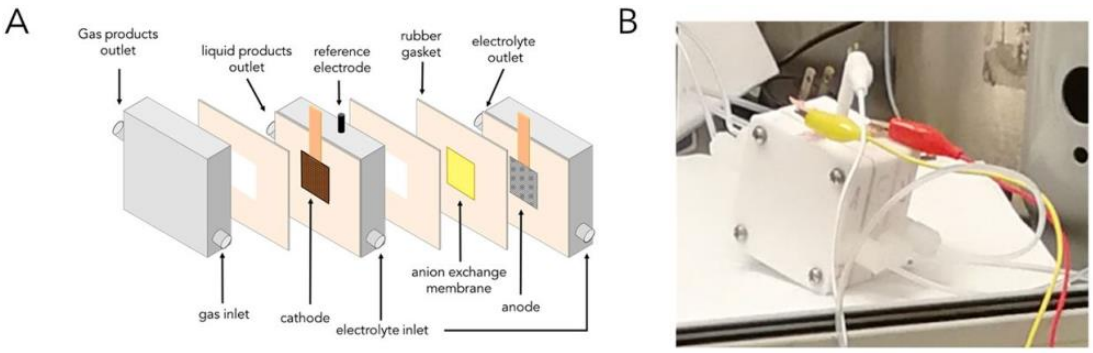

Figure 2.16: GDE flow cell configuration: (a) schematic illustration, (b) photograph[189] Image is originated from C. Chen, Y. Li, S. Yu, S. Louisia, J. Jin, M. Li, M. B. Ross and P. Yang, Joule, 2020, 4, 1688–1699.

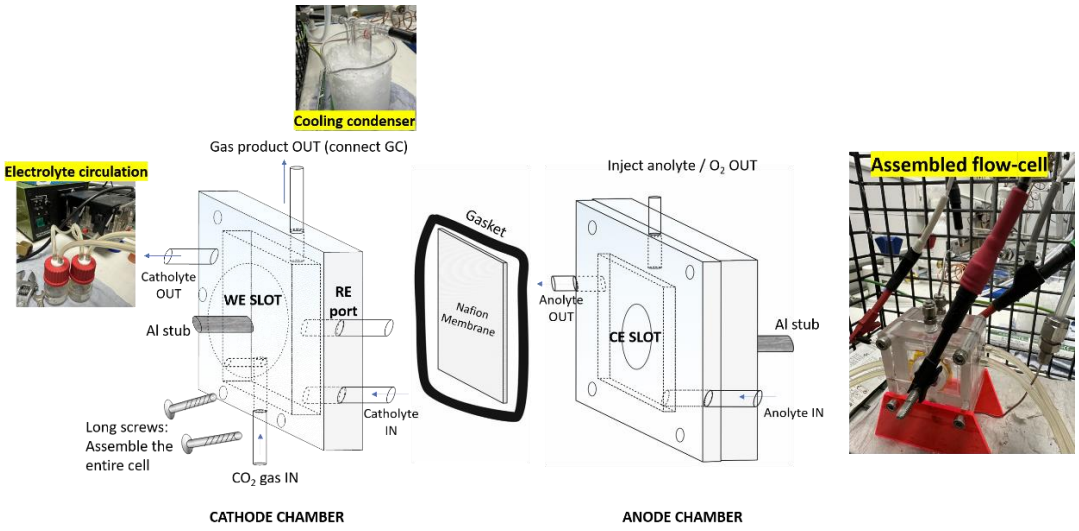

Figure 2.17: The self-designed configuration of the flow-cell for CO_2RR.

Generally, the H-cell configuration designed for CO_2RR has limited mass transfer capacity and large solution resistance, and how to efficiently deliver CO_2 gas directly to the working electrode surface is also a key issue. Our working electrode design is not porous preventing access of CO_2 to the catalyst in a GDE design. As shown in Figure 2.17, some characteristics of traditional H-cell and GDE designs were used for the cathode and anode chambers in this project. In the cathode and anode chambers, liquid in/out ports connected with an external peristaltic pump for circulating the catholyte and anolyte were added, to aid mass transfer effects in the

CO_2RR process and maintain constant bulk pH. At the same time, the CO_2 gas in port was positioned at the bottom of the chamber, and a small plastic tube used to transport CO_2 gas directly onto the working electrode surface to enhance the concentration of CO_2 near the electrode surface. In addition, the thickness of the entire cell has been greatly reduced, which directly reduce the distance between each electrode (distance between WE and RE: 5 mm, distance between WE and CE: 25 mm) to reduce the cell resistance to support CO_2 electrolysis at higher current density and lower overpotential. Moreover, external to the cathode chamber, a cooling condenser has been added between the gas out port and the GC to prevent the humidity in gas samples from entering the GC and damaging the column. The gas tightness of the closed reactor has been tested and there was no gas leakage during the reactions. The main body of the reactor was constructed from polycarbonate to allow visualisation of CO_2 gas bubbling, and anolyte and catholyte levels during reaction and a Nafion-117 membrane.

Usually, when running CO_2RR with the flow cell, WE and RE need to be installed in the cathodic chamber, CE need to be installed in the anodic chamber, and the small plastic tube for transmitting CO_2 should be fixed so that the tube tip is close to the WE surface. Next, the Nafion membrane is carefully placed on the gasket, then placed between the two chambers, and the entire flow cell is tightly secured with Sawgelok screws. The flow cell is then connected to the pump through rubber tubes, and the electrolyte is injected into the two chambers respectively, the entire cell is sealed by Sawgelok screw cap. Then the pump can be started, when the electrolyte circulation is stable, CO_2 gas can be continuously injected into the cathode chamber. The gas outlet of the flow cell is connected to the subsequent waterproof device and GC.

3. Dimension-tunable copper nanowire (CuNWs): Growth and electrochemical characterization

Aims

Nanowire (NW) based structures can optimize the properties of functional materials and endow them widespread application due to the large surface area-to volume ratio (SA:V), abundant active sites and excellent photophysical properties[190–194] A lot of researchers have explored the use of NW structures for electrochemistry, aiming to improve electrocatalysis and electrochemical energy storage and conversion technologies.[195,196] Especially, due to the good conductivity, stability and low cost, copper nanowires (CuNWs) have been widely investigated. An anodic aluminum oxide membrane (AAO) is an ideal template for the synthesis of CuNWs due to its good mechanical strength, thermal stability, scalability (pore (channel) length and distance between pores can be adjustable with the anodizing process), and ordered porous nanostructures are possible. Generally, the strategy of preparing CuNWs through AAO porous templates, in most studies is to control the size of CuNWs by changing the diameter of etched AAO template pores and filling completely with Cu.[197] In subsequent processing, it is necessary to widen or completely remove the AAO template to provide access to the surface of the CuNWs. The aim of this work is to grow uniform and free-standing CuNWs in AAO templates by electrodeposition of variable length and width in a single template. The dimension of CuNWs can be partially tuned by exploring the deposition current and time parameters instead of relying on the template controlling the diameter of CuNWs. In this way, even with the AAO template retained, the CuNWs can fully contact with the electrolyte during the electrochemical reactions, which ensures access to reactive sites on the surface of the electrode. The electrochemical behaviour and mass transfer to the electrode surface can be studied using redox probes and the electrochemical surface area and roughness of the CuNW-AAO electrodes can be estimated by double-layer capacitance measurements. This provides guidance for the application of CuNW-AAO electrodes in electrocatalytic reactions.

3.1. Results and Discussion

3.1.1. Physical characterization of the CuNW-AAO electrodes

3.1.1.1. The morphology of Au coating on AAO template

The thermal-evaporated Au coating on AAO template is a vital to grow uniform CuNWs. The Au coating can serve as a working electrode (WE) for CuNW growth and provides an ohmic contact for the CuNW electrode in later electrocatalytic reactions. When a 300 nm gold coating was deposited on a porous AAO template, the morphology can be seen by SEM (Figure 3.1) that, due to the porous structure of AAO, Au was mainly deposited on the template, where the empty channels were not completely covered, resulting in the porous morphology of Au coating. The porous Au coating could not provide a homogeneous platform for CuNW growth, which was not conducive to the rapid and uniform growth of CuNWs.

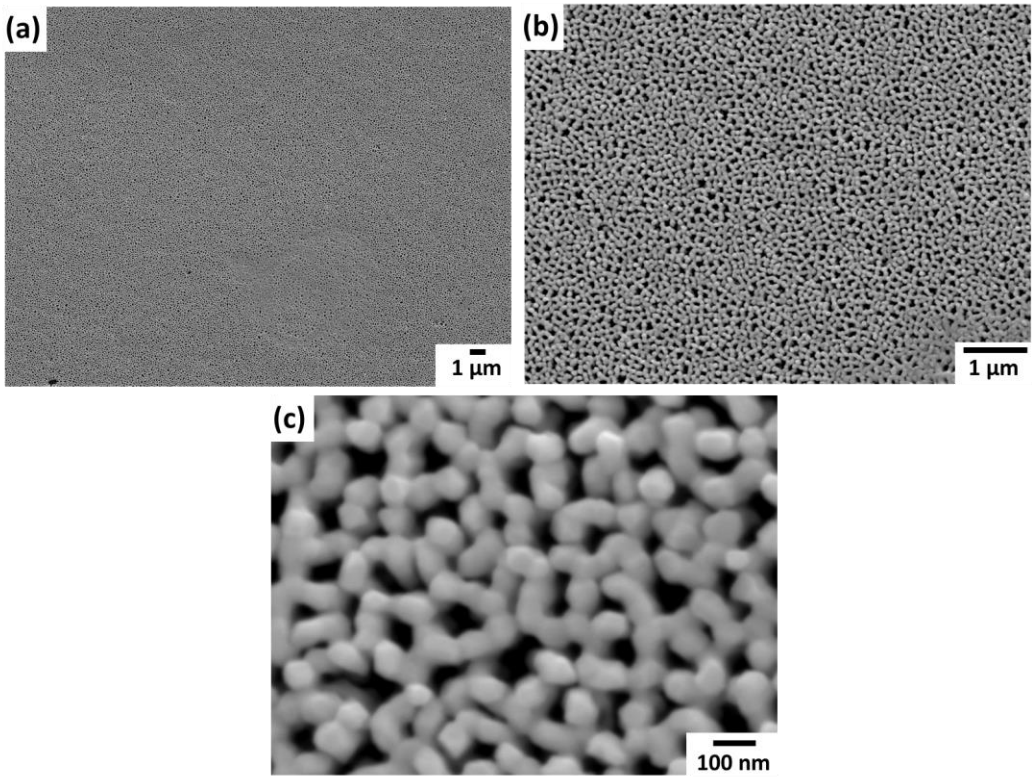

Figure 3.1: SEM images of the porous Au coating on AAO membrane: (a) x 3 700, (b) x 15 000, (c) x100 000.

The pores of the coating can be covered by increasing the thickness of Au coating,[198] but too much Au evaporation will lead to the increased costs and material waste. High temperature treatment close to the melting point of gold (1064 °C) was

explored to slightly melt the Au to fill the pores and strengthen Au coating adhesion to the AAO template. Optimisation, monitored by SEM, showed that Au deposited AAO template heated at 770 °C for 10 min in a tube furnace provided a homogeneous film without distorting or damaging he AAO template. From SEM (Figure 3.2 (a)), it can be found that the Au coating after high temperature annealing can almost completely cover the entire surface of the AAO template. There are some uncovered pores in a few areas. Under high magnification (Figure 3.2 (b)), the surface of Au coating is very dense. Figure 3.3 more clearly shows the change of morphology and structure of Au coating from porous to dense before and after high temperature treatment, which is more conducive to supporting the uniform growth of CuNWs.

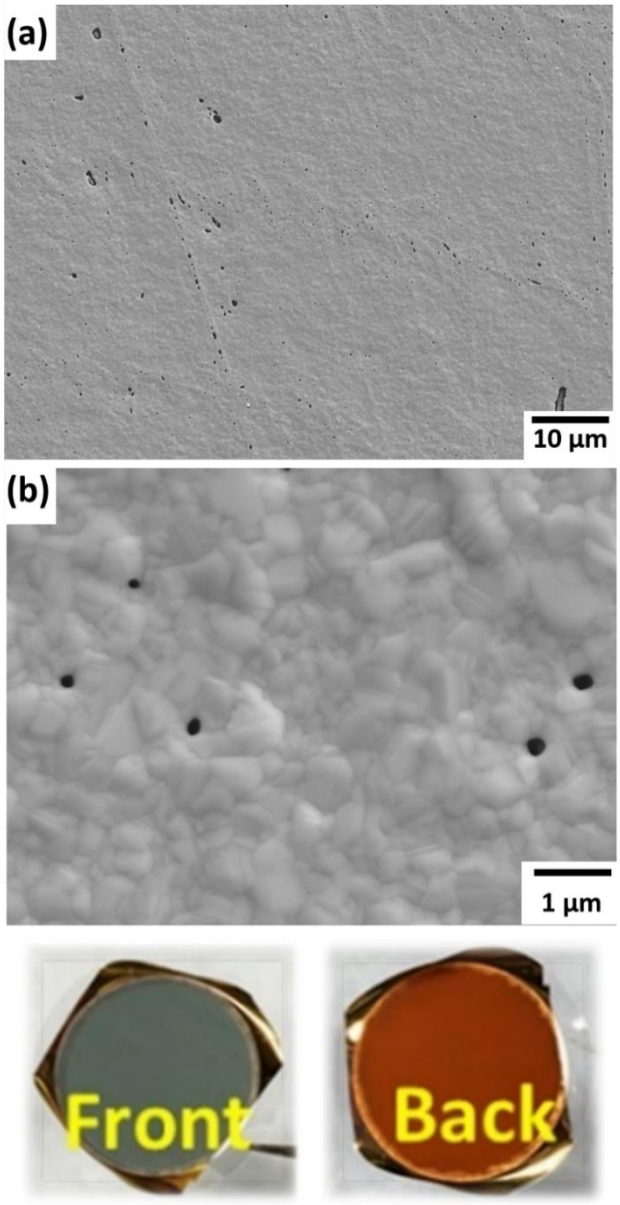

Figure 3.2: SEM images of the high-temperature annealed Au coating on AAO membrane: (a) x 1 500, (b) x 15 000, and the photos of front and back surface of AAO membrane.

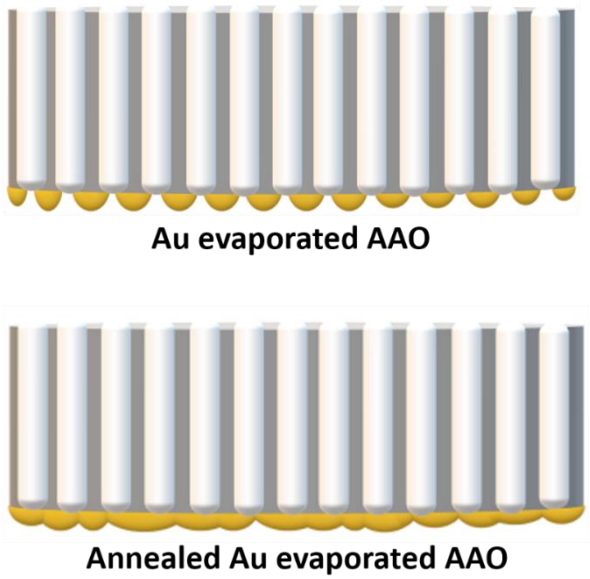

Figure 3.3: Schematic diagram of Au coating on AAO template before and after high-temperature annealing.

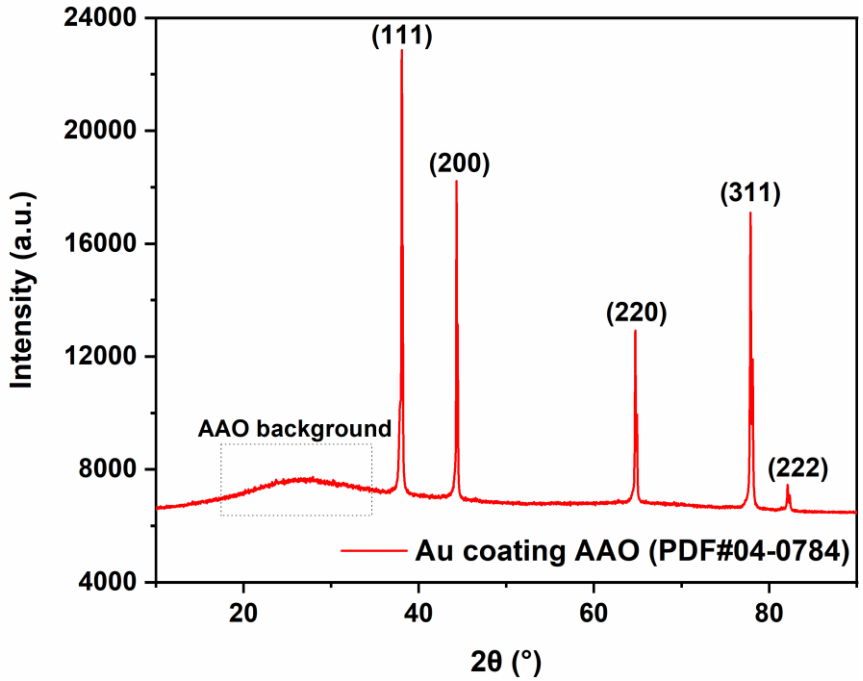

Figure 3.4: XRD pattern of the evaporated Au coating on AAO membrane.

Figure 3.4 shows the XRD pattern of evaporated Au coating. High intensity diffraction peaks at 38.18°, 44.39°, 64.58°, 77.55° and 81.72° correspond to the lattice constants of Au, respectively.[199] Combined with the SEM data, it can be concluded that Au completely covers one side of the template well.

3.1.1.2. The morphology of CuNW-AAO electrodes

After confirming the dense morphology of Au coating, CuNWs were then grown on the Au evaporated AAO templates by electrochemical deposition. As described in the experimental section, electrodeposition in a three-electrode system was carried out by a galvanostatic square wave pulsed deposition technique. As shown in Figure 3.5 (a), when a certain pulsed current was applied, the square waveforms are uniform and continuous overall, and the potential response is also stable. It should be noted that in section 3.1.2 (Figure 3.9) analogous experiments show an induction period ascribed to CuNW nucleation. Here the lack of an induction period is attributed to incomplete sealing of the membrane edges allowing electrolyte penetration and Cu growth from the edges of the membrane. The sealing method was improved throughout the project to limit CuNW growth from the front of the porous membrane. However as seen in Figure 3.5 (b), in this preliminary study there are no spikes in potential, indicating that CuNW growth is quite uniform. This is important because when CuNW-AAO is used as an electrocatalytic electrode, the uniformity and stability of CuNWs is expected to directly affect the activity and selectivity of electrocatalytic reactions.

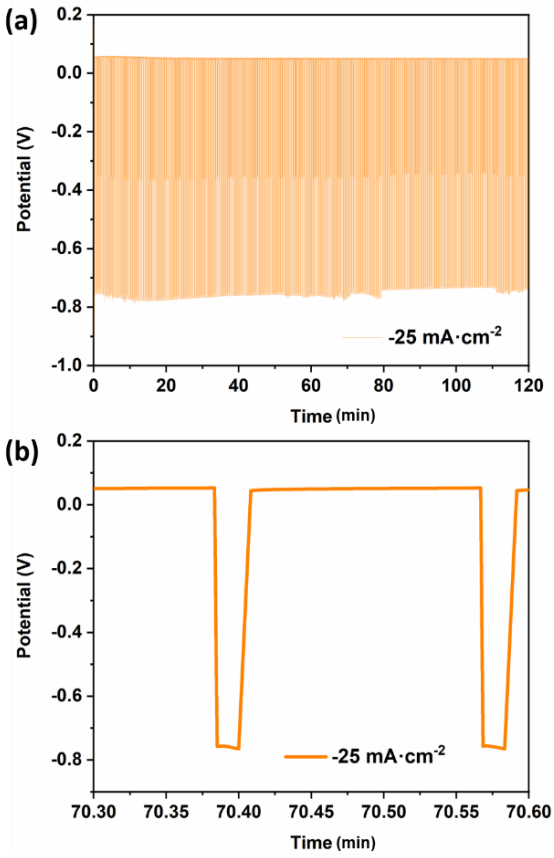

Figure 3.5: Potential waveform recorded during a square pulsed electrodeposition of CuNWs (a) at -25 mA·cm^{-2} for 2 h, (b) locally amplified square waveform.

To observe the state of CuNWs existing in the CuNW-AAO electrode, the CuNW-AAO electrode obtained in Figure 3.5 was carefully removed from the Al disc, then was cut into some small pieces for SEM observation of the electrode surface morphology. It should be noted that cutting was performed using a scalpel which results in damage and breakage of the CuNWs near the surface. Alternatively focussed ion beam (FIB) milling could be used to minimise damage but was not deemed necessary at this stage of the project, because as hwon later the AAO membrane can be removed chemically using strong base. Small pieces of electrode were mounted on a 90° cross-section specimen stage. As shown in Figure 3.6 (a), at low magnification, the electrodeposited CuNWs could be clearly seen distributed throughout the AAO template channels. The length of CuNWs does not reach beyond the thickness of AAO template. At high magnification (Figure 3.6 (b)), CuNWs standing independently in the channels can be clearly seen, with varying lengths due to damage but with quite uniform diameter. To be able to observe more clearly and estimate the length and width distribution of CuNWs, it is necessary to remove the AAO template to release CuNWs from the template.

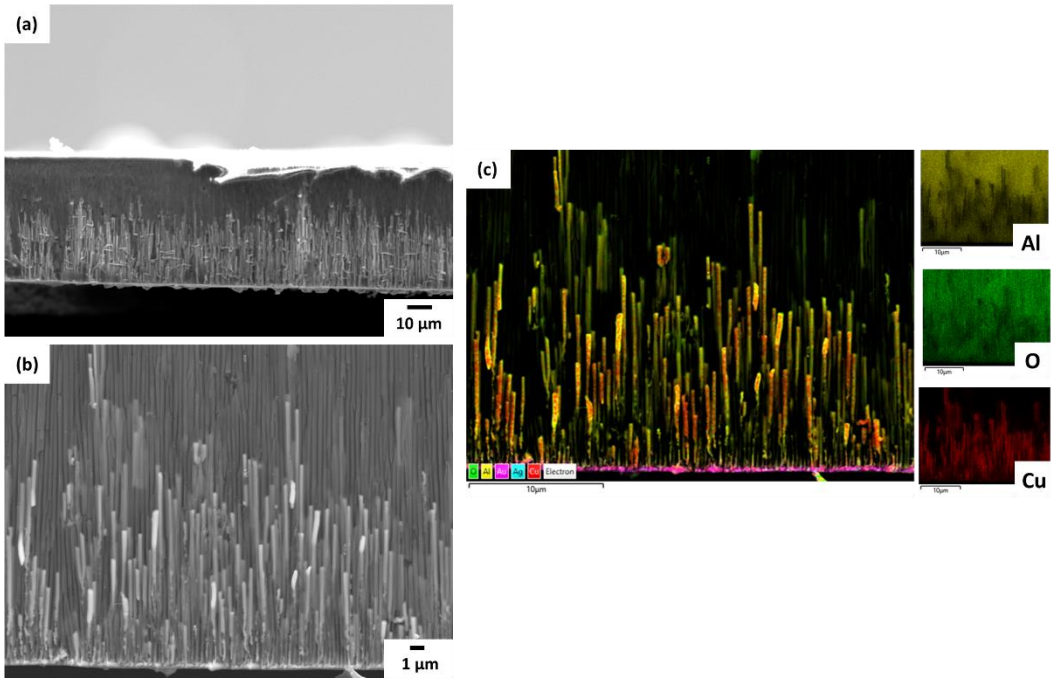

Figure 3.6: Surface morphology and elemental analysis of deposited CuNW-AAO electrode (obtained at -25 mA·cm^{-2} for 2 h, the sample in Figure 3.5): (a) SEM cross-section view of CuNW-AAO electrode (x 650), (b) SEM cross-section view of CuNW-AAO electrode (x 3 700), (c) EDX Elemental mapping of CuNW-AAO electrode from cross-section view (with Al-K, O-K, Cu-K).

To get a clearer observation of the CuNWs pieces of CuNW-AAO electrodes were treated for 1 hour with 0.1 M NaOH solution to remove the AAO template to expose more CuNWs. The morphology of the treated CuNW-AAO electrodes were observed by SEM. From the cross-section view in Figure 3.7 (a) (c), comparing with the existence of intact AAO template (in Figure 3.6), it is clearer to see many free-standing CuNWs can be obtained by the square-wave pulsed electrodeposition, and the height of the most NWs is similar. From the top view in Figure 3.7 (b), it can be seen that many CuNWs are distributed uniformly and densely. In Figure 3.8 (a)-(d), the distribution of Cu, Al and O elements confirms the successful preparation of CuNWs. There are still some detected signals of Al indicates that there is still some residual Al_2O_3 membrane present, while the slightly higher content of O element than Al indicates there may be a thin oxide layer of Cu_xO on the surface of some exposed CuNWs, which was later confirmed by PXRD in better quality samples (see section 3.1.2, Figure 3.10).

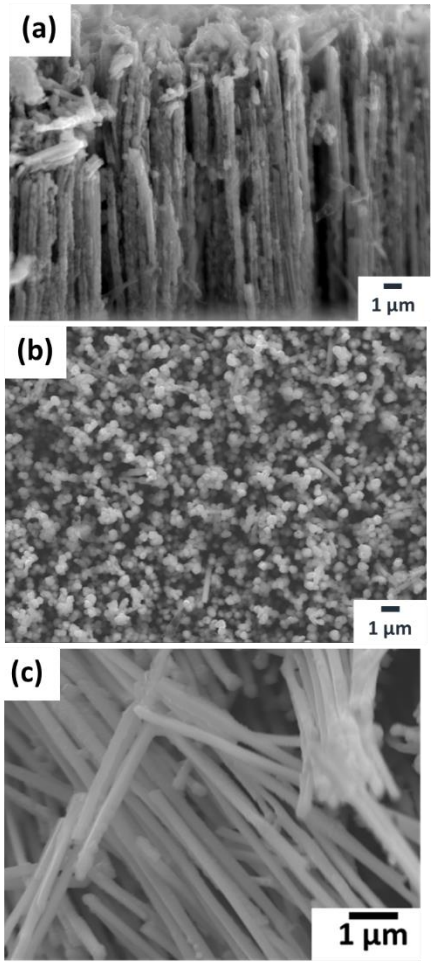

Figure 3.7: Surface morphology of deposited CuNW-AAO electrode with the treatment of 0.1 M NaOH for 1 h (-25 $mA \cdot cm^{-2}$ for 2 h, the sample in Figure 3.5): (a) SEM cross-section view of CuNW-AAO, (b) SEM planform view of CuNW-AAO (c) SEM cross-section view of CuNW-AAO (at a very clear area with high magnification).

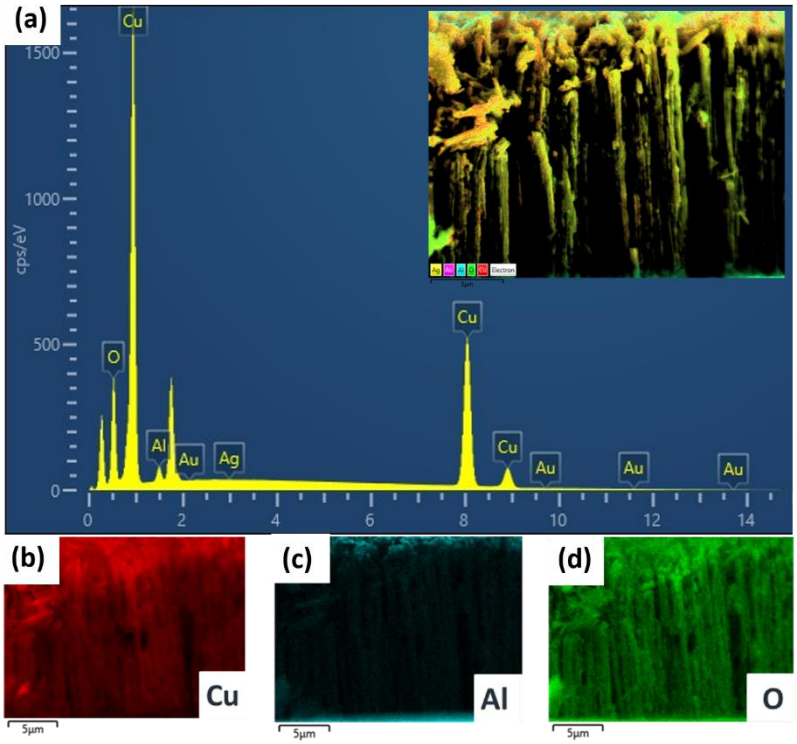

Figure 3.8: Elemental analysis of deposited CuNW-AAO electrode with the treatment of 0.1 M NaOH for 1 h (-25 mA·cm^{-2} for 2 h, the sample in Figure 3.5): (a) EDX spectrum of CuNW-AAO, insert: Elemental mapping of CuNW-AAO, (b) EDX mapping of Cu-K, (c) EDX mapping of Al-K, (d) EDX mapping of O-K.

It is clear that independent and uniform CuNWs can be obtained successfully by square-wave pulsed electrodeposition. When considering the potential applications of CuNW-AAO as an electrode material for electrocatalytic reactions, adjustable dimensions could be beneficial. This is because greater surface area could give greater current density and the dimension of nanocatalysts can affect adsorption and selectivity of intermediate product in the catalytic reactions, and affect the selectivity of the final product.[200,201] Therefore, varying the width and length of CuNWs was studied as described in the next section.

3.1.2. Varying the length and width of CuNW-AAO electrodes

In literature work,[202–204] the CuNW dimensions are regulated using hard anodized AAO templates with different pore diameters and thickness. However, it was envisaged that it would be difficult for electrolyte to access the CuNW surface because the growing CuNWs would fill the AAO pore completely. Nevertheless, our aim was to retain the AAO template, to modify the microenvironment in which the

electrode operates. Therefore, different current density and duration of CuNW deposition was explored to resize the CuNWs rather than regulating the size with templates of different sizes. When a relatively low current density (-25 $mA \cdot cm^{-2}$) was applied, as shown in Figure 3.9 (a) (c), initially a higher potential is required, which we attribute to nucleation and Cu growing on the Au layer and filling the bottom of the AAO porous channels. After, the potential stabilises reducing slowly, indicating that growth requires less energy to maintain the same rate (current) of deposition, presumably due to less diffusion required. The surface morphology of the CuNW-AAO electrode was observed by SEM. All the CuNW-AAO electrodes in Figure 3.9 were treated with 0.1 M NaOH solution for 1 h to remove some of the AAO template. From the cross-section of SEM, independent and uniform CuNWs could be obtained in 1-2 hours. From CuNW length distribution (Figure 3.9 (b) (d)), the median CuNW length is 10-15 μm in 1 hour deposition at -25 $mA \cdot cm^{-2}$. When the duration was extended to 2 hours, the median CuNW length can reach 22-30 μm. According to the electrodeposition parameters (in Table 3.1), it can also be calculated that Cu mass density can reach 2.49 $mg \cdot cm^{-2}$ in 1 hour and 5.40 $mg \cdot cm^{-2}$ in 2 hours, assuming 100% Faradaic efficiency for Cu electrodeposition, but confirming that there is a positive correlation between the total charge passed and the length of CuNWs during deposition. For further verification, the applied current density was increased to -50$\cdot mA \cdot cm^{-2}$, and the duration was reduced to 0.5 h to make the amount of passed charge consistent with that in Figure 3.9 (a). In Figure 3.9 (e), due to the higher current density, the CuNW growth was accelerated, and the time for potential to reach steady state was shortened. SEM shows uniformly grown CuNWs. From the length distribution (Figure 3.9 (f)), the median CuNW length is still around 10 μm. and in Table 3.1, is shown the Cu mass density of 3.25 $mg \cdot cm^{-2}$ is similar to that of CuNWs obtained at -25 $mA \cdot cm^{-2}$ in 1 hour. However, the distribution of lengths appears to be smaller for -50 $mA \cdot cm^{-2}$ and some bubbling is seen during deposition at -50 $mA \cdot cm^{-2}$ indicating that hydrogen reduction is occurring in addition to Cu deposition. This is unsurprising given the large negative voltage (-3 V to -2 V vs.Ag/AgCl) and comparison to the conditions of CO_2RR described in Chapter 5 where large amounts of hydrogen at detected using gas chromatography. Therefore, at increasing current density (and more negative voltage) H_2 production will be increasingly competitive with Cu deposition although at the same current density CuNW length appears correlated with passed charge. Changing the current density could therefore provide an opportunity to tune CuNW morphology. Moreover, according to clear SEM images, the diameter distributions of CuNW shown in Figure 3.9 (a), (d) and (g) are about 260-310 nm, 230-280 nm and 280-330 nm, respectively.

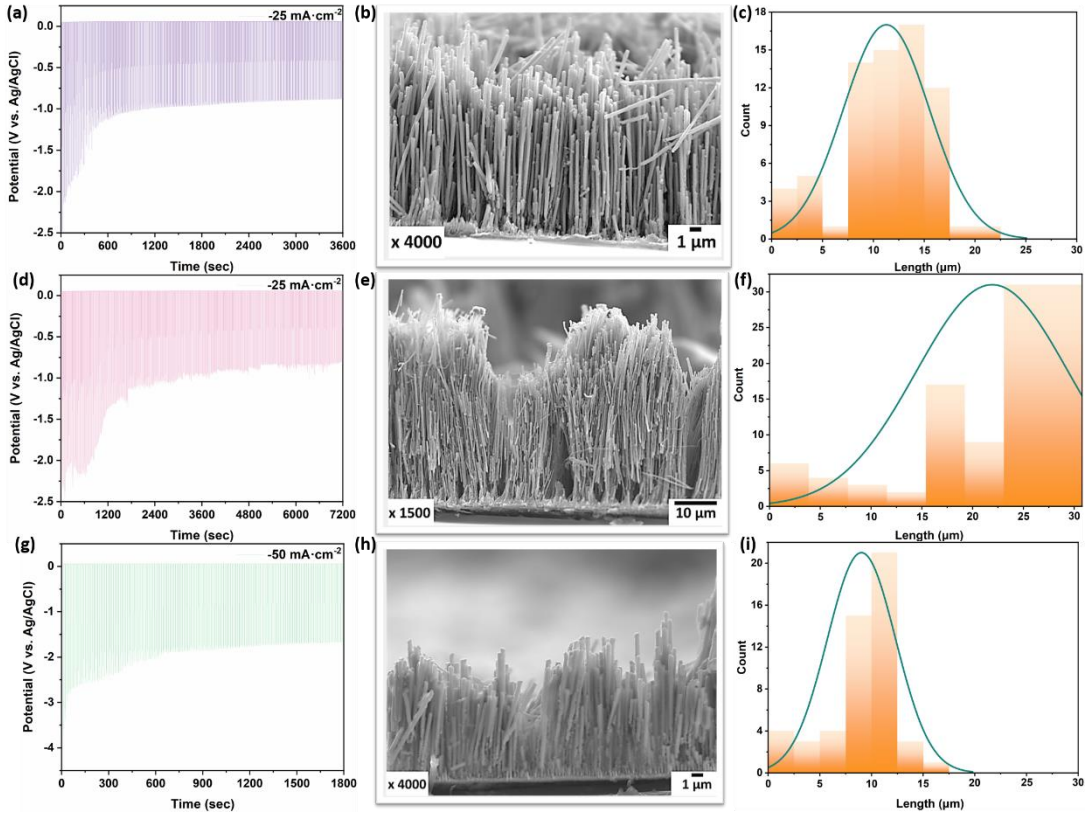

Figure 3.9: CuNWs length regulation: (a) Potential recorded during a square pulsed electrodeposition of CuNWs at -25 mA·cm^{-2} for 1 h. (b) SEM cross-section image of (a). (c) CuNW length distribution of -25 mA·cm^{-2} for 1 h. (d) Potential recorded during a square pulsed electrodeposition of CuNWs at -25 mA·cm^{-2} for 2 h. (e) SEM cross-section image of (d). (f) CuNW length distribution of -25 mA·cm^{-2} for 2 h. (g) Potential recorded during a square pulsed electrodeposition of CuNWs at -50 mA·cm^{-2} for 0.5 h. (h) SEM cross-section image of (g). (i) CuNW length distribution of -50 mA·cm^{-2} for 0.5 h. (All the CuNW-AAO electrodes were treated with 0.1 M NaOH for 1 h for morphology observation.)

Table 3.1: The electrodeposition parameters of CuNW-AAO electrodes.

Sample	*Measured passed charge (C)*	*Calculated (100% FE) Cu mass (mg)*	*Calculated (100% FE) Cu mass density (mg·cm^{-2})*
CuNW-AAO electrode (at -25 mA·cm^{-2} for 1 h)	7.56	2.49	2.49
CuNW-AAO electrode (at -25 mA·cm^{-2} for 2 h)	16.40	5.40	5.40
CuNW-AAO electrode (at -50 mA·cm^{-2} for 0.5 h)	9.89	3.25	3.25

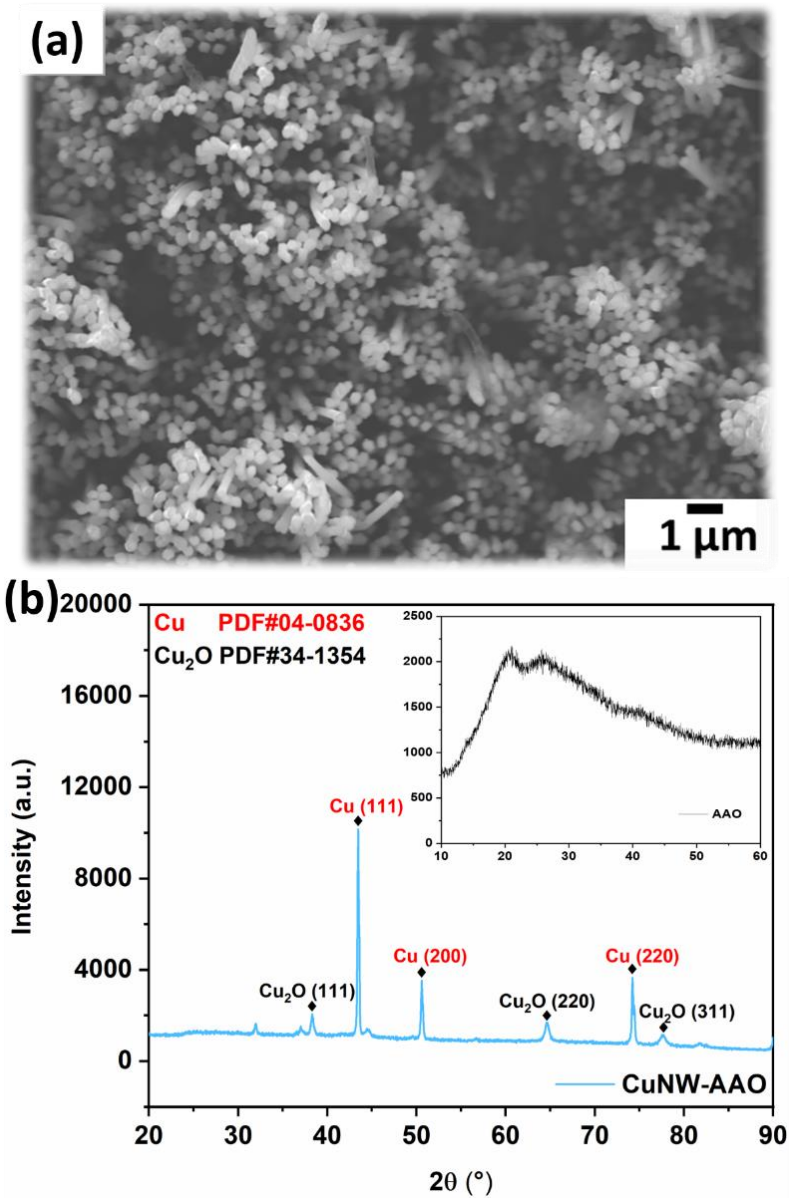

Figure 3.10: (a) SEM planform image of electrodeposited CuNW-AAO electrode at -25 mA·cm^{-2} for 2 h (The sample in Figure 3.9 (d), 0.1 M NaOH treatment for 1 h). (b) XRD pattern of CuNW-AAO electrode, inset: XRD pattern of AAO membrane.

From the SEM planform image of CuNW in Figure 3.10 (a), CuNWs with good uniformity and coverage can be clearly seen. X-ray diffractograms (XRD) reveals the polycrystalline structure of deposited CuNW (in Figure 3.10 (b)).[205,206] The characteristic peaks Cu(111), Cu(200), Cu(220) are relative to the cubic structure of copper, which was confirmed comparing to the JCPDS database. Also, oxidation of the Cu surface is evident from peaks corresponding to Cu_2O and is confirmed by XPS presented in Chapter 4.[207,208] For porous AAO templates, an amorphous peak is usually displayed at 2θ = 20-30°.[209,210]

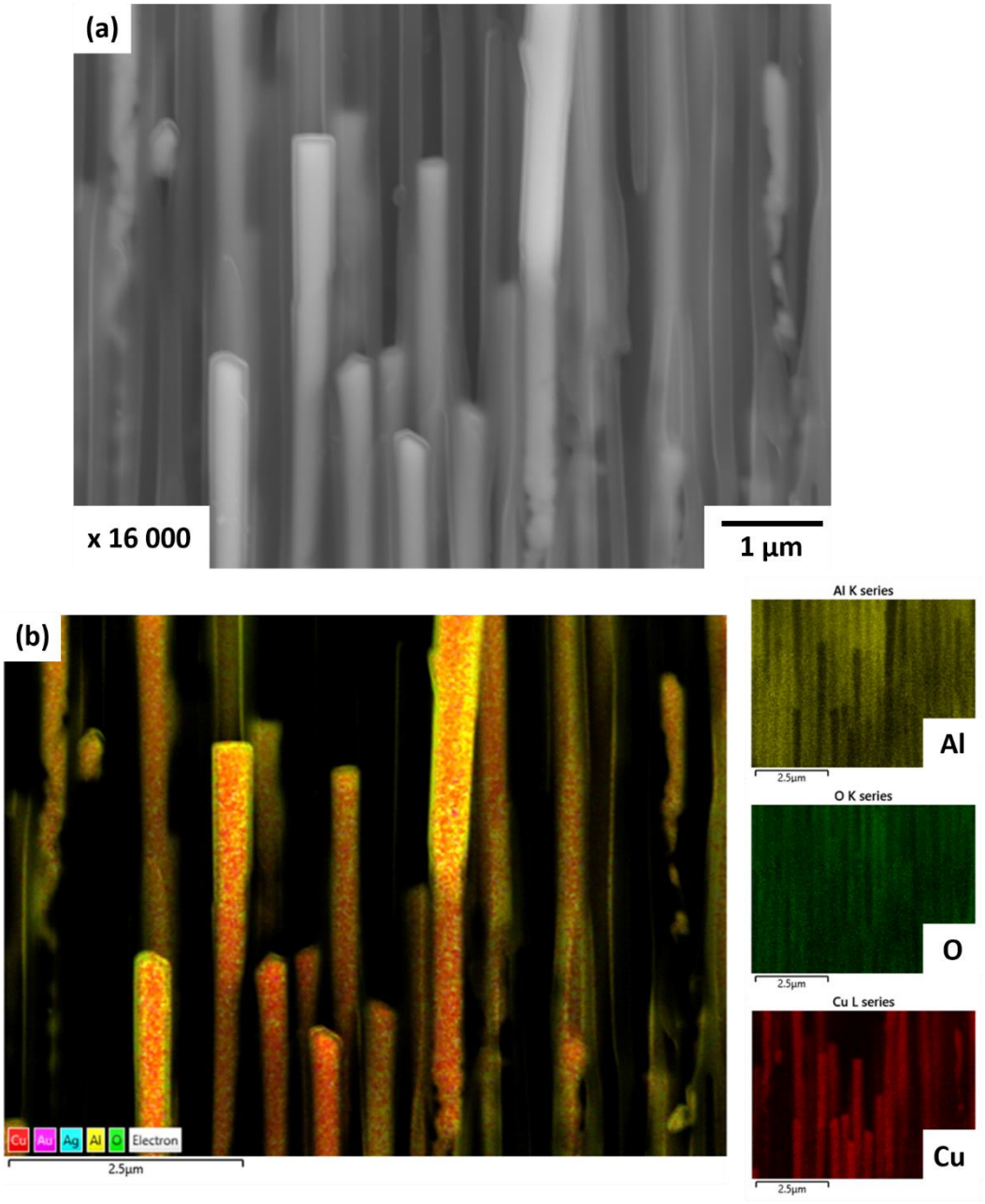

Figure 3.11: SEM cross-section image and EDX (Cu Al elemental) analysis of CuNW-AAO electrode at -50 mA·cm^{-2} for 0.5 h (The sample in Figure 3.9 (g) with the existence of AAO membrane).

Having control of the length of CuNWs by changing the passed charge at a particular current density, the influence of deposition conditions on the CuNW diameter was explored to partly to avoid complete filling of pores and improve access to the electroactive surface area of CuNWs. Based on Figure 3.9 (g), CuNW obtained under the condition of -50 mA·cm^{-2} for 0.5 h has the largest diameter, and it is easier to clearly observe the growth state of CuNW in the AAO membrane on SEM at high magnification (whether the diameter of CuNW completely fills the inside of the AAO

membrane). In Figure 3.11 (a), at high magnification, the deposited CuNWs can be clearly observed by SEM and EDS. In addition, the EDX mapping in Figure 3.11 (b), show both Al, O and Cu signals indicating that CuNW surface is still covered with some of the membrane, it is difficult to directly determine whether CuNWs have completely filled the channels of AAO template. It should also be noted that the membrane walls are also likely to be porous and that electrolyte could diffuse laterally through the membrane as well as parallel to the porous channels.

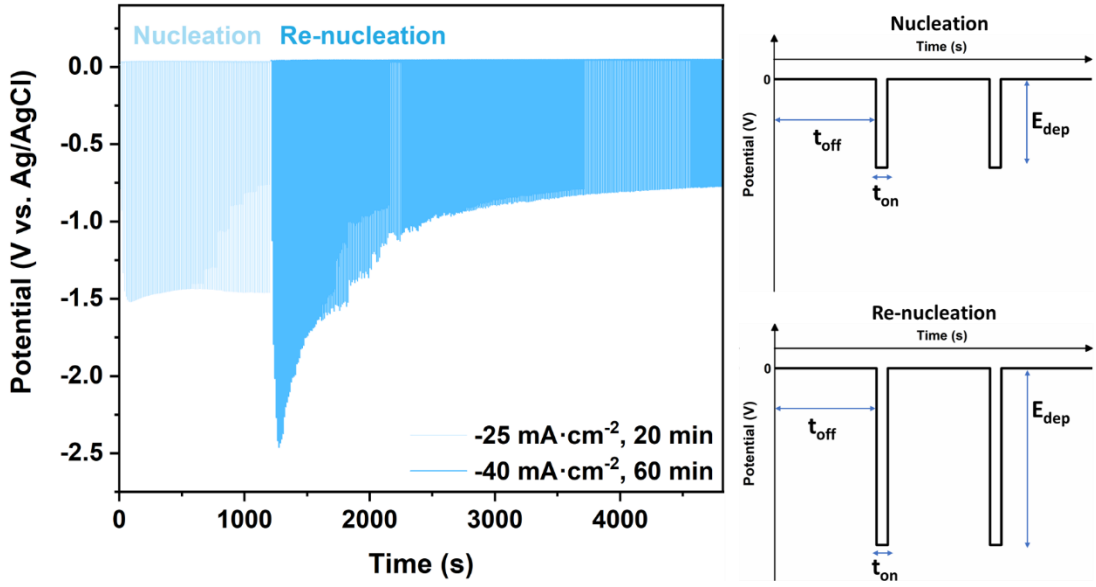

Figure 3.12: Applied potential recorded during a two-step square pulsed electrodeposition of CuNWs.

The effect of current density can be measured by comparing the widths of the CuNWs in Figure 3.9 grown at -25 and -50 mA·cm^{-2}. The diameter distributions of CuNW shown in Figure 3.9 (a), (d) and (g) are about 260-310 nm, 230-280 nm and 280-330 nm, respectively. We believe that there is no significant difference in the CuNW diameter distribution obtained by electrodeposition under the above three different conditions, which may be since when CuNW growth is performed on the Au substrate with a single current density, it is easier to fill the AAO internal channels uniformly and continuously. An alternative approach was also attempted using two-step pulsed electrodeposition. The first stage incorporated nucleation, usually a relatively low current density of -10 mA·cm^{-2} to -25 mA·cm^{-2} was applied, which was assumed to be conducive to uniform filling of the partially porous Au layer and lower volume of the template which would serve as a foundation for further growth of CuNWs.[211,212] The second step was performed at a relatively high current density (-

40 mA·cm^{-2} to -50 mA·cm^{-2}) with the aim of improving the longitudinal growth rate of CuNWs to give narrower CuNWs. The potential response obtained under two-step galvanostatic pulse electrodeposition is shown in Figure 3.12. In this example the first stage, a current density of -25 mA·cm^{-2} was applied for 20 min, the potential response is maintained around -1.5 V vs.Ag/AgCl due to Cu deposition within the Au layer and filling of the irregular bottom of the AAO template and there is a relatively high potential even at lower current densities. On increasing the current density to -40 mA·cm^{-2} for 60 min there is an increase in potential to -2.5V vs.Ag/AgCl followed by gradual decrease to -0.8 V which is lower than that seen in single step deposition at comparable current density (Figure 3.9 (g)).

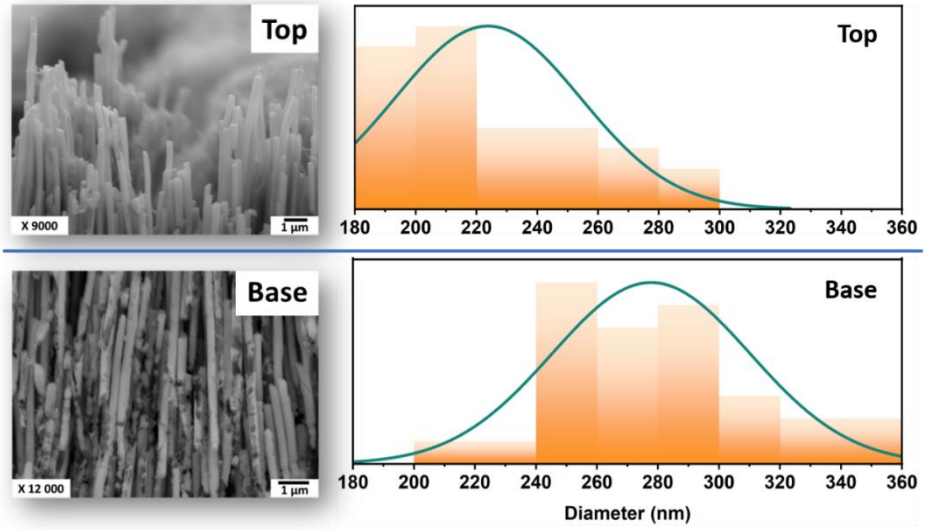

Figure 3.13: Morphology and diameter distribution of CuNW-AAO electrode acquired by a two-step square pulsed electrodeposition: top and base images of CuNWs. (The sample in Figure 3.12, 0.1 M NaOH treatment for 1 h)

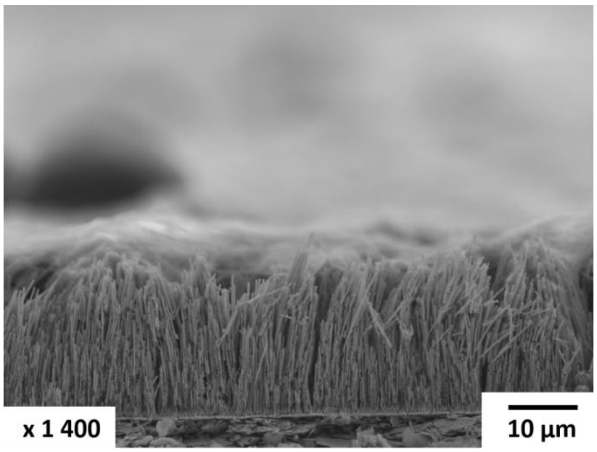

Figure 3.14: Cross-section SEM image of CuNW-AAO electrode acquired by a two-step square pulsed electrodeposition. (The sample in Figure 3.12, 0.1 M NaOH treatment for 1 h)

The cross-section morphology of CuNWs obtained by two-step square pulsed electrodeposition was observed by SEM after the electrode was treated with 0.1M NaOH for 1 h, is shown in Figure 3.13 and Figure 3.14, showing a quite uniform distribution of CuNWs. The passed charge is 9.52 C and the Cu mass density can reach 5.22 mg·cm^{-2} which is similar to values in Table 3.1. The median length of the two-step (at -25 mA·cm^{-2} for 20 min then -50 mA·cm^{-2} for 60 min) CuNWs is 20 μm which compares to ~26 μm for single step deposition (at -25 mA·cm^{-2} for 120 min). Analysis of the width of the CuNWs from two-step deposition shows the base of the deposited CuNWs have a diameter between 240 and 300 nm whereas toward the top the diameter is distributed between 180 and 220 nm. And the growth rate of two-step deposited CuNW is ~4.2 nm·min^{-1} which compares to ~3.6 nm·min^{-1} for single step deposition, indicating a narrowing at higher growth rate.

Control of CuNW morphology within a single AAO template is desirable to achieve regulation of the microenvironment at the CuNW electroactive surface. Changing the applied current density and time of deposition does give a measure of control, particularly length although there remain challenges to achieving truly homogeneous CuNW growth.

3.1.3. Electrochemical characterization for CuNW-AAO electrodes

ECSA can reflect the active surface area of the electrode, as described in the experimental section (Chapter 2), which is usually proportional to the double-layer capacitance (C_{dl}) obtained in cyclic voltammograms. To further ascertain that the CuNWs inside the electrodes can maintain the optimal electrochemically active surface area without being blocked by the template walls, we first performed the multiple CV measurements on the obtained original CuNW-AAO electrodes (the CuNW-AAO electrode was obtained by two-step electrodeposition with a lower current density of -10 mA·cm^{-2} for 60 min at the first step and a higher current density of -50 mA·cm^{-2} for 60 min at the second step for ECSA measurements. The electrodeposition curve and Cu mass loading is shown in Appendix 2 Figure A 2.1). Then, CuNW-AAO electrodes were immersed in 0.1 M NaOH solution for either 0.5 h or 1 h to remove some of the AAO template and increase the exposure of CuNWs (0.5 h CuNW-AAO electrode) and (1.0 h CuNW-AAO electrode) and multiple CV measurements performed. The corresponding ECSA and R_f can be evaluated based on these three electrodes and compared to a Cu foil electrode, respectively to evaluate the active surface area and active sites. All the multiple CV measurements

were performed in a non-Faradic potential region (-0.6 V to -0.8 V vs.Ag/AgCl) and in N_2-saturated 0.1 M Na_2SO_4 solution.

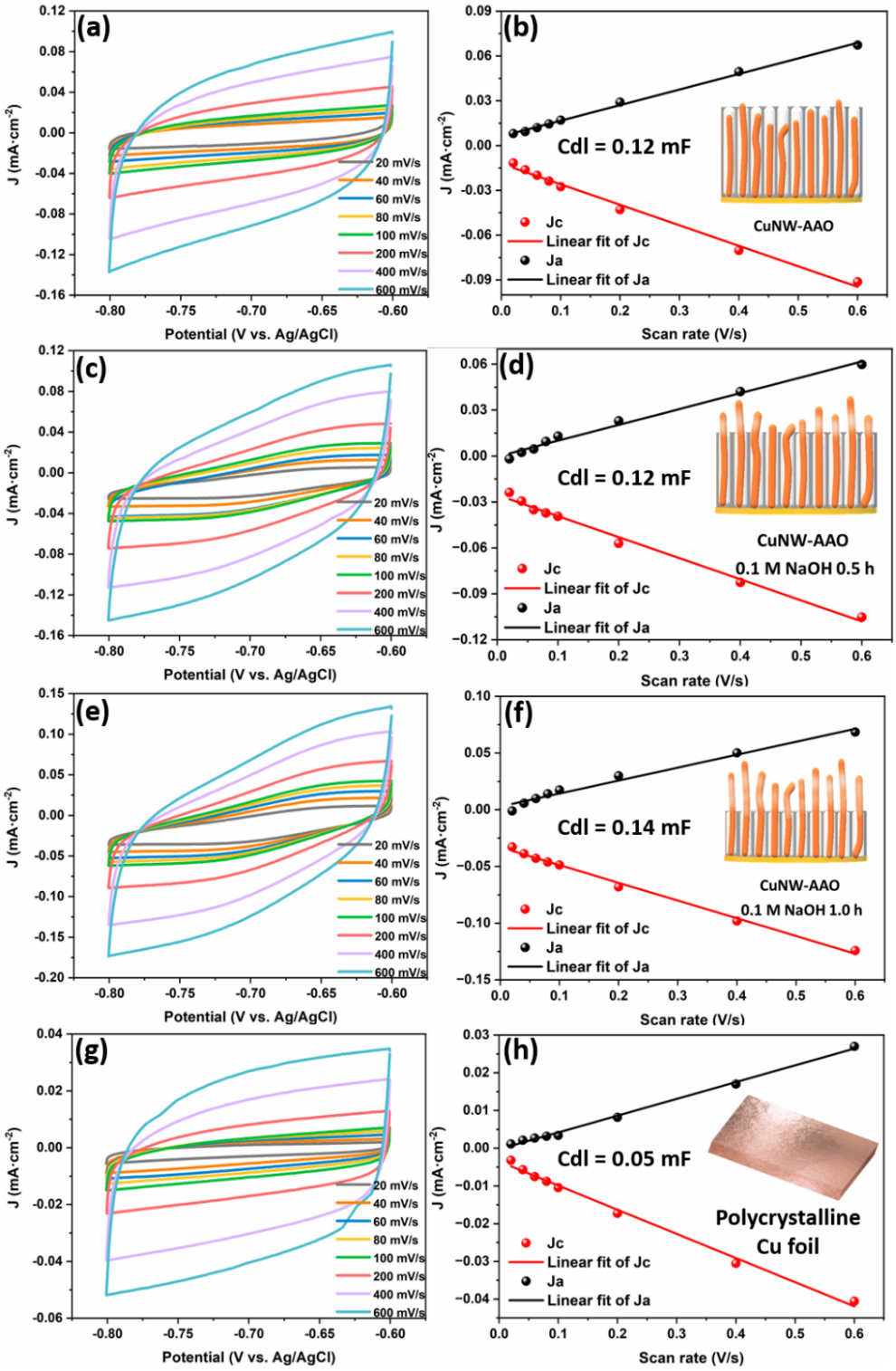

Figure 3.15: Electrochemical surface area measurements (ECSA) of CuNWs-AAO electrodes: (a) cyclic voltammograms (CVs) of CuNWs-AAO electrode. (b) Linear fitting for double-layer capacitance of CuNWs-AAO electrode. (c) CVs of 0.5 h CuNWs-AAO electrode. (d) Linear fitting for double-layer capacitance of 0.5 h CuNWs-AAO electrode. (e) CVs of 1.0 h CuNWs-AAO electrode. (f) Linear fitting for double-layer capacitance of 1.0 h CuNWs-AAO electrode. (g) CVs of flat Cu foil electrode. (f) Linear fitting for double-layer capacitance of flat Cu foil electrode. (All measurements were proceeded in N_2-saturated 0.1 M Na_2SO_4 solution.)

As shown in Figure 3.15 (a)-(d), by normalizing the current response, the ECSA of CuNW electrodes gives a surface area of approximately 3.2 $cm^2 \cdot cm^{-2}$ within 0.5 h of NaOH solution treatment, indicating that even if the AAO template was not removed, the CuNWs inside could fully contact the electrolyte and did not completely fill the template channels. When most of the AAO template was removed, as shown in Figure 3.15 (e) (f), the ECSA of the CuNW electrodes slightly increase to 3.7 $cm^2 \cdot cm^{-2}$, possibly due to more exposure to fresh CuNWs. In contrast, the R_f of Cu foil is 1.72 compared with the standard smooth Cu (the C_{dl} of standard smooth Cu is 29 μF,[213] and the R_f can be regarded as 1), the ECSA of flat Cu foil electrode only reaches 1.72 $cm^2 \cdot cm^{-2}$, which is only half of CuNW-AAO electrode (in Figure 3.15 (g) (h)). It indicates that the introduction of NW structure brings larger active surface area and possibly higher electrochemical activity to the electrodes. On the other hand, when the R_f of Cu foil is defined as 1 for reference, the R_f of CuNW-AAO electrode, 0.5 h CuNW-AAO electrode and 1.0 h CuNW-AAO electrode are 2.4, 2.4 and 2.8, respectively, indicating that CuNWs has greater roughness and potentially greater electrochemically active sites. Based on the results above, both ECSA and R_f of the CuNW-AAO electrode are greater than that of the flat Cu foil electrode. Simultaneously, compared with the electrochemical surface area of CuNWs reported in the literature (are listed in Appendix 1 Table A 1.3), we have successfully prepared CuNWs with large electrochemical surface area while retaining the AAO template. It is worth noting that the above results are based on our assumption that the diffusion behaviour of the electrode surface is linear. However, it can be seen that for 0.5 h CuNWs-AAO electrode and 1.0 h CuNWs-AAO electrode, the CV curves do not look like a perfect fit to linear diffusion, which suggests that for a CuNW-AAO electrode with a rough surface nanostructure, it is over simplified to analyze the electrode surface diffusion process only by using a linear diffusion model. The diffusion mechanism of the electrode surface will be further discussed in Figure 3.18.

The porous structure and Faradic behaviour inside the CuNW-AAO electrode, can be further studied using a redox couple probe.[214,215] As a redox probe, 1,1'-Dimethyl-4,4'-bipyridinium dichloride (also known as methylviologen, MV) can be used to explore the cyclic voltammetric behavior of metal and non-metal electrodes due to its distinct redox couple.[216–221] Figure 3.16 shows the cyclic voltammograms of a Cu foil electrode in the range of -0.4 V to -1.2 V vs.Ag/AgCl at different scan rates. Two couples of redox peaks can be observed at the potential of -1.0 V and -0.7 V, which is corresponding to the process of of $MV^0 \rightleftarrows MV^+ \rightleftarrows MV^{2+}$, respectively. Due to the possible hydrogen evolution reaction in aqueous electrolyte, we focused on the

measurements by the electrochemical behaviour of the $MV^{+} \rightleftarrows MV^{2+}$ reactions (reversible redox peaks: peak I and peak II, $i_{pa}/i_{pc} \approx 1$) on electrodes. To monitor the $MV^{+} \rightleftarrows MV^{2+}$ reactions on CuNW-AAO electrodes by methylviologen redox probe, cyclic voltammograms of CuNW-AAO electrodes in 1 mM methylviologen electrolyte at different scan rates were recorded as shown in Figure 3.17.

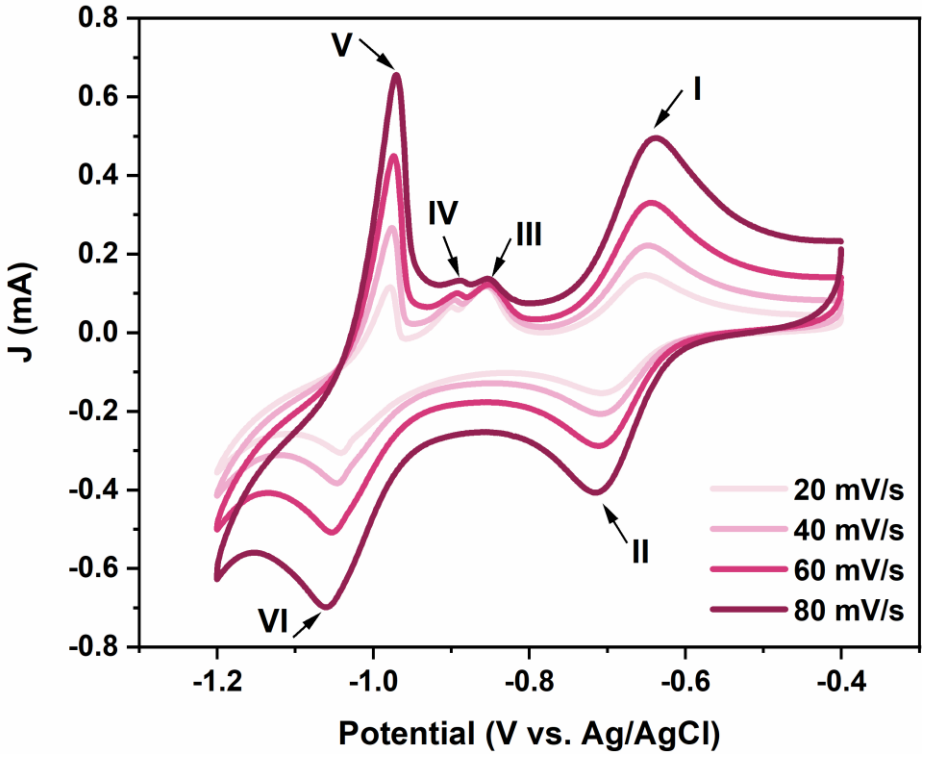

Figure 3.16: Cyclic voltammogram of Cu foil electrode in the range of -0.4 V to -1.2 V vs.Ag/AgCl at different scan rates measured in aqueous N_2-saturated 0.1 M Na_2SO_4 solution containing 10 mM di-methyl viologen di-chloride.

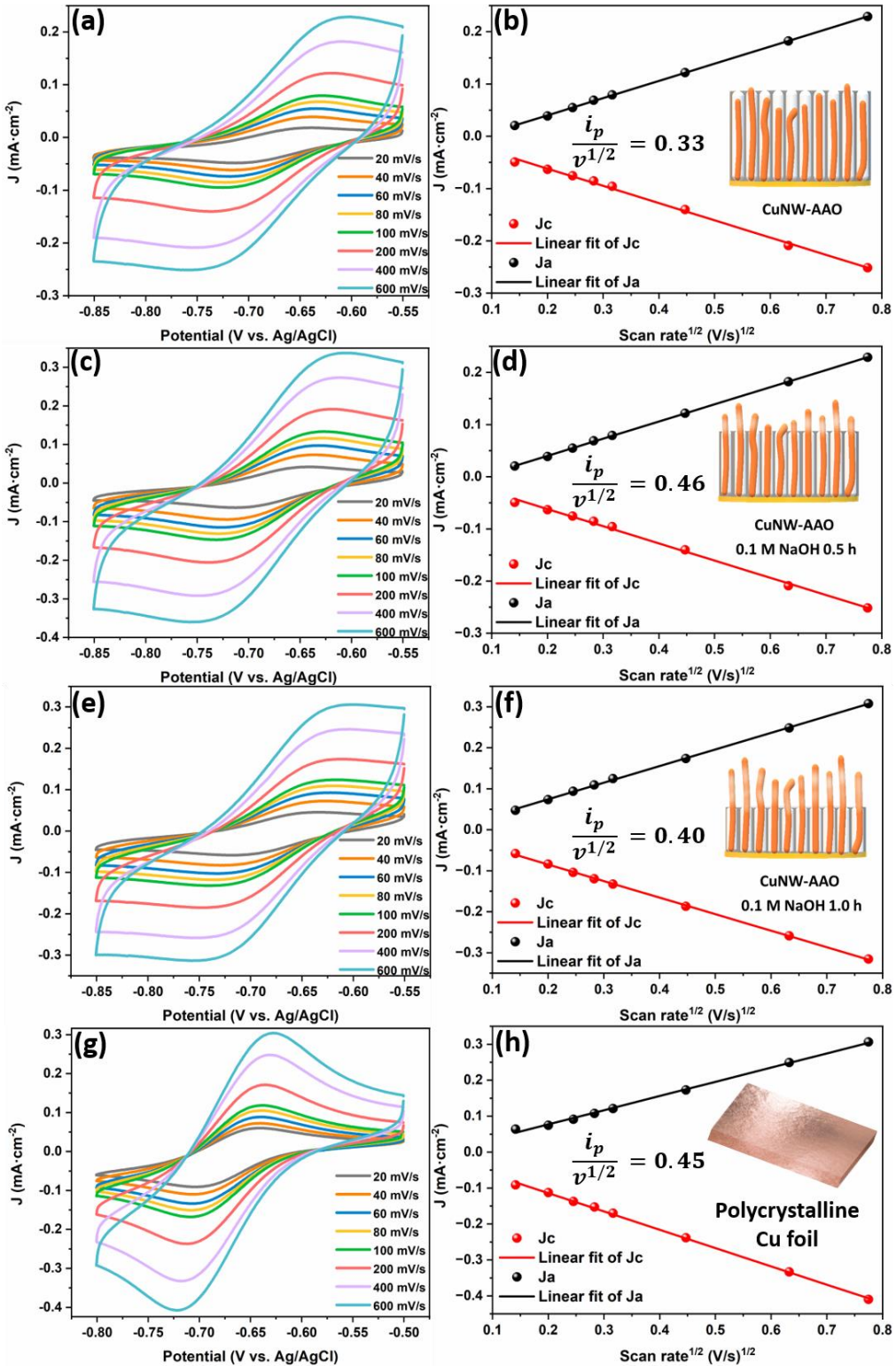

Figure 3.17: Electrochemical active surface area measurements (ECSA) of CuNWs-AAO electrodes: (a) CVs of CuNWs-AAO electrode. (b) Linear fitting for redox couple via Randles-Ševčík of CuNWs-AAO electrode. (c) CVs of 0.5 h CuNWs-AAO electrode. (d) Linear fitting for redox couple via Randles-Ševčík of 0.5 h CuNWs-AAO electrode. (e) CVs of 1.0 h CuNWs-AAO electrode. (f) Linear fitting for redox couple via Randles-Ševčík of 1.0 h CuNWs-AAO electrode. (g) CVs of flat Cu foil electrode. (f) Linear fitting for redox couple via Randles- Ševčík of flat Cu foil electrode. (All measurements were performed in N_2-saturated 0.1 M Na_2SO_4 solution containing 10 mM di-methyl viologen di-chloride.)

Assuming that mass transfer is only controlled by linear diffusion during the reaction, the resulting cyclic voltammograms follow the Randles-Ševčík equation, where the peak current should be linearly proportional to the square root of the scan rate ($\frac{I_{peak}}{v^{1/2}} = (2.69 \times 10^5) \times n^{\frac{3}{32}} \times A \times D^{\frac{1}{2}} \times C$).[222,223] In Figure A 2.19 (Appendix 2), by observing the relationship between the potential at peak current of different electrodes and the scan rate, it can be seen that the peak potential basically does not change with the scan rate at lower scan rates, and a slight peak deviation will be caused when the scan rate is higher. So, the Randles-Ševčík equation can be applied according to the reversible redox peaks. Figure 3.17 (a) (b) shows that with the AAO template, the ratio of peak current response to square root of the scan rate is 0.33. According to the Randles-Ševčík equation, the ECSA of the CuNW electrode is 0.58 $cm^2 \cdot cm^{-2}$. In Figure 3.17 (c)-(f), after removing AAO template to different extent (0.5 h to 1.0 h NaOH treatment), the ratios of peak current response to square root of the scan rate reach to 0.46 and 0.40, respectively and the corresponding ECSA are 0.80 $cm^2 \cdot cm^{-2}$ and 0.70 $cm^2 \cdot cm^{-2}$, respectively. For flat Cu foil electrode, the ratio is 0.45 with the ECSA is 0.79 $cm^2 \cdot cm^{-2}$. The absolute values of surface area are dependent on accurate knowledge of all the parameters in the Randles-Ševčík equation, particularly the diffusion coefficient. However, importantly the results show that the electrochemical surface area of the CuNW can be accessed in the presence of the AAO and that CuNW did not completely fill the pores of the AAO template. Nevertheless, the ECSA of CuNW electrodes calculated by the MV redox probe are generally lower than that calculated by the double-layer capacitance presumably indicating slower diffusion throughout the CuNW structure in the presence of AAO. If it is assumed the double-layer capacitance measurements reflect the relative ECSA then the redox couple data can be used to estimate the differences in diffusion based on the Randles-Ševčík equation.

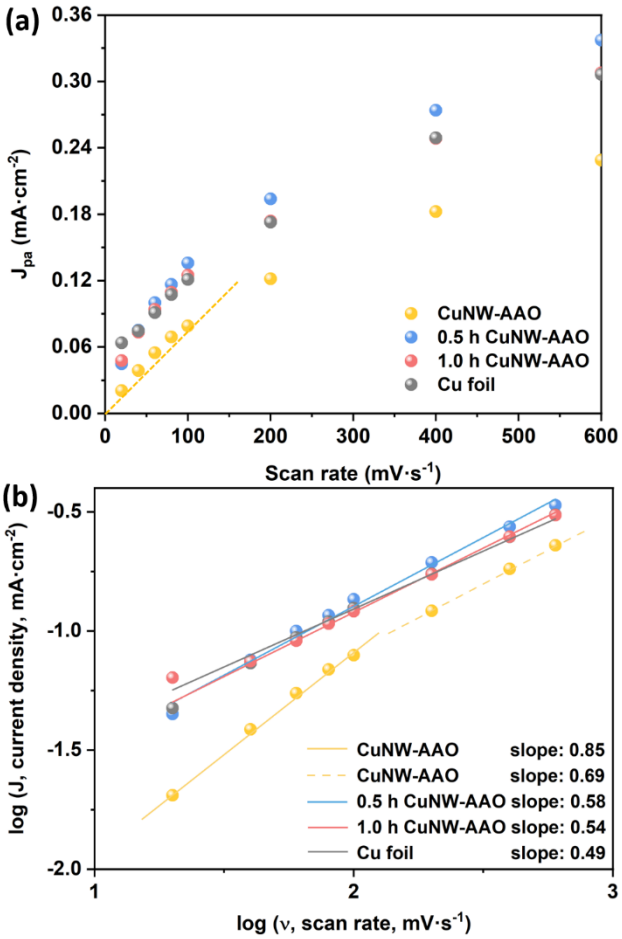

Figure 3.18: Scan rate plots of CuNW-AAO and Cu foil electrode: (a) Anodic peak current vs scan rate. (b) logi vs logv plots (anode), insert: logi vs logv plots on CuNW-AAO electrode (when scan rate lower than 100 mV·s^{-1}). The measurements were performed in N_2-saturated 0.1 M Na_2SO_4 solution containing 10 mM di-methyl viologen di-chloride.

On a flat electrode surface, usually mass transfer is dominated by linear semi-infinite diffusion, and the peak current in cyclic voltammograms is proportional to the square root of the scan rate, following the Randles-Ševčík equation as shown in Figure 3.17. On a porous electrode surface, thin-layer diffusion dominates mass transfer due to limited diffusion, resulting that the peak current is proportional to the scan rate.[224,225] From the linear relationship between the anodic peak current and the scan rate in Figure 3.18 (a), it can be seen that when scan rates are lower than 100 mV·s^{-1}, the peak current respond on the CuNW-AAO electrode with AAO template is proportional to the scan rate (Scan rates lower than 100 mV·s^{-1} and higher than 100 mV·s^{-1} have significantly different slopes, and the slope lower than 100 mV·s^{-1} passed through zero.), which is a characteristic of thin layer electrochemical behavior. (It has been confirmed above that CuNWs did not completely fill the template channels.) It may be due to the existence of AAO, MV molecules could be trapped in the narrow

gap (tens or hundreds of nanometers) between CuNWs and template channels, resulting in limited diffusion. When the template was partially removed using NaOH CuNW exposure increased to the electrolyte causing MV molecules unable to be trapped near the electrode surface, the current response in the reaction was mainly due to the contribution of semi-infinite diffusion. Similarly, for flat Cu foil electrodes, mass transfer is dominated by semi-infinite diffusion due to the absence of any nanostructures and rough surfaces. Logarithmic relation between anodic peak current and scan rate provides more evidence for the contribution of thin layer diffusion on the CuNW-AAO electrode. When the linear slope is 0.5, the mass transfer is controlled by semi-infinite diffusion, and when it is 1.0, the mass transfer is controlled by thin-layer diffusion.[226,227] In Figure 3.18 (b), after removing the AAO template, the slope of 0.5 CuNW-AAO and 1.0 CuNW-AAO electrodes are close to 0.5, which is similar to that of flat Cu foil electrode, both of which are controlled by semi-infinite diffusion. The slope of CuNW-AAO electrode is 0.69, especially when the scan rates are lower than 100 $mV \cdot s^{-1}$, the slope is as high as 0.85, indicating that thin-layer diffusion and semi-infinite diffusion contribute to the mass transfer. By combining the double-layer capacitance and redox probe results, the ECSA and R_f of the electrode as well as the mass transfer mechanism indicates that the CuNW surface is available for redox electrochemistry and that the porous AAO membrane does not severely restrict access to electrolyte, which will be important for use as an electrocatayst described in Chapter 5.

3.1.4. Electrochemical impedance measurements (EIS) for CuNW-AAO electrodes

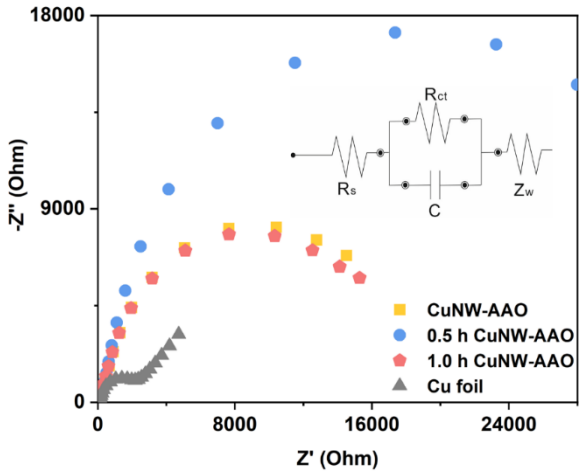

Figure 3.19: Electrochemical impedance: Nyquist plots of EIS and equivalent circuit R(CR)W for impedance fitting for CuNW-AAO and Cu foil electrodes at open circuit potential in 0.1 M Na_2SO_4.

Table 3.2: The fitting parameters of EIS for CuNW-AAO and Cu foil electrodes at open circuit potential.

Electrode	R_s *(Ohm·cm^{-2})*	*C (mF)*	R_{ct} *(Ohm·cm^{-2})*	Z_w *(mOhm·cm^{-2})*
CuNW-AAO	30.02±1.38	0.42±0.032	12970±1400.76	0.98±0.064
0.5 h CuNW-AAO	48.58±1.75	0.24±0.013	25230±3052.83	0.83±0.053
1.0 h CuNW-AAO	39.52±1.70	0.27±0.019	13510±1378.02	0.92±0.067
Cu foil	30.64±1.50	0.08±0.008	1543±151.21	0.73±0.054

Electrochemical impedance spectroscopy can be used to further understand the impedance changes during electron and mass transfer on the electrode. In the process, the Nyquist diagram consists of a capacitance-reactance arc, which is in the high frequency region, representing the electrochemical reaction process, and a Warburg diffusion characteristic in the low frequency region, representing the solution diffusion process. Therefore, the equivalent circuit was selected as $R_s(CR_{ct})W$. The impedance fitting for CuNW-AAO and Cu foil electrodes as shown in Figure 3.19 (impedance raw data for CuNW-AAO and Cu foil electrodes is shown in Appendix 2 (Figure A 2.13), each electrode has a semicircle in the high frequency region, and the radius of the semicircle represent the charge transfer resistance. Based on the equivalent circuit fitting (Table 3.2), the charge transfer resistances (R_{ct}) of all the CuNW-AAO electrode are much higher than that of the flat Cu foil electrode, resulting in a low electron transfer rate. At the low frequency, Warburg impedance characteristics appear on the flat Cu foil electrode which means the surface diffusion occurs on the electrode surface.[228,229] However, for the CuNW-AAO electrodes, the residual AAO template results in limited diffusion. So, the sloped lines do not appear in the low frequency region due to the influence of large charge transfer resistance, which explains the CuNW-AAO electrode mass transfer can be co-affected by semi-infinite diffusion and thin-layer diffusion.

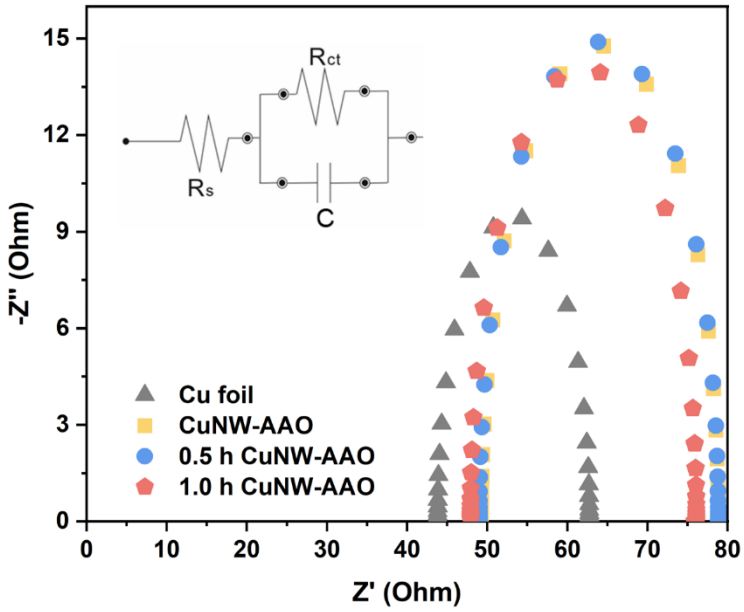

Figure 3.20: Electrochemical impedance: Nyquist plots of EIS and equivalent circuit R(CR) for impedance fitting for CuNW-AAO and Cu foil electrodes at -0.4 V (vs.RHE) in 0.1 M Na_2SO_4. (Nyquist plots are from the fitted data.)

Table 3.3: The fitting parameters of EIS for CuNW-AAO and Cu foil electrodes at -0.4 V (vs.RHE).

Electrode	R_s (Ohm·cm^{-2})	C (mF)	R_{ct} (Ohm·cm^{-2})
CuNW-AAO	49.27±0.80	0.017±0.002	29.55±1.20
0.5 h CuNW-AAO	49.03±0.94	0.025±0.004	29.79±1.46
1.0 h CuNW-AAO	47.90±1.18	0.023±0.004	28.19±1.84
Cu foil	43.80±0.40	0.035±0.003	18.93±0.57

EIS data was also measured as -0.4 V (vs.RHE), common potential used for CO_2RR. Due to the presence of HER side reaction, the mass transfer reaction in the low frequency region was seriously disturbed and the diffusion impedance data could not be fitted. A simplified Randles circuit (R(CR)) was used to analyze the activation control reactions only in the high frequency region. In Figure 3.20 and Table 3.3 (impedance raw data for CuNW-AAO and Cu foil electrodes is shown in Appendix 2 (Figure A 2.14), it can be seen from the intercept of the high-frequency semicircle on

the X axis and the R_s fitting value that the R_s of Cu foil is the smallest (43.80 Ω) and the R_s of CuNW-AAO electrode is the largest (49.27 Ω). This is because in the presence of the AAO template, the contact between the electrolyte and the Cu surface is partially impeded, resulting in an increase in R_s. Even if 0.1 M NaOH solution was used to treat the CuNW-AAO electrode for 0.5 h, this obstacle still existed due to the AAO template that still existed in a large area, and the R_s value hardly changed (49.03 Ω). When the CuNW-AAO electrode was further treated to 1 h, part of the AAO could be removed, more CuNWs were exposed to the electrolyte, and it was easier to contact the electrolyte, and R_s was reduced (47.90 Ω). Compared with the R_s measured at the open circuit potential in Table 3.2, the R_s value at -0.4V (vs.RHE) generally increases, which is due to the presence of HER in the electrolyte. HER will disturb or hinder the contact between the electrode and the electrolyte to a certain extent. Similarly, comparing R_{ct} of different CuNW-AAO electrodes shows that CuNWs can be exposed more when treated with 0.1 M NaOH solution for CuNW-AAO electrode to 1 h the mobility of electrons and ions on the surface charge layer of the electrode can be enhanced to a certain extent. In general, if the ion migration rate is slow during the CO_2RR process, it will accumulate on the electrode surface, which could reduce the current density of CO_2RR, but may also alter the selectivity of reaction if intermediates are retained for longer within the microenvironment the CuNW-AAO electrode.

3.2. Conclusions

Electrochemical parameters can be adapted to adjust the morphology and dimensions of CuNWs particularly length between 10-30 μm at a given current density. Different current densities and deposition can also be applied using a two-step process to regulate the diameter of CuNW between 180 and 300 nm. Even in the presence of the AAO templates, CuNWs are electrochemically accessible. It has been found that ECSA and R_f of CuNW-AAO electrodes are 2.4 times and 2.8 times of flat Cu foil electrode, respectively. The mass transfer mechanism of CuNW-AAO electrodes was further investigated by MV redox probe, indicating that the existence of nanostructure and AAO templates could introduce the thin layer electrochemical effect different from the semi-infinite diffusion on Cu flat foil electrode. Combining with EIS, it is confirmed that the mass transfer process on the CuNW-AAO electrode can be described as between semi-infinite and thin layer diffusion. When the CuNW-AAO electrode was treated for 1 h with 0.1 M NaOH to remove some AAO template, increased CuNW exposure can be achieved, and the electrode has larger electrochemical area, roughness and smaller charge transfer resistance. When being used as an electrode for catalysis such as CO_2RR regulation of diffusion could play a role in reaction selectivity due to the residence time of intermediates such as adsorbed CO, hydrocarbons, and oxygenates which are a key to C-C coupling and the generation of C_{2+} products which is the aim of this project.

4. Interfacial design strategies for CuNW-AAO electrodes: Construction of a stable hydrophobic coating and surface electrochemical characterization

Aims

Nanowire electrocatalysts with large reaction surface area and roughness, controllably exposed crystal surface orientation, highly flexible and adjustable length and density have been widely used in the electrochemical conversion of carbon dioxide into high value-added fuels.[230–237] Ulrich et al. explained the effects of regulating the diameter, length and density of the 3D Cu nanowire network obtained by electrodeposition on the gaseous reactants transport and reaction product kinetics during the CO_2 reduction reactions.[238] A range of hydrocarbons especially C_{2+} products could be obtained in the potential range of -0.5 to -0.93 V vs.RHE. Lyu et al. increased the surface roughness and surface defect density of the catalyst by partially oxidizing the Cu nanowires, which could facilitate high selectivity to ethylene (FE above 50%) at low overpotentials.[239] Zhang et al. constructed the in-situ stacking faults and twin boundaries for small CuO nanowires to promote the coupling of $*CO$ during the CO_2 reduction reaction.[240] As a result, CuO nanowires with defects had a up to 62% FE for ethylene at a low potential of -0.56 V vs.RHE.

Although the nanowire electrocatalysts have been widely applied in the electrochemical CO_2 reduction reactions, there are still some challenges in maintaining long-term stable operation of catalytic systems and producing high value-added products: (i) the low solubility of the gaseous CO_2 in aqueous solution could easily lead to the low CO_2 concentration near the electrode surface. The first-order kinetics will limit the CO_2 reduction reaction rate and make it easier for the active sites on the electrode surface to combine with the electrolyte (H^+), thus improving the efficiency of HER side reaction;[241] (ii) the selectivity of CO_2 reduction reaction is still low, especially toward the multi-carbon products, and the widely studied nanocatalysts generally show high overpotential and low reaction rate for the multi-electron transfer steps;[242,243] (iii) due to the unstable properties of the implicated $Cu^{\delta+}$ active sites in the process of CO_2 reduction reaction, it is easy to cause self-reduction and microstructure changes, resulting in changes in the hydrophobicity of the catalyst surface, changing the dynamic equilibrium at the gas-liquid-solid interfaces. It will not be conducive to improving the selectivity toward multi-carbon products and the stability of the reaction system.[244–246] Therefore, the rational regulations of the microenvironment on the surface of the nanoelectrodes will help to maintain the

dynamic balance at the gas-liquid-solid three-phase interfaces in the reaction, so as to improve the selectivity of the catalyst towards multi-carbon products and the stability of the catalytic system.

In the past few years, more and more researches have focused on improving the stability of electrocatalytic system and the selectivity towards specific products by adjusting the surface microenvironment of electrocatalysts. The microenvironment of electrocatalysts mainly includes hydrophobicity, adsorbability, electronegativity and polarity, and local (atomic/molecular) structures.[247–249] In addition to the structure of the catalyst itself, from the perspective of the solid-liquid-gas interfaces, the mass transfer process in the electrochemical CO_2 reduction reactions have gradually attracted attention. Zhong et al. introduced the quaternary ammonium cation surfactant on the surface of Cu nanowire catalysts and found that the linear long chain surfactant could increase the FE of HCOOH, while the branched long chain surfactant could significantly increase the FE of CO.[250] Simultaneously, the HER side reaction caused by protons on the electrode surface could be inhibited. The electrode-electrolyte interface microenvironment tuned to control the product selectivity and increase the total FE has been realized. Liang et al. modified the CuO nanoparticles with polyvinylidene fluoride (PVDF) to improve the catalyst hydrophobicity.[251] Through the interface modelling, it has been revealed that the hydrophobic polymer could resist the water diffusion, increase the pH value near the catalyst surface, thus suppressing the HER side reaction, and increase the FE of C_2H_4 stably.

However, for copper-based catalysts, the most studies related to controlling product selectivity by modifying surface microenvironment still focus on C_1 products. The surface modification of polycrystalline copper with different functional groups such as aryl, amino, acylamino and ether groups has been studied. It has been found that hydrophilicity is conducive to the formation of HCOOH, cationic hydrophobe is conducive to CO as product, and protons have selectivity towards the byproduct H_2.[252] Poly(4-vinylpyridine) (P4VP) has also been used to chemically modify the polycrystalline copper electrodes, proving that the P4VP layer can enhance the surface hydrophobicity by inhibiting the mass transport of H_2O and HCO_3^- from the electrolyte bulk to the catalytic active sites. The reaction had an increasing selectively towards HCOOH at lower potentials and reduced the HER.[253] By regulating the surface hydrophobicity of the catalysts, C_1 products such as CO and HCOOH in CO_2RR are mainly targeted, while the selectivity of C_{2+} products is still low. Therefore, it is important to find suitably synergistic modifications to enhance the selectivity of C_{2+} products in the reactions when designing the catalyst local microenvironment.

From the perspective of electrochemical behaviours of the electrodes, few studies have discussed in detail about the effects of the molecular modification on the electrochemical area, surface roughness, and electrochemical impedance of the catalyst electrodes. The use of molecular modifications can increase the surface hydrophobicity of the catalyst usually because the molecules will form a dense hydrophobic monolayer on the catalyst surface, impeding the mass transfer of water and even CO_2 gas.[254] The distribution of reactive active sites on the catalyst surface can be effectively evaluated through the electrochemical behaviour of the catalyst electrodes, so as to determine the impact of molecular modification on the electrochemical active sites, for example, whether the original electrochemical active sites on the surface are blocked and affect the selectivity of C_{2+} products. Moreover, the mechanism of mass transfer in the CO_2RR process can be clearly understood through the electrochemical impedance, which will open up new ways to modulate the mass transfer of CO_2-H_2O-electrolyte and product selectivity.

The main objective of this chapter is to change the wetting ability and electrochemical performance of the Cu-based electrodes via regulating the local environment of the electrode surface. On the basis of successfully obtaining the CuNWs with adjustable dimension, excellent uniformity and large surface area by electrodeposition, in this chapter, different kinds of silane molecules were used to functionalize the CuNW-AAO electrode surface, and construct hydrophobic three-phase interfaces. It is expected that by controlling the surface wetting ability of the electrodes, the CO_2 concentration near the electrode surface during the CO_2RR will be increased which will be conducive to mass transfer, charge transfer and reaction intermediate concentration on the surface as shown in Figure 4.1. Furthermore, promoting C-C coupling and improving the selectivity of the reaction to C_{2+} products. In order to clearly understand the effect of the catalyst-electrolyte interface on the electrochemical performance of the catalysts, the Helmholtz double-layer capacitance (DLC, the current density normalized to geometric area was calculated) and methylviologen (MV) redox probe were applied in exploring the electrochemical behaviour of different silane coating modified electrodes. Based on the different electrochemical behaviour of the electrodes, the influence of the coating on the electrochemical surface area-activity and mass transfer process of the electrode was further explored. Therefore, we expect that the electrochemical parameters in the study will help guide development of copper-based catalysts used for CO_2RR.

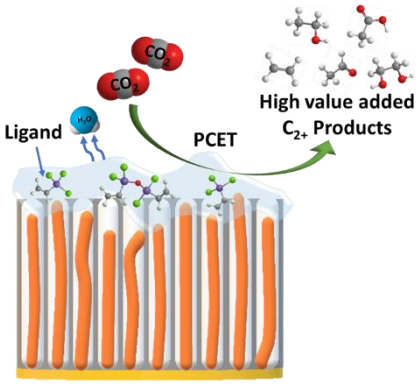

Figure 4.1: Effect of surface functionalization on CuNWs in CO_2 reduction reactions.

4.1. Results and Discussion

4.1.1. Physical characterization of the Cu-based electrodes

4.1.1.1. X-ray photoelectron spectroscopy (XPS) on Cu foil

First, the electropolished Cu foil and the 0.1 M methyltrichlorosilane coating modified Cu foil (0.1-MTS-Cu foil) were characterized by X-ray photoelectron spectroscopy (XPS). Table 4.1 shows the values (%) of the surface composition obtained from the spectrum.

Table 4.1: XPS composition analysis of Cu foil and CuNW-AAO electrodes.

	Molar percentage (%)						*Cu molar percentage (%)*		
Sample	**Cu_{2p}**	**C_{1s}**	**Cl_{2p}**	**Si_{2p}**	**Al_{2p}**	**O_{1s}**	**Cu^{+}**	**Cu^{2+}**	**Cu^{+}/Cu^{2+} molar ratio**
Cu foil	3.93	56.61	0.70	12.78	0	23.65	64.84	35.16	1.84
MTS-Cu foil	0.22	45.21	0	23.90	0	30.67	64.15	35.85	1.79
CuNW-AAO	1.69	65.84	0.90	2.83	0	27.39	74.26	25.74	2.89
MTS-CuNW-AAO	0.35	62.77	0.85	11.79	0	23.72	64.68	35.32	1.83
DTS-CuNW-AAO	2.82	52.33	4.21	12.18	0	27.93	29.40	70.60	0.42
TPS-CuNW-AAO	2.77	60.09	3.34	5.91	0	27.16	48.17	51.83	0.93
TES-CuNW-AAO	5.27	52.25	2.71	3.64	0	35.15	36.35	63.65	0.57
AAO	0	22.41	0	5.80	25.35	39.49	0	0	-
MTS-AAO	0	40.62	0	22.25	6.88	30.25	0	0	-

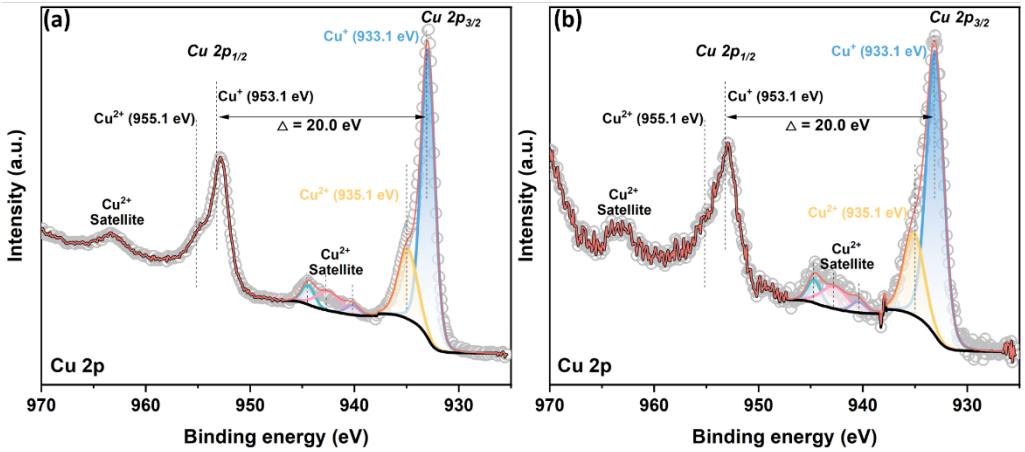

Figure 4.2: Cu 2p XPS patterns of Cu foil: (a) electropolished Cu foil, (b) 0.1-MTS-Cu foil.

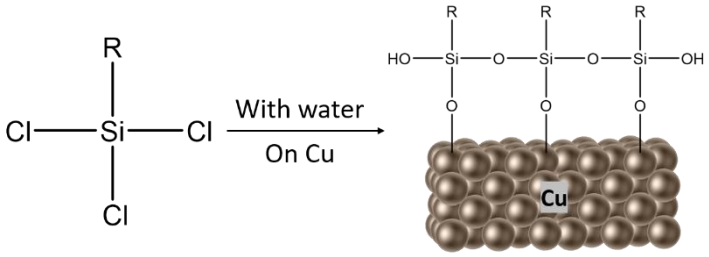

Scheme 4.1: Chlorosilane coating formation on Cu surface.

Figure 4.2 shows the XPS of Cu 2p core level for electropolished Cu foil and 0.1-MTS-Cu foil. The gray scatters represent the raw data; The coloured lines represent the fitting peaks of each composition, the red lines are the sum of the fitting peaks, and the black lines are the background baselines. The spectrum of Cu 2p can be deconvolution to the spin-orbit doublet peaks of Cu $2p_{3/2}$ and Cu $2p_{1/2}$ at 933.1 eV and 953.1 eV, and the energy separation is 20 eV. It indicates the presence of CuO with Cu^{+} state. Also, the spin-orbit doublet peaks of Cu $2p_{3/2}$ and Cu $2p_{1/2}$ at 935.1 eV and 955.1 eV confirm the presence of CuO with Cu^{2+} state.[255–257] And there are two satellite peaks located at 963.1 and 944.4 eV respectively, which are caused by the shake up process when surplus electrons are excited to a higher energy state.[258] In addition, the composition analysis of Cu foil before and after modification with 0.1 M MTS is shown in Table 4.1. It can be seen that the Cu 2p molar values of Cu foil modified by 0.1 M MTS coating is much lower than that of the electropolished Cu foil, because the MTS molecule has leaded to a coating covering the surface of Cu, as shown in Scheme 4.1. Cu^{0} was not detected on the surface of both, which may be due to the existence of Cu_xO_y layer on CuNWs. The detection of C 1s and Si 2p on the electropolished Cu foil surface may be due to contamination of the sample and

'adventitious' carbon silicate 'dirt' are seen in XPS samples exposed to air. Moreover, the high molar ratio of Cu^{+} and Cu^{2+} ($[Cu^{+}]/[Cu^{2+}]$) indicates that both surface compositions are predominantly Cu_2O. In addition, except for AAO and MTS-AAO in Table 4.1, Al cannot be detected on the other samples because it was covered by Cu.

4.1.1.2. XPS on CuNW-AAO electrodes

Next, 0.1 M methyltrichlorosilane coating modified CuNW-AAO electrode (0.1-MTS-CuNW-AAO), 0.1 M dodecyltrichlorosilane coating modified CuNW-AAO electrode (0.1-DTS-CuNW-AAO), 0.1 M trichloro(phenyl)silane coating modified CuNW-AAO electrode (0.1-TPS-CuNW-AAO), 0.1 M (3-aminopropyl) triethoxysilane coating modified CuNW-AAO electrode (0.1-TES-CuNW-AAO) and the unmodified CuNW-AAO electrode were characterized by XPS, respectively. Table 4.1 shows the values (%) of the surface composition obtained from the spectrum.

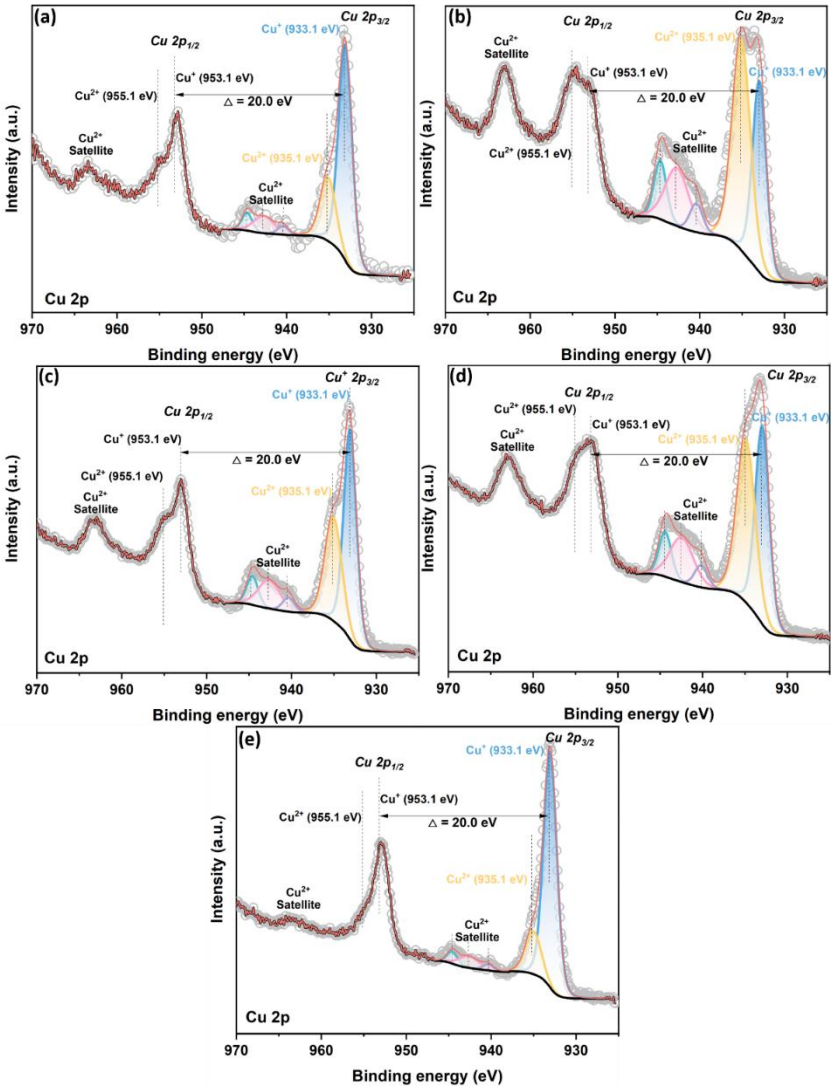

Figure 4.3: Cu 2p XPS patterns of CuNW-AAO electrodes: (a) 0.1-MTS-CuNW-AAO, (b) 0.1-DTS-CuNW-AAO, (c) 0.1-TPS-CuNW-AAO, (d) 0.1-TES-CuNW-AAO, (e) CuNW-AAO.

In Figure 4.3, similar to the spectrum of Cu foil, the Cu $2p_{3/2}$ peak (at the binding energy of 933.1 eV) is identified as the Cu^+ state, and the Cu $2p_{3/2}$ peak (at the binding energy of 935.1 eV) is identified as the Cu^{2+} state. The two satellite peaks in Cu 2p are caused by the shake up process caused by the open 3d shell of Cu^{2+}.[259] It can be confirmed that Cu_xO is still the main component on the silane modified CuNW-AAO electrodes and unmodified CuNW-AAO electrode surfaces. In Table 4.1, bare AAO membranes are coated with silane as shown by the increase in Si content and reduction of Al. And each component molar values of 0.1-MTS-CuNW-AAO are similar to 0.1-MTS-Cu foil, indicating that MTS molecules can be bonded to cover both CuNW and AAO surfaces as coating. When DTS, TPS, TES were used as coatings to cover the composite CuNW-AAO, there is an increase in Si content for all as may be expected. However, for these composites the molar values of Cu 2p increased for all samples except MTS. This may be due to the fact that the binding force of DTS, TPS, TES to AAO (Al_2O_3) is stronger than to Cu. A stable coating on the surface of AAO can be formed, so that some CuNWs are still exposed. Furthermore, based on the values of $[Cu^+]/[Cu^{2+}]$, it can be seen that silane modification tends to promote oxidation of the CuNW surface. CuO is mainly present in 0.1-MTS-CuNW-AAO, due to the further oxidation of Cu_2O layer on the surface of CuNW presumably by the oxygen in the environment, whereas 0.1-DPS-CUNw-AAO, 0.1-TPS-CuNW-AAO and 0.1-TES-CuNW-AAO mainly contain cuprous oxide (Cu_2O or Cu^+). [260] Therefore, it can be clear that the four silanes, MTS, DTS, TPS and TES, can be combined with the AAO template and CuNW respectively and cover the surface to form a coating. Among them, MTS has a strong binding force with Cu and shows a tendency to promote the oxidation of CuNW surface to CuO. DTS, TPS and TES tend to combine with the AAO template, and their oxidizing ability on the CuNW surface is relatively low. And we need to further evaluate the stability of different silane coatings on both CuNW and AAO template.

4.1.1.3. Wetting ability measurements on Cu foil

To evaluate the effect of silane coatings on the hydrophobicity of Cu surface, the contact angle measurements were performed on 0.1 M methyltrichlorosilane coating modified Cu foil (0.1-MTS-Cu foil), 0.1 M dodecyltrichlorosilane coating modified Cu foil electrode (0.1-DTS-Cu foil), 0.1 M trichloro(phenyl)silane coating modified Cu foil electrode (0.1-TPS-Cu foil), 0.1 M (3-aminopropyl) triethoxysilane coating modified Cu foil electrode (0.1-TES-Cu foil) and the unmodified Cu foil electrode, respectively. The electrolyte for CO_2RR was used for the contact angle

measurements to assess possible changes in the local chemical environment on the electrode surface under CO_2RR conditions. Usually, in the contact angle measurement, by analyzing the interfacial forces of solid-liquid-air boundaries, the following relationship exists:

$$\sigma_{s-g} = \sigma_{l-s} + \sigma_{l-g}cos\theta \qquad \text{Eq. 4-1}$$

where θ is the contact angle (°) measured through the denser phase, σ_{s-g} is the interfacial tension of solid-gas, σ_{l-s} is the interfacial tension of liquid-solid, and σ_{l-g} is the interfacial tension of liquid-gas. When θ is < 90°, the droplet is wetting; When θ is > 90°, the droplet is de-wetting.

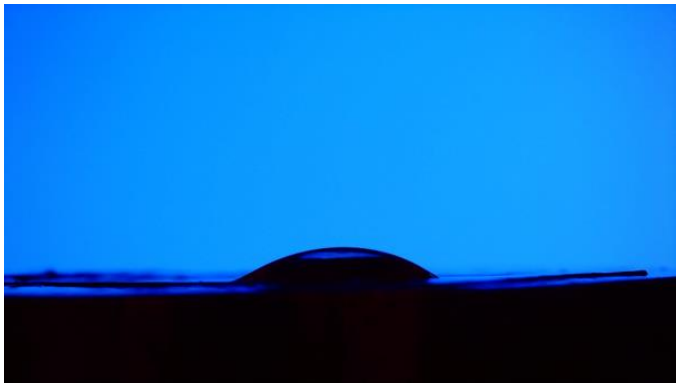

Figure 4.4: The contact angle measurements of unmodified Cu foil.

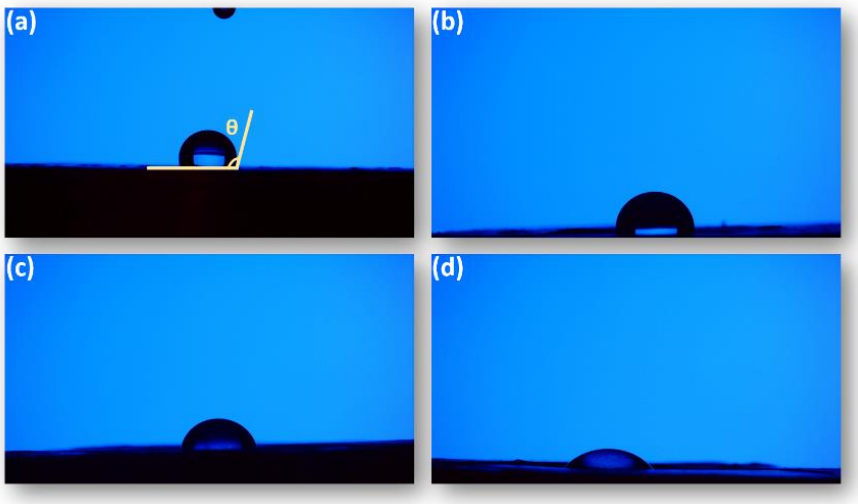

Figure 4.5: The contact angle measurements of silane modified Cu foil: (a) 0.1-MTS-Cu foil, (b) 0.1-DTS-Cu foil, (c) 0.1-TPS-Cu foil, (d) 0.1-TES-Cu foil.

Table 4.2: The contact angle average values of unmodified and 0.1 M silane modified Cu foil.

Sample	*Contact angle (°)*
Cu foil	25.5±2
0.1-MTS-Cu foil	110.7±5
0.1-DTS-Cu foil	88.2±4
0.1-TPS-Cu foil	79.1±6
0.1-TES-Cu foil	46.4±8

All contact angle measurement results are the average values of the measurement results in five different areas on each sample to avoid any artefacts caused by pinning. First, it can be seen from Figure 4.4 that the fresh electropolished Cu foil surface is hydrophilic with a contact angle of 25.5°. In Figure 4.5, the surface of Cu foil becomes hydrophobic when modified with MTS, DTS, TPS, TES coatings. As shown in Table 4.2, the contact angles of 0.1-MTS-Cu foil, 0.1-DTS-Cu foil, 0.1-TPS-Cu foil, 0.1-TPS-Cu foil and 0.1-TES-Cu foil are 110.7°, 88.2°, 79.1° and 46.4°, respectively. It is confirmed that MTS, DTS and TPS molecules are easier to form coating on Cu surface. It is because that the condensation reactions between the -OH on the hydrolyzed silane molecules, prompting the formation of the Si-O-Si structure so that the surface can maintain a stable hydrophobicity. At present, the silane coating shows good stability on the Cu surface without any current passing through. However, when Cu is used as an electrocatalytic electrode, a higher current density is usually applied. At this time, whether the silane coating can still cover the Cu surface stably will be discussed in detail in part 4.1.2.

4.1.1.4. Wetting ability measurements on AAO membranes and CuNW-AAO electrodes

Next, the contact angle measurements were performed on 0.1 M methyltrichlorosilane coating modified AAO membrane (0.1-MTS-AAO), 0.1 M dodecyltrichlorosilane coating modified AAO membrane (0.1-DTS-AAO), 0.1 M trichloro(phenyl)silane coating modified AAO membrane (0.1-TPS-AAO), 0.1 M (3-

aminopropyl) triethoxysilane coating modified AAO membrane (0.1-TES-AAO) and the unmodified AAO membrane.

Figure 4.6: The contact angle measurements of AAO membrane.

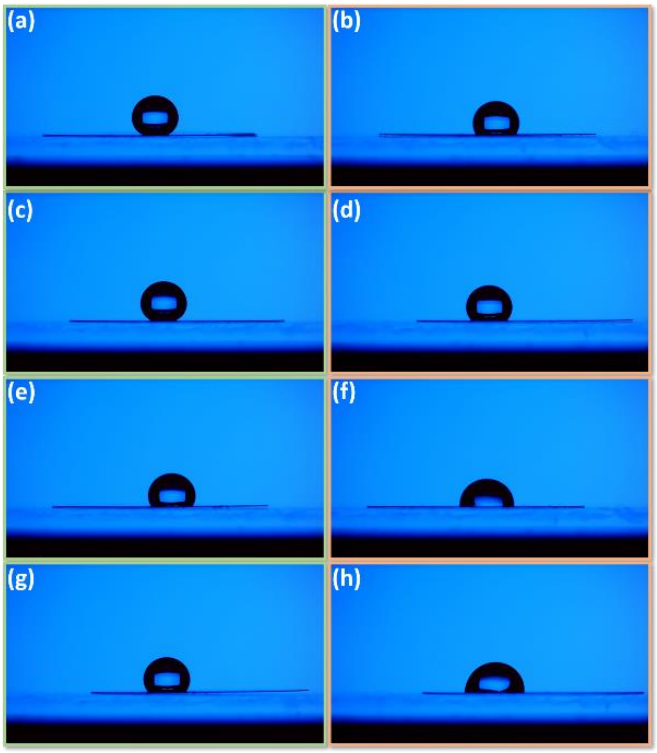

Figure 4.7: The contact angle measurements of silane modified AAO membrane: (a) 0.1-MTS-AAO membrane, (b) 0.1-MTS-AAO membrane after soaking in electrolyte overnight (c) 0.1-DTS-AAO membrane, (d) 0.1-DTS-AAO membrane after soaking in electrolyte overnight, (e) 0.1-TPS-AAO membrane, (f) 0.1-TPS-AAO membrane after soaking in electrolyte overnight, (g) 0.1-TES-AAO membrane, (h) 0.1-TES-AAO membrane after soaking in electrolyte overnight.

Table 4.3: The contact angle average values of unmodified and 0.1 M silane modified AAO membrane.

Sample	*Contact angle (°)*	*Contact angle (°) after being soaked in 0.1 M $KHCO_3$ overnight*
AAO	Less than 10	-
0.1-MTS-AAO	144.9	127.0±3
0.1-DTS-AAO	151.8	138.2±3
0.1-TPS-AAO	104.4	101.8±6
0.1-TES-AAO	113.6	93.4±7

In Figure 4.6, the pure AAO membrane is hydrophilic with a contact angle less than 10°. After being modified by MTS, DTS, TPS, and TES coatings, the surface hydrophobicity of AAO can be greatly improved, as shown in Figure 4.7 (a) (c) (e) (g) and Table 4.3, the contact angles of 0.1-MTS-AAO, 0.1-DTS-AAO, 0.1-TPS-AAO, 0.1-TPS-AAO and 0.1-TES-AAO are 144.9°, 151.8°, 104.4° and 113.6°, respectively. In order to further evaluate the stability of silane modified AAO templates in CO_2RR electrolyte, the samples were soaked in 0.1 M $KHCO_3$ solution overnight. After being dried, the contact angles were measured again as shown in Figure 4.7 (b) (d) (f) (h). In Table 4.3, the contact angles of 0.1-MTS-AAO, 0.1-DTS-AAO, 0.1-TPS-AAO, 0.1-TPS-AAO and 0.1-TES-AAO are 127.0°, 138.2°, 101.8° and 93.4°, respectively. It can be found that silane coatings can form a dense and stable ultra hydrophobic layer on AAO template, which will be conducive to the stability of the local chemical environment on the electrode surface during CO_2RR.

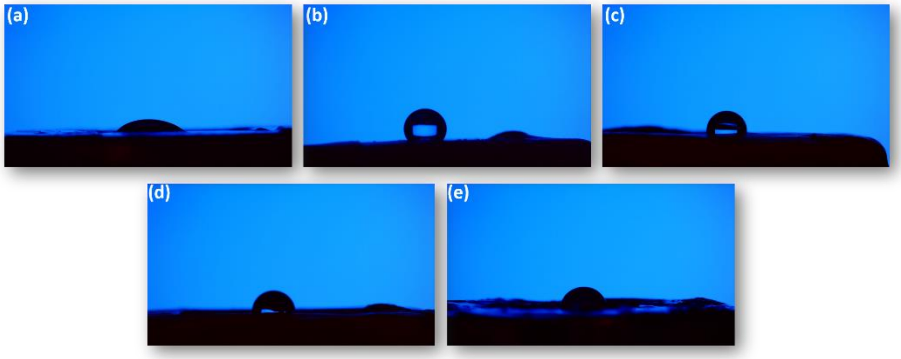

Figure 4.8: The contact angle measurements of silane modified CuNW-AAO electrodes: (a) 0.1-MTS-CuNW-AAO, (b) 0.1-DTS-CuNW-AAO, (c) 0.1-TPS-CuNW-AAO, (d) 0.1-TES-CuNW-AAO electrodes.

Table 4.4: The contact angle average values of unmodified and 0.1 M silane modified CuNW-AAO electrodes.

Sample	*Contact angle (°)*
CuNW-AAO	37.3±2
0.1-MTS-CuNW-AAO	129.1±3
0.1-DTS-CuNW-AAO	91.4±2
0.1-TPS-CuNW-AAO	76.6±9
0.1-TES-CuNW-AAO	69.3±6

Finally, the surface contact angles of CuNW-AAO electrodes modified with different silanes (0.1-MTS-CuNW-AAO, 0.1-DTS-CuNW-AAO, 0.1-TPS-CuNW-AAO, 0.1-TES-CuNW-AAO) were measured. As shown in Figure 4.8 and Table 4.4, the contact angle of unmodified CuNW-AAO electrode is only 37.3°, the contact angles of 0.1-MTS-CuNW-AAO, 0.1-DTS-CuNW-AAO, 0.1-TPS-CuNW-AAO and 0.1-TES-CuNW-AAO electrodes are 129.1°, 91.4°, 76.6° and 69.3°, respectively. Consistent with the results of XPS, MTS has good binding ability to both Cu and AAO membrane and can cover the electrode surface completely.

Based on wetting ability measurements on both AAO membrane and CuNW-AAO electrodes, we found that similar to the XPS results, MTS has a stronger binding ability to Cu and is able to form a complete and stable hydrophobic coating on Cu surface (The contact angles always maintain greater than 100° on the MTS coating modified Cu foil or CuNW-AAO electrode.). The DTS, TPS and TES coatings have more advantages in their ability to bind AAO membrane, making it easier to form a stable and hydrophobic coating on the surface of the AAO membrane. Especially for TPS and TES, the contact angles on the CuNW-AAO electrode surface decreased significantly (compared to on AAO membrane). This may lead to CuNW-AAO electrodes used for electrocatalytic reactions to exhibit different electrochemical properties under different silane modifications.

4.1.2. Electrochemical characterization of Cu-based electrodes

4.1.2.1. Electrochemical characterization of MTS, DTS, TPS and TES modified Cu foil electrodes

In order to study the effect of different types silane coatings on the electrochemical surface area of CuNW electrodes, the active surface area of electrodes was measured as the ECSA of different electrodes. To understand the effect of silane coatings on the electrochemical behaviour of Cu, the double-layer capacitance measurements on Cu foil electrodes modified with (0.1 M) MTS, DTS, TPS and TES coatings (as 0.1-MTS-Cu foil, 0.1-DTS-Cu foil, 0.1-TPS-Cu foil and 0.1-TES-Cu foil electrodes). The multiple CV scans were performed in the non-Faradaic potential region (-0.6 V to -0.8 V vs.Ag/AgCl) in N_2-saturated 0.1 M Na_2SO_4 solution to assess the corresponding ECSA and R_f of the electrodes.

By normalizing the current response to the geometric surface area of electrodes, in Figure 4.9 and Table 4.5, compared with C_{dl} of Cu, the C_{dl} of Cu foil modified by 0.1 M MTS, DTS, TPS and TES coatings all increased, and correspondingly the R_f value also increased significantly. This may be due to the fact that the reduced stability of silane coatings immersed in the electrolyte may lead to further hydrolysis when the double-layer capacitance measurements were performed. The hydrolytic byproduct of the silane coatings is HCl, which could etch the Cu surface. So, the roughness of the electrode surface therefore increased. Because the degree of hydrolysis of different silanes in the electrolyte is different, the difference between R_f is formed. It also can be seen that C_{dl} values of the four electrodes modified with the silanes did not decrease a lot comparing with the unmodified Cu foil, indicating that the 0.1 M silane coating will not block the most of active areas and active sites on the Cu electrode surface, and may not bring negative influence on the mass transfer on the electrode surface.

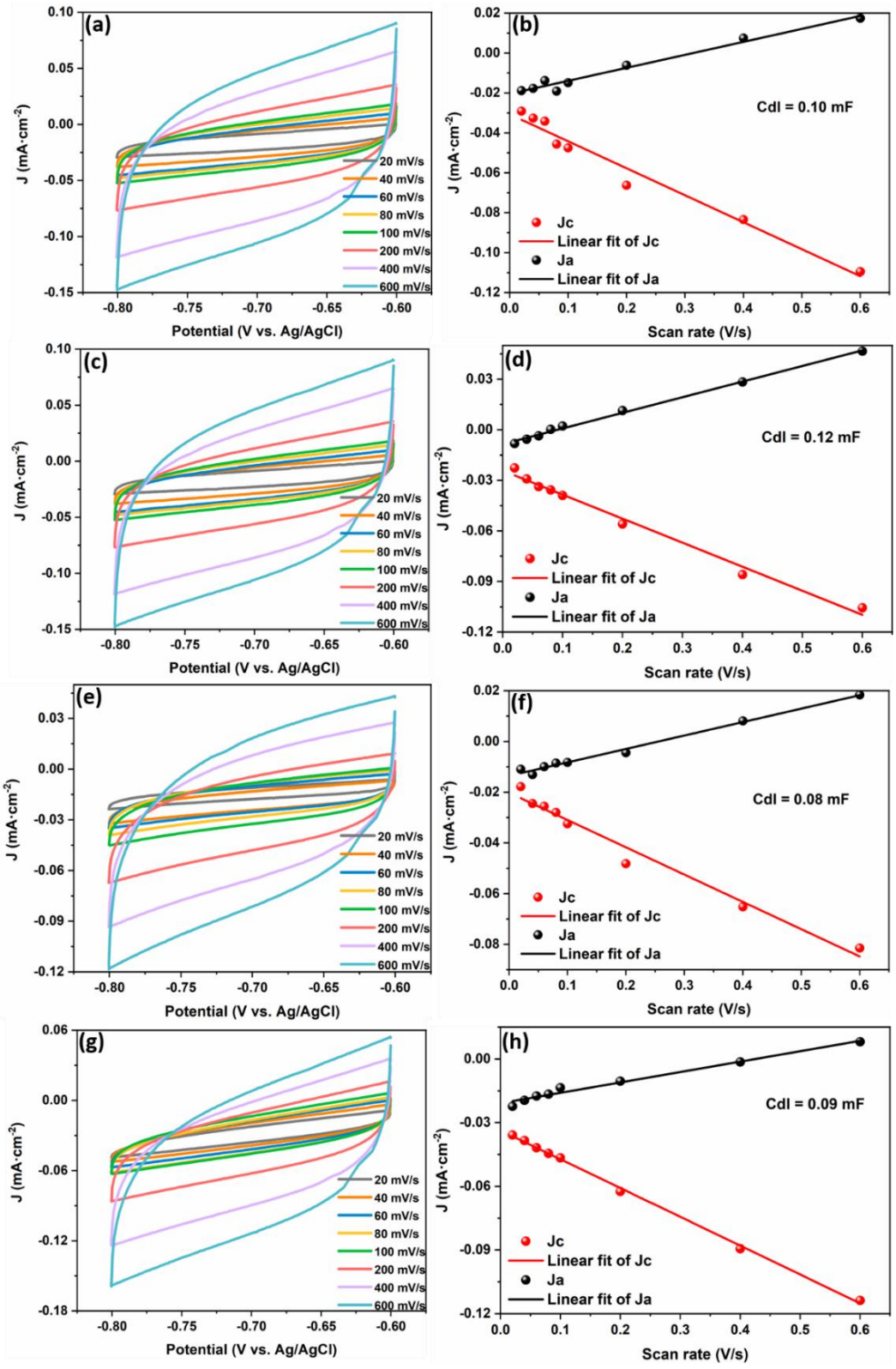

Figure 4.9: ECSA of Cu foil electrodes: (a) CVs of 0.1-MTS-Cu foil electrode. (b) Linear fitting for double-layer capacitance of 0.1-MTS-Cu foil electrode. (c) CVs of 0.1-DTS-Cu foil electrode. (d) Linear fitting for double-layer capacitance of 0.1-DTS-Cu foil electrode. (e) CVs of 0.1-TPS-Cu foil electrode. (f) Linear fitting for double-layer capacitance of 0.1-TPS-Cu foil electrode. (g) CVs of 0.1-TES-Cu foil electrode. (h) Linear fitting for double-layer capacitance of 0.1-TES-Cu foil electrode. (All measurements were proceeded in N_2-saturated 0.1 M Na_2SO_4 solution.)

Table 4.5: The double-layer capacitance and roughness factor of 0.1 M silane modified/unmodified Cu foil electrodes based on Figure 4.9.

Electrode	C_{dl} $(mF \cdot cm^2)$	Roughness $(R_f)^*$
Cu foil	0.05	1.72
0.1-MTS-Cu foil	0.10	3.45
0.1-DTS-Cu foil	0.12	4.14
0.1-TPS-Cu foil	0.08	2.76
0.1-TES-Cu foil	0.09	3.10

*All roughness is calculated with the standard smooth Cu as reference (C_{dl} = 29 μF, R_f = 1).

Next, ECSA measurements of silane modified Cu foil electrodes were performed by using MV redox probe. In Figure 4.10, from the relationship between the potential at peak current of different electrodes and the scan rate, it can be seen that the peak potential basically does not change with the scan rate at lower scan rates, and a slight peak deviation will be caused when the scan rate is higher. So, the Randles-Ševčík equation can be applied according to the reversible redox peaks. According to the Randles-Ševčík equation, the peak current in CV should have a linear relationship with the square root of the scanning rates. In Figure 4.10 and Table 4.6, according to the Randles-Ševčík equation, it can be calculated that the ECSA of 0.1-MTS-Cu foil, 0.1-DTS-Cu foil, 0.1-TPS-Cu foil and 0.1-TES-Cu foil electrodes are 0.36 $cm^2 \cdot cm^2$, 0.85 $cm^2 \cdot cm^2$, 0.36 $cm^2 \cdot cm^2$ and 0.78 $cm^2 \cdot cm^2$, respectively. Compared with Cu foil, the ECSA of 0.1-MTS-Cu foil and 0.1-TPS-Cu foil electrodes decreased to a certain extent, which may be due to the good stability of MTS and TPS coatings in the electrolyte when there was a low current applied. It was less affected by current and silane hydrolysis. This means that when using $MV^{2+} \leftrightarrow MV^{+}$ to measure the electrochemical surface area of the electrodes, part of the MV may be blocked by the MTS and TPS hydrophobic coating layers, resulting in a low electrochemical surface area. For the 0.1-DTS-Cu foil electrode, part hydrolysis of the DTS coating may lead to more Cu exposure to the electrolyte, which also makes it easier for MV to reach the electrode surface for redox reaction. At the same time, the surface roughness of the electrode was increased due to the HCl produced by hydrolysis, and the electrochemical surface area was also increased accordingly. However, the 0.1-TES-Cu foil electrode is not the same as the above two cases, the electrode surface state is closer to the unmodified Cu foil, which may be due to the

instability of TES coating in the electrolyte, resulting in a large area of loss of the TES coating.

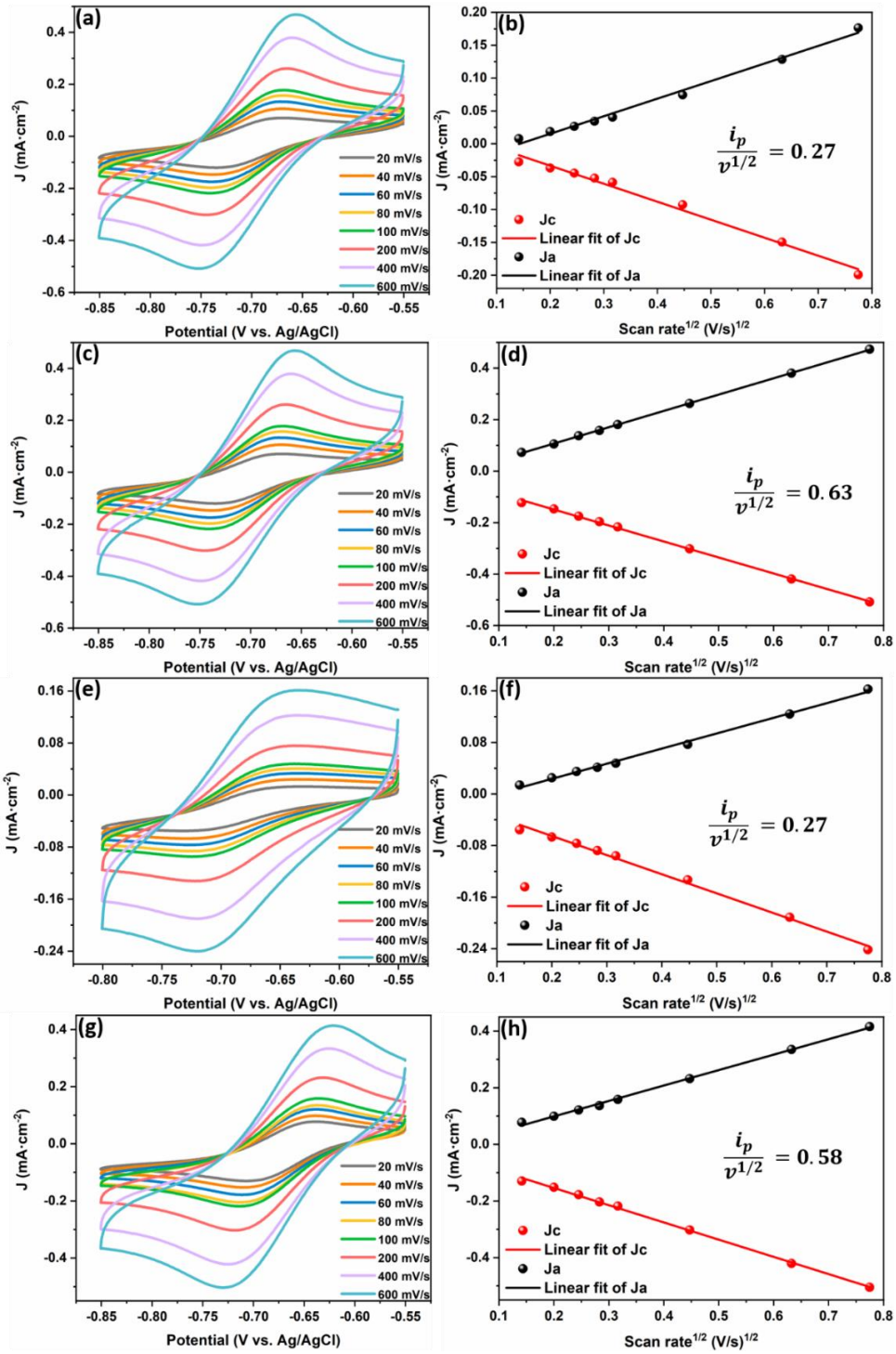

Figure 4.10: ECSA of Cu foil electrodes: (a) CVs of 0.1-MTS-Cu foil electrode. (b) Linear fitting for $MV^{2+} \leftrightarrow MV^{+}$ via Randles-Ševčík of 0.1-MTS-Cu foil electrode. (c) CVs of 0.1-DTS-Cu foil electrode. (d) Linear fitting for $MV^{2+} \leftrightarrow MV^{+}$ via Randles-Ševčík of 0.1-DTS-Cu foil electrode. (e) CVs of 0.1-TPS-Cu foil electrode. (f) Linear fitting for $MV^{2+} \leftrightarrow MV^{+}$ via Randles-Ševčík of 0.1-TPS-Cu foil electrode. (g) CVs of 0.1-TES-Cu foil electrode. (h) Linear fitting for $MV^{2+} \leftrightarrow MV^{+}$ via Randles-Ševčík of 0.1-TES-Cu foil electrode. (All measurements were performed in N_2-saturated 0.1 M Na_2SO_4 solution containing 10 mM di-methyl viologen di-chloride.)

Table 4.6: The ECSA of 0.1 M silane modified/unmodified Cu foil electrodes based on Figure 4.10.

Electrode	$ECSA\ (cm^2 \cdot cm^2)$
Cu foil	0.79
0.1-MTS-Cu foil	0.36
0.1-DTS-Cu foil	0.85
0.1-TPS-Cu foil	0.36
0.1-TES-Cu foil	0.78

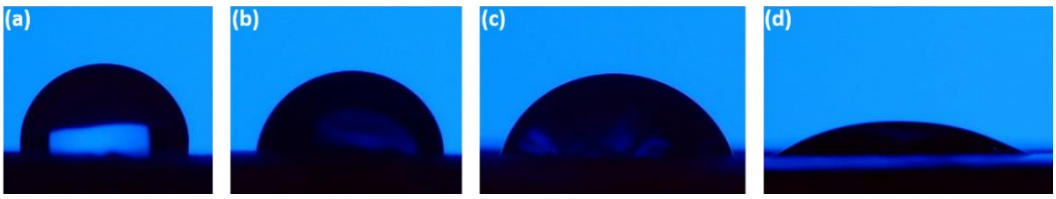

Figure 4.11: The contact angle measurements of 0.1 M silane modified Cu foil electrodes after ECSA measurements: (a) 0.1-MTS-Cu foil, (b) 0.1-DTS-Cu foil, (c) 0.1-TPS-Cu foil, (d) 0.1-TES-Cu foil electrodes.

Table 4.7: The contact angle average values of 0.1 M silane modified Cu foil electrodes after ECSA measurements.

Sample	*Contact angle (°)*
0.1-MTS-Cu foil	98.8±10
0.1-DTS-Cu foil	81.0±10
0.1-TPS-Cu foil	74.2±11
0.1-TES-Cu foil	Less than 25.0

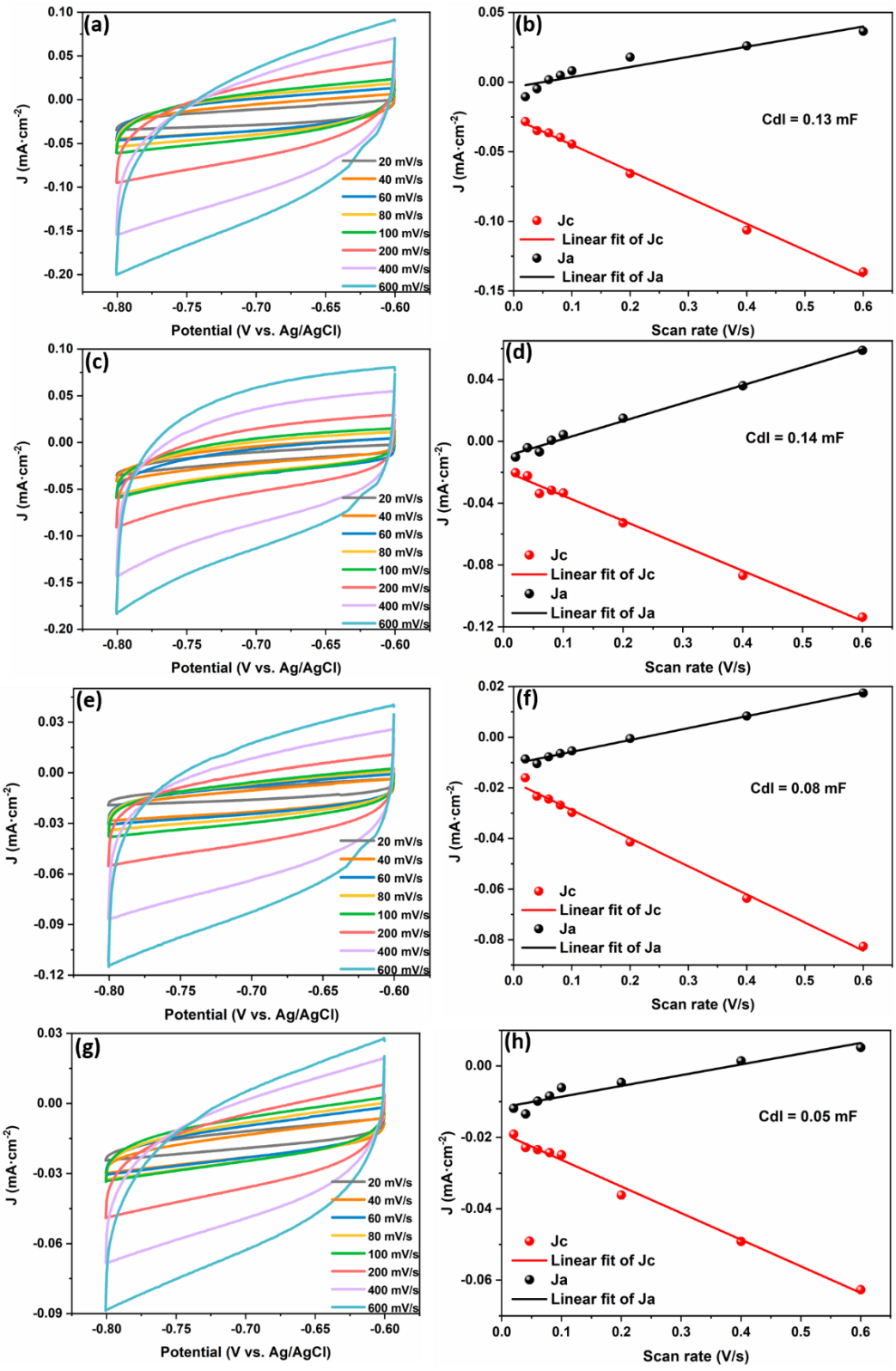

Figure 4.12: ECSA of Cu foil electrodes: (a) CVs of 0.004-MTS-Cu foil electrode. (b) Linear fitting for double-layer capacitance of 0.004-MTS-Cu foil electrode. (c) CVs of 0.004-DTS-Cu foil electrode. (d) Linear fitting for double-layer capacitance of 0.004-DTS-Cu foil electrode. (e) CVs of 0.004-TPS-Cu foil electrode. (f) Linear fitting for double-layer capacitance of 0.004-TPS-Cu foil electrode. (g) CVs of 0.004-TES-Cu foil electrode. (h) Linear fitting for double-layer capacitance of 0.004-TES-Cu foil electrode. (All measurements were proceeded in N_2-saturated 0.1 M Na_2SO_4 solution.)

In order to further observe whether the silane coating on the Cu foil surface remains stable after a certain current was applied, the contact angles of Cu foil modified with different silanes were measured again after the ECSA measurements. In Figure 4.11 and Table 4.7, for 0.1-MTS-Cu foil and 0.1-DTS-Cu foil electrodes, although the surface hydrophobicity has a certain degree of reduced but stays a larger contact angle of 98.8° and 81.0°, respectively. For 0.1-TPS-Cu foil electrode, the contact angle was nearly unchanged. It confirmed that under the condition of low current passing through, 0.1 M MTS, DTS and TPS coatings can remain relatively stable on Cu foil, and there is only a small coating loss. The small coating loss most likely due to hydrolysis. The 0.1 M TES coating was almost completely lost, and 0.1-TES-Cu foil is no longer hydrophobic.

Table 4.8: The double-layer capacitance and roughness factor of 0.004 M silane modified/unmodified Cu foil electrodes based on Figure 4.12.

Electrode	$C_{dl}\ (mF \cdot cm^2)$	*Roughness* (R_f)
0.004-MTS-Cu foil	0.13	4.48
0.004-DTS-Cu foil	0.14	4.83
0.004-TPS-Cu foil	0.08	2.76
0.004-TES-Cu foil	0.05	1.72

*All roughness is calculated with the standard smooth Cu as reference (C_{dl} = 29 μF, R_f = 1).

In order to further confirm that using 0.1 M silane to modify Cu foil electrodes will not block the Cu surface and lead to the loss of reactive sites, we also tried ECSA measurements with very low concentrations (0.004 M) silane modified Cu foil electrodes to determine if the higher concentration (0.1 M) silane coatings will have a negative impact on Cu foil electrodes by comparison. The multiple CV scans of Cu foil electrodes modified with 0.004 M MTS, DTS, TPS and TES coatings (0.004-MTS-Cu foil, 0.004-DTS-Cu foil, 0.004-TPS-Cu foil and 0.004-TES-Cu foil) were performed in the non-Faradic potential region (-0.6 V to -0.8 V vs.Ag/AgCl) in N_2-saturated 0.1 M Na_2SO_4 solution to assess the corresponding ECSA and Rf of the electrodes. By normalizing the current response to the geometric surface area of electrodes, the linear slopes in Figure 4.12 and Table 4.8 indicate that the C_{dl} values of 0.004-MTS-

Cu foil and 0.004-DTS-Cu foil electrodes are higher than those of 0.004-TPS-Cu foil, 0.004-TES-Cu foil and pure Cu foil electrode (as mentioned in Chapter 3, the C_{dl} value of pure Cu foil electrode is 0.05 mF measured under the same test conditions). In addition, the reduction current of high scan rate has “steps” feature at high potential, it is the artefacts in the data due to iR compensation. This suggests that the electrode active surface areas of 0.004-MTS-Cu foil and 0.004-DTS-Cu foil are larger, and possibly electrochemical activity is higher as well.[261,262] On the other hand, compared to 0.1 M silane modified Cu foil, 0.004-MTS-Cu foil and 0.004-DTS-Cu foil electrodes have slightly higher R_f, which may be because that the low concentration of silane coating is less stable than the high concentration of silane coating when a certain current was applied to Cu foil. As a result, more active sites on the Cu surface would be exposed to the electrolyte due to the enhanced coating hydrolysis. However, the difference of R_f is not large, indicating that MTS and DTS coatings can be relatively stable on Cu foil surface under the condition of current passing, with only a small part of the loss. For 0.004-TPS-Cu foil, the R_f did not change, indicating that the TPS coating could also form a stable bond with Cu in the presence of low current. The R_f of 0.004-TES-Cu foil is similar to that of unmodified Cu foil, indicating that when there was a low current passing through the electrode, the TES coating was destroyed due to poor bonding ability, perhaps most of it fell off the Cu surface.

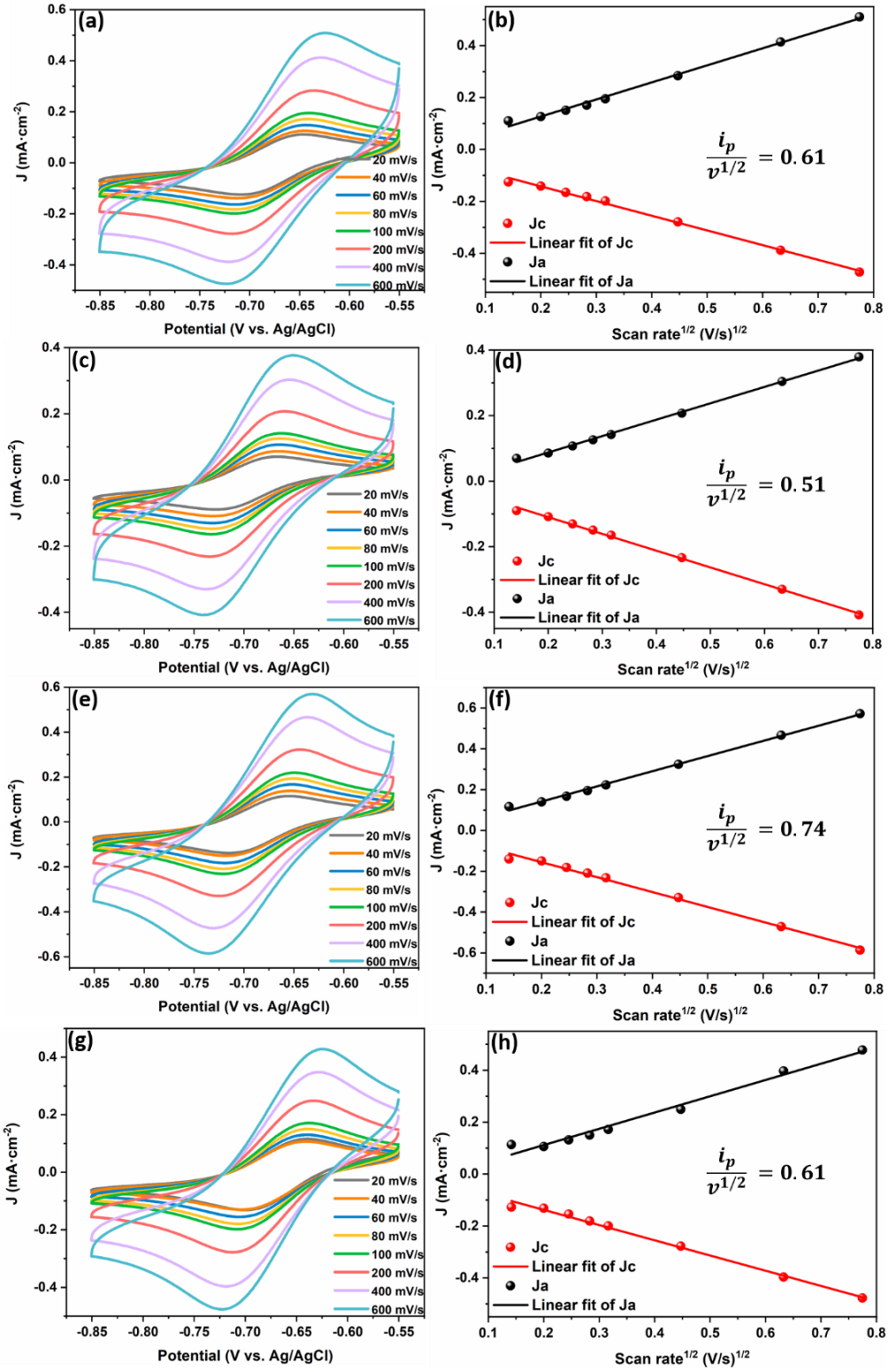

Figure 4.13: ECSA of Cu foil electrodes: (a) CVs of 0.004-MTS-Cu foil electrode. (b) Linear fitting for $MV^{2+} \leftrightarrow MV^{+}$ via Randles-Ševčík of 0.004-MTS-Cu foil electrode. (c) CVs of 0.004-DTS-Cu foil electrode. (d) Linear fitting for $MV^{2+} \leftrightarrow MV^{+}$ via Randles-Ševčík of 0.004-DTS-Cu foil electrode. (e) CVs of 0.004-TPS-Cu foil electrode. (f) Linear fitting for $MV^{2+} \leftrightarrow MV^{+}$ via Randles-Ševčík of 0.004-TPS-Cu foil electrode. (g) CVs of 0.004-TES-Cu foil electrode. (h) Linear fitting for $MV^{2+} \leftrightarrow MV^{+}$ via Randles-Ševčík of 0.004-TES-Cu foil electrode. All the measurements were in 10 mM MV in 0.1M Na_2SO_4. (All measurements were performed in N_2-saturated 0.1 M Na_2SO_4 solution containing 10 mM di-methyl viologen di-chloride.)

Table 4.9: The ECSA of 0.004 M silane modified Cu foil electrodes based on Figure 4.13.

Electrode	$ECSA\ (cm^2 \cdot cm^2)$
0.004-MTS-Cu foil	0.82
0.004-DTS-Cu foil	0.68
0.004-TPS-Cu foil	0.99
0.004-TES-Cu foil	0.82

In addition, In Figure 4.13 and Table 4.9, according to the Randles-Ševčík equation, it can be calculated that the ECSA of 0.004-MTS-Cu foil, 0.004-DTS-Cu foil, 0.004-TPS-Cu foil and 0.004-TES-Cu foil electrodes are 0.82 cm^2, 0.68 cm^2, 0.99 cm^2 and 0.82 cm^2, respectively. Among them, the ECSA of 0.004-MTS-Cu foil, 0.004-TPS-Cu foil and 0.004-TES-Cu foil electrodes are all greater than Cu foil. This may be because when the concentration of silane coating was greatly reduced, the stability of the coating was correspondingly weakened. This dynamic change of local environment on the electrode surface caused more Cu to be exposed to the electrolyte, providing more site for the occurrence of $MV^{2+} \leftrightarrow MV^{+}$, thus the measured electrochemical surface area increased. For 0.004-DTS-Cu foil electrode, even if the concentration of DTS was reduced, most of the stable coating still covered the Cu surface, which would prevent some of MV on the Cu surface for redox reaction, resulting in the electrochemical surface area of the electrode was still slightly lower than that of Cu foil.

Figure 4.14: The contact angle measurements of 0.004 M silane modified Cu foil electrodes after ECSA measurements: (a) 0.004-MTS-Cu foil, (b) 0.004-DTS-Cu foil, (c) 0.004-TPS-Cu foil electrodes, (d) 0.004-TES-Cu foil electrodes.

Table 4.10: The contact angle average values of 0.004 M silane modified Cu foil electrodes after ECSA measurements.

Sample	*Contact angle (°)*
0.004-MTS-Cu foil	40.7±5
0.004-DTS-Cu foil	71.6±12
0.004-TPS-Cu foil	64.3±8
0.004-TES-Cu foil	Less than 25.0

In combination with the ECSA and R_f of 0.004 M silane modified Cu foil electrodes, to further verify the stability of the silane coating when a low current was applied on the electrodes, contact angle measurements were performed on the electrodes again after ECSA measurements. As shown in Figure 4.14 and Table 4.10, the contact angle of 0.004-MTS-Cu foil, 0.004-TPS-Cu foil and 0.004-TES-Cu foil electrodes decreased significantly. In particular, there was scarcely any TES coating on the surface of 0.004-TES-Cu foil. For 0.004-DTS-Cu foil electrode, the contact angle did not change much, it still had a certain hydrophobicity, which is consistent with the ECSA measurement results.

4.1.2.2. Electrochemical characterization of MTS, DTS, TPS and TES modified CuNW-AAO electrodes

The electrocatalytic electrode used for CO_2RR consists of conducting CuNWs and insulating AAO template. After determining the effect of silane coating on the electrochemical behaviour of Cu foil, we also evaluated the effect of silane coating on the overall electrochemical surface area and local chemical environment of CuNW-AAO electrodes. First, the CuNW-AAO electrodes were modified with low and high concentrations of MTS (0.004-MTS-CuNW-AAO and 0.1-MTS-CuNW-AAO), respectively. Both the 0.004-MTS-CuNW-AAO and 0.1-MTS-CuNW-AAO were obtained via two-step electrodeposition, and the deposition curves and Cu mass on the electrode were shown in Appendix 2 (Figure A 2.2: 0.004-MTS-CuNW-AAO, Figure A 2.3: 0.1-MTS-CuNW-AAO). The multiple CV measurements were performed in a non-Faradic region. First, due to the better fit of the normalized cathode current, the following ECSA calculations are based on the measured cathode current values.

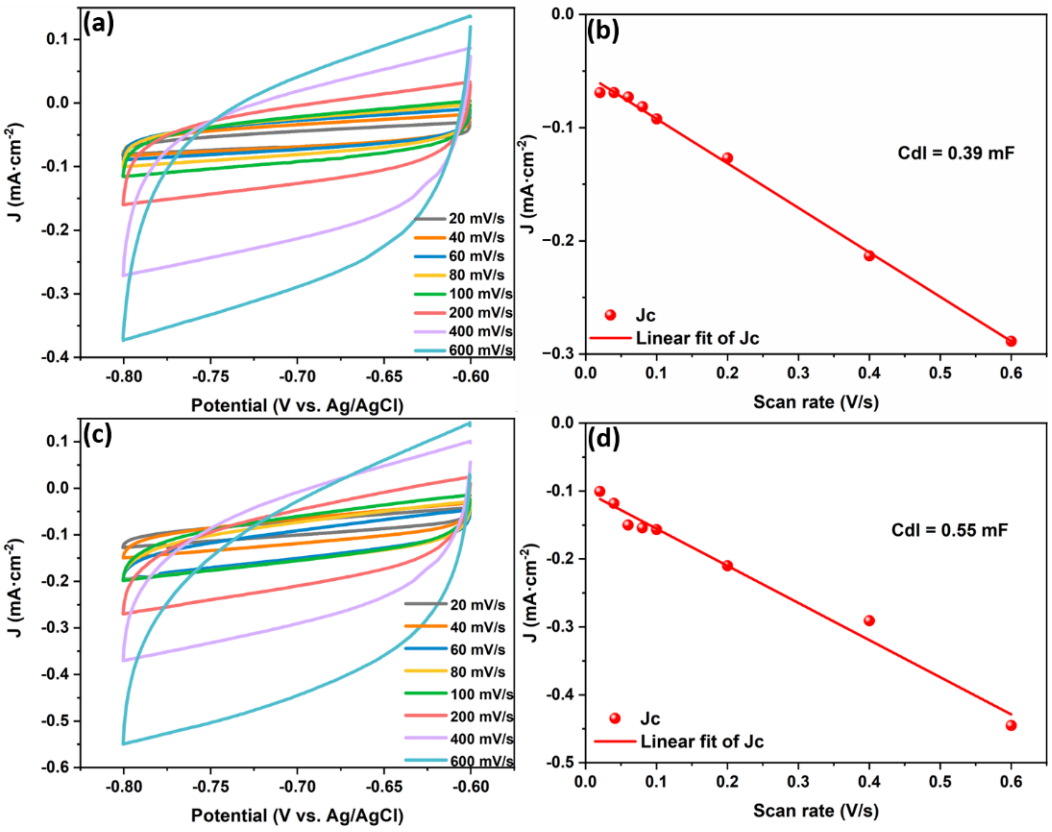

Figure 4.15: ECSA of CuNW-AAO electrodes: (a) CVs of 0.004-MTS-CuNW-AAO electrode. (b) Linear fitting for double-layer capacitance of 0.004-MTS-CuNW-AAO electrode. (c) CVs of 0.1-MTS-CuNW-AAO electrode. (d) Linear fitting for double-layer capacitance of 0.1-MTS-CuNW-AAO electrode. (All measurements were proceeded in N_2-saturated 0.1 M Na_2SO_4 solution.)

Table 4.11: The double-layer capacitance and roughness factor of MTS modified/unmodified CuNW-AAO electrodes based on Figure 4.15.

Electrode	C_{dl} $(mF \cdot cm^2)$	Roughness (R_f)
CuNW-AAO	0.14	4.83
0.004-MTS-CuNW-AAO	0.39	13.45
0.1-MTS-CuNW-AAO	0.55	18.97

*All roughness is calculated with the standard smooth Cu as reference (C_{dl} = 29 μF, R_f = 1).

It is shown in Figure 4.15 that MTS coatings with very different concentrations could not cause significant changes in the electrochemically active surface area of

CuNW-AAO electrodes. Different from the literature report, 1-octadecanethiol modified Cu dendrite electrode ($ECSA = 3 \times 10^{-3}\ cm^2 cm^{-2}$),[263] the introduction of MTS coatings will not compactly cover the entire electrode surface resulting in a sharp decline in ECSA and loss of active sites.[251] The C_{dl} value of 0.1-MTS-CuNW-AAO electrode is higher than that of common Cu particle electrode ($C_{dl} = 0.39\ mF$) and is close to Cu dendrite electrode ($C_{dl} = 0.60\ mF$).[246] MTS coating is also different from the ionomer-coated Cu, the $C_{dl}$of all Nafion coated samples were same as pure Cu ($C_{dl} = 0.59\ mF$).[264] From Table 4.11, MTS coating can improve the roughness of the electrode to a certain extent, ensuring sufficient reactive active sites. Compared with the CuNW-AAO electrode, due to the hydrolysis of MTS coating, the by-product HCl will etch the CuNW surface in electrolyte, resulting in a significant increase in the R_f of both 0.004-MTS-CuNW-AAO and 0.1-MTS-CuNW-AAO. And with the increase of MTS concentration, the more produced HCl has a more obvious effect on the CuNW surface etching.

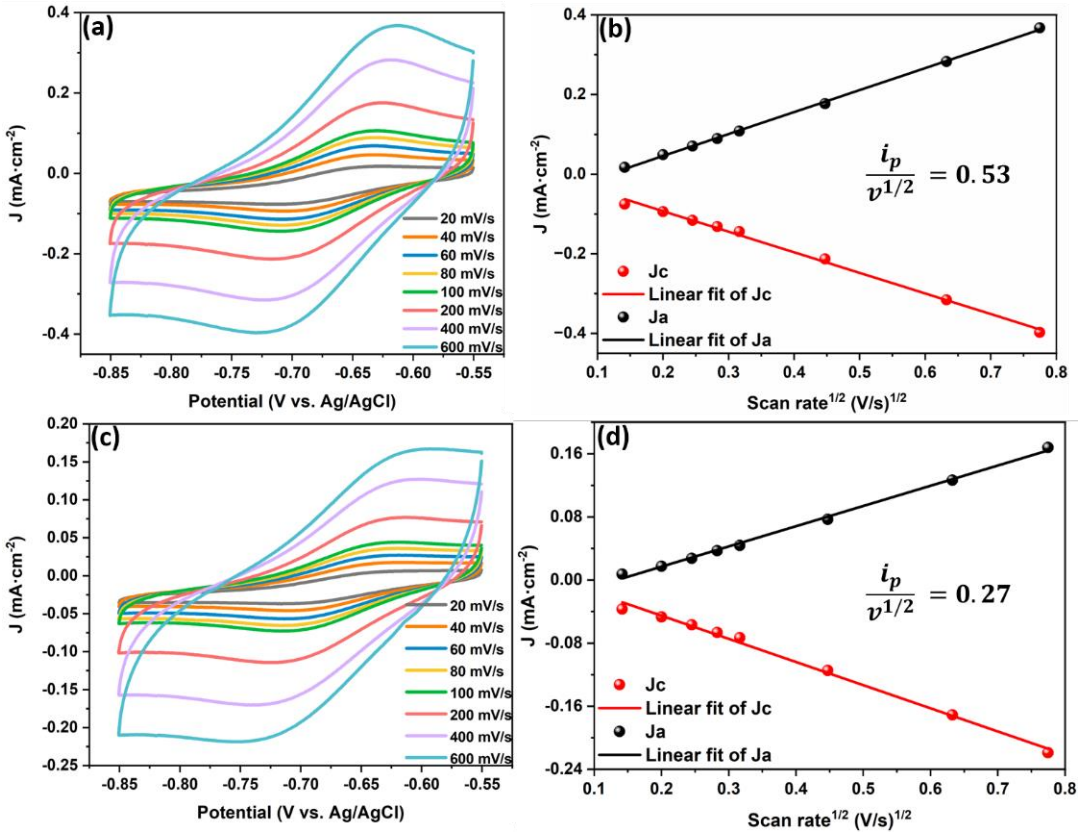

Figure 4.16: ECSA of CuNW-AAO electrodes: (a) CVs of 0.004-MTS-CuNW-AAO electrode. (b) Linear fitting for $MV^{2+} \leftrightarrow MV^{+}$ via Randles-Ševčík of 0.004-MTS-CuNW-AAO electrode. (c) CVs of 0.1-MTS-CuNW-AAO electrode. (d) Linear fitting for $MV^{2+} \leftrightarrow MV^{+}$ via Randles-Ševčík of 0.1-MTS-CuNW-AAO electrode. (All measurements were performed in N_2-saturated 0.1 M Na_2SO_4 solution containing 10 mM di-methyl viologen di-chloride.)

Table 4.12: The ECSA of MTS modified/unmodified CuNW-AAO electrodes based on Figure 4.16.

Electrode	$ECSA\ (cm^2 \cdot cm^2)$
CuNW-AAO	0.70
0.004-MTS-CuNW-AAO	0.72
0.1-MTS-CuNW-AAO	0.36

In Figure 4.16 and Table 4.12, according to the Randles-Ševčík equation, it can be calculated that the ECSA of 0.004-MTS-CuNW-AAO, 0.1-MTS- CuNW-AAO are 0.72 cm^2 and 0.36 cm^2. The electrochemical surface area of 0.004-MTS-CuNW-AAO is close to the unmodified CuNW-AAO electrode ($ECSA = 0.70\ cm^2$, calculated in Chapter 3). This is due to the poor stability of low concentrations MTS coating on the CuNW surface, and the coating may fell off when the current was applied. For 0.1-MTS-CuNW-AAO electrode, the smaller ECSA is because there were still relatively stable MTS covering on the CuNW surface, blocking part of MV from contacting with CuNW.

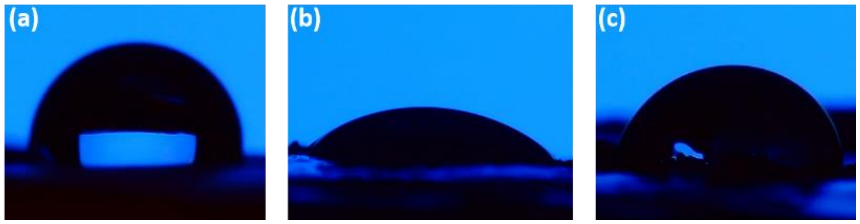

Figure 4.17: The contact angle measurements of MTS modified CuNW-AAO electrodes before and after ECSA measurements: (a) 0.004-MTS-CuNW-AAO (before ECSA), (b) 0.004-MTS-CuNW-AAO, (c) 0.1-MTS-CuNW-AAO.

Table 4.13: The contact angle average values of MTS modified CuNW-AAO electrodes before and after ECSA measurements.

Sample	*Contact angle (°)*
0.004-MTS-CuNW-AAO (before ECSA)	89.8±3
0.004-MTS-CuNW-AAO	42.6±2
0.1-MTS- CuNW-AAO	65.0±6

The contact angle of the 0.004-MTS-CuNW-AAO electrode was reduced to 42.6° after the ECSA measurements, confirming the instability of low concentrations of MTS, which can partially fall off when a current was applied (as shown in Figure 4.17 and Table 4.13). The contact angle of 0.1-MTS-CuNW-AAO electrode is reduced by half to 65.0°, and the stability of MTS with high concentration was better. Under the synergistic effect of MTS coating on CuNW surface and on AAO surface, the hydrophobicity of the electrode can be still higher than that of the 0.004-MTS-CuNW-AAO electrode.

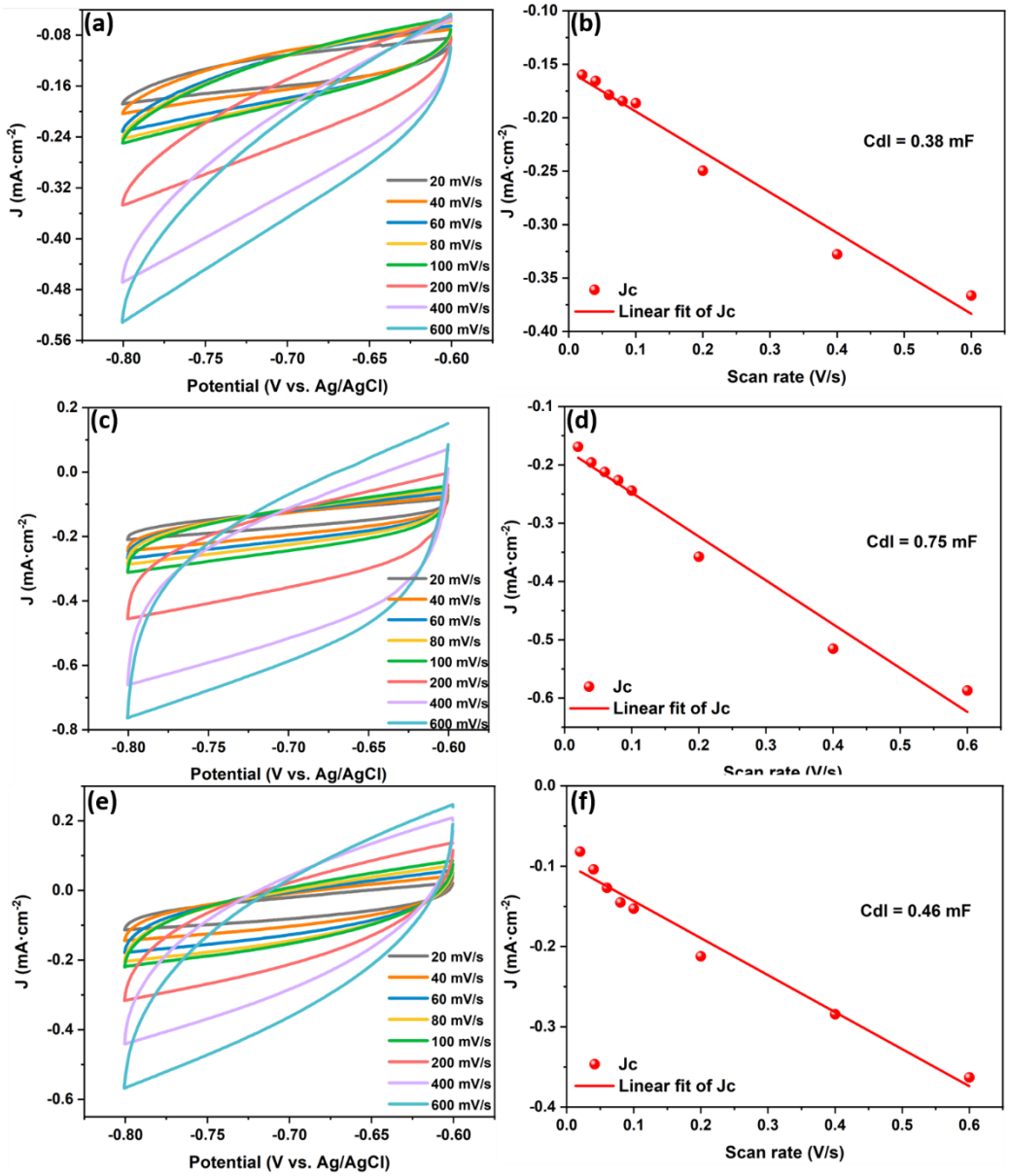

Figure 4.18: ECSA of CuNW-AAO electrodes: (a) CVs of 0.1-DTS-CuNW-AAO electrode. (b) Linear fitting for double-layer capacitance of 0.1-DTS-CuNW-AAO electrode. (c) CVs of 0.1-TPS-CuNW-AAO electrode. (d) Linear fitting for double-layer capacitance of 0.1-TPS-CuNW-AAO electrode. (e) CVs of 0.1-TES-CuNW-AAO electrode. (f) Linear fitting for double-layer capacitance of 0.1-TES-CuNW-AAO electrode. (All measurements were proceeded in N_2-saturated 0.1 M Na_2SO_4 solution.)

Table 4.14: The double-layer capacitance and roughness factor of 0.1 M silane modified CuNW-AAO electrodes based on Figure 4.18.

Electrode	$C_{dl}\ (mF \cdot cm^2)$	*Roughness (R_f)*
0.1-DTS-CuNW-AAO	0.38	13.10
0.1-TPS-CuNW-AAO	0.75	25.86
0.1-TES-CuNW-AAO	0.46	15.86

*All roughness is calculated with the standard smooth Cu as reference (C_{dl} = 29 μF, R_f = 1).

Next, the double-layer capacitances were also characterized for 0.1-DTS-CuNW-AAO, 0.1-TPS-CuNW-AAO and 0.1-TES-CuNW-AAO electrodes. The 0.1-DTS-CuNW-AAO, 0.1-TPS-CuNW-AAO and 0.1-TES-CuNW-AAO electrodes were obtained by two-step electrodeposition, and the deposition curves and Cu mass on the electrode were shown in Appendix 2 (Figure A 2.4: 0.1-DTS-CuNW-AAO, Figure A 2.5: 0.1-TPS-CuNW-AAO, Figure A 2.6: 0.1-TES-CuNW-AAO). In Figure 4.18 and Table 4.14, it can be found that the R_f of 0.1-DTS-CuNW-AAO, 0.1-TPS-CuNW-AAO and 0.1-TES-CuNW-AAO electrodes are significantly higher than that of unmodified CuNW-AAO electrode. This is because the high concentration of silane coating in the electrolyte brings more produced HCl by hydrolysis, which makes the CuNW further etched. Among them, 0.1-TPS-CuNW-AAO electrode has greater roughness than other electrodes, which may be because 0.1-TPS-CuNW-AAO electrode has the largest peak current response, which can have a great effect on the stability of TPS coating and promote the etching of CuNW as well.

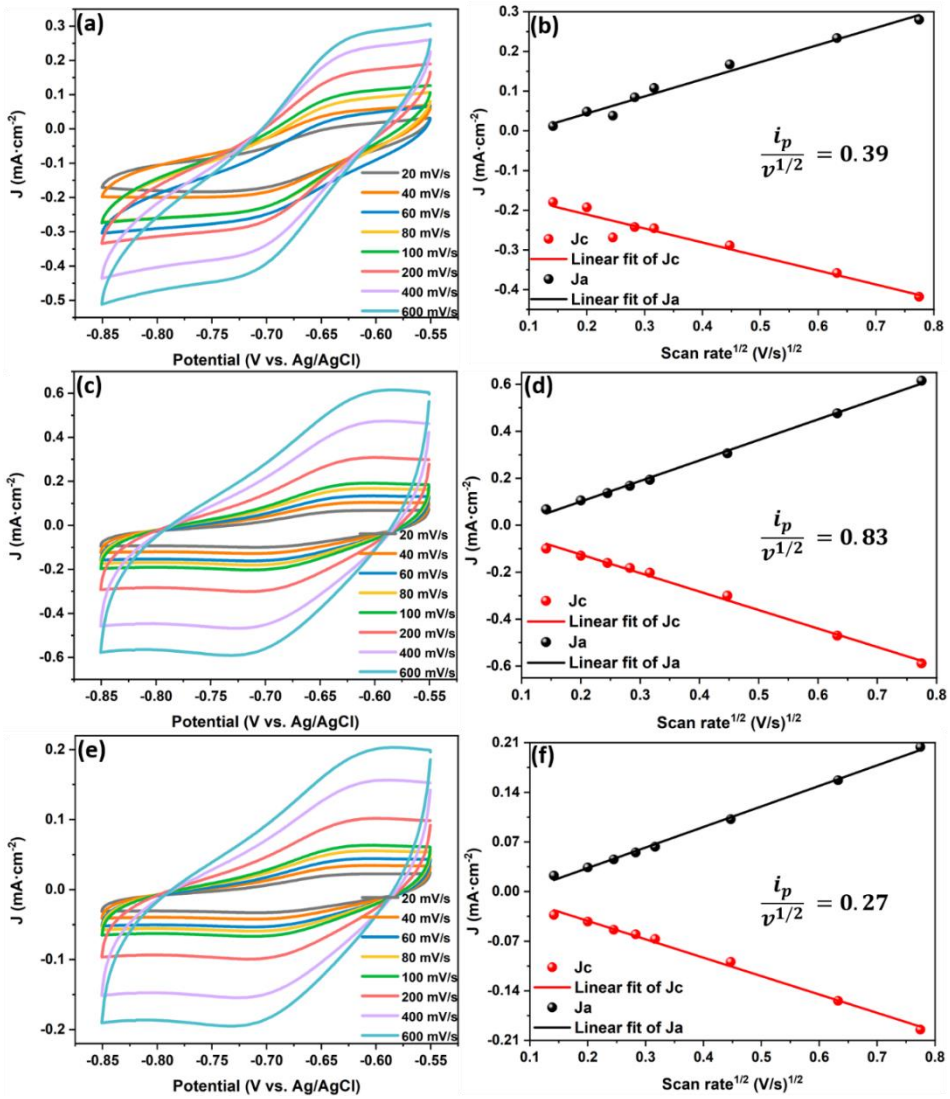

Figure 4.19: ECSA of CuNW-AAO electrodes: (a) CVs of 0.1-DTS-CuNW-AAO electrode. (b) Linear fitting for $MV^{2+} \leftrightarrow MV^{+}$ via Randles-Ševčík of 0.1-DTS-CuNW-AAO electrode. (c) CVs of 0.1-TPS-CuNW-AAO electrode. (d) Linear fitting for $MV^{2+} \leftrightarrow MV^{+}$ via Randles-Ševčík of 0.1-TPS-CuNW-AAO electrode. (e) CVs of 0.1-TES-CuNW-AAO electrode. (f) Linear fitting for $MV^{2+} \leftrightarrow MV^{+}$ via Randles-Ševčík of 0.1-TES-CuNW-AAO electrode. (All measurements were performed in N_2-saturated 0.1 M Na_2SO_4 solution containing 10 mM di-methyl viologen di-chloride.)

Table 4.15: The ECSA of 0.1 M silane modified CuNW-AAO electrodes based on Figure 4.19.

Electrode	$ECSA\ (cm^2 \cdot cm^2)$
0.1-DTS-CuNW-AAO	0.53
0.1-TPS-CuNW-AAO	1.12
0.1-TES-CuNW-AAO	0.36

In Figure 4.19 and Table 4.15, according to the Randles-Ševčík equation, it can be calculated that the ECSA of 0.1-DTS-CuNW-AAO, 0.1-TPS-CuNW-AAO and 0.1-TES-CuNW-AAO electrodes are 0.53 cm^2, 1.12 cm^2 and 0.36 cm^2. The results are similar to C_{dl} calculated by the double-layer capacitance.

First, the 0.1-DTS-CuNW-AAO electrode has a smaller ECSA than the unmodified CuNW-AAO electrode because the stable DTS coating present on the CuNW and AAO surfaces blocked the contact between MV and the Cu surface, resulting in a smaller electrochemical surface area. The 0.1-TPS-CuNW-AAO electrode has the highest peak current response and the largest ECSA in the ECSA measurements, which can be attributed to the fact that the TPS and Cu bonding ability is not so stable, and the TPS coating on the CuNW surface fell off, resulting in more Cu exposed to the electrolyte and more easily in contact with MV. At the same time, the remaining TPS coating on the AAO surface also helped to maintain the stability of the local chemical microenvironment on the electrode surface and maintain sufficient active sites. Then, the ECSA of 0.1-TES-CuNW-AAO electrode decreased significantly. Based on the instability of TES coating, this may be due to the severe hydrolysis of TES coating leading to the complete loss of the coating, which not only has an etching effect on CuNW, but also may destroy the AAO template to some extent.

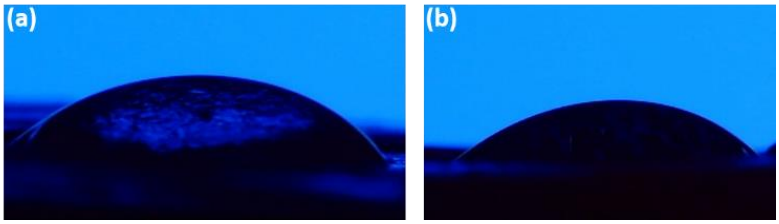

Figure 4.20: The contact angle measurements of 0.1 M silane modified CuNW-AAO electrodes after ECSA measurements: (a) 0.1-DTS-Cu foil, (b) 0.1-TPS-Cu foil, (c) 0.1-TES-CuNW-AAO electrodes.

Table 4.16: The contact angle average values of 0.1 M silane modified CuNW-AAO electrodes after ECSA measurements.

Sample	*Contact angle (°)*
0.1-DTS- CuNW-AAO	51.3±7
0.1-TPS- CuNW-AAO	46.5±9
0.1-TES- CuNW-AAO	-

To further verify the stability of different silane coatings in ECSA measurements, contact angles measurements were performed on electrodes after ECSA. In Figure 4.20 and Table 4.16, it can be seen that 0.1-DTS-CuNW-AAO electrodes can still maintain a certain contact angle, because relatively stable DTS coatings were still distributed on the surface of CuNW and AAO templates, with only partial loss. The contact angle of the 0.1-TPS-CuNW-AAO electrode decreased to a certain extent. Combined with the ECSA of the electrode, it was again confirmed that although the TPS coating on the CuNW surface was not stable enough, there was still a relatively stable TPS coating on the AAO template to help the electrode maintain a certain contact angle and a relatively stable local surface environment. For 0.1-TES-CuNW-AAO electrodes, the electrode surface became completely hydrophobic and the contact angle cannot be obtained, which may be due to the loss of both CuNW and AAO templates caused by the unstable hydrolysis of TES coating.

4.1.2.3. Mass transfer mechanism of Cu-based electrodes

In order to further explore the mechanism of mass transfer during the reaction, the factors affecting the mass transfer of the electrode can be determined by the scanning rates. As it can be seen in Figure 4.21, from the linear relationships between the anodic peak currents and the scan rates, for 0.004-MTS-Cu foil, 0.004-DTS-Cu foil, 0.004-TPS-Cu foil and 0.004-TES-Cu foil electrodes (modified with a low concentration of silane coating), the peak currents of all samples are not proportional to the scan rates, the diffusions dominate the mass transfer, and the electrode surface still meets the characteristics of planar electrode.

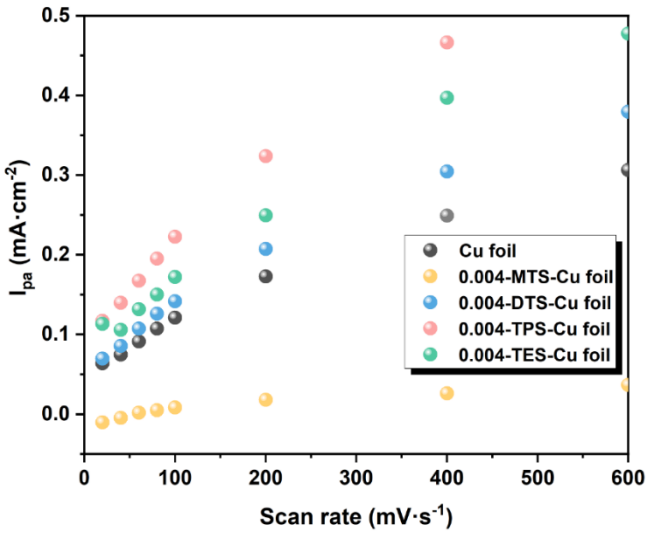

Figure 4.21: Anodic peak current *vs* scan rates of 0.004 M silane modified and unmodified Cu foil electrode.

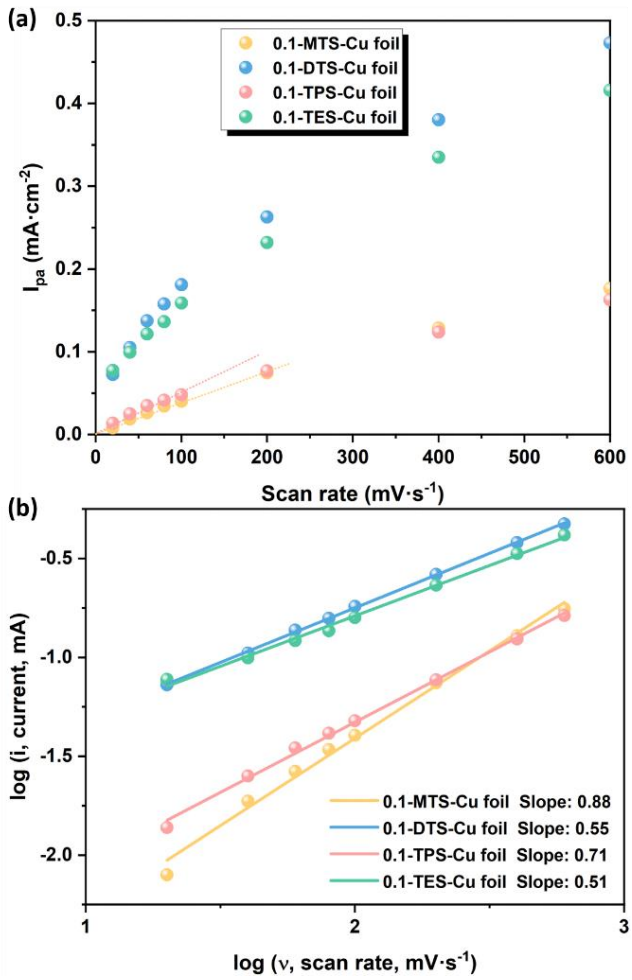

Figure 4.22: Scan rate study of 0.1 M silane modified Cu foil electrode: (a) anodic peak current *vs* scan rates, (b) logi *vs* logv plots (anode).

However, in Figure 4.22 (a), for 0.1-MTS-Cu foil, 0.1-DTS-Cu foil, 0.1-TPS-Cu foil and 0.1-TES-Cu foil electrodes (modified with a high concentration of silane coating), it can be found that the peak currents of 0.1-DTS-Cu foil and 0.1-TES-Cu foil electrodes are not proportional to the scan rates. It indicates that the diffusion is still the dominant mass transfer mode. For 0.1-MTS-Cu foil and 0.1-TPS-Cu foil electrodes, there is a proportional relationship between the peak currents and scan rates, indicating that the diffusion can be limited by the MTS and TPS coatings, and the electrode surfaces have the characteristics of porous structures, the thin layer electrochemistry was involved in the reactive mass transfer process.[265,266] From the relationship between the logarithm of peak currents and the logarithm of scan rates (in Figure 4.22 (b)), the fitting slopes of 0.1-DTS-Cu foil and 0.1-TES-Cu foil electrodes are 0.55 and 0.51, respectively. It indicates that the mass transfer is mainly controlled by electrochemical diffusion. The fitting slopes of 0.1-MTS-Cu foil and 0.1-

TPS-Cu foil electrodes are 0.88 and 0.71, respectively, which confirm that both the thin layer electrochemistry and the diffusion made a contribution to the mass transfer process. This may be due to the fact that the combined MTS and TPS coating on the Cu foil surface changes the thickness of the diffusion layer or the roughness on the electrode surface in the local chemical environment, thus the thin layer electrochemistry characteristics can be found in the electrochemical process.[267]

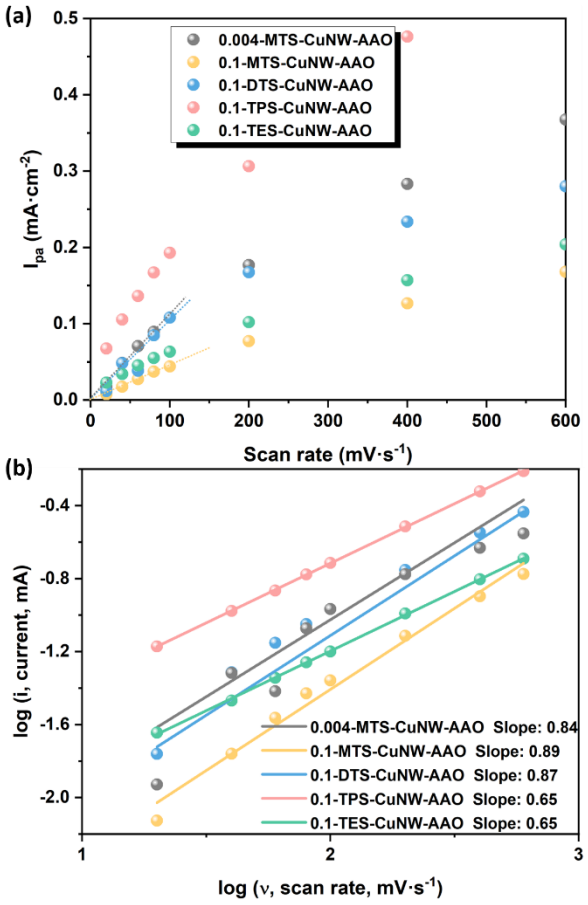

Figure 4.23: Scan rate study of silane modified and unmodified CuNW-AAO electrodes: (a) anodic peak current *vs* scan rates, (b) logi *vs* logv plots (anode).

Subsequently, the electrochemical mass transfer behaviour of the silane-modified CuNW-AAO electrodes were investigated. As shown in Figure 4.23 (a), for 0.004-MTS-CuNW-AAO, 0.1-MTS-CuNW-AAO and 0.1-DTS-CuNW-AAO electrodes, the anodic peak currents are proportional to the scan rates, that is, the thin layer electrochemistry was associated with mass transfer on electrode surface. However, 0.1-TPS-CuNW-AAO and 0.1-TES-CuNW-AAO electrodes do not have the same electrochemical characteristics. Furthermore, through the relationship between the

logarithm of peak currents and the logarithm of scan rates (in Figure 4.23 (b)), the fitting slopes of 0.004-MTS-CuNW-AAO, 0.1-MTS-CuNW-AAO and 0.1-DTS-CuNW-AAO electrodes are 0.84, 0.89 and 0.87, respectively. As already confirmed in Chapter 3, the unmodified 1.0 CuNW-AAO electrode has a slope close to 0.5 and its electrochemical mass transfer characteristics were similar to a planar electrode. Therefore, it can be assumed that the local chemical environment of the CuNW-AAO electrodes modified with MTS and DTS changed. And the changes of hydrophobicity and roughness adjust the thickness of the diffusion layer on the electrode surface, thus changing the mass transfer mode in reactions. The change of mass transfer mode may benefit the CO_2 gas capture on the electrode surface and the gas concentration in the three-phase interface when the electrode is used as a CO_2RR catalyst, which may further improve the catalytic efficiency of the catalyst. However, for 0.1-TPS-CuNW-AAO and 0.1-TES-CuNW-AAO electrodes, the coated electrodes still maintain mass transfer characteristics similar to the planar electrodes, which may be caused by the potential shedding of unstable TPS and TES coatings.

4.1.3. Electrochemical impedance measurements of Cu-based electrodes

4.1.3.1. Electrochemical impedance measurements (EIS) of MTS, DTS, TPS and TES modified Cu foil electrodes

In order to further understand the impedance changes during the process of mass transfer on electrodes, the electrochemical impedances of Cu foil electrodes modified with different kinds and different concentrations of silanes were measured. The equivalent circuit shown in Figure 4.24 inset was applied. After fitting the experimental data to the equivalent values, the circuit model was determined which consists of solution resistance (R_s), charge transfer resistance (R_{ct}) and double-layer capacitor (C) components.[268,269] As can be seen from Table 4.17 and Figure 4.24 (impedance raw data for Cu foil electrodes is shown in Appendix 2 (Figure A 2.15), it can be seen that the Nyquist plots of all electrodes shows a captance arc, which accords with the basic characteristics of R(CR) circuit. The arc radius (R_{ct}) of the Cu foil electrodes modified with high concentration silane is generally lower than that of the Cu foil electrodes modified with low concentration silane, indicating that the high concentration of silane coating is conducive to electron transfer in the reaction. In addition, the R_s values of the Cu foil electrodes with high concentration of silane modification are generally slightly larger than those of the low concentration silane-modified Cu foil electrodes. It is possibly because the thicker hydrophobic layer

introduced by the high concentration silane reduce the solution contacting the electrode surface.

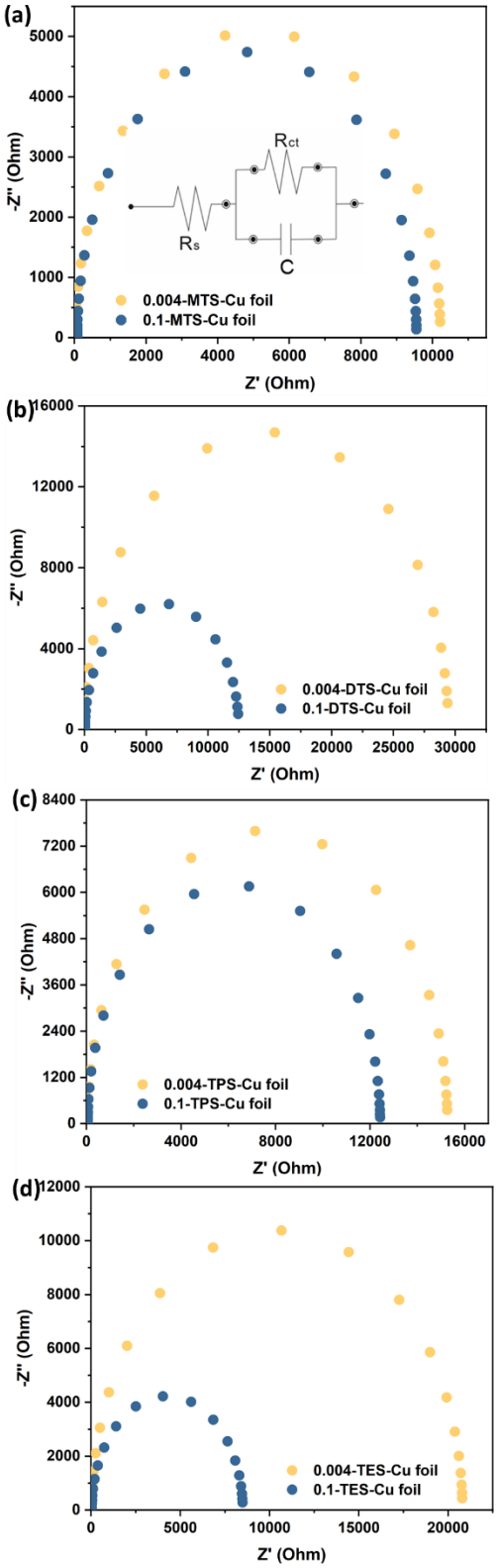

Figure 4.24: Nyquist plot of EIS and equivalent circuit R(CR) for impedance fitting for Cu foil electrode at open circuit potential in 0.1 M Na_2SO_4: (a) on MTS-Cu foil electrodes, (b) on DTS-Cu foil electrodes, (c) on TPS-Cu foil electrodes, (d) on TES-Cu foil electrodes. (Nyquist plots are from the fitted data.)

Table 4.17: The fitting parameters of EIS for silanes modified and unmodified Cu foil electrodes at open circuit potential.

Electrode	*R_s (Ohm·cm^2)*	*C (mF·cm^2)*	*R_{ct} (Ohm·cm^2)*
0.004-MTS-Cu foil	29.06±3.28	0.04±0.005	10190±1528
0.1-MTS-Cu foil	75.20±8.77	0.03±0.004	9481±1426
0.004-DTS-Cu foil	29.43±3.08	0.02±0.020	29400±4242
0.1-DTS-Cu foil	46.68±4.19	0.08±0.009	12440±1832
0.004-TPS-Cu foil	45.70±4.26	0.02±0.002	15220±1855
0.1-TPS-Cu foil	49.20±5.38	0.002±0.000	12370±1624
0.004-TES-Cu foil	38.09±4.04	0.002±0.000	20760±2713
0.1-TES-Cu foil	39.20±4.14	0.006±0.001	8460±1298
	R_s (Ohm·cm^2)	*C (mF)*	*R_{ct} (Ohm·cm^2)*	*Z_W (mOhm·cm^2)*
Cu foil	30.64±1.50	0.08±0.008	1543±151.21	0.73±0.054

4.1.3.2. EIS of MTS, DTS, TPS and TES modified CuNW-AAO electrodes

By contrast, from the impedance spectroscopy of 0.004-MTS-CuNW-AAO, 0.1-MTS-CuNW-AAO, 0.1-DTS-CuNW-AAO, 0.1-TPS-CuNW-AAO and 0.1-TES-CuNW-AAO electrodes at open circuit potential in 0.1 M Na_2SO_4 (Figure 4.25 and Table 4.18, and the impedance raw data is shown in Appendix 2 Figure A 2.16), it shows that R_s and R_{ct} of all CuNW electrodes are smaller than those of Cu foil, indicating that the introduction of nanowire structures and silane coatings are conducive to improving mass transfer during the reaction. Compared with the EIS of the 1.0 h CuNW-AAO electrode in Chapter 3, the R_s and R_{ct} of all the CuNW-AAO electrodes modified with silane are significantly reduced. Similarly, the high concentration of silane coating coverage reduces the R_{ct} of the electrode, which is conducive to improving the activity and reaction efficiency of the electrocatalyst. Interestingly, in Chapter 3, we found that the Warburg impedance characteristics at low frequencies only existed on the unmodified Cu foil electrode. However, we also

found the Warburg impedance characteristics on 0.1-TES-CuNW-AAO electrode due to its small charge transfer resistance (Figure 4.25 (b) and Table 4.19). Consistent with the electrochemical behaviour (ECSA) of 0.1-TES-CuNW-AAO, the less stable TES coating can be severely damaged during electrochemical measurements, resulting in the surface of the electrode tends to be unmodified CuNW-AAO electrode.

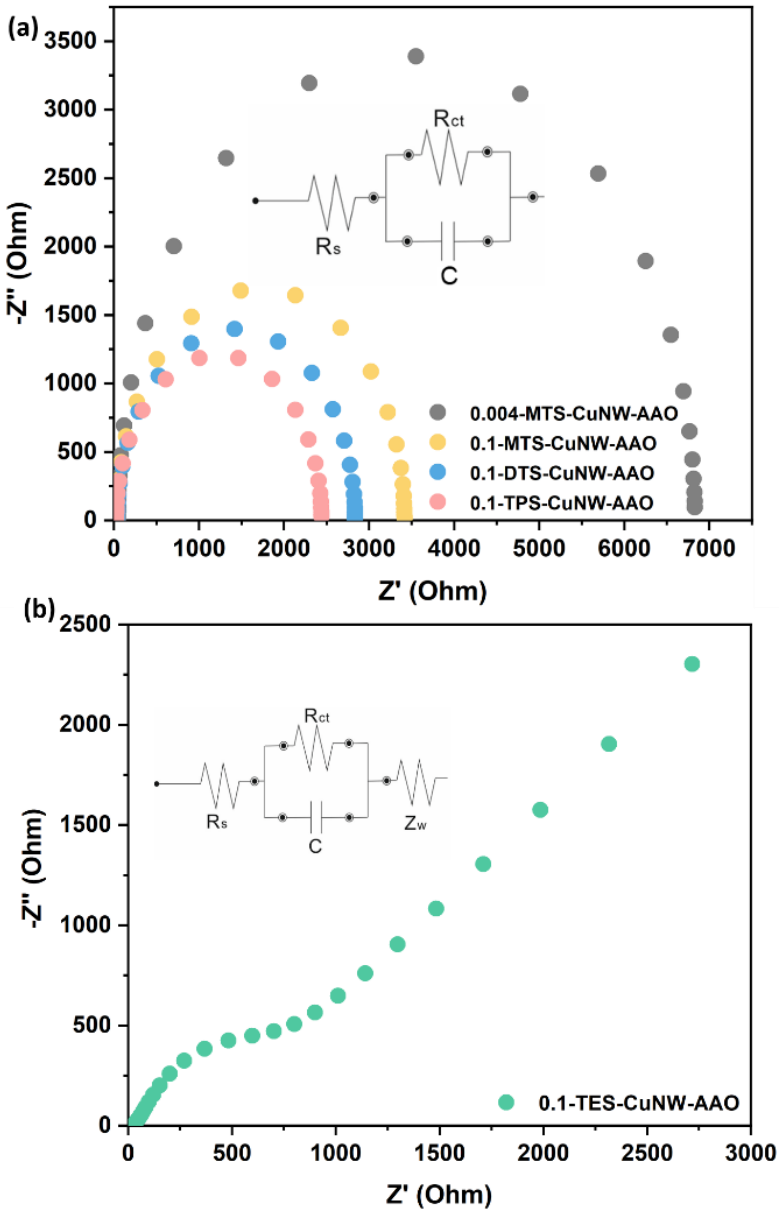

Figure 4.25: Nyquist plot of EIS and equivalent circuit for impedance fitting for CuNW-AAO electrode at open circuit potential in 0.1 M Na_2SO_4: (a) on MTS/DTS/TPS-CuNW-AAO electrodes [R(CR)], (b) on TES-CuNW-AAO electrode [R(CR)W]. (Nyquist plots are from the fitted data.)

Table 4.18: The fitting parameters of EIS for silanes modified CuNW-AAO electrodes at open circuit potential.

Electrode	R_s (Ohm·cm²)	C (mF·cm²)	R_{ct} (Ohm·cm²)
0.004-MTS-CuNW-AAO	48.24±5.41	0.003±0.0003	6781±941
0.1-MTS-CuNW-AAO	29.30±3.80	0.003±0.0004	3386±463
0.1-DTS-CuNW-AAO	40.98±5.55	0.005±0.0007	2793±316
0.1-TPS-CuNW-AAO	26.88±2.56	0.008±0.0010	2414±295

Table 4.19: The fitting parameters of EIS for 0.1-TES-CuNW-AAO electrode at open circuit potential.

Electrode	R_s (Ohm·cm²)	C (mF·cm²)	R_{ct} (Ohm·cm²)	Z_W (Ohm·cm²)
0.1-TES-CuNW-AAO	21.15±0.025	0.20±0.118	395.3±0.117	0.00123±0.042

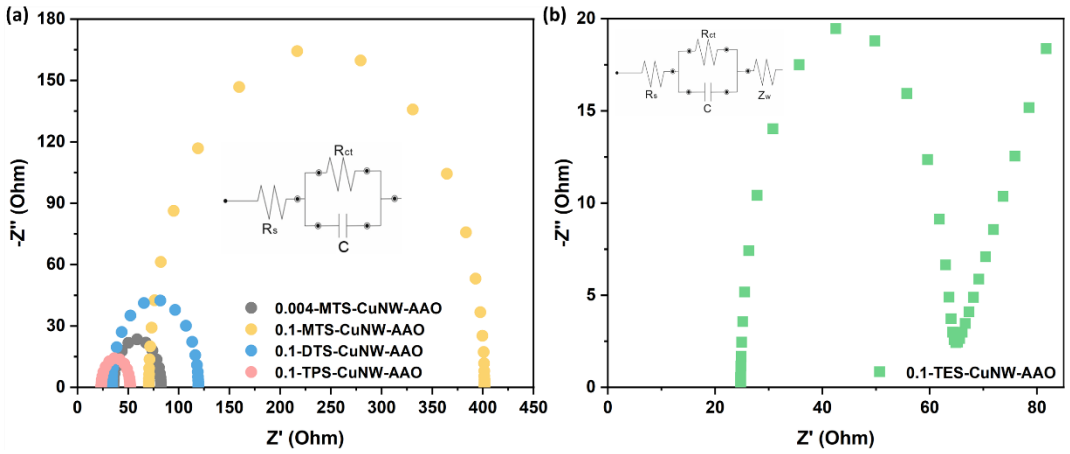

Figure 4.26: Nyquist plot of EIS and equivalent circuit for impedance fitting for CuNW-AAO electrode at -0.8 V (vs.RHE) in 0.1 M Na_2SO_4.: (a) on MTS/DTS/TPS-CuNW-AAO electrodes [R(CR)], (b) on TES-CuNW-AAO electrode [R(CR)W]. (Nyquist plots are from the fitted data.)

Table 4.20: The fitting parameters of EIS for silanes modified CuNW-AAO electrodes at -0.8V (vs.RHE).

Electrode	R_s (Ohm·cm^2)	C (mF·cm^2)	R_{ct} (Ohm·cm^2)
0.004-MTS-CuNW-AAO	35.67±1.11	0.005±0.0007	46.83±2.34
0.1-MTS-CuNW-AAO	70.63±4.42	0.001±0.0001	330.9±19.55
0.1-DTS-CuNW-AAO	34.95±1.59	0.002±0.0002	85.34±4.72
0.1-TPS-CuNW-AAO	23.64±0.46	0.013±0.0013	28.46±1.02

Table 4.21: The fitting parameters of EIS for 0.1-TES-CuNW-AAO electrode at -0.8 V (vs.RHE).

Electrode	R_s (Ohm·cm^2)	C (mF·cm^2)	R_{ct} (Ohm·cm^2)	Z_W (Ohm·cm^2)
0.1-TES-CuNW-AAO	24.72±0.575	0.07±0.006	38.64±1.592	0.15±0.028

EIS data was also measured as -0.8 V (vs.RHE), common potential used for CO_2RR. Due to the presence of HER side reaction, the mass transfer reaction in the low frequency region is seriously disturbed, and the diffusion impedance data cannot be fitted. A simplified Randels circuit (R(CR)) is used to analyze the activation control response only in the high frequency region. In Figure 4.26 and Table 4.20 (impedance raw data for CuNW-AAO electrodes is shown in Appendix 2 Figure A 2.17), it can be seen from the intercept and R_s fitting values of the high-frequency semicircles on the X axis that R_s of 0.1-DTS-CuNW-AAO and 0.1-TPS-CuNW-AAO electrodes are smaller (34.95 Ω and 23.64 Ω). Due to the instability of DTS and TPS coatings under electrolyte and current conditions, causing the partial coating falling off, the electrolyte is more likely to come into contact the CuNW. The R_s of 0.1-MTS-CuNW-AAO electrode is larger (70.63 Ω). This is because the more stable MTS coating covers the CuNW and AAO template surfaces, and the contact between the electrolyte and

the CuNW surface is partially stopped, resulting in an increase in R_s. In particular, the 0.1-TES-CuNW-AAO electrode exhibits Warburg impedance characteristics (Figure 4.26 (b) and Table 4.21). Due to the wastage of TES coatings during testing and the influence on CuNW and AAO templates, the 0.1-TES-CuNW-AAO electrodes approach the impedance characteristics of unmodified CuNW-AAO, showing an approximate semi-infinite diffusion.

4.2. Conclusions

In this chapter, we used different kinds and concentrations of silane molecules to change the wetting ability and local chemical environment of the copper-based electrode surfaces, and studied the influence of the surface environment regulating strategies on the electrochemical performance. By comparing the effects of silane coating on the wettability and electrochemical behaviours of Cu foil and CuNW-AAO electrodes, the effects of the modifier on Cu catalyst and AAO support template were determined. From the contact angle tests, it has been known that a hydrophobic layer has been successfully constructed on the electrode surface (contact angle > 100°), which will help construct a three-phase interface for CO_2RR to improve the capture of CO_2 gas at the electrode surface. Next, ECSA measurements showed that the silane-modified CuNW-AAO electrode still maintained a higher electrochemical surface area (0.5-1.1 cm^2) than the molecular-coated CuNW electrode ($3x10^{-3}$ cm^2) in the literature. It is shown that the silane coating can improve the hydrophobicity of the electrode without losing the active surface area and active sites of the electrode. At the same time, when a certain current is applied, different silane coatings on the electrode will disengage to different degrees, and the active sites and active surface area on the Cu will not be blocked in a large area. On the 0.1 M silane modified CuNW-AAO electrodes, the generally large R_f value indicates that the application of current on the electrode will promote the hydrolysis of the silane coating, and then the etching Cu surface will significantly improve the surface roughness. At the same time, after the tests, the electrode surface can still maintain different degrees of hydrophobicity, because there is still a certain amount of silane coating on the insulating AAO template surface, which is conducive to maintaining the microenvironmental stability of the electrode surface. From EIS, it was found that the CuNW-AAO electrodes modified with silane had significantly lower R_s and R_{ct} than the unmodified CuNW-AAO electrodes, which is very conducive to improving reaction efficiency in CO_2RR.

5. Electrochemical reduction of carbon dioxide (CO_2) towards multi-carbon products through control of proton coupled electron transfer

Aims

At present, some single carbon products (C_1) and multi-carbon products (C_{2+}) with high Faraday efficiency (FE) have been obtained on copper through the design of surface morphology and microstructure of copper-based electrocatalysts.[213,270–273] However, (i) at high reduction current densities, the catalytic site stability is generally poor; (ii) Cu-based catalysts have high selectivity for HER side reactions (usually causing selectivity losses higher than 20%-40% in CO_2RR);[274,275] (iii) It is difficult to accurately control the selectivity of Cu-based catalysts for C_1/C_{2+} products, and the yield of C_{2+} products is still low, which still exists in widely studied Cu-based catalysts. Therefore, the application of carbon dioxide electrolysis in the industrial field is greatly limited. To improve CO_2RR technology from the laboratory level to a practical carbon cycle technology that can be applied to real industry, it is crucial to be able to generate more economically effective C_{2+} products at high current densities while ensuring the long-term operational stability of Cu-based catalysts.

From the perspective of microstructure in CO_2RR system, heterogeneous electrocatalysis usually occurs at the solid-liquid-gas three-phase interface composed of solid catalyst, liquid electrolyte and gaseous CO_2 gas source. The catalytic performance of CO_2RR depends on the reactive sites on the catalyst surface and the stability of the three-phase interface environment to a great extent. ***Reaction active sites***, especially for reducing CO_2 into C_{2+} products, a process that involves multiple proton-coupled electron steps of different reaction intermediates bonded to the reactive sites. For example, the rapid formation and dimerization of $*CO$ intermediates are generally rate-limiting steps for C_{2+} products generation. The instability of the active sites will result in poor catalytic activity and low product selectivity of the reaction. Wu et al. found a kind of intermediate oxidation state of $Cu^{\delta+}$ ($0 < \delta < 2$) as the active site, the presence of $Cu^{\delta+}$ can promote the further coupling of $*CO$ adsorbed on the surface of Cu to form a precursor for the formation of C_{2+} products.[276] It will make a faster reaction rate and higher C_{2+} FE in CO_2RR on Cu-based catalysts. However, CO_2RR usually occurs at a relatively higher reduction current, it will also cause $Cu^{\delta+}$ self-reduction reaction, so that it is difficult for active sites to maintain the reaction activity for a long time, which is not conducive to the stability of the catalyst.[277]

Three-phase interface, the microenvironment on Cu-based catalyst surface involves electron transport and reaction mass transfer in CO_2RR, dominating the kinetics of the entire reaction.[278] When the three-phase interface is lost, both the reactive active sites and the catalytic activity will be reduced. In addition, when the contact between the catalyst surface and the CO_2 gas phase interface is inadequate, the surface adsorption of $*H$ increases, which will be conducive to increasing HER. Therefore, controlling gas transport and adsorption of reaction intermediates on the three-phase interface by regulating the Cu-based catalysts surface microenvironment is critical for achieving high C_{2+} FE. The strategies of modifying catalyst surface microenvironment mainly involve regulating hydrophobicity, adsorbability, electronegativity and local pH.[279–282] Many studies have suggested that improving the hydrophobicity of the catalyst surface can effectively lower HER and improve CO_2RR activity.[283–286] Zeng et al designed a Cu-I/PTFE gas diffusion electrode by introducing a hydrophobic PTFE gas diffusion layer.[287] The introduction of PTFE increased the contact angle of the gas diffusion layer surface to more than 150°, which was conducive to the increase of CO_2 concentration on the electrode surface and enhanced the adsorption capacity of CO_2 on the Cu-I surface. In addition, using in-situ surface-enhanced Raman spectroscopy (SERS), it was observed that$\cdots OH$ radicals supplied by the hydrophobic surface could maintain the Cu^+ sites on the catalyst surface, thus improving the binding ability of the catalyst and $*CO$ intermediates to promote C-C coupling and achieve high selectivity for C_2H_4 (FE up to 70.2%). This system can steadily produce C_2H_4 for 150 hours. However, more exploration is needed to achieve the goal of having a high selectivity for C_2+ products. Although in the above work, it can achieve a higher C_2H_4 yield, accompanying, it still has a higher HER yield (35% to 45%) at a more negative overpotential (-1.2 V - 1.5 V vs.RHE) at higher current densities. Therefore, when regulating the microenvironment on the catalyst surface through constructing a hydrophobic layer, it is still necessary to consider how to inhibit the transport of water in the three-phase interface and efficiently, steadily transport CO_2 gas source to the catalytic active sites.

Lin and colleagues realized the adjustment the $*CO/*H$ ratio on the Cu electrode by modifying the catalyst surface with alkyl mercaptan with different alkyl chain lengths.[288] In this study, they found the alkyl chain length could determine the hydrophobicity of the modified layer anchored on the copper surface. When the hydrophobicity of the modified layer is increased, it will promote the mass transfer of CO_2 gas and restrain the transfer of H_2O, which can increase the bonded $*CO/*H$ ratio on the catalyst surface. Due to the depletion of $*H$, the trend of catalysis towards

HER is weakened, and it is conducive to C-C coupling further the formation of C_{2+} products. Under the modification of different alkyl mercaptans, the ratio of C_2H_5OH and C_2H_4 produced on Cu-based catalyst can be adjusted within a certain range (0.90 to 1.92), so that the maximum FE of C_2H_5OH and C_{2+} can reach 53.7% and 86.1%, respectively. By controlling the targeted combination of Cu-based catalyst and $*CO/*H$, it can be achieved that the electrode can have a high selectivity of C_{2+} products. However, direct modification of the Cu surface usually results in a catalyst with limited stability due to Cu catalyst restructuring and loss of the surface modification such as mercaptans.

Modifying the hydrophobicity of Cu by introducing surface layers is considered to be key to improving the catalytic selectivity of C_{2+} products due to the increase of CO_2 gas concentration in the three-phase interface. The main purpose of this chapter is to achieve the aqueous electrocatalytic conversion of CO_2 to C_{2+} chemicals with high Faradic efficiency (partial current density) by adjusting the local microenvironment near the surface of the Cu-based catalyst, and to overcome the challenges commonly found in existing studies like low catalytic activity, high HER efficiency and poor electrode stability. Based on the functionalization of the Cu-based catalyst electrode surface using different types of silane molecules in the previous chapter, the hydrophobic three-phase interface can be successfully constructed while ensuring that the electrochemical surface area of the Cu active sites is still accessible. The aim of this chapter is to test silane molecule modified Cu foil and CuNW-AAO electrodes designed with in a partially hydrophobic environment directly at the Cu surface or near to the surface to increase the relative concentration of CO_2 compared to H_2O. By altering the electrode surface microenvironment, the proton activity will be regulated so that $*CO$ can dominate on the catalyst electrode surface. In this way, the C-C coupling process will be promoted to form more intermediate products used for C_{2+} product formation. We hoped that the hydrophobic silane modification of the AAO template would provide a more stable platform for mass transfer, charge transfer and reaction intermediate concentration on the surface of Cu-based catalyst electrodes with stable mechanical properties compared to directly attaching hydrophobic groups to the Cu surface, which will be very beneficial for improving the selectivity of CO_2RR for C_{2+} products and system stability.

5.1. Results and Discussion

5.1.1. Electrochemical characterization of the Cu-based electrodes

In general, the catalytic activity of an electrocatalyst depends on the distribution of active sites on the surface.[289] The electrochemical surface active area (ECSA) obtained by measuring the double-layer capacitance of the electrocatalyst can be used to evaluate the number of active sites on the electrocatalyst surface. Based on the research results in Chapter 4, the silane modified CuNW-AAO electrodes have a larger electrochemical surface area and roughness (R_f) than the unmodified CuNW-AAO electrode and Cu foil electrode, and the surface modification of CuNW-AAO electrode may help improve the catalytic activity of the electrode when used as a CO_2RR catalyst. In this chapter, to further determine the electrochemical surface active area of the CuNW-AAO electrode when used as a CO_2RR catalyst, multiple CV scans on the Cu foil electrode and the CuNW-AAO electrode in N_2-saturated 0.1 M $KHCO_3$ was performed to assess the corresponding ECSA and R_f of the electrodes.

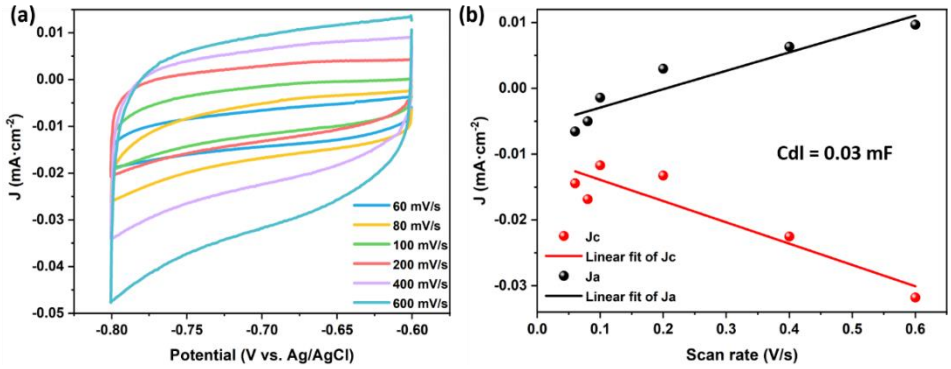

Figure 5.1: ECSA of Cu foil electrodes: (a) Multiple CVs of Cu foil electrode. (b) Linear fitting for double-layer capacitance of Cu foil electrode. All measurements were proceeded in N_2-saturated 0.1 M $KHCO_3$ solution.

Based on the current responses of Cu foil electrode normalized to the geometric surface area, the C_{dl} value of Cu foil is 0.03 mF which can be calculated from the mean linear fitting of the scan rates of the anodic and cathodic peak currents of Cu foil respectively in Figure 5.1. Comparing with the C_{dl} of Cu foil measured in N_2-saturated 0.1 M Na_2SO_4 (0.05 mF, discussed in Chapter 3), it did not change much, indicating that the two different electrolyte media have little impact on the evaluation of the electrochemical surface active area of Cu foil. In addition, the C_{dl} of Cu foil electrode was similar to the C_{dl} of electropolished Cu foil measured in 0.1 M $KHCO_3$ in other work (Ummireddi et al. reported the C_{dl} of electropolished Cu foil was 0.04 mF).[290]

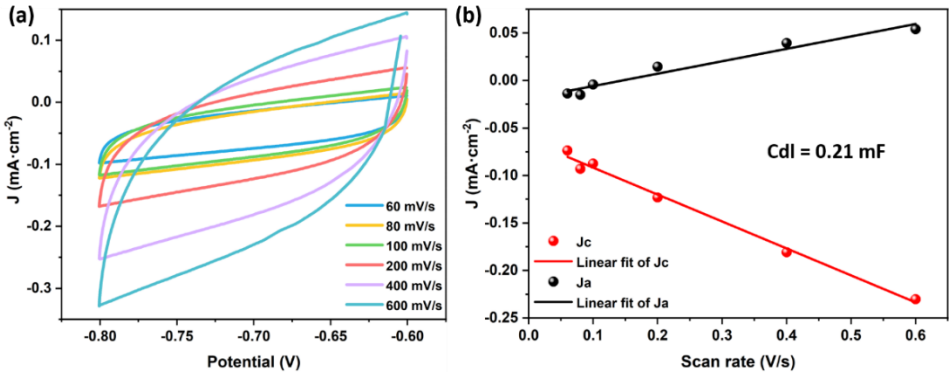

Figure 5.2: ECSA of CuNW-AAO electrodes: (a) Multiple CVs of CuNW-AAO electrode (obtained by two-step electrodeposition with the treatment of 0.1 M NaOH for 1 h, and the deposition curves and Cu mass on the electrode were shown in Appendix 2 Figure A 2.7). (b) Linear fitting for double-layer capacitance of CuNW-AAO electrode. All measurements were proceeded in N_2-saturated 0.1 M $KHCO_3$ solution.

Next, multiple CVs of CuNW-AAO electrode (obtained by two-step electrodeposition with the treatment of 0.1 M NaOH for 1 h, and the deposition curves and Cu mass on the electrode were shown in Appendix 2 Figure A 2.7) was measured in N_2-saturated 0.1 M $KHCO_3$ electrolyte. As shown in Figure 5.2, the C_{dl} value of CuNW-AAO electrode is 0.21 mF. When the R_f value of Cu foil electrode is regard as 1 as a reference, then the R_f of CuNW-AAO electrode is 7. Furthermore, it has been calculated in Chapter 3 that the ECSA of Cu foil electrode is 1.72 $cm^2 \cdot cm^{-2}$. In Figure 5.2, the calculated ECSA of CuNW-AAO electrode is 3.15 $cm^2 \cdot cm^{-2}$. The larger ECSA and R_f measured on CuNW-AAO electrode in 0.1 M $KHCO_3$ electrolyte demonstrate the large number of active sites on the CuNW-AAO electrode per geometric surface area, which is attributed to the NW structure. Under these conditions the CuNW active sites appear to be accessible to the electrolyte in the presence of the AAO template.

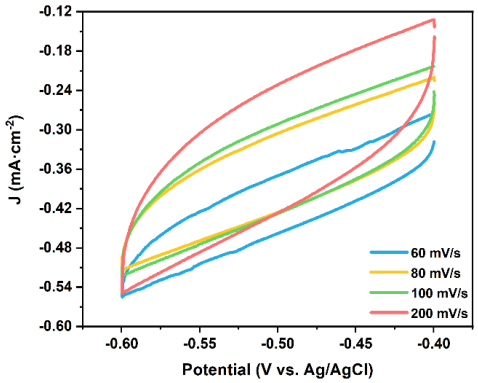

Figure 5.3: Multiple CVs of 0.1-TPS-CuNW-AAO electrode (obtained by two-step electrodeposition with the treatment of 0.1 M NaOH for 1 h, and the deposition curves and Cu mass on the electrode were shown in Appendix 2 Figure A 2.8). All measurements were proceeded in CO_2-saturated 0.1 M $KHCO_3$ solution.

Next, multiple CVs measurements were performed on the silane molecule modified CuNW-AAO electrodes obtained in Chapter 4 to evaluate the ECSA of CuNW-AAO electrodes with hydrophobic surface. To evaluate the ECSA and catalytic active sites of the silane modified CuNW-AAO electrode more accurately when applied in CO_2RR, as an example, the multiple CVs were obtained on 0.1-TPS-CuNW-AAO electrode (obtained by two-step electrodeposition with the treatment of 0.1 M NaOH for 1 h, and the deposition curves and Cu mass on the electrode were shown in Appendix 2 Figure A 2.8) in the CO_2-saturated 0.1 M $KHCO_3$ electrolyte. As shown in Figure 5.3, the relationship between the anodic or cathodic current responses and the scan rates does not fit a linear relationship model (the irregular CVs were also obtained on other 0.1-MTS-CuNW-AAO, 0.1-DTS-CuNW-AAO and 0.1-TES-CuNW-AAO electrode), as there is no regular relationship between the current responses and the scan rates. The bubbles on the electrode surface could be obviously observed during the measurements. Although the CVs measurements were proceeded in a non-Faraday region of -0.4 V to -0.6 V vs.Ag/AgCl (0.2 V to 0 V vs.RHE), due to the presence of CO_2 in the electrolyte, as shown by the reduction potentials of each product in Table A 1.1, it may still be possible some chemical half-reactions interfere with ECSA measurements, although the magnitude of the current responses are similar to CVs obtained in N_2-saturated 0.1 M Na_2SO_4 electrolyte (Figure 4.15 (c) in Chapter 4). The non-linearity clearly indicates a significant change on addition of silane and instability in capacitance measurements not seen in the absence of silane. Restricted access of aqueous electrolyte due to hydrophobic silanes near the Cu surface would modify the wetting and capacitance of the electrode. Instability of the silane coating or AAO template would also cause variations and at this time, it is not possible to quantify Figure 4.15.

5.1.2. Electrochemical CO_2 reduction reaction on Cu foil electrodes

Before electrocatalytic evaluation of the prepared unmodified/modified CuNW-AAO electrodes, a control experiment was performed to examine whether the introduction of silane molecules has an effect on the electrocatalytic activity of Cu. The catalytic activity of Cu foil electrodes modified with different silane molecules in a flow cell containing 0.1 M $KHCO_3$ electrolyte was investigated. The electrodes used for CO_2RR catalytic activity evaluation were electrochemical polished Cu foil, 0.004-MTS-Cu foil, 0.1-MTS-Cu foil, 0.1-DTS-Cu foil, 0.1-TPS-Cu foil and 0.1-TES-Cu foil.

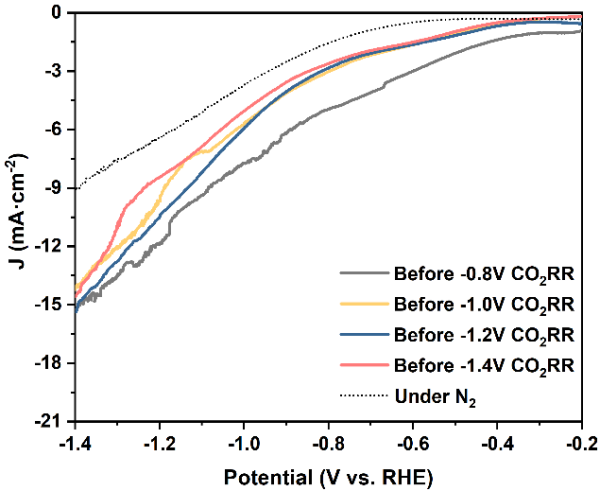

Figure 5.4: LSVs of Cu foil electrode in 0.1 M $KHCO_3$ saturated by N_2 and CO_2 with a scan rate of 10 $mV \cdot s^{-1}$. (Each LSV measurement was performed before CO_2RR at each reduction potential.)

Firstly, the electrochemical polished Cu foil electrode was used for continuous CO_2 electrocatalytic reduction reactions at different reduction potentials. The electrodes were tested by linear sweep voltammetry (LSV) before each reaction. In Figure 5.4, it can be seen from the LSVs obtained on the Cu foil electrode that compared with the curve obtained under N_2, Cu foil presents a higher reduction current response in the presence of CO_2, indicating that CO_2 gas can diffuse to the electrode surface and electrocatalytic reduction occurred.

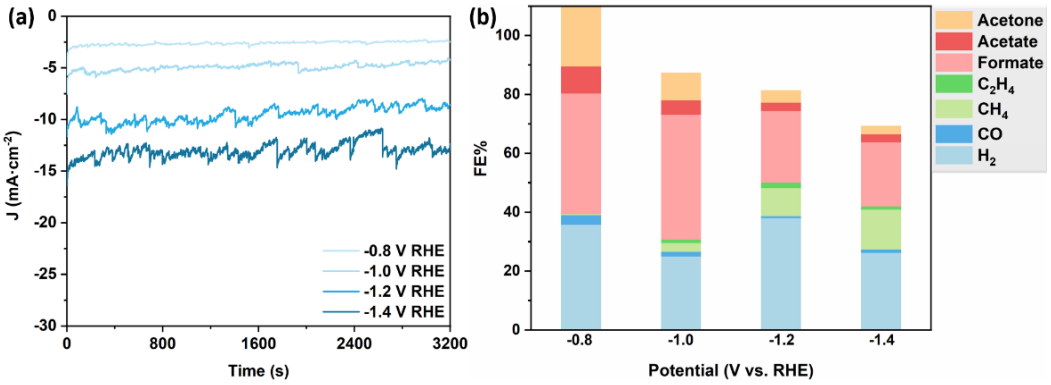

Figure 5.5: CO_2RR on Cu foil electrode: (a) Chronoamperometric experiments in 0.1 M $KHCO_3$ saturated by CO_2. (b) Faradaic efficiencies of gas and liquid products at different applied potentials from CO_2RR.

Table 5.1: Faradic efficiency of gas and liquid products on Cu foil electrode in 0.1 M $KHCO_3$ saturated with CO_2.

Faradic efficiency (FE, %)

E (V RHE)	*CO*	*CH_4*	*C_2H_4*	*H_2*	*Formic acid (l*)*	*Acetate (l)*	*Acetone (l)*	*Ethanol (l)*	*n-Propanol (l)*	*J ($mA \cdot cm^{-2}$)*	*Total*
-0.8	3.2	0.4	0	35.7	40.9	9.2	22.2	0	0	-2.61	**111.7**
-1.0	1.6	3.0	1.1	24.9	42.5	4.9	9.4	0	0	-4.90	**87.4**
-1.2	0.6	9.6	1.8	38.0	24.3	2.8	4.2	0	0	-9.52	**81.4**
-1.4	1.1	13.6	1.1	26.2	21.7	2.8	2.8	0	0	-13.03	**69.3**

*l**: *Liquid products.*

Next, CO_2RR on Cu foil electrode in the potential range of -0.8 V to -1.4 V (vs.RHE) was evaluated in a flow cell with a three-electrode system. In Figure 5.5 and Table 5.1, formic acid is the main product of the CO_2 reduction on Cu at different potentials. When the reduction potentials were -0.8 V and -1.0 V (vs.RHE), the maximum $FE_{formic\ acid}$ reached about 42.5%, and the partial current density for formic acid ($J_{formic\ acid}$) were -1.07 $mA \cdot cm^{-2}$ and 2.08 $mA \cdot cm^{-2}$ at -0.8 V and -1.0 V, respectively. Notably, higher concentrations of acetate and acetone were detected in the potential range of -0.8 V to -1.0 V (vs.RHE). According to the literature reports, it is difficult to produce a large amount of acetate and acetone ($FE_{acetate}$ and $FE_{acetone}$ are usually below 1% and 0.1%, respectively) on Cu foil within this specific potential range, and the expected general products obtained on Cu usually are CO (FE ~10%), CH_4 (FE ~40%), C_2H_4 (FE ~20%), formic acid (FE ~20%), ethanol (FE ~10%), n-propanol (FE ~4%).[291–294] These compounds are likely impurities introduced in the electrolyte from the lacquer used to electrically insulate the Al stub electrode under the Kapton and PTFE tape allowing only a window of the working electrode to be in contact with the electrolyte. In Figure 5.5, as CO_2RR is performed at different potentials, the electrolyte is changed and the FE of both acetate and acetone continues to decrease, which would be expected for leaching. Control experiments were performed that showed heating electrodes for 1h at 100 ^oC prior to CO_2RR

significantly reduced acetone and acetate to ~1%. A control experiment where no current is passed did not show any of the products in Table 5.1 indicating that if acetone and acetate come from the lacquer leaching only occurs on electrolysis. A third control experiment was performed without CO_2 bubbling which was replaced with N_2 gas and current was passed showing only hydrogen was produced significantly with 95% FE. An isotope experiment using $^{13}CO_2$ could be used to confirm which products are from CO_2RR but time and expense prevented this before submission. When the reduction potential was increased to -1.2 V and -1.4 V (vs.RHE), FE_{CH4} increased significantly to 13.6%, while FE_{C2H4} still remained at 1% to 1.8%, indicating that although Cu foil has the potential to produce C_{2+} products, it tends to produce more single carbon products. Simultaneously, the entire CO_2RR processes were accompanied by HER, and FE_{H2} is slightly lower than that on the general Cu foil in the literature.[295–298] Moreover, the total reaction FE at each potential was less than 100%, which was probably caused by some leaking or part of the current attributable to other unknown chemical reactions that result in leaching of acetone and acetate.

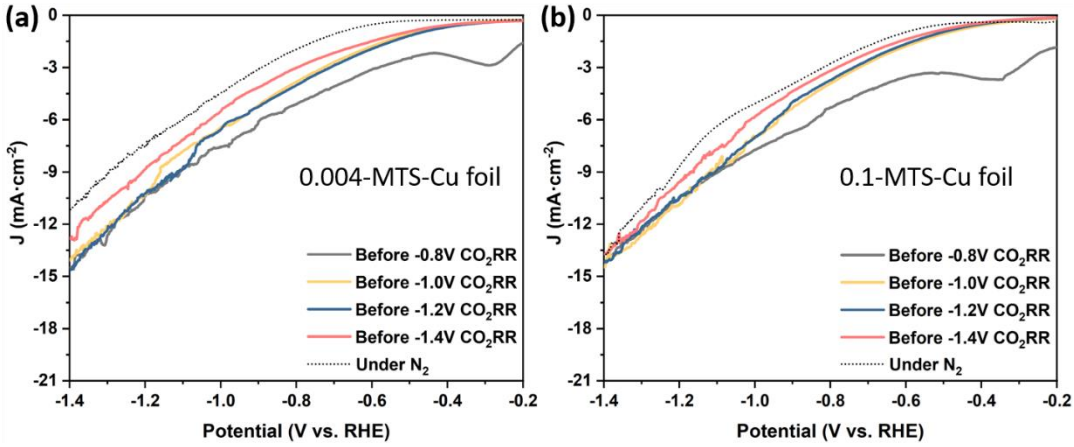

Figure 5.6: LSVs of 0.004-MTS-Cu foil and 0.1-MTS-Cu foil electrodes in 0.1 M $KHCO_3$ saturated by N_2 and CO_2 with a scan rate of 10 $mV \cdot s^{-1}$.

LSV measurements were also performed on 0.004-MTS-Cu foil and 0.1-MTS-Cu foil, respectively, as shown In Figure 5.6. The current responses of LSVs under CO_2 atmosphere is slightly higher than that under N_2 atmosphere, which shows that the hydrophobic Cu surface modified by silane molecules will not cause total blocking

of active sites and, CO_2 can still diffuse to the Cu surface and the electrocatalytic reduction still occurs. Also, by comparing the Cu foil surface modified with different MTS concentrations, the current responses of Cu is not negatively affected by soaking the electrode in a higher concentration of silane, indicating saturation of Cu sites that react with silane can be achieved without deactivating the electrode. In addition, the first LSV measurement before CO_2RR (Gray curves of -0.8 V vs.RHE in Figure 5.6) has a significant reduction peak at about -0.3 V (vs.RHE). Combined with the XPS characterization results in Chapter 4 (large amount of Cu^+ existed on the surface of MTS-Cu foil electrode), the reduction peak could be attributed to Cu_2O or $Cu_x(O_3SiR)_y$ being reduced first on the electrode surface.

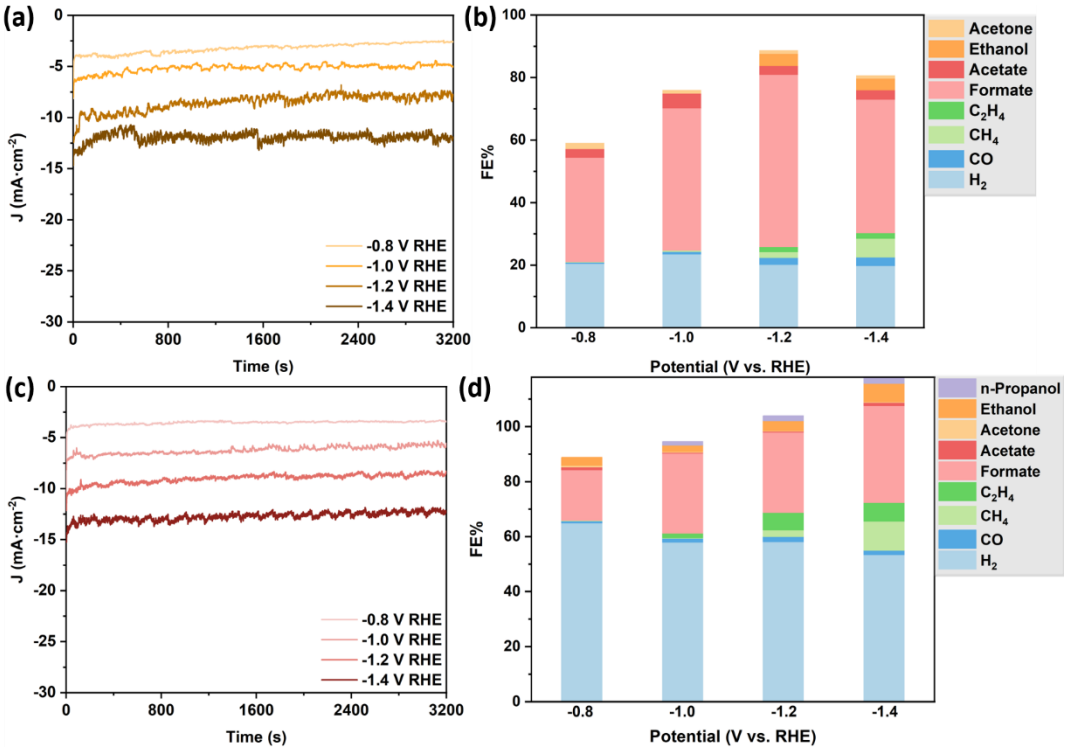

Figure 5.7: CO_2RR on MTS-Cu foil electrodes: (a) Chronoamperometric experiments on 0.004-MTS-Cu foil electrode in 0.1 M $KHCO_3$ saturated by CO_2. (b) Faradic efficiencies of gas and liquid products on 0.004-MTS-Cu foil electrode at different applied potentials from CO_2RR. (c) Chronoamperometric experiments on 0.1-MTS-Cu foil electrode in 0.1 M $KHCO_3$ saturated by CO_2. (d) Faradic efficiencies of gas and liquid products on 0.1-MTS-Cu foil electrode at different applied potentials from CO_2RR.

Table 5.2: Faradic efficiency of gas and liquid products on 0.004-MTS-Cu foil electrode in 0.1 M $KHCO_3$ saturated with CO_2.

Faradic efficiency (FE, %)

E (V RHE)	*CO*	*CH_4*	*C_2H_4*	*H_2*	*Formic acid (l)*	*Acetate (l)*	*Acetone (l)*	*Ethanol (l)*	*n-Propanol (l)*	*J ($mA \cdot cm^{-2}$)*	*Total*
-0.8	0.3	0.2	0	20.4	33.3	2.8	1.9	0	0	-3.21	**59.0**
-1.0	0.8	0.5	0	23.8	45.5	4.7	1.2	0	0	-5.15	**76.0**
-1.2	2.2	1.8	1.6	20.1	55.1	2.8	1.1	3.9	0	-8.51	**88.6**
-1.4	2.7	6.0	1.8	19.7	42.7	3.0	1.0	3.7	0	-11.92	**80.7**

Table 5.3: Faradic efficiency of gas and liquid products on 0.1-MTS-Cu foil electrode in 0.1 M $KHCO_3$ saturated with CO_2.

Faradic efficiency (FE, %)

E (V RHE)	*CO*	*CH_4*	*C_2H_4*	*H_2*	*Formic acid (l)*	*Acetate (l)*	*Acetone (l)*	*Ethanol (l)*	*n-Propanol (l)*	*J ($mA \cdot cm^{-2}$)*	*Total*
-0.8	0.8	0.2	0	65.0	18.4	1.0	0.5	3.0	0	-3.53	**88.8**
-1.0	1.4	0.3	1.6	57.9	29.1	0.3	0.3	2.3	1.3	-6.21	**94.5**
-1.2	1.9	2.4	6.4	58.1	29.1	0.4	0.2	3.5	1.9	-8.98	**103.9**
-1.4	1.6	10.6	6.7	53.4	35.3	1.1	0.3	6.6	2.5	-12.70	**118.2**

For the product distribution on both 0.004-MTS-Cu foil and 0.1-MTS-Cu foil electrodes, in Figure 5.7, Table 5.2 and 5.3, it shows that compared to the bare Cu foil electrode, 0.004-MTS-Cu foil electrode has a greater ability to convert CO_2 to formic acid, with $FE_{formic\ acid}$ up to 55.1% at -1.2 V vs.RHE. The formation of a large amount of formic acid may be due to the hydrophobic Cu foil surface provides more reaction sites for CO_2, which can promote the combination of CO_2 and H^+ coupled e^- to produce $*OOCH$ intermediate to form formic acid.[299,300] To confirm whether the produced formic acid is related to the decomposition of $KHCO_3$ electrolyte, the electrolysis under -0.8 V to -1.2 V vs.RHE were performed in N_2-saturated $KHCO_3$ solution. It is found that the partial current density ($J_{formic\ acid}$) in N_2-saturated electrolyte is much lower than that in CO_2 saturated electrolyte (as shown in the Appendix 3 Figure A 3.1-Figure A 3.8 for details), and the $FE_{formic\ acid}$ in N_2-saturated $KHCO_3$ electrolyte under different potentials is about 0.6%-6%. The results show that only a very small amount of HCO_3^- derived carbon species were involved in the electrocatalytic reduction process. For 0.004-MTS-Cu foil electrode, HER was also slightly suppressed compared to Cu foil. Interestingly, when the reduction potential was more negative than -1.0 V vs.RHE, more C_{2+} products (especially a new product ethanol) could be obtained. When the surface of Cu foil was modified with a higher concentration of MTS layer (0.1-MTS-Cu foil electrode), $FE_{formic\ acid}$ decreased, but the C_{2+} products increased. When the potential was applied at -1.4 V vs.RHE, FE_{C2H4} reached 6.7% and $FE_{ethanol}$ reached 6.63%. n-propanol also appeared as a reduction product in the process of CO_2 electrocatalytic reduction. Interestingly the intensity of HER also increased significantly which is difficult to rationalise unless some hydrogen is derived from instability of the MTS coating or MTS 'activates' parts of the Cu surface for HER perhaps by removing surface impurities.

The $FE_{acetate}$ and $FE_{acetone}$ decreased significantly compared to Figure 5.5 Cu foil, because these electrodes were dried at 100 °C for 1 hour after being modified with silane coating, to reduce volatile components in the lacquer. CO_2RR experiments under the same conditions without any applied potential showed very weak NMR peak associated with acetate and acetone in the ^{1}H NMR spectrum. (The original NMR spectrum is shown in Appendix 3 Figure A 3.9)

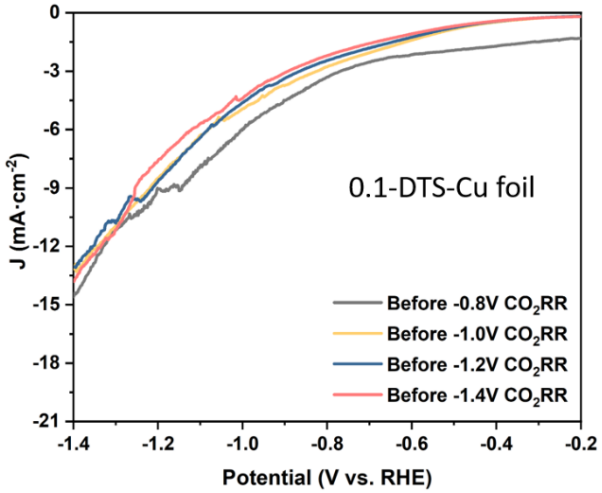

Figure 5.8: LSVs of 0.1-DTS-Cu foil electrode in 0.1 M $KHCO_3$ saturated by N_2 and CO_2 with a scan rate of 10 $mV \cdot s^{-1}$.

Based on the apparent effect of more C_2 products using 0.1 M concentration MTS on Cu other silane modified Cu foil electrodes were investigated for CO_2RR. For 0.1-DTS-Cu foil electrode, from the LSV measurements in Figure 5.8, we can see that the maximum current responses of the electrode are still stable in the range of -13 $mA \cdot cm^{-2}$ to -15 $mA \cdot cm^{-2}$, without significant change. In addition, the reduction peak at about -0.3 V (vs.RHE) is not observed due to the presence of a large amount of Cu^{2+} on the 0.1-DTS-Cu foil electrode surface instead of Cu^{+}. (In Chapter 4, it has been confirmed via the XPS characterization results.)

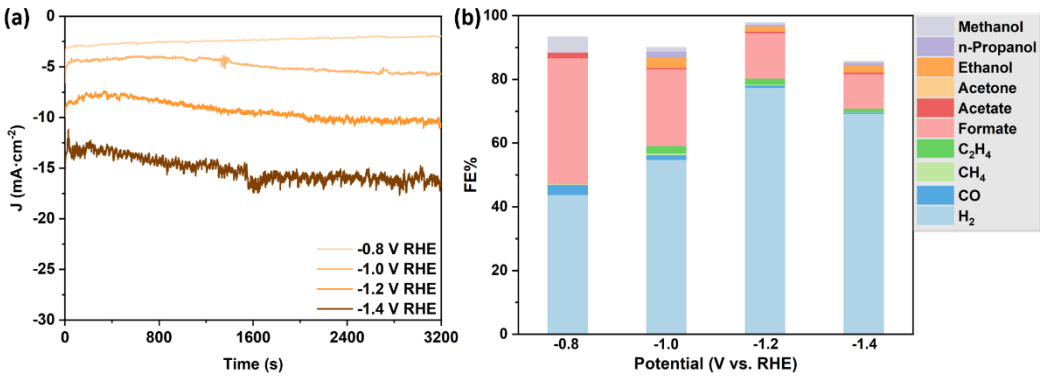

Figure 5.9: CO_2RR on 0.1-DTS-Cu foil electrode: (a) Chronoamperometric experiments in 0.1 M $KHCO_3$ saturated by CO_2. (b) Faradic efficiencies of gas and liquid products at different applied potentials from CO_2RR.

Table 5.4: Faradic efficiency of gas and liquid products on 0.1-DTS-Cu foil electrode in 0.1 M $KHCO_3$ saturated with CO_2.

	Faradic efficiency (FE, %)											
E (V RHE)	*CO*	*CH_4*	*C_2H_4*	*H_2*	*Formic acid (l)*	*Acetate (l)*	*Acetone (l)*	*Ethanol (l)*	*n-Propanol (l)*	*Methanol (l)*	*J ($mA \cdot cm^{-2}$)*	*Total*
-0.8	3.1	0.3	0	43.8	39.5	1.8	0	0	0	4.8	-2.36	**93.3**
-1.0	1.4	0.6	2.3	54.8	24.1	0.4	0	3.3	1.9	1.2	-4.87	**90.0**
-1.2	0.7	0.3	1.9	77.5	14.2	0.4	0	1.7	0.5	0.6	-9.36	**97.8**
-1.4	0.3	0.1	1.1	69.3	10.9	0.5	0	2.1	0.9	0.4	-15.20	**85.6**

As can be seen from the product distribution of CO_2RR on 0.1-DTS-Cu foil electrode (in Figure 5.9 and Table 5.4), HER is the main reaction on Cu foil modified with high concentration of DTS (FE_{H2} can reach 77.5%). Secondly, the conversion rate of formic acid remained at a high level, in the potential range of -0.8 V to -1.4 V (vs.RHE), $FE_{formic\ acid}$ could be stable at 10.9% to 39.5%. Only a small amount of C_{2+} products could be detected, and the highest selectivity (FE_{C2+} is about 8%) of 0.1-DTS-Cu foil electrode to C_{2+} products can be obtained at -1.0 V (vs.RHE). Overall, the distribution of products and the corresponding conversion rates on 0.1-DTS-Cu foil electrode are similar to those on Cu foil, which may be caused by the degradation of the unstable DTS coating, so that most of the catalytic surface was still the pure Cu and it has the similar catalytic selectivity as Cu.

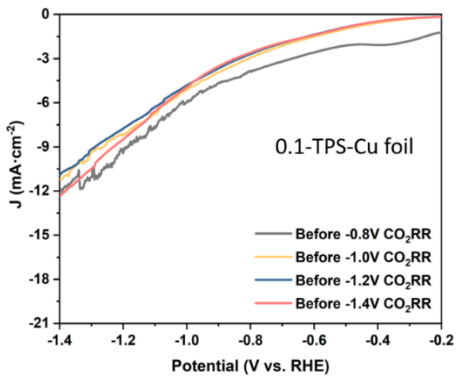

Figure 5.10: LSVs of 0.1-TPS-Cu foil electrode in 0.1 M $KHCO_3$ saturated by N_2 and CO_2 with a scan rate of 10 $mV \cdot s^{-1}$.

For 0.1-TPS-Cu foil electrode in Figure 5.10, there is little difference among the maximum current responses from LSVs before CO_2RR reaction at different potentials, indicating that the electrode surface state did not change significantly throughout CO_2RR testing. Moreover, the hydrophobic layer on the electrode surface did not cause a sharp change in the number of active sites. The maximum current responses on the 0.1-TPS-Cu foil electrode are slightly lower than those on 0.1-MTS-Cu foil electrode and 0.1-DTS-Cu foil electrode, probably due to the smaller ECSA. (Chapter 4 Figure 4.9.)

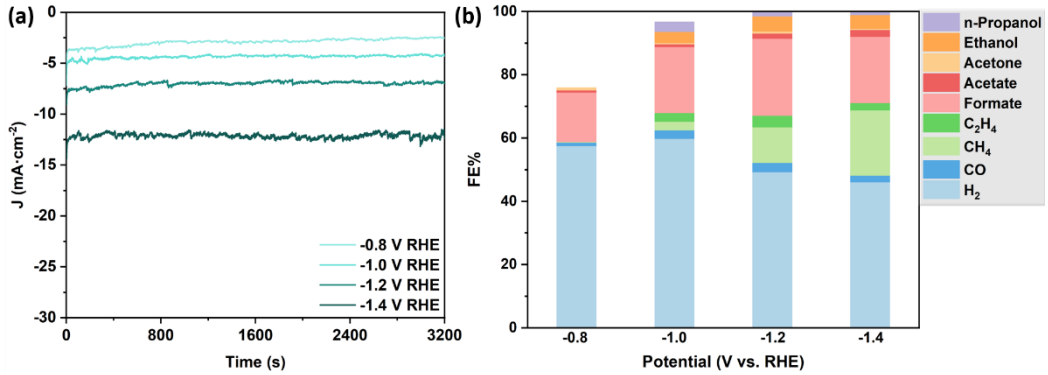

Figure 5.11: CO_2RR on 0.1-TPS-Cu foil electrode: (a) Chronoamperometric experiments in 0.1 M $KHCO_3$ saturated by CO_2. (b) Faradic efficiencies of gas and liquid products at different applied potentials from CO_2RR.

Table 5.5: Faradic efficiency of gas and liquid products on 0.1-TPS-Cu foil electrode in 0.1 M $KHCO_3$ saturated with CO_2.

Faradic efficiency (FE, %)

E (V RHE)	*CO*	*CH_4*	*C_2H_4*	*H_2*	*Formic acid (l)*	*Acetate (l)*	*Acetone (l)*	*Ethanol (l)*	*n-Propanol (l)*	*J ($mA·cm^{-2}$)*	*Total*
-0.8	1.1	0.2	0	57.5	15.6	0.7	0.7	0	0	-2.9	**75.8**
-1.0	2.7	2.7	2.8	59.8	20.8	0.9	0.5	3.5	3.1	-4.4	**96.7**
-1.2	3.0	11.2	3.7	49.2	24.3	1.7	0.6	4.9	2.6	-7.0	**101.1**
-1.4	2.1	20.6	2.3	46.1	20.9	2.3	0.3	4.5	2.2	-12.1	**101.1**

Through analysis of obtained products (in Figure 5.11 and Table 5.5), the H_2 production rate on 0.1-TPS-Cu foil electrode was slightly lower than that on 0.1-DTS-Cu foil electrode. Like the results obtained on 0.1-MTS-Cu foil electrode, the electrode showed higher selectivity for C_{2+} products in the range of -1.0 V to -1.4 V (vs.RHE), with the FE_{C2+} of 10.7%, 13.4%, and 11.4% as the potential increased. A higher FE_{C2+} is derived from the C-C coupling on the electrode surface. When C-C coupling is promoted, it will facilitate the formation of $*COCO$ intermediates and weaken the coverage of $*H$ on the electrode surface. At the same time, the electrode also showed an excellent ability to reduce CO_2 to CH_4 (FE_{CH4} can reach 20.6%) at a higher potential. It also shows that the main reaction intermediate on the electrode surface is $*COH$, and more $*COH$ can be produced into CH_4 by combining with proton-coupled electron, rather than being dimerized to form $*COHCOH$ intermediate to produce more ethanol. It was again demonstrated that the stability of the silane coating on the Cu foil surface was not stable enough to provide a sustained hydrophobic environment to construct a stable three-phase interface to ensure sufficient CO_2 conversion to $*CO$ binding to the electrode surface and dimerization on the electrode surface.

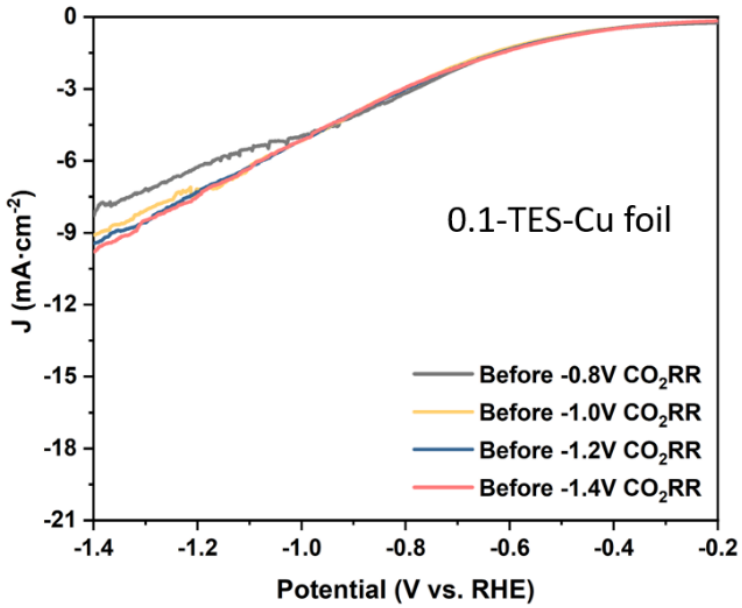

Figure 5.12: LSVs of 0.1-TES-Cu foil electrode in 0.1 M $KHCO_3$ saturated by N_2 and CO_2 with a scan rate of 10 $mV \cdot s^{-1}$.

Finally, on 0.1-TES-Cu foil electrode (in Figure 5.12), the maximum current responses in LSV measurements hardly changes significantly, which has the same

trend as the above electrodes. However, the maximum current responses were slightly lower, which may also be due to the limited ECSA. (Chapter 4 Figure 4.9.) Overall, there was no negative effect on the diffusion of CO_2 to the electrode surface to participate in the reaction.

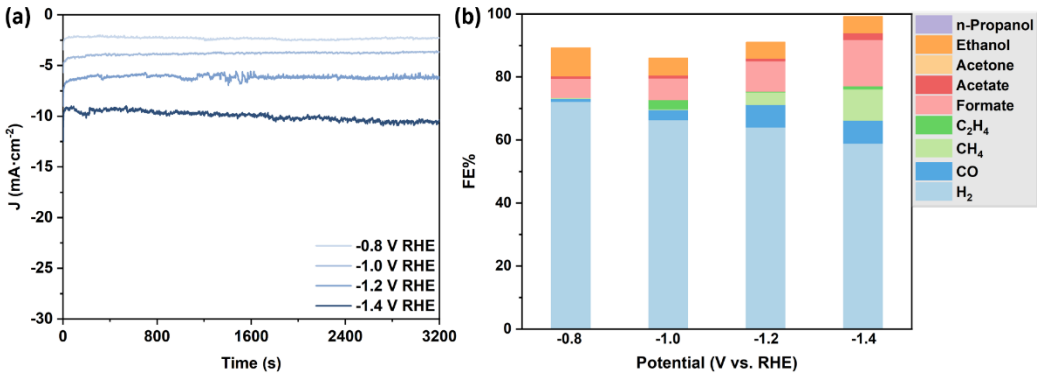

Figure 5.13: CO_2RR on 0.1-TES-Cu foil electrode: (a) Chronoamperometric experiments in 0.1 M $KHCO_3$ saturated by CO_2. (b) Faradic efficiencies of gas and liquid products at different applied potentials from CO_2RR.

Table 5.6: Faradic efficiency of gas and liquid products on 0.1-TES-Cu foil electrode in 0.1 M $KHCO_3$ saturated with CO_2.

	Faradic efficiency (FE, %)										
E (V RHE)	*CO*	*CH_4*	*C_2H_4*	*H_2*	*Formic acid (l)*	*Acetate (l)*	*Acetone (l)*	*Ethanol (l)*	*n-Propanol (l)*	*J ($mA·cm^{-2}$)*	*Total*
-0.8	1.0	0.3	0	72.1	6.0	0.8	0	9.0	0	-2.3	**89.3**
-1.0	3.2	0.2	2.9	66.3	6.9	1.0	0	5.5	0	-3.8	**86.0**
-1.2	7.2	3.9	0.2	64.0	9.7	0.9	0	5.1	0	-6.2	**91.0**
-1.4	7.3	9.9	1.0	58.9	14.7	2.2	0	5.3	0	-10.0	**99.2**

Through the different FE of products obtained on the 0.1-TES-Cu foil electrode (as shown in Figure 5.13 and Table 5.6), HER again increased as the dominant reaction, and the conversion rate of formic acid decreased somewhat (the highest $FE_{formic\ acid}$ is only 14.7% at -1.4 V (vs.RHE)), but the FE_{CO} increased significantly. It shows that the $*CO$ intermediates present on the electrode surface are more reduced to CO. For C_{2+} products, 0.1-TES-Cu foil electrode only ethanol ($FE_{ethanol}$ maintained at 9%-5%) was detected. This may be because ethanol and C_2H_4 share the same intermediate ($*CHCOH$), and the reaction intermediate ($*CHCHOH$) to generate ethanol has a higher concentration than the reaction intermediate to generate C_2H_4 ($*CCH$). The intermediate $*CCH$ is formed by elimination of water, which is less favoured when the Cu surface has a relatively low coordination surface and oxidation state promoting ethanol production.[301,302]

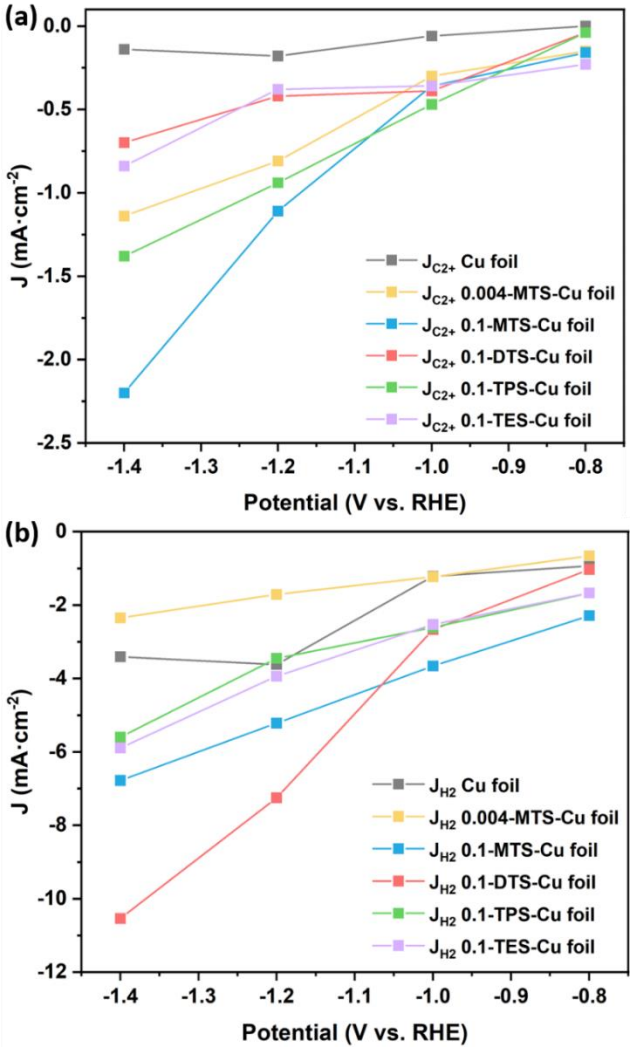

Figure 5.14: Partial current density in CO_2RR toward (a) C_{2+} products (J_{C2+}) and (b) H_2 (J_{H2}) on 0.004-MTS-Cu foil electrode, 0.1-MTS-Cu foil electrode, 0.1-DTS-Cu foil electrode, 0.1-TPS-Cu foil electrode and 0.1-TES-Cu foil electrode in 0.1 M $KHCO_3$ saturated by CO_2.

As can be seen from the partial current density (J_{C2+}) of C_{2+} products in Figure 5.14, the silane modified Cu foil electrodes have a better ability to produce C_{2+} products than the unmodified Cu foil electrode, in which 0.1-MTS-Cu foil electrode has the best performance in producing C_{2+}. This may be due to the introduction of silane molecule, which increases the concentration of CO_2 at the three-phase interface on the catalyst surface and promote CO_2 combined with the proton coupled electron to produce $*CO$, enriched $*CO$ can further dimerize to form the intermediates for the formation of C_{2+} products. However, there is still a large amount of hydrogen evolution in the CO_2RR process. It can be seen from the partial current density of H_2 (J_{H2}) that the introduction of high concentration silane not only enhances the binding of the active sites to the reaction intermediates, but also enhances the binding of $*H$, resulting in more H_2 formation, which can be seen most obviously on the 0.1-DTS-Cu foil electrode. In contrast, HER is slower when the Cu foil surface is modified with a low concentration of silane (0.004-MTS-Cu foil electrode).

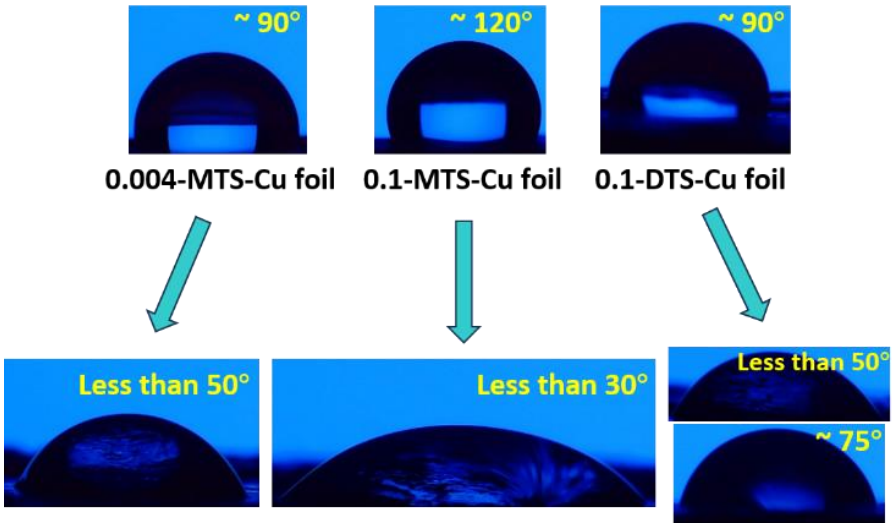

Figure 5.15: The contact angle measurements of 0.004-MTS-Cu foil, 0.1-MTS-Cu foil and 0.1-DTS-Cu foil electrodes: before and after CO_2RR.

To further determine the stability of the silane coating on the surface of Cu foil during CO_2RR, the contact angle measurements were performed on the electrode surfaces before and after the reactions. As shown in Figure 5.15, the contact angles of 0.004-MTS-Cu foil, 0.1-MTS-Cu foil, and 0.1-DTS-Cu foil electrodes before CO_2RR are about 90°, 120° and 90°, respectively. After CO_2RR, for 0.004-MTS-Cu foil electrode, the obtained contact angles are generally less than 50°, while the contact angles of the 0.1-MTS-Cu foil electrode are below 30°. For 0.1-DTS-Cu foil electrodes,

most of the area contact angles on the surface are below 50°, and some contact angles obtained near the edge of the window area used for CO_2RR that can be maintained around 75°. For 0.1-TPS-Cu foil and 0.1-TES-Cu foil electrodes, the contact angles before the reaction are consistent with those reported in chapter 4 (about 80° and 50°, in chapter 4 Table 4.2), but it is difficult to measure the contact angles again on the surface after CO_2RR. The surface is no longer hydrophobic. In addition, the contact angle measurements on 0.1-MTS-Cu foil electrodes after a single CO_2RR (only running a reaction at -0.8 V (vs.RHE)) is similar to after the continuous CO_2RR. Therefore, the initial product of silane modification undergoes a rapid change on CO_2RR to give a new more stable surface that retains lower hydrophobicity leading to the changes in product distribution compared to bare Cu foil. The product distribution appears to be dependent on the silane coating. An estimate of the amount of silane present on the Cu surface after reaction is 5×10^{14} (0.8 nmol) based on 1 cm^{-2} surface area and close packing of five silane molecules nm^{-2} which is likely to be much less given the ESCA, and XPS data which show significant surface Cu is present. At each potential CPE CO_2RR occurred over 3200 s. A current density of 1 $mA \cdot cm^{-2}$ gives 3.2 C (33 μmol) of electrons. Therefore, over four potentials and with greater partial current densities the silane coating is very unlikely to be the origin of the products observed. However, only a $^{13}CO_2$ could definitively confirm the origin of the carbon-based products.

5.1.3. Electrochemical CO_2 reduction reaction on CuNW-AAO electrodes

Determining the effect of silane coating on Cu was in part examined to understand if silane coating of CuNW-AAO electrodes would affect either or both the hydrophobicity of the electrochemically inert AAO and Cu electrode. Section 5.1.2 showed that silane does modify Cu foil electrode, which would complicate interpretation of CuNW-AAO data as both CuNW and AAO will be modified perhaps to variable extents. The mass transfer at the three-phase interface will also be more complicated. It is not only necessary to consider the effect of silane coating on the catalytic performance of Cu, the silane layer covering the AAO template changes the microenvironment near the catalyst surface, but also has an impact on the mass transfer in the three-phase interface. We should also consider the accurate evaluation of the CO_2 reduction performance of CuNW-AOO under the synergistic effect of the Cu catalyst and the microenvironment. Therefore, we performed CO_2RR on unmodified CuNW-AAO, 0.1-MTS-CuNW-AAO, 0.1-DTS-CuNW-AAO, 0.1-TPS-CuNW-AAO, and 0.1-TES-CuNW-AAO electrodes, respectively. All CuNW-AAO

electrodes used in this chapter were obtained by two-step deposition (the first step deposition was under -10 $mA \cdot cm^{-2}$ for 60 min, the second step deposition was under -50 $mA \cdot cm^{-2}$ for 180 min.).

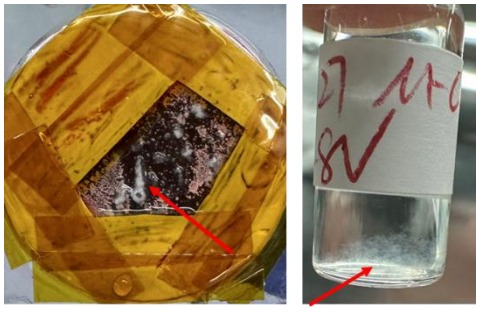

Figure 5.16: The photo of broken CuNW-AAO electrode with the white flocculent substances on surface and in catholyte after CO_2RR.

Initially, we found that when CO_2RR experiments were performed on unmodified CuNW-AAO and 0.1-MTS-CuNW-AAO electrodes, common reduction products such as CO, CH_4 and formic acid could not be detected, accompanied by a very large amount of H_2 generation (far exceeding the total CO_2RR reaction efficiency). After running the reaction, some white flocculent substances appeared on the electrode surface and in the collected cathode electrolyte as the photos shown in Figure 5.16. In severe cases, the electrode surface was craked and pitted. Because the current density for CO_2RR is generally high, CO_2RR is usually accompanied by HER and significant bubbling. The gold layer under the AAO template used to grow the CuNW appeared to separate from the Al disc which is glued using Ag paint. Either hydrogen begins to accumulate in this layer or electrolyte penetrates the electrode. Either could lead to H_2 pressure behind the gold/AAO/CuNW electrode causing lifting and cracking and exposure of the Al disc to electrolyte followed by more rapid H_2 production. Optimization of the sample preparation method was required to prevent H_2 accumulation, and some specific measures are listed in Table 5.7:

Table 5.7: CuNW-AAO electrode samples preparation via different methods and the performance in CO_2RR.

Sample	***Connection layer process***	***Electrode performance in CO_2RR***
S1 CuNW-AAO (Ag painting, on Al disc)	*S1-a)* Manual press of Au evaporated AAO template onto Ag paint coated Al disc. *S1-b)* Weighted press of Au evaporated AAO template to reduce voids between the Al disc coated with Ag paint.	*S1-a)* White flocculent appeared and a large amount of HER occurred, the electrode surface was slightly damaged. (CO_2RR products cannot be detected.) *S1-b)* White flocculent appeared and a large amount of HER occurred, the electrode surface was slightly damaged. (CO_2RR products cannot be detected.)
S2 CuNW-AAO (Ag epoxy, on Al disc)	*S2-a)* Manual press of Au evaporated AAO template onto Ag epoxy coated Al disc. *S2-b)* Weighted press of Au evaporated AAO to reduce voids between the Al disc coated with Ag epoxy.	*S2-a)* White flocculent appeared but slightly reduced and a large amount of HER occurred. (CO_2RR products cannot be detected.) *S2-b)* The adhesive ingredient in epoxy blocked a large area of the template channels preventing CuNW electrodeposition.
S3 CuNW-AAO (Ag epoxy, on Cu disc)	Manual press Au evaporated AAO template onto the Ag epoxy coated Cu disc.	White flocculent did not appear but a large amount of HER occurred. (CO_2RR products cannot be detected.)
S4 CuNW-AAO (on Cu disc)	Au evaporated AAO template was taped onto a Cu disc directly without conductive adhesive. CuNW electrodeposition did not occur normally.	-
S5 CuNW-AAO (Ag epoxy, on Cu disc, extend CuNW deposition time)	Manual press of Au evaporated AAO template onto Ag epoxy coated Cu disc. The duration of Cu electrodeposition was prolonged.	White flocculent did not appear, there was still a large amount of HER occurrence (compared with HER of S1-S3, it showed a significant decrease trend, but still exceeded 100%.). (CO_2RR products could not be detected.)

In general, the CuNW-AAO electrode was obtained by method of S1-a) shown in Table 5.7, but it was found that the electrode was easily damaged by generated H_2 attack between the template and Al disc substrate in CO_2RR, and common products of CO_2RR could not be detected because HER and electrode corrosion dominated giving a white flocculant assumed to be Al_2O_3. Other methods described in Table 5.7 aimed to exclude voids behind the Au coating to prevent H_2 building up sufficient pressure to cause the electrode to fracture. In contrast to Ag paint, Ag epoxy could fill voids but the pressure applied to the gold/AAO template unfortunately led to blocking of a large area of the template channels and prevented CuNW electrodeposition. Then, to eliminate any Al electrochemistry which may also have been leading to H_2 production Cu foil was fixed on the Al disc under the Cu disc substrate, and whilst the white flocculent no longer appeared, there was still a large amount of HER that caused damage to the surface of the CuNW-AAO electrode and carbon-based products were not detected. It was also attempted to physically fix gold/AAO on a Cu disc, owever, CuNW electrodeposition failed due to overload potential during electrodeposition. An attempt was also made to fill the AAO channels, from -10 $mA \cdot cm^{-2}$ for 60 min, and -50 $mA \cdot cm^{-2}$ for 180 min to -10 $mA \cdot cm^{-2}$ for 90 min, and -50 $mA \cdot cm^{-2}$ for 240 min. CO_2RR again gave a significant amount of HER but a significant decrease compared to S1-S3 results, but still more than 100%), and carbon products were still not detected.

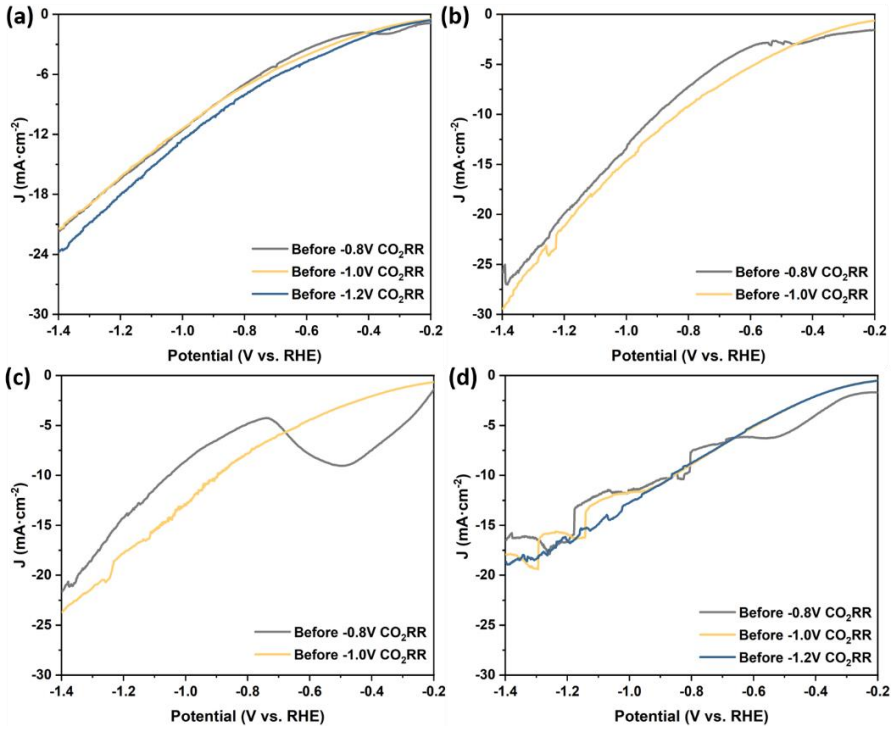

Figure 5.17: LSVs of the CuNW-AAO electrodes in 0.1 M $KHCO_3$ saturated by CO_2 with a scan rate of 10 $mV \cdot s^{-1}$: (a) LSVs of S1-a. (b) LSVs of S2-a. (c) LSVs of S3. (d) LSVs of S5.

In Figure 5.17, LSV measurements obtained on S1-a, S2-a, S3 and S5 show that the CuNW-AAO electrodes have a larger current response than the Cu foil electrodes, which is attributed to the introduction of the NW structure allowing the catalyst to have a larger catalytic active surface area. The initial LSV curves in (a)-(d) show a significant reduction peak of Cu^+ appearing at about -0.4 V (vs.RHE), which is due to the presence of large amounts of Cu_2O on the CuNW surface (see XPS characterization in Chapter 4). If CuNW-AAO electrode has catalytic activity on CO_2RR, the large amount of H_2 produced inside the electrode, leads to electrode damaged, and it is not possible to determine the reduction products. In addition, (c) and (d) are CuNW-AAO electrodes based on the Cu disc, which show stronger Cu^+ reduction peaks, and prove that Cu disc is also involved in the electrocatalytic process, which is caused by the penetration of the electrolyte into the electrode. (The XPS characterization results in Chapter 4 confirmed that a large amount of Cu_2O also exists on the surface of Cu foil.)

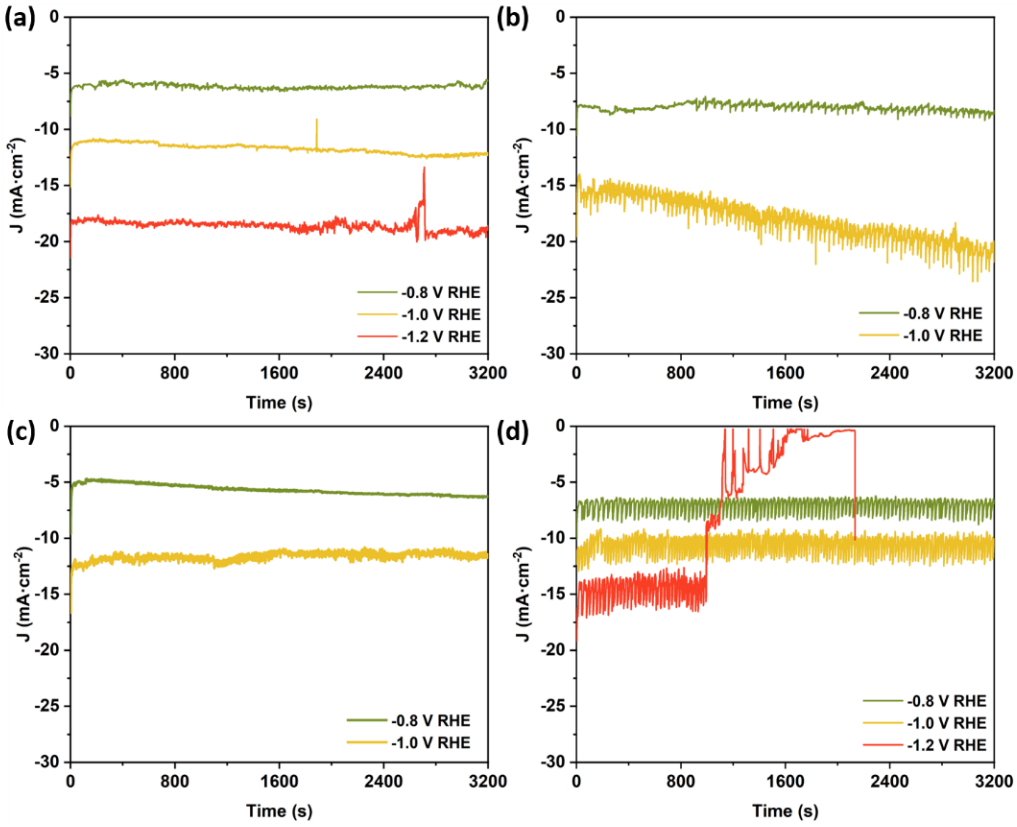

Figure 5.18: The chronoamperometric experiments in 0.1 M $KHCO_3$ saturated by CO_2: (a) on S1-a. (b) on S2-a. (c) on S3. (d) on S5.

In Figure 5.18, it can be seen from the CO_2RR process on S1-a, S2-a, S3 and S5 that all CuNW-AAO electrodes have high current densities at different reduction potentials. Theoretically, under such high current densities, some reduction products such as CO, CH_4, formic acid even C_2H_4 and ethanol should be detected. However, in fact, it is difficult to accurately detect the above products, that is, most of the current was used to drive HER, masking any CO_2RR catalytic activity. In addition, we also attempted to perform CO_2RR experiments on silane modified CuNW-AAO electrodes, and the results were like those of unmodified CuNW-AAO electrodes, with no successful detection of gaseous and liquid reduction products due to rapid electrode damage induced by H_2 mechanical stress.

5.2. Conclusions

In this chapter, a series of CO_2RR experiments at different reduction potentials on Cu foil electrodes modified with different kinds and concentrations of silane molecules, were evaluated. The influence of Cu surface microenvironment on the stability of the three-phase interface, mass transfer process and catalytic performance of the electrode was studied. The introduction of silane did not cause blockage or loss of the reactive active sites on Cu foil. Moreover, due to the introduction of silane molecules, the CO_2 concentration in the three-phase interface may increase, which is conducive to the dimerization of $*CO$ intermediates to form the following intermediate used to produce C_{2+} products. Therefore, the silane modified Cu foil electrodes have stronger catalytic activity than the unmodified Cu foil electrode to convert CO_2 into C_{2+} products. Especially on the 0.1-MTS-Cu foil electrode, the maximum FE_{C2+} can reach 17.31%. At the same time, we also found that the introduction of silane with high concentrations not only enhanced the binding of the active sites to the reaction intermediates, but also enhanced the effect of binding $*H$, resulting in more H_2 formation. When the surface of Cu foil was modified with low concentration silane, HER will be weakened to a certain extent. When further understand the synergistic effect of silane on the regulation of microenvironment on CuNW catalyst and AAO template, the catalytic performance of CuNW-AAO electrode cannot be evaluated due mechanical instability of the electrode due either to hydrogen pressure or electrolyte penetration leading to hydrogen pressure. However, there is a large amount of HER occurring inside the electrode demonstrating reactivity, indicating that if mechanical stability can be improved the CO_2RR could occur.

6. Conclusions and future work

This project aimed to construct and investigate new Cu-based electrocatalysts based on CuNW embedded in a hydrophobic anodized aluminium oxide membrane for the CO_2 reduction reaction. Uniformly distributed CuNWs were successfully prepared in AAO porous templates by a square-wave pulsed electrodeposition method. The length and diameter distribution of CuNW can be controlled by adjusting deposition time and current density. The electrochemical behaviour analysis of the CuNW-AAO electrode confirms that the electrode has large ECSA and R_f, reflective of electrolyte penetration throughout the AAO and electrochemistry occurring along the length of the CuNWs. Different silane molecules were used to modify the surface of the electrodes, which successfully increased the hydrophobicity of the electrode surface. This was envisaged to help construct the three-phase interface of CO_2RR and improve the CO_2 gas capture at the electrode, whilst reducing HER. The electrochemical behaviour analysis of the hydrophobic electrode shows that the silane modified CuNW-AAO electrode can still maintain a large ECSA and R_f, and the silane coating can improve the hydrophobicity of the electrode without losing the active surface area and active sites of the electrode. Control experiments showed that silane modification occurs for both AAO and Cu surfaces. The hydrolysis of the silane coating on Cu appears to etch the CuNWs to a certain extent, which increased the surface roughness of CuNWs. Silane modified Cu surfaces appear to promote the catalytic activity for the conversion of CO_2 to C_{2+} products. This local microenvironmental control strategy enables the activity of protons to be reduced (and HER) on the electrode surface during the CO_2RR process and facilitates C-C coupling to form more desired C_{2+} products, likely via dimerization of $*CO$ intermediates to form the intermediates for the C_{2+} products. Unfortunately, although silane modified CuNW-AAO electrodes are electrochemically active for reversible MV oxidation-reduction cycles under CO_2RR evolution of hydrogen bubbles in water leads to mechanical instability and electrode destruction.

The following summarizes the remaining challenges in the project and further improvements that can be made in the future:

6.1. Optimization of method and parameters for pulsed electrodeposited CuNW

Currently, the morphology and size of the CuNW can be adjusted by changing the electrochemical parameters during the electrodeposition process. The length

distribution of the obtained CuNW is generally 10-30 μm, and the diameter distribution between 180-300 nm. The diameter of CuNW can be further controlled by applying different current densities in a two-step electrodeposition process. The ECSA and R_f of electrodeposited CuNW can reach 2.4 and 2.8 times than that of planar Cu foil electrodes by electrochemical characterization. According to the mass transfer mechanism of MV redox probe on the surface of CuNW-AAO electrode, it has been found that the mass transfer on CuNW-AAO electrode has a thin layer electrochemical characteristic of semi-infinite diffusion due to the existence of nanostructure and AAO template. When NaOH treatment is used to remove part of the AAO template on the CuNW-AAO electrode, increased CuNW exposure can be achieved, resulting in the electrode having a larger electrochemical surface area, roughness, and a smaller charge transfer resistance.

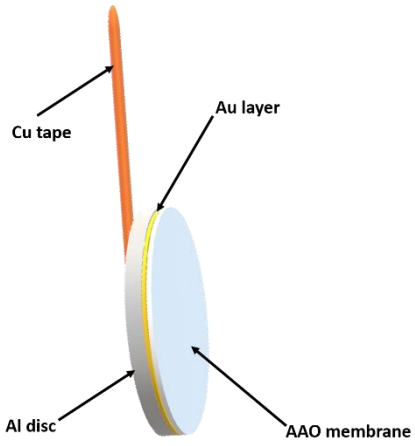

Figure 6.1: The configuration of AAO membrane on Al disc used for CuNW electrodeposition.

Electrodeposition occurs on an Al disc adapted to fit into the CO_2RR flow cell Figure 6.1). In future work, the Al substrate can be replaced either with a Cu disc or other material with good conductivity that is less prone to corrosion under CO_2RR electrolysis that may be contributing to the excessive hydrogen production and mechanical instability.

Although the CuNWs in this project already have larger ECSA and R_f, compared with some reported Cu nano-catalysts with three-dimensional structures, such as Cu foam, Cu dendrites, etc.,[303–305] the ECSA of CuNW still has room for improvement. In future work, the Cu mass loading per unit area of the electrode surface can be further increased by fine control of the electrodeposition current

density and deposition time, to modify morphology and enhance the overall ECSA and R_f of the whole electrode perhaps through alternating low and high current density deposition pulses.

6.2. Stability improvement of CuNW-AAO electrode for CO_2RR

In the project, a series of CO_2RR experiments were carried out on bare Cu-based electrodes with silane modified local microenvironment on surface, and it has been found that the improvement of hydrophobicity of the electrode surface is conducive to the increase of CO_2 concentration at the three-phase interface near the electrode surface in CO_2RR, which could promote the dimerization of $^*CO$ intermediates and form more C_{2+} products. Especially on the 0.1-MTS-Cu foil electrode, FE_{C2+} can reach a maximum of 17.31%. Silane modification of other high surface area Cu catalysts such as foams could be investigated.

The catalytic performance of the CuNW-AAO electrode cannot be evaluated due to mechanical instability of the electrode caused by hydrogen pressure or electrolyte penetration. Therefore, the stability of the CuNW-AAO electrode for CO_2RR is still the main problem that needs to be solved in future work. Alternative conductive binders with low inherent porosity to bind the gold-AAO template directly to a substrate could minimize volume where H_2 could accumulate. At the same time, it is possible to continue to try more hydrophobic coatings with better stability in the electrolyte to improve the stability of the whole CuNW-AAO electrode in CO_2RR.

Additional surface characterisation of the silane coating after initial CO_2RR would be useful to understand the speciation and distribution of the silicon species which leads to greater C_{2+} products and could be achieved using high resolution XPS and SEM-EDS. This could help identify future strategies to increase stability and the proportion of C_{2+} products.

6.3. CO_2RR reactor improvement

Developing and improving reactors is also a key factor in improving the mass transfer and CO_2 conversion. In general, the cell size, structural design and membrane material, as well as experimental parameters, can affect the current density, selectivity and stability in CO_2RR. In this project, some characteristics of traditional H-cell and GDE designs were used for the cathode and anode chambers. In the cathode and anode chambers, liquid in/out ports connected with an external

peristaltic pump for circulating the catholyte and anolyte were added, to aid mass transfer effects in the CO_2RR process and maintain constant bulk pH. At the same time, the CO_2 gas in port was positioned at the bottom of the chamber, and a small plastic tube used to transport CO_2 gas directly onto the working electrode surface to enhance the concentration of CO_2 near the electrode surface. In the process of running CO_2RR through the reactor, there are still some noteworthy issues that should be considered to improve the reactor design. For example, the tip of plastic tube used to transport CO_2 gas should be kept at a reasonable distance from the gas product outlet of the cell, otherwise the electrolyte is very easily pushed into the outlet and down the line into the GC, damaging the column. Second, when designing the slots for fixing electrodes in the cell, the design could be simplified to reduce the size of the Al disc necessary for CuNW deposition. The primary aim of this project was to modify CO_2RR selectivity, but it is also clear that practical current densities cannot be achieved with an H-cell and that only polymer electrolyte membrane or GDE cells can give currents approaching the industrially desired minimum of -1 $A \cdot cm^{-2}$. Ideally the CuNW-AAO assembly could be prepared and supported on a carbon mesh electrode so that CO_2-H_2O mixtures could be fed through the rear of the assembly to maximise mass transport and current without ‘back pressure buildup. However, this would present significant challenges to bind an AAO membrane to carbon and grow Cu NW with predictable morphology.

Appendix-1

Table A 1.1: Possible half-reactions of electrochemical reduction of CO_2.

Product	Electrochemical reduction half-reactions	E^0 (V vs. RHE) (0.1 M $KHCO_3$ pH = 7)	No. of (e^-)	Standards NMR data		
				Chemical shift (^1H)	Nucleus	J coupling (Hz)
Bicarbonate	Electrolyte	-	-	-	$KHCO_3$	-
DMSO	Internal standard	-	-	2.6	$(CH_3)_3SO$	s
Hydrogen	$2H^+ + 2e^- \rightleftharpoons H_2$	-0.414	2	-	-	-
Carbon monoxide	$CO_{2(g)} + 2H^+ + 2e^- \rightleftharpoons CO_{(g)} + H_2O$	-0.51	2	-	-	-
	$CO_{2(g)} + 2H_2O_{(l)} + 2e^- \rightleftharpoons CO_{(g)} + H_2O$					
Formic acid	$CO_{2(g)} + 2H^+ + 2e^- \rightleftharpoons HCOOH_{(l)}$	-0.61	2	8.33	HCOOH	s
	$CO_{2(g)} + 2H_2O_{(l)} + 2e^- \rightleftharpoons HCOO^-_{(aq)}$					
Oxalic acid	$2CO_{2(g)} + 2H^+ + 2e^- \rightleftharpoons (COOH)_{2(aq)}$	−0.87	2	8.20	$(COOH)_2$	s (br)
	$2CO_{2(g)} + 2e^- \rightleftharpoons (COO^-)_{2(aq)}$					
Formaldehyde	$CO_{2(g)} + 4H^+ + 4e^- \rightleftharpoons HCHO_{(l)} + H_2O_{(l)}$	-0.48	4	-	-	
	$CO_{2(g)} + 3H_2O_{(l)} + 4e^- \rightleftharpoons HCHO_{(l)} + 4OH^-$					
Acetic acid	$CO_{2(g)} + 4H^+ + 4e^- \rightleftharpoons CH_3COOH$	-0.26	4	2.08	CH_3COOH	s
Carbon	$CO_{2(g)} + 4H^+ + 4e^- \rightleftharpoons C_{(s)} + 2H_2O$	-	4	-	-	-
	$CO_{2(g)} + 2H_2O_{(l)} + 4e^- \rightleftharpoons C_{(s)} + 4OH^-$					

Methanol	$CO_{2(g)} + 6H^+ + 6e^- \rightleftharpoons CH_3OH_{(l)} + H_2O_{(l)}$ $CO_{2(g)} + 5H_2O_{(l)} + 6e^- \rightleftharpoons CH_3OH_{(l)} + 6OH^-$	-0.38	6	3.34	CH_3OH	s
Glyoxal	$CO_2 + 6H^+ + 6e^- \rightleftharpoons (HCO)_2 + 2H_2O$	-0.16	6	-	$(OH)_2CHCH(OH)_2$	s
Methane	$CO_{2(g)} + 8H^+ + 8e^- \rightleftharpoons CH_{4(g)} + 2H_2O$ $CO_{2(g)} + 6H_2O_{(l)} + 8e^- \rightleftharpoons CH_{4(g)} + 2H_2O$	-0.24	8	3.34	CH_3OH	-
Glycolaldehyde	$2CO_2 + 7H_2O + 8e^- \rightleftharpoons (OH)_2CHCH_2OH + 8OH^-$	-0.03	8	3.43 5.04	$(OH)_2CHCH_2OH$ $(OH)_2CHCH_2OH$	d, 5.15 t, 5.12
Acetate	$2CO_{2(g)} + 5H_2O_{(l)} + 8e^- \rightleftharpoons CH_3COO^-{}_{(l)} + 7OH^-$	-	8	1.79	CH_3COO^-	s
Acetaldehyde	$2CO_2 + 8H_2O + 10e^- \rightleftharpoons CH_3CH(OH)_2 + 10OH^-$	0.05	10	9.55 5.13 2.12 1.20	CH_3CHO $CH_3CH(OH)_2$ CH_3CHO $CH_3CH(OH)_2$	q, 2.93 q, 5.37 d, 2.93 d, 5.37
Ethylene glycol	$2CO_2 + 10e^- + 10H^+ \rightleftharpoons HOCH_2CH_2OH + 2H_2O$	0.20	10	3.55	$HOCH_2CH_2OH$	s
Ethylene	$2CO_{2(g)} + 12H^+ + 12e^- \rightleftharpoons C_2H_{4(g)} + 4H_2O_{(l)}$ $2CO_{2(g)} + 8H_2O_{(l)} + 12e^- \rightleftharpoons C_2H_{4(g)} + 12OH^-$	-0.34	12	-	-	-
Ethanol	$2CO_2 + 12H^+ + 12e^- \rightleftharpoons CH_3CH_2OH_{(l)} + 3H_2O_{(l)}$ $2CO_2 + 9H_2O_{(l)} + 12e^- \rightleftharpoons CH_3CH_2OH_{(l)} + 12OH^-$	−0.33	12	1.06 3.53	CH_3CH_2OH CH_3CH_2OH	t, 7.08 q, 7.32
Methylglyoxal	$3CO_2 + 12e^- + 12H^+ \rightleftharpoons C_3H_4O_2 + 4H_2O$	0.02	12	-	-	-
Ethane	$2CO_2 + 10H_2O + 14e^- \rightleftharpoons C_2H_6 + 14OH^-$	−0.27	14	-	-	-

Hydroxyacetone	**$2CO_2 + 14H^+ + 14e^- \rightleftharpoons CH_3C(=O)CH_2OH + 4H_2O$**	0.46	14	2.02 4.25	$CH_3C(=O)CH_2OH$ $CH_3C(=O)CH_2OH$	s
Acetone	**$CO_2 + 16H^+ + 16\ e^- \rightleftharpoons CH_3COCH_3$**	-0.14	16	2.1	CH_3COCH_3	s
Propionaldehyde	**$3CO_2 + 16e^- + 11H_2O \rightleftharpoons CH_3CH_2CHO + 16OH^-$**	0.14	16	9.57 4.85 2.44 1.47 0.92	CH_3CH_2CHO $CH_3CH_2CH(OH)_2$ CH_3CH_2CHO $CH_3CH_2CH(OH)_2$ CH_3CH_2CHO	s t, 5.87 q, 7.32 dt, 7.57 12.94 t, 7.32
Allyl alcohol	**$3CO_2 + 16e^- + 11H_2O \rightleftharpoons CH_2=CHCH_2OH + 16OH^-$**	0.11	16	5.17 5.9 3.99	$CH_2=CHCH_2OH$ $CH_2=CHCH_2OH$ $CH_2=CHCH_2OH$	d, 17.33 m dt, 5.13 1.46
n-Propanol	**$3CO_2 + 13H_2O + 18e^- \rightleftharpoons CH_3CH_2CH_2OH + 18OH^-$**	−0.32	18	0.77 1.42 3.44	$CH_3CH_2CH_2OH$ $CH_3CH_2CH_2OH$ $CH_3CH_2CH_2OH$	t, 7.57 sextet, 7.32 6.49
2,3 - Furandiol	**$4CO_2 + 14e^- + 14H^+ \rightleftharpoons C_4H_4O_3 + 5H_2O$**	0.01	14	6.145 7.030	-	-

The standard potential under standard conditions (SHE based values were at 1.0 atm and 25 ^oC and were calculated according to the standard Gibbs energies of the reactants in reactions).

Table A 1.2: Reported Copper based electrocatalysts with different morphologies for CO_2RR.

Electrocatalysts	**Preparation method**	**Potential (V vs RHE)**	**Current density J ($mA.cm^{-2}$)**	**Faradaic efficiencies of major products (FE%)**	**Electrolyte**	**Stability (h)**	**Ref.**
Cu foil							
Sigma-Aldrich Cu foil	Two-step (mechanical- and electro-) polishing	-0.79	-1.39	H_2 (61.0), formate (13.1)	0.1 M $KHCO_3$	N/A	306
		-0.89	-2.18	H_2 (51.0), formate (20.7)			
		-0.98	-2.86	H_2 (33.7), C_2H_4 (24.0)			
		-1.06	-5.12	H_2 (34.0), C_2H_4 (25.0)			
		-1.15	-6.58	H_2 (26.7), C_2H_4 (30.0)			
Goodfellow Cu foil	Two-step (mechanical- and electro-) polishing	-0.79	-1.52	H_2 (55.7), formate (13.8)	0.1 M $KHCO_3$	N/A	306
		-0.88	-2.40	H_2 (45.0), formate (15.8)			
		-0.98	-2.63	H_2 (43.7), formate (16.4)			
		-1.03	-7.23	H_2 (26.0), C_2H_4 (31.0)			
		-1.15	-6.77	H_2 (26.7), C_2H_4 (28.7)			
Alfa-Aesar Cu foil	Two-step (mechanical- and electro-) polishing	-0.79	-1.79	H_2 (58.3), formate (13.9)	0.1 M $KHCO_3$	N/A	306
		-0.88	-2.72	H_2 (47.7), formate (17.1)			
		-0.98	-2.30	H_2 (40.0), C_2H_4 (15.3)			
		-1.03	-5.38	H_2 (31.0), C_2H_4 (27.7)			

		-1.15	-5.66	H_2 (28.7), C_2H_4 (20.7)			
Eurofysica Cu foil	Two-step (mechanical- and electro-) polishing	-0.79 -0.88 -0.97 -1.06 -1.14	-1.88 -2.36 -3.18 -5.06 -7.06	H_2 (61.3), formate (7.9) H_2 (52.3), formate (10.4) H_2 (39.7), formate (15.2) H_2 (27.0), C_2H_4 (23.3) H_2 (30.7), C_2H_4 (30.7)	0.1 M $KHCO_3$	N/A	306
Mateck Cu foil	Two-step (mechanical- and electro-) polishing	-0.79 -0.89 -0.98 -1.03 -1.13	-1.15 -1.83 -2.84 -7.52 -7.93	H_2 (58.0), formate (16.0) H_2 (46.3), formate (21.6) H_2 (35.3), C_2H_4 (18.0) H_2 (28.3), C_2H_4 (27.0) H_2 (26.3), C_2H_4 (29.0)	0.1 M $KHCO_3$	N/A	306
Electropolished Cu	Electropolishing	-0.8 -0.9 -1.0 -1.1 -1.2 -1.3	-	H_2 (88.1), CH_4 (0.4) H_2 (88.8), CH_4 (0.1) H_2 (69.7), CH_4 (1.5) H_2 (68.7), CH_4 (10.8) H_2 (63.4), CH_4 (17.9) H_2 (68.2), CH_4 (18.6)	0.1 M $KHCO_3$	N/A	307
Cu foil	mechanical- and electro- polishing	-0.67 -0.75	-	H_2 (76.2), CO (18.4) H_2 (61.8), formate (19.2)	0.1 M $KHCO_3$	N/A	156

		-0.82 -0.89 -0.96 -1.01 -1.05 -1.09 -1.14 -1.17		H_2 (43.8), formate (22.7) H_2 (37.7), formate (24.6) H_2 (30.2), formate (17.4) H_2 (25.4), C_2H_4 (17.9) H_2 (22.6), C_2H_4 (26.0) H_2 (22.2), CH_4 (29.6) H_2 (32.5), CH_4 (39.9) H_2 (55.7), CH_4 (40.4)			
Cu wafer coupon	-	-0.60	~ -0.9	H_2 (16.0), CO (45.0)	0.5 M $NaHCO_3$	N/A	[308]
O_2 plasma-Cu foil	Electropolishing Cu foil then plasma etch	-0.90	-	C_2H_4 (60.0), H_2 (35.0)	0.1 M $KHCO_3$	N/A	[309]
Cu nanowire (CuNW)							
2.0 µm-Cu nanowire arrays 2.4 µm-Cu nanowire arrays 5.0 µm-Cu nanowire arrays 7.3 µm-Cu nanowire arrays	two-step synthesis of $Cu(OH)_2$ and CuO nanowire then electrochemical reduction to Cu nanowire arrays	-1.10	~ -2.8 ~ -3.0 ~ -3.9 ~ -3.9 ~ -4.0	H_2 (63.7), formate (18.4) H_2 (52.0), formate (19.0) H_2 (46.0), formate (23.5) H_2 (44.3), C_2H_4 (16.6) H_2 (44.2), formate (17.5)	0.1 M $KHCO_3$	5	[310]

8.1 µm-Cu nanowire arrays							
Cu nanowire networks	ion-track technology	-0.50 -0.60 -0.72 -0.75 -0.82	-1.62 -2.36 -7.42 -6.71 -11.96	H_2 (~ 60), formate (~ 5) H_2 (~ 59), formate (~ 9) H_2 (~ 53), formate (~ 13) H_2 (~ 61), C_2H_4 (~ 7) H_2 (~ 58), formate (~ 8)	0.1 M $KHCO_3$	N/A	[311]
2.9 µm-FGR-CuNW 5.8 µm-FGR-Cu NW 7.6 µm-FGR-Cu NW 4.6 µm-ER-Cu NW 9.1 µm-ER-Cu NW 9.1 µm-ER-Cu NW	Electrochemically reduction (ER) of CuO and forming gas reduction (FGR) of CuO	-0.6	~ -2.8 ~ -3.0 ~ -3.9 ~ -3.9 ~ -4.0 ~ -4.0	H_2 (~ 82), CO (~ 6) H_2 (~ 80), CO (~ 8) H_2 (~ 81), CO (~ 7) H_2 (~ 65), CO (~ 10) H_2 (~ 42), CO (~ 18) H_2 (~ 38), CO (~ 22)	0.1 M $KHCO_3$	N/A	[312]
Cu nanowire	Electropolishing	-0.5	~ -2.50	CO (~ 53), formate (~ 25)	0.1 M $KHCO_3$	N/A	[313]
Cu nanowire	Anodic oxidation process	-1.5	~ -25	H_2 (~ 36), C_2H_4 (~ 19.8)	0.1 M $KHCO_3$	10	[314]
$Cu(OH)_2$ nanowire	One-step solution-immersion method then electrochemically reduced	-0.45 -0.57 -0.66 -0.75	-0.23 -0.66 -1.01 -2.29	H_2 (53.7), CO (19.9) formate (35.6), CO (29.7) formate (47.4), CO (20.4) H_2 (34.0), formate (25.0)	0.1 M $KHCO_3$	40	[315]

		-0.81 -0.85 -0.93 -1.08	-6.85 -10.55 -37.52 -39.60	H_2 (42.7), n-propanol (12.4) H_2 (43.9), C_2H_4 (12.5) H_2 (79.6), C2H5OH (1.0) H_2 (79.3), formate (1.1)			
Cu_2O nanowire/Cu mesh (Cu_2O-PE)	Oxidation then annealing	-0.70 -0.80 -0.90 -0.95 -1.00 -1.06 -1.10 -1.15	~ -1.5 ~ -2.3 ~ -8.0 ~ -10.0 ~ -12.5 ~ -19.0 ~ -32.0 ~ -39.0	H_2 (37.6), formate (35.7) H_2 (34.6), formate (37.7) H_2 (33.4), formate (30.2) H_2 (30.8), C_2H_4 (19.1) H_2 (39.6), C_2H_4 (21.5) H_2 (34.3), C_2H_4 (30.0) H_2 (41.2), C_2H_4 (29.8) H_2 (43.7), C_2H_4 (28.5)	0.1 M $KHCO_3$	-	[316]
(One wire) Cu_2O nanowire/Cu mesh (Cu_2O-ME)	Oxidation then annealing	-0.70 -0.80 -0.90 -0.95 -1.00 -1.06 -1.10	~ -4.0 ~ -5.0 ~ -9.0 ~ -21.0 ~ -41.0 ~ -68.0 ~ -79.0	H_2 (32.3), CO (26.0) H_2 (31.8), formate (30.0) H_2 (32.6), formate (19.7) H_2 (28.9), C_2H_4 (25.3) C_2H_4 (36.1), C_2H_5OH (24.1) C_2H_4 (39.1), C_2H_5OH (31.3) C_2H_4 (42.4), C_2H_5OH (31.3)	0.1 M $KHCO_3$	-	[316]

		-1.15	~ -100.0	C_2H_4 (42.2), C_2H_5OH (34.5)			
50 nm wide-Cu nanowire	Solvothermal synthesis	-1.10	-	H_2 (~ 70.0), CO (~ 13.0)	0.1 M $KHCO_3$	-	317
Cu nanoparticle (CuNP)							
Cu nanoparticle	Anodic oxidation process then electrochemical reduction	-1.50	-22.5	H_2 (~ 30.0), C_2H_4 (~ 22.5)	0.1 M $KHCO_3$	10	314
Cu nanoparticle on glassy carbon	Thermal evaporation	-1.35	-	CH_4 (~ 75.0), H_2 (~ 25.0)	0.1 M $NaHCO_3$	-	318
Cu nanoparticle	Electrochemical deposition	-0.99	~ -14.0	H_2 (~ 65.0), C_2H_4 (~ 13.0)	0.1 M $KHCO_3$	6	319
Drop casted CuNP film	Colloidal method	-0.80 -1.00 -1.20	~ -3.0 ~ -5.0 ~ -14.0	CO (2.1), C_2H_4 (0.3) CO (1.2), C_2H_4 (0.5) CH_4 (5.8), C_2H_4 (10.8)	0.1 M $KHCO_3$	-	320
Cu-tetracyanoquinodimethane derived Cu nanoparticles	Solvothermal synthesis	-1.10 -1.30	-	C_2H_4 (46), CO (15.0) C_2H_4 (56.0), H_2 (25.0)	0.5 M $KHCO_3$	12 8	321
Cu nanocube (CuCB)							
60% graphene oxide doped Cu nanocube	Hydrothermal method	-1.00	~ -4.7	H_2 (~ 40.0), C_2H_4 (~ 23.0)	0.1 M $NaHCO_3$	24	322

Cu nanocube	Microwave hydrothermal method	-0.60 -0.70 -0.80	~ -7.5 ~ -11.0 ~ -15.0	H_2 (~ 70.0), CO (~ 16.0) H_2 (~ 50.0), CO (~ 20.0) H_2 (~ 60.0), CO (~ 18.0)	0.1 M $KHCO_3$	-	[323]
80 nm-Cu nanocube 170 nm-Cu nanocube 390 nm-Cu nanocube	Electrochemical deposition	-1.10	~ -2.50 ~ -4.00 ~ -5.50	CO (~ 19.0), C_2H_4 (~18.0) C_2H_4 (~ 27.5), C_2H_4 (~17.5) H_2 (~ 27.0), C_2H_4 (~18.0)	0.1 M $KHCO_3$	12	[324]
24 nm-Cu nanocube 44 nm-Cu nanocube 63 nm-Cu nanocube	Solvothermal method	-1.10	~ -5.50 ~ -3.00 ~ -3.80	H_2 (47.6), formate (15.2) C_2H_4 (41.1), H_2 (20.5) H_2 (32.3), C_2H_4 (~ 24.9)	0.1 M $KHCO_3$	-	[325]
Other Cu catalysts							
Cu nanosheet	Anodic oxidation process then electrochemical reduction	-1.50	-37.5	C_2H_4 (~ 32.7), C_2H_5OH (25.8)	0.1 M $KHCO_3$	10	[314]
Cu mesocrystals	Electrochemical deposition	-0.99	~ -25.0	H_2 (~ 40), C_2H_4 (27.2)	0.1 M $KHCO_3$	6	[319]
Cu nanoneedle	Sol – gel	-0.70 -0.90 -1.00 -1.10	~ -18.0 ~ -30.0 ~ -38.0 ~ -57.0	H_2 (27.6), formate (56.2) H_2 (32.7), formate (49.0) H_2 (27.9), formate (38.3) H_2 (42.3), formate (40.7)	0.1 M $KHCO_3$	5	[326]

		-1.20 -1.40 -1.60	~ -80.0 ~ -110.0 -	H_2 (48.8), formate (29.7) H_2 (49.9), formate (25.5) H_2 (52.3), formate (23.9)			
Cu nanodendrites	Electrochemical deposition	-2.00	-170	C_2H_4 (57), CH_4 (9)	0.1 M KBr	2.3	[327]

Table A 1.3: Reported ECSA and R_f of Copper based electrocatalysts.

Electrode	C_{dl} $(\mu F \cdot cm^2)$	***ECSA*** (cm^2)	***Roughness factor***	***Ref.***
Electropolished Cu	46.5	1.55	-	[307]
Cu foil	51.4	-	-	[328]
Electropolished Cu foil	29	-	1	[329]
Electropolished Cu foil O_2 plasma (20 W 2min)-Cu foil O_2 plasma (100 W 2min)-Cu foil O_2 plasma (100 W 10min)-Cu foil	47.4 1250 2070 4250	-	1 26.4 43.7 89.7	[309]
2.9 µm-FGR-CuNW 5.8 µm-FGR-Cu NW 7.6 µm-FGR-Cu NW 4.6 µm-ER-Cu NW 9.1 µm-ER-Cu NW 9.1 µm-ER-Cu NW	1800 2600 4500 4000 6500 11200	-	-	[312]
Electropolished CuNW	10470	-	356	[313]

Electropolished CuNW (annealing at 150 °C) Electropolished CuNW (annealing at 300 °C)	4220 676		145 23	
CuNW	8400	-	9.98	[314]
$Cu(OH)_2$ nanowire	2390	-	79.8	[315]
Cu_2O nanowire/Cu mesh (Cu_2O-PE) (One wire) Cu_2O nanowire/Cu mesh (Cu_2O-ME) CuO nanowire/Cu mesh (CuO-PE) (One wire) CuO nanowire/Cu mesh (CuO-ME) Cu nanowire/Cu mesh (Cu-PE) (One wire) Cu nanowire/Cu mesh (Cu-ME)	2170 2860 2840 2970 85 65	-	90.3 95.3 94.7 99.0 2.83 2.17	[316]

Appendix-2

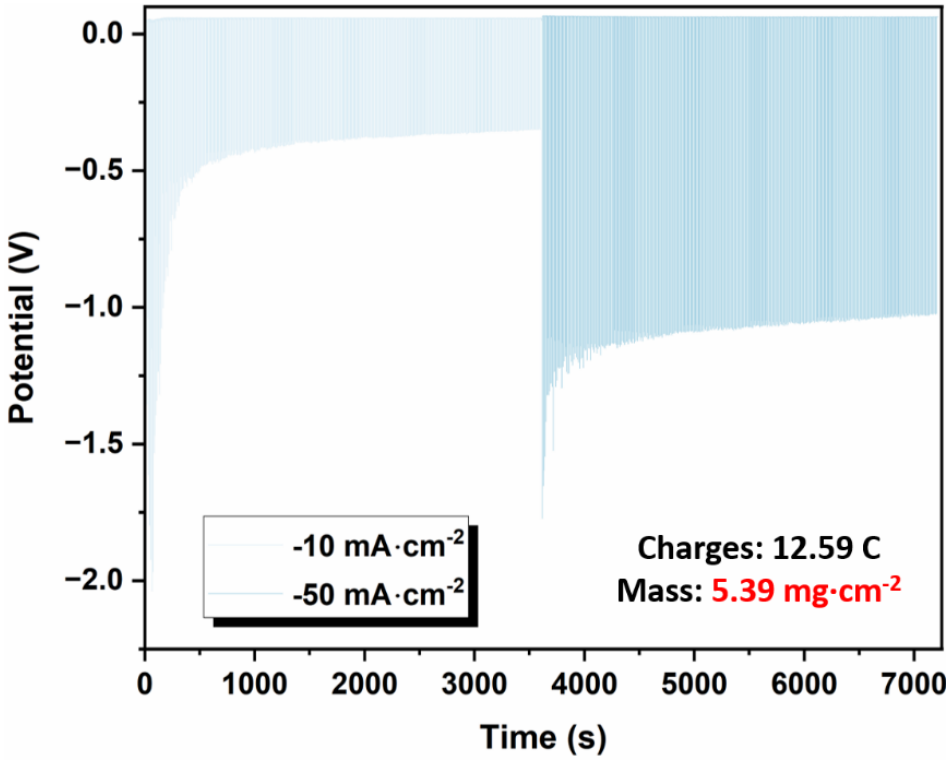

Figure A 2.1: Applied potential recorded during a 2-step square pulsed electrodeposition of CuNWs (1st: -10 mA·cm^{-2} for 60 min, 2nd: -50 mA·cm^{-2} for 60 min).

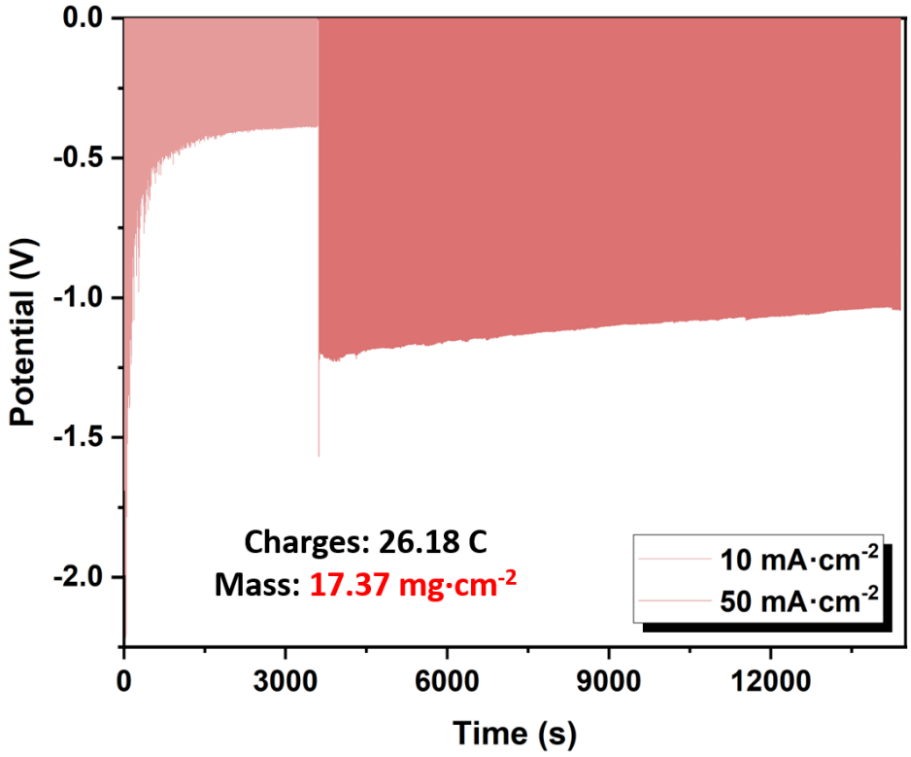

Figure A 2.2: Applied potential recorded during a 2-step square pulsed electrodeposition of CuNWs (1st: -10 mA·cm^{-2} for 60 min, 2nd: -50 mA·cm^{-2} for 180 min).

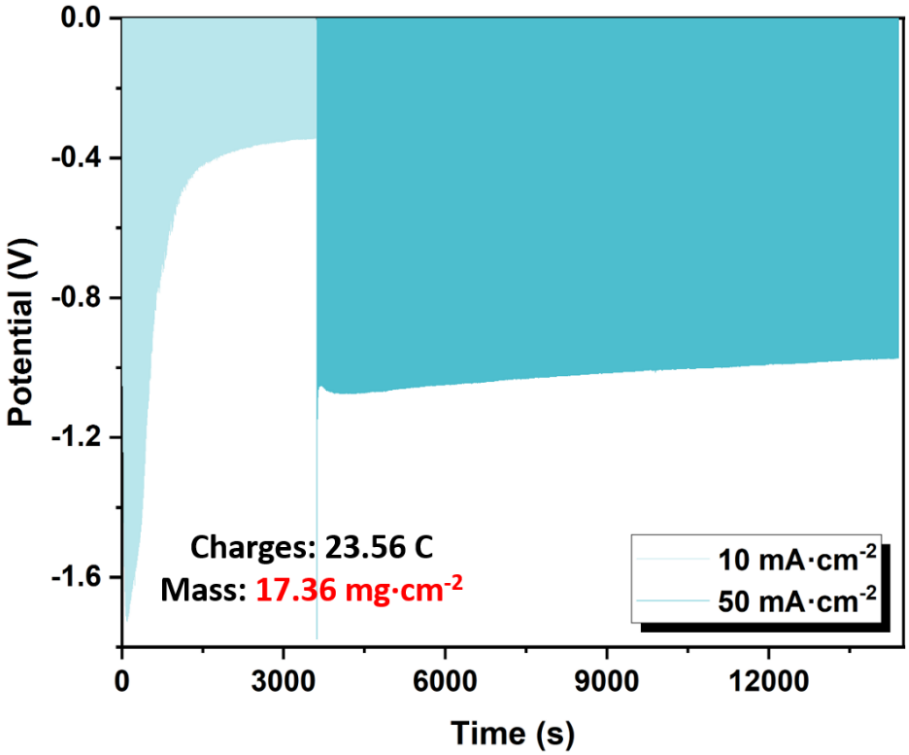

Figure A 2.3: Applied potential recorded during a 2-step square pulsed electrodeposition of CuNWs (1st: -10 mA·cm^{-2} for 60 min, 2nd: -50 mA·cm^{-2} for 180 min).

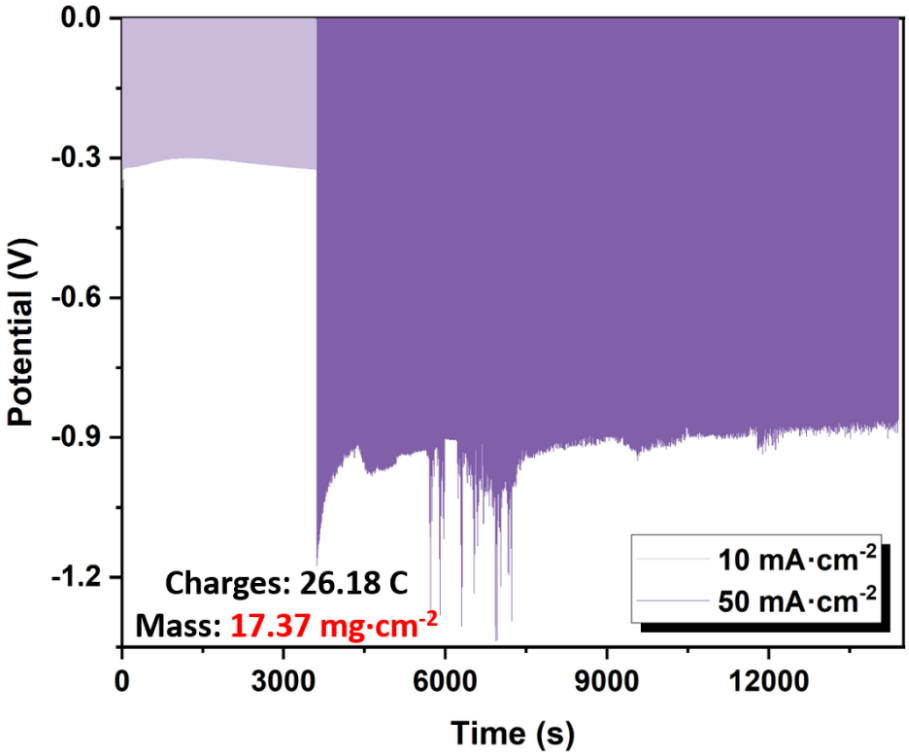

Figure A 2.4: Applied potential recorded during a 2-step square pulsed electrodeposition of CuNWs (1st: -10 mA·cm^{-2} for 60 min, 2nd: -50 mA·cm^{-2} for 180 min).

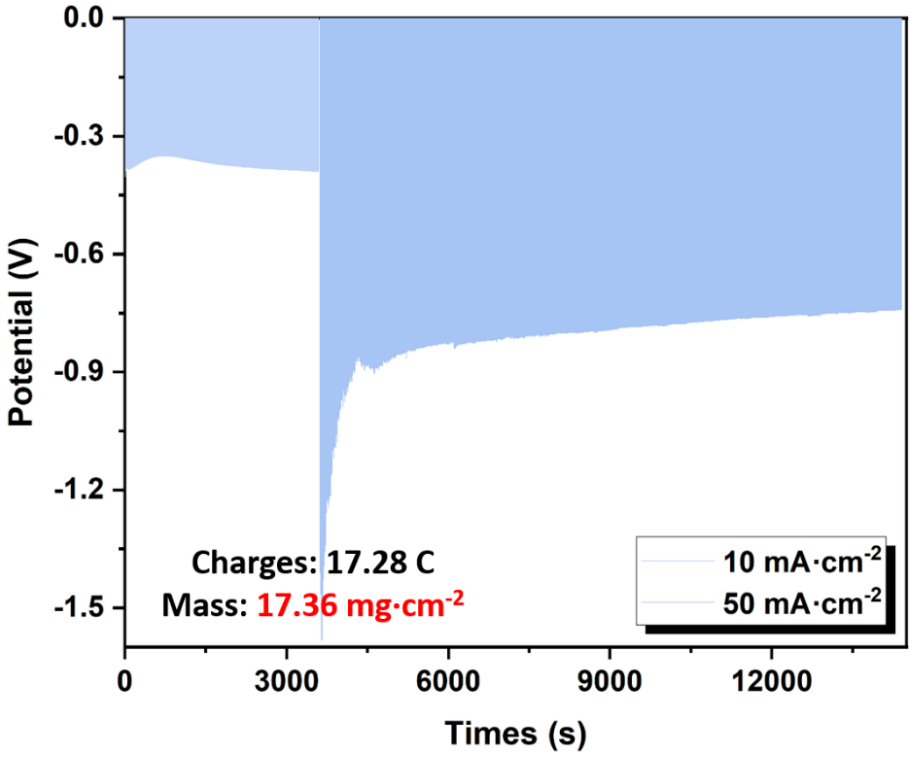

Figure A 2.5: Applied potential recorded during a 2-step square pulsed electrodeposition of CuNWs (1st: -10 mA·cm^{-2} for 60 min, 2nd: -50 mA·cm^{-2} for 180 min).

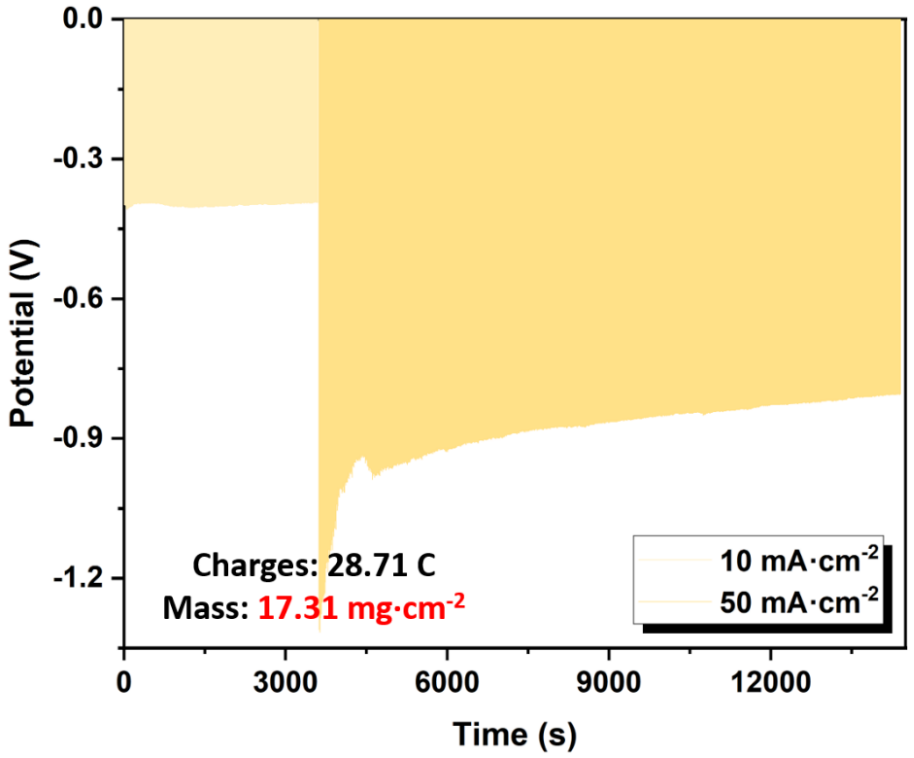

Figure A 2.6: Applied potential recorded during a 2-step square pulsed electrodeposition of CuNWs (1st: -10 mA·cm^{-2} for 60 min, 2nd: -50 mA·cm^{-2} for 180 min).

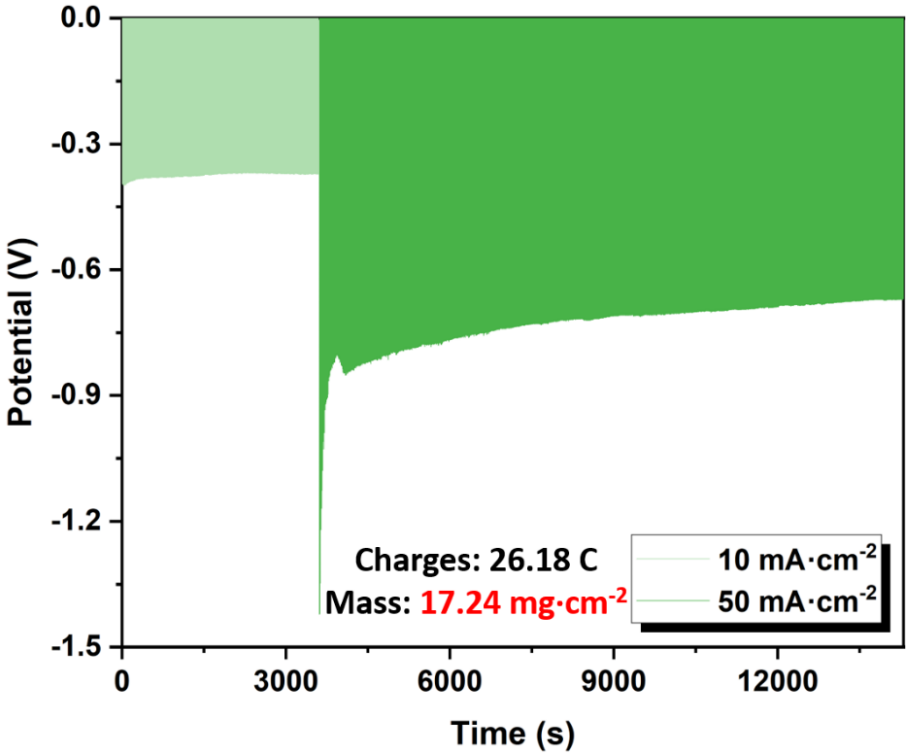

Figure A 2.7: Applied potential recorded during a 2-step square pulsed electrodeposition of CuNWs (1st: -10 mA·cm^{-2} for 60 min, 2nd: -50 mA·cm^{-2} for 180 min).

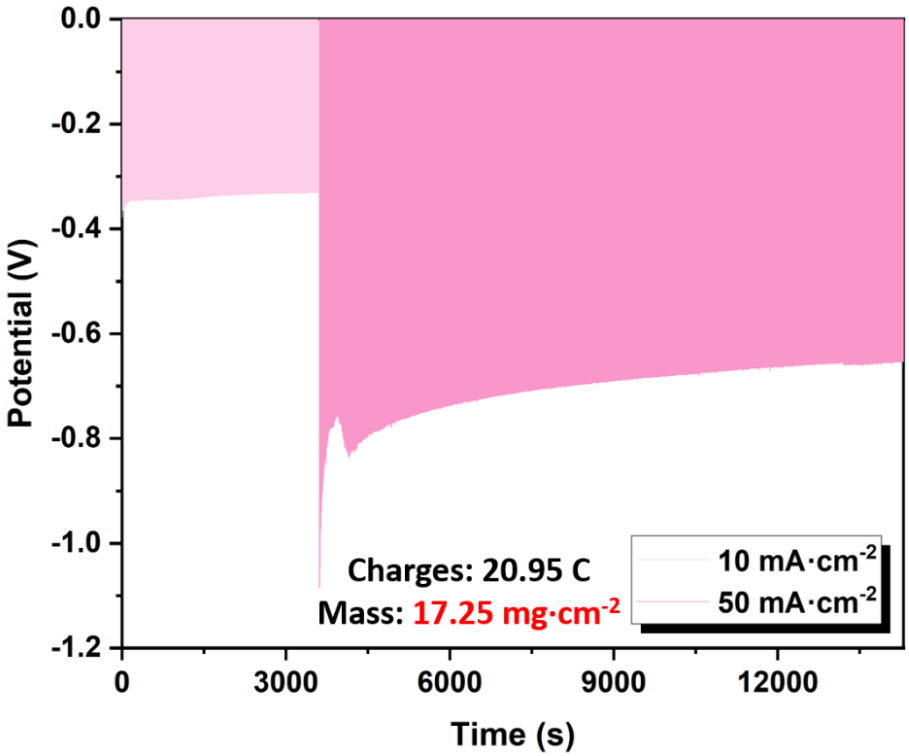

Figure A 2.8: Applied potential recorded during a 2-step square pulsed electrodeposition of CuNWs (1st: -10 mA·cm^{-2} for 60 min, 2nd: -50 mA·cm^{-2} for 180 min).

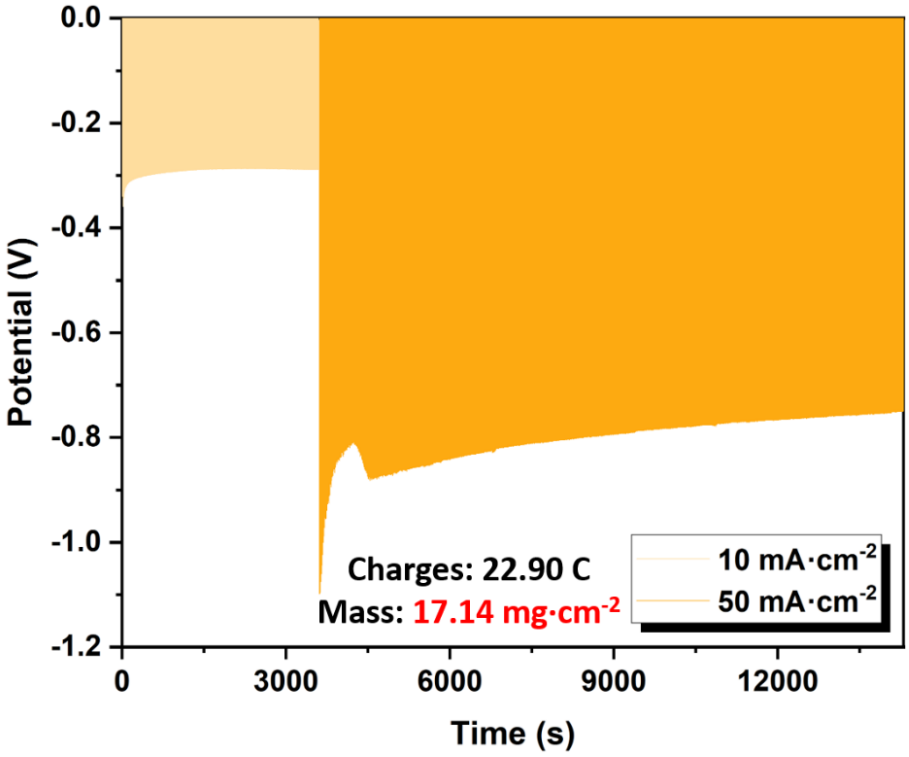

Figure A 2.9: Applied potential recorded during a 2-step square pulsed electrodeposition of CuNWs (1st: -10 mA·cm^{-2} for 60 min, 2nd: -50 mA·cm^{-2} for 180 min).

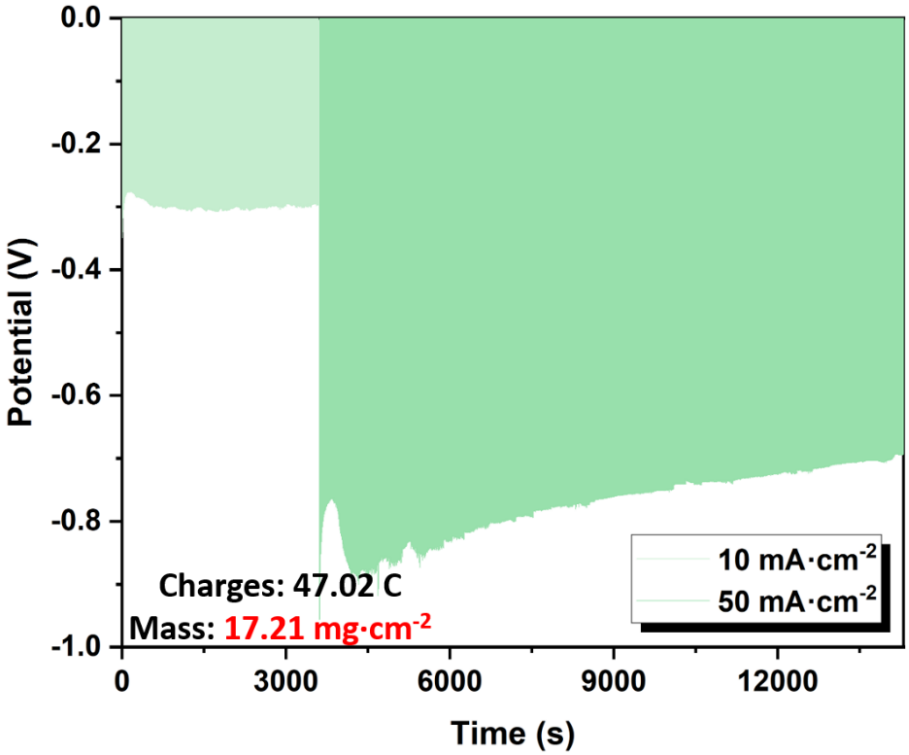

Figure A 2.10: Applied potential recorded during a 2-step square pulsed electrodeposition of CuNWs (1st: -10 mA·cm^{-2} for 60 min, 2nd: -50 mA·cm^{-2} for 180 min).

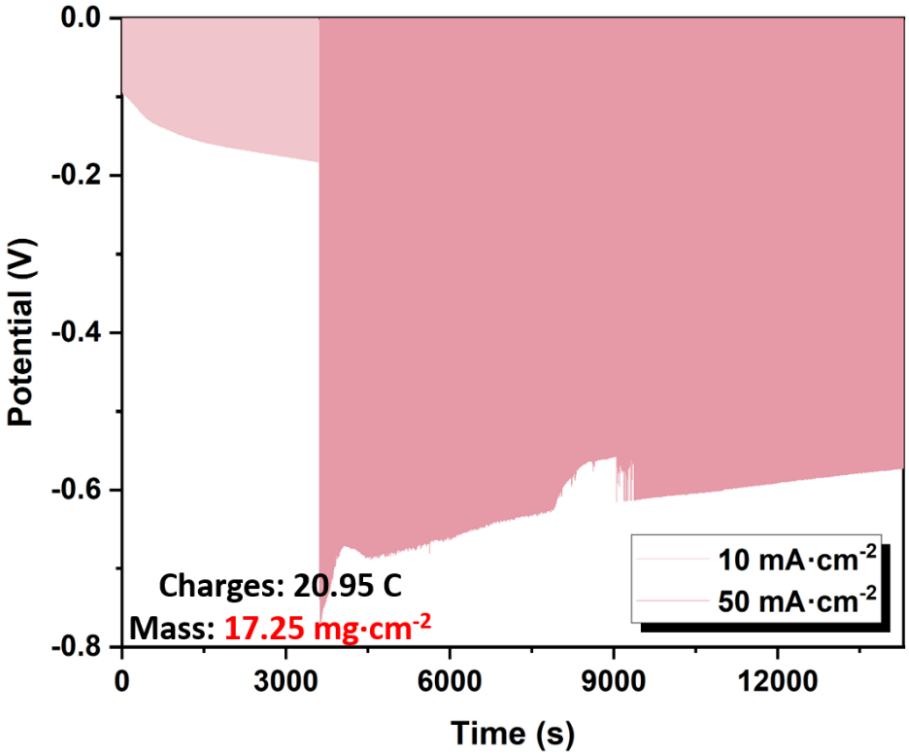

Figure A 2.11: Applied potential recorded during a 2-step square pulsed electrodeposition of CuNWs (1st: -10 mA·cm^{-2} for 60 min, 2nd: -50 mA·cm^{-2} for 180 min).

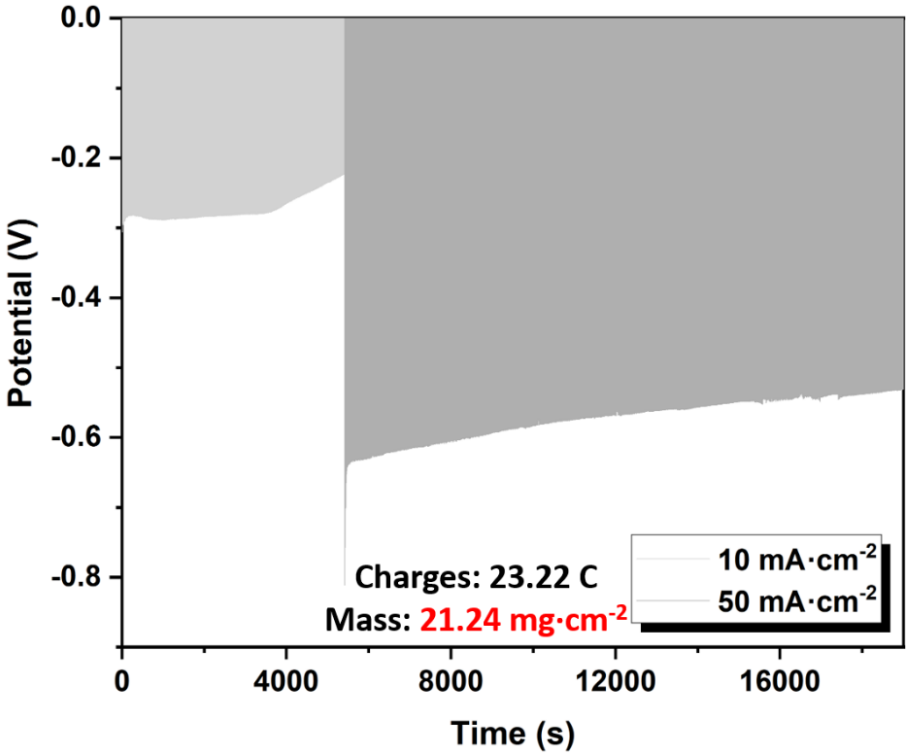

Figure A 2.12: Applied potential recorded during a 2-step square pulsed electrodeposition of CuNWs (1st: -10 mA·cm^{-2} for 90 min, 2nd: -50 mA·cm^{-2} for 240 min).

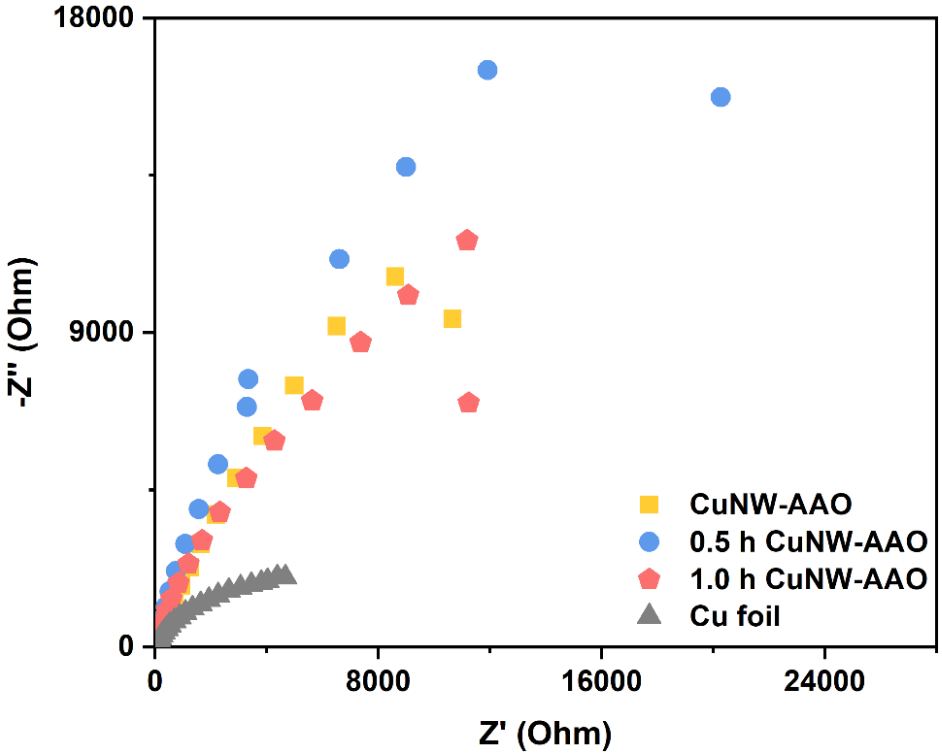

Figure A 2.13: Electrochemical impedance: Nyquist plots of EIS for CuNW-AAO and Cu foil electrodes at open circuit potential in 0.1 M Na_2SO_4.

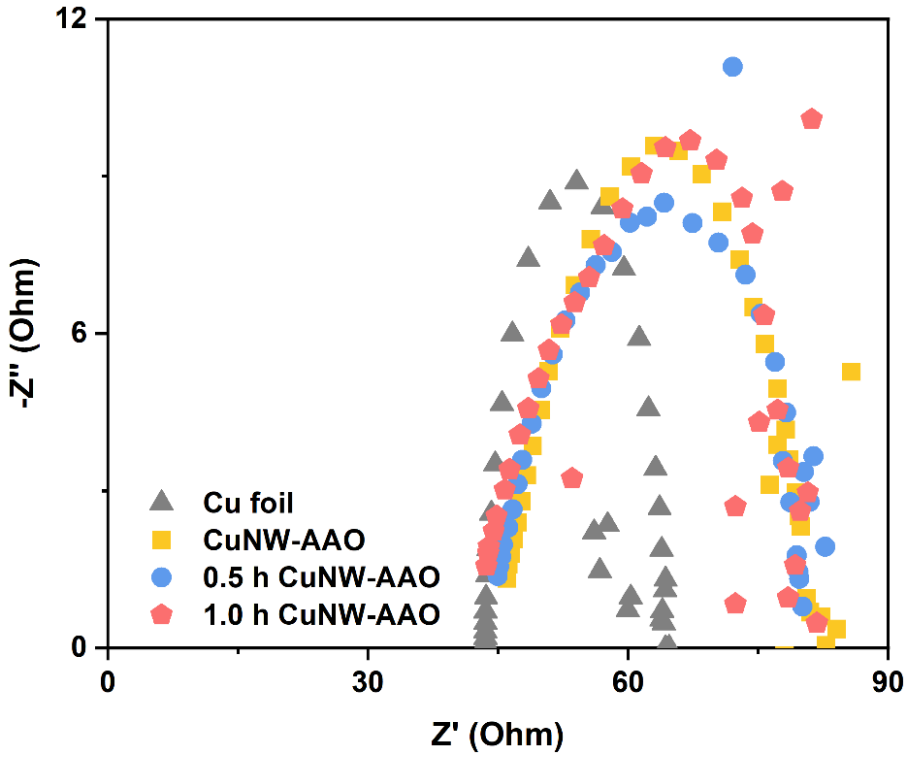

Figure A 2.14: Electrochemical impedance: Nyquist plots of EIS for CuNW-AAO and Cu foil electrodes at -0.4 V (vs.RHE) in 0.1 M Na_2SO_4.

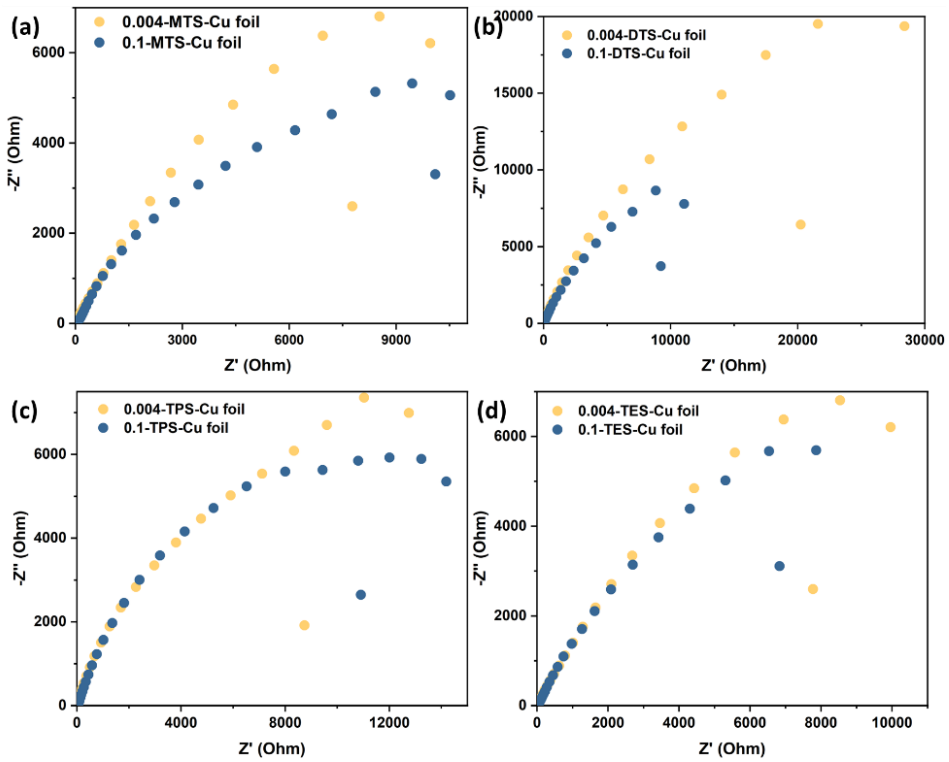

Figure A 2.15: Nyquist plot of EIS for CuNW-AAO electrode at open circuit potential in 0.1 M Na_2SO_4: (a) on MTS-Cu foil electrodes, (b) on DTS-Cu foil electrodes, (c) on TPS-Cu foil electrodes, (d) on TES-Cu foil electrodes.

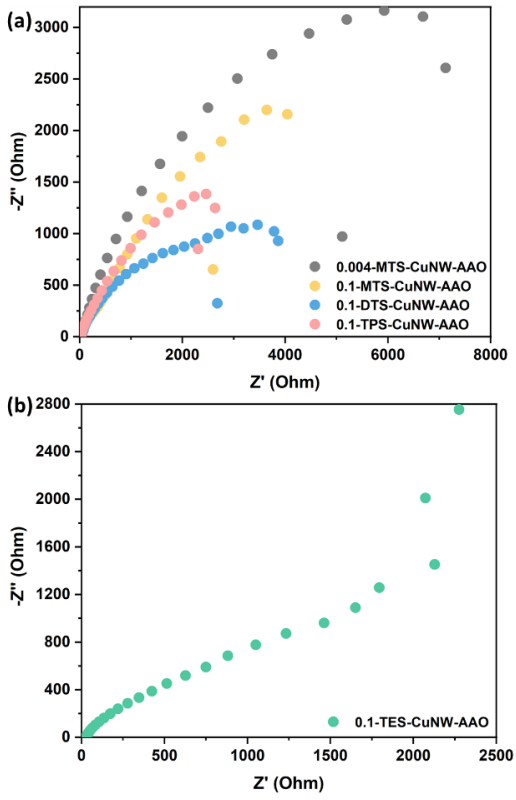

Figure A 2.16: Nyquist plot of EIS for CuNW-AAO electrode at open circuit potential in 0.1 M Na_2SO_4: (a) on MTS/DTS/TPS-CuNW-AAO electrodes, (b) on TES-CuNW-AAO electrode.

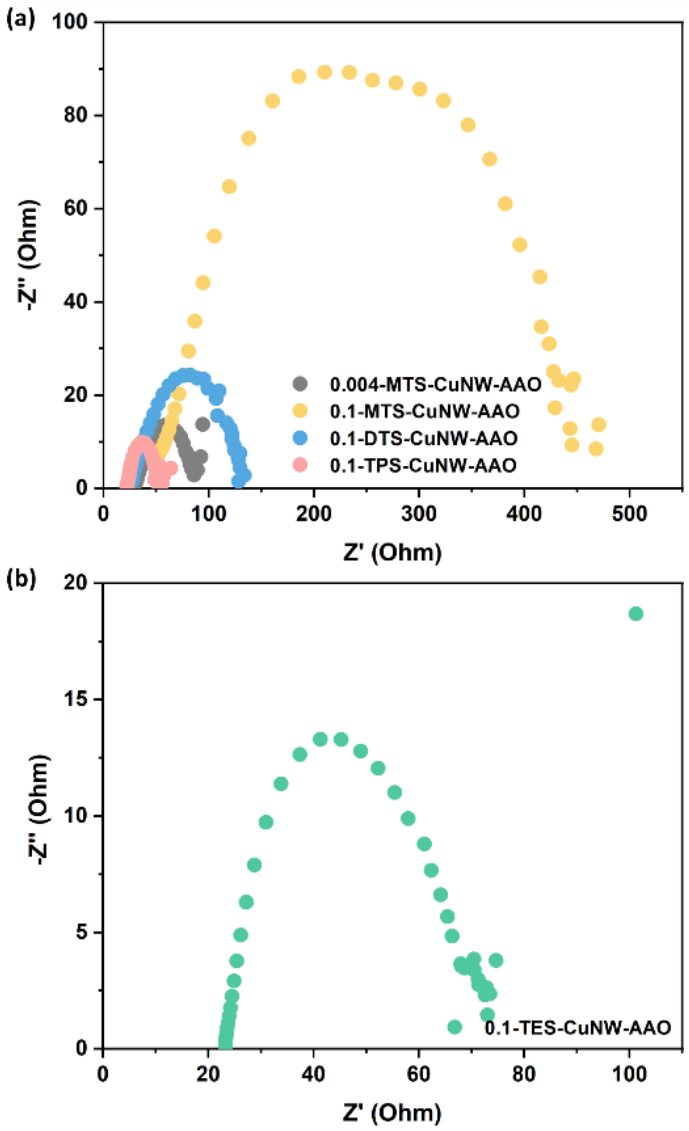

Figure A 2.17: Nyquist plot of EIS for CuNW-AAO electrode at at -0.8 V (vs. RHE) in 0.1 M Na_2SO_4: (a) on MTS/DTS/TPS-CuNW-AAO electrodes, (b) on TES-CuNW-AAO electrode.

Operation of iR compensation on potentiostat:

iR compensation is applied to correct for the potential drop (between two ends of a conducting wire during current flow, such as iR drop) caused by the electrolyte solution between the working electrode and the reference electrode, where R is the resistance of electrolyte. When performing iR compensation:

1. Create a cell as in Figure A 2.18 The capacitor can be 1 to 10 µF. And the iR compensation resistance is 100 Ω, the resistance between counter and reference electrode is 1000 Ω (which represents the electrolyte resistance, meaning the iR drop is 10% of the value of the Electrolyte resistance).

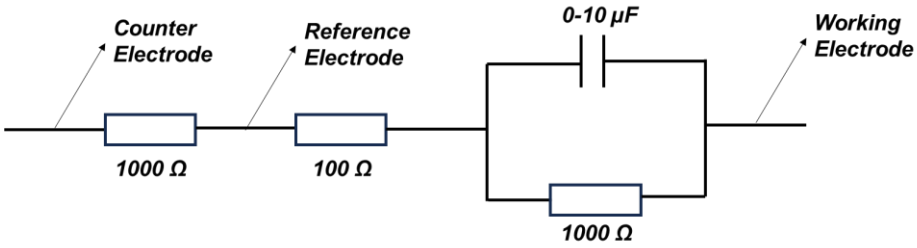

Figure A 2.18: A dummy cell circuit for iR compensation.

2. Then, setup an EIS measurement on potentiostat to validate the instrument and components in use.
3. Next, create a linear sweep voltammogram without iR compensation, the maximum potential applied is 1 V, while the current registered is 908 µA. According to $U = R\,x\,I$, $1\,V = (1000 + 100)\,Ohm\,x\,Amp$, the current information includes the iR compensation resistance of 100 Ω.
4. Then, setup an EIS measurement on potentiostat to validate the instrument and components in use.
5. Set the potentiostat to compensate for the iR drop, which means the 100 Ω iR drop should be eliminated up to a current value of 1 mA (as if the 100 Ω is disappeared, and only the electrolyte resistance of 1000 Ω is in the circuit). Therefore, the potentiostat will need to increase the applied voltage to overcome the 100 Ω resistance.
6. Set the potentiostat to compensate for the iR drop, which means the 100 Ω iR drop should be eliminated up to a current value of 1 mA (as if the 100 Ω is disappeared, and only the electrolyte resistance of 1000 Ω is in the circuit). Therefore, the potentiostat will need to increase the applied voltage to overcome the 100 Ω resistance.
7. Create a linear sweep voltammogram with iR compensation. the maximum applied potential is 1.095 mV, but as the compensation is enabled, the current registered is 1 mA, meaning the measurement includes the 100 Ω iR drop being compensated. If these tests cohere with the above results, then this means the potentiostat is correctly measuring the Ir compensation value and compensates correctly the applied voltages for

the iR drop in the circuit. This proves the potentiostat to be working properly for iR compensation.

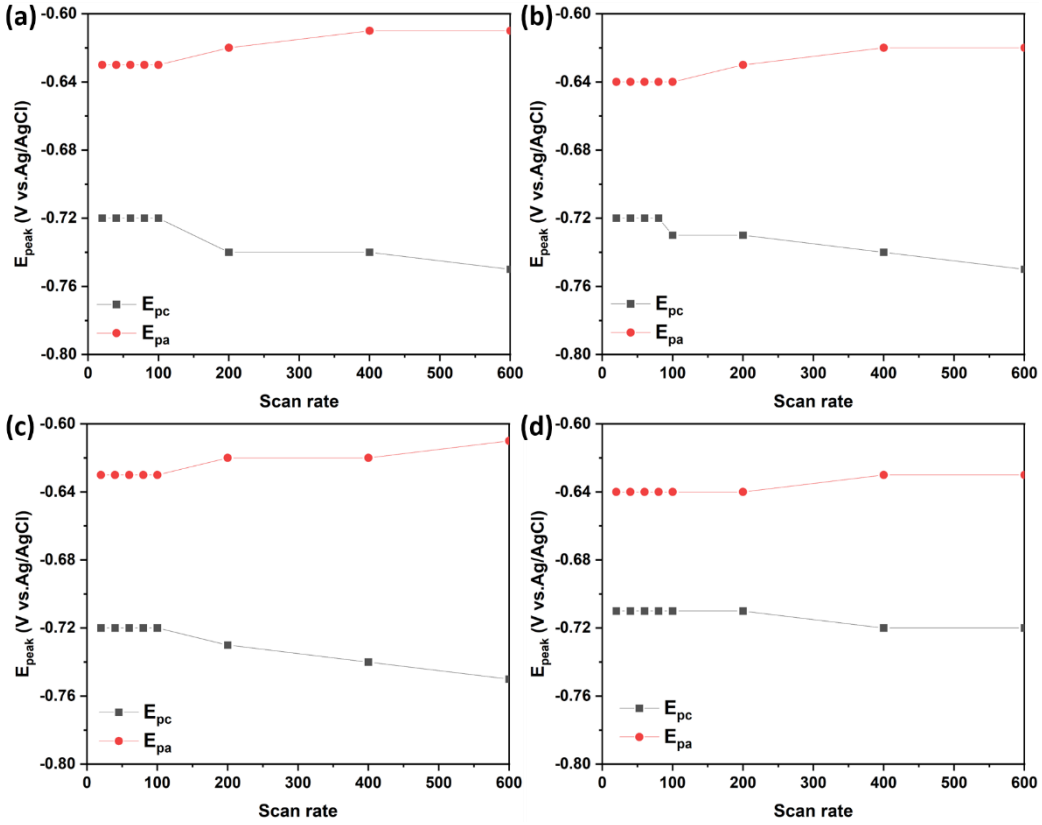

Figure A 2.19: The relationship between peak potential (E_p, V vs.Ag/AgCl) and scan rate ($mV \cdot s^{-1}$): (a) CuNW-AAO electrode, (b) 0.5 h CuNW-AAO electrode, (c) 1.0 h CuNW-AAO electrode, (d) Cu foil electrode.

Appendix-3

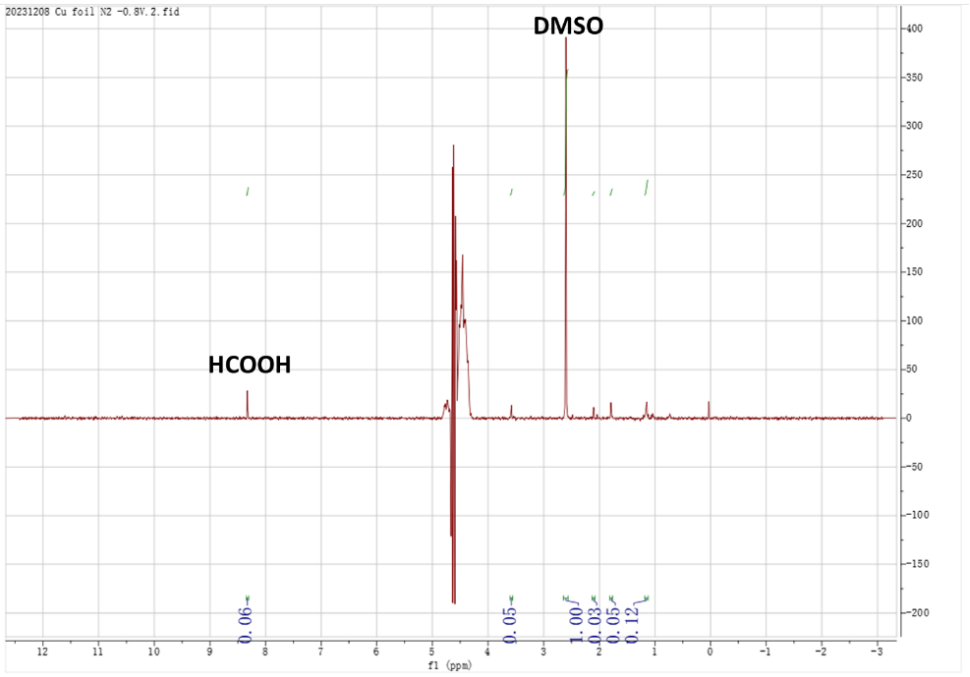

Figure A 3.20: ^{1}H NMR spectrum of liquid products on 0.1-MTS-Cu foil electrode in 0.1 M $KHCO_3$ saturated by N_2 (at -0.8 V vs. RHE).

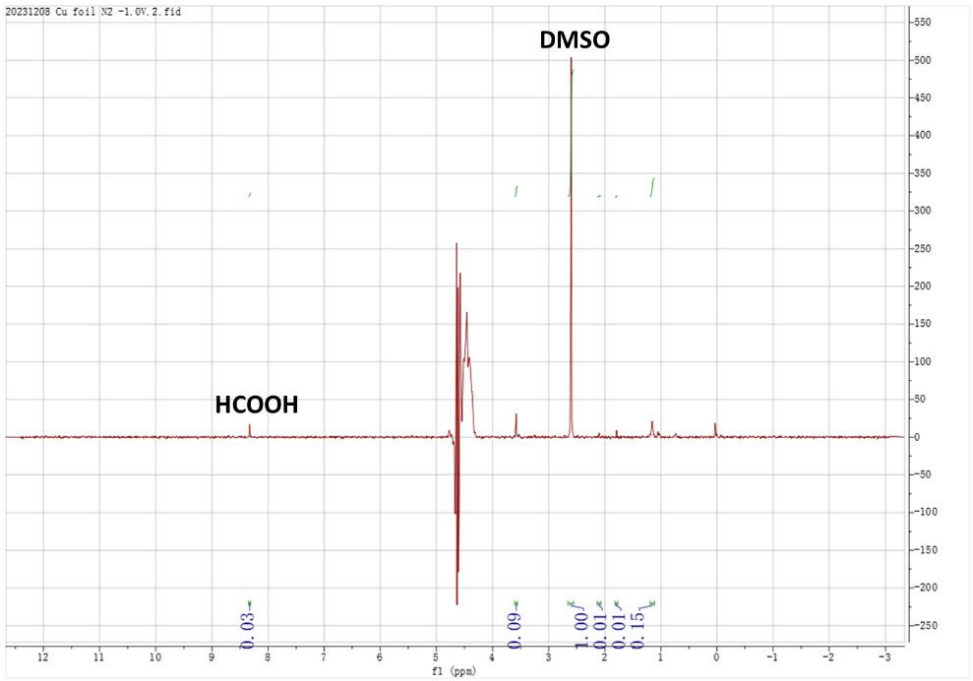

Figure A 3.21: ^{1}H NMR spectrum of liquid products on 0.1-MTS-Cu foil electrode in 0.1 M $KHCO_3$ saturated by N_2 (at -1.0 V vs. RHE).

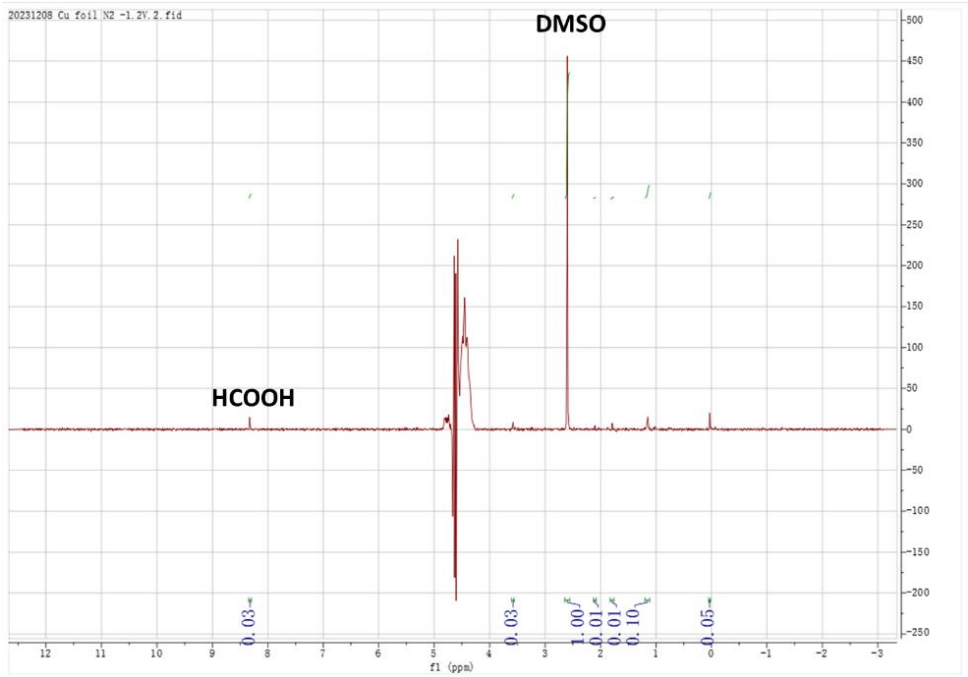

Figure A 3.22: ^{1}H NMR spectrum of liquid products on 0.1-MTS-Cu foil electrode in 0.1 M $KHCO_3$ saturated by N_2 (at -1.2 V vs. RHE).

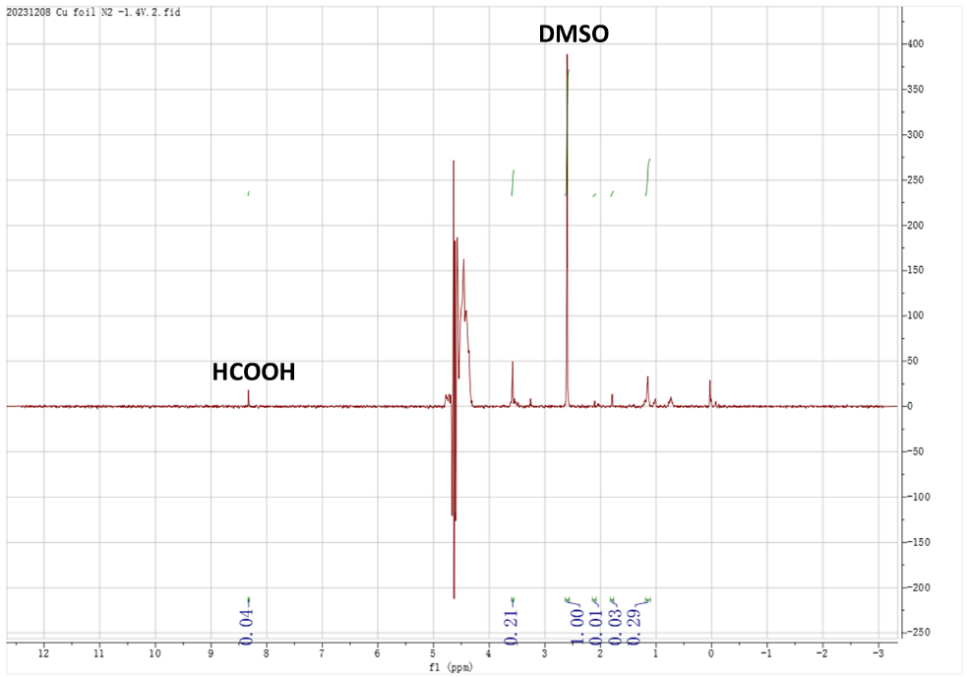

Figure A 3.23: ^{1}H NMR spectrum of liquid products on 0.1-MTS-Cu foil electrode in 0.1 M $KHCO_3$ saturated by N_2 (at -1.4 V vs. RHE).

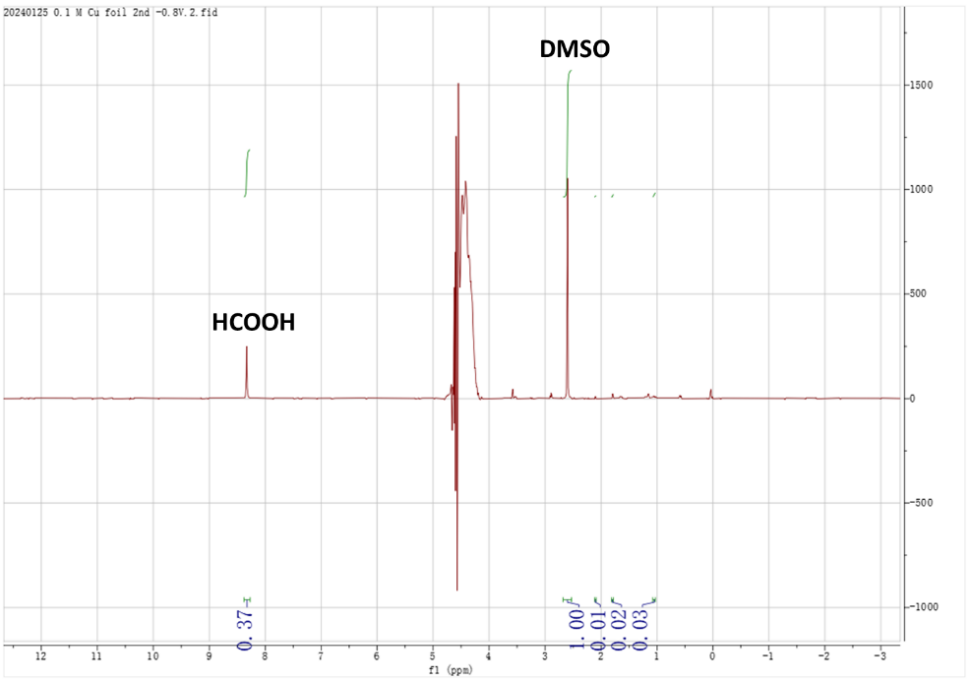

Figure A 3.24: ^{1}H NMR spectrum of liquid products on 0.1-MTS-Cu foil electrode in 0.1 M $KHCO_3$ saturated by CO_2 (at -0.8 V vs. RHE).

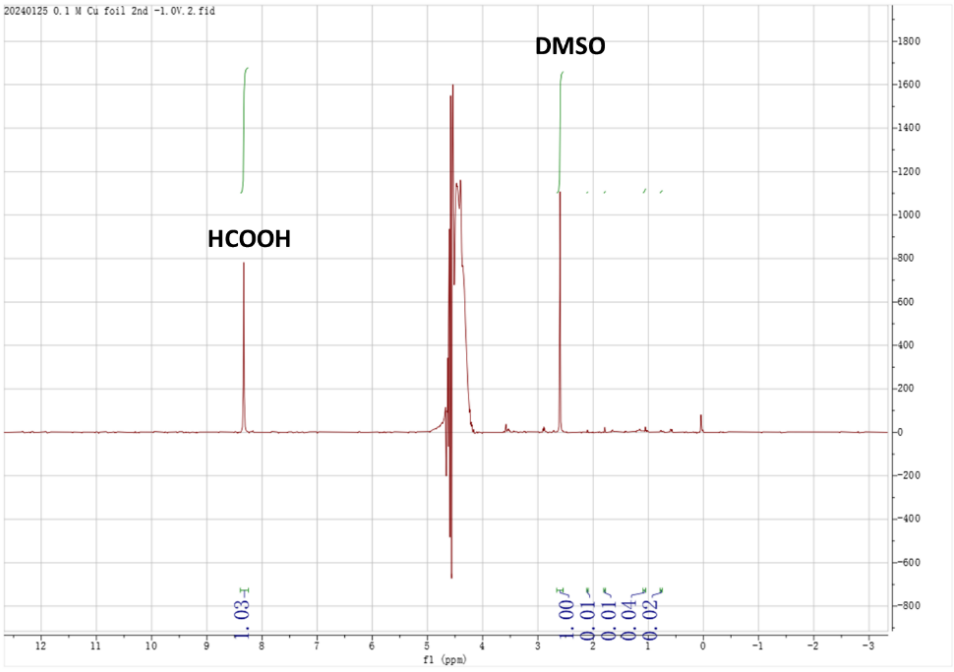

Figure A 3.25: ^{1}H NMR spectrum of liquid products on 0.1-MTS-Cu foil electrode in 0.1 M $KHCO_3$ saturated by CO_2 (at -1.0 V vs. RHE).

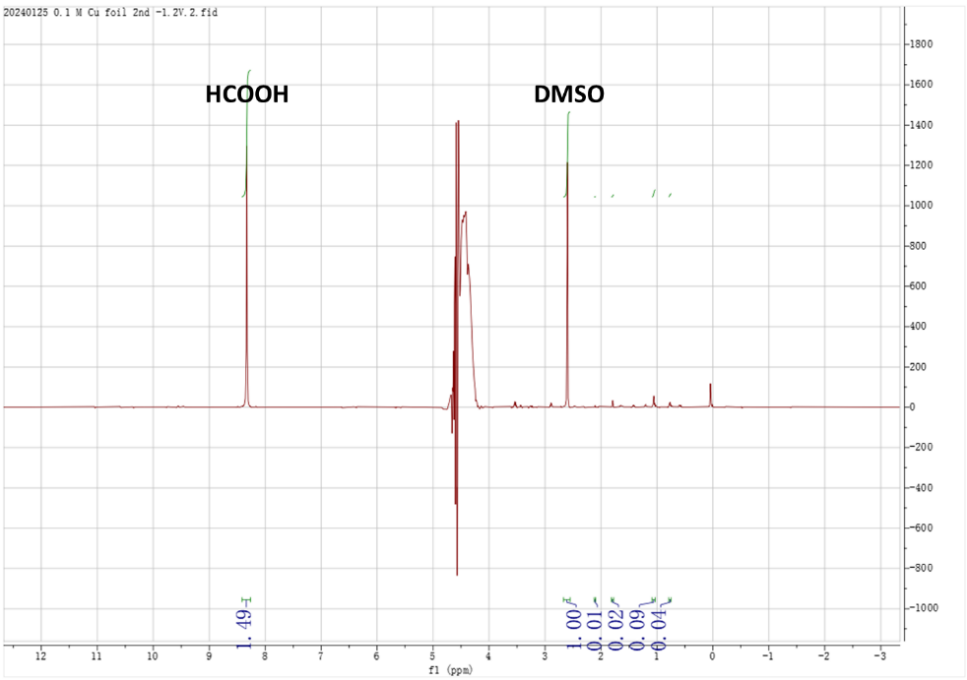

Figure A 3.26: ^{1}H NMR spectrum of liquid products on 0.1-MTS-Cu foil electrode in 0.1 M $KHCO_3$ saturated by CO_2 (at -1.2 V vs. RHE).

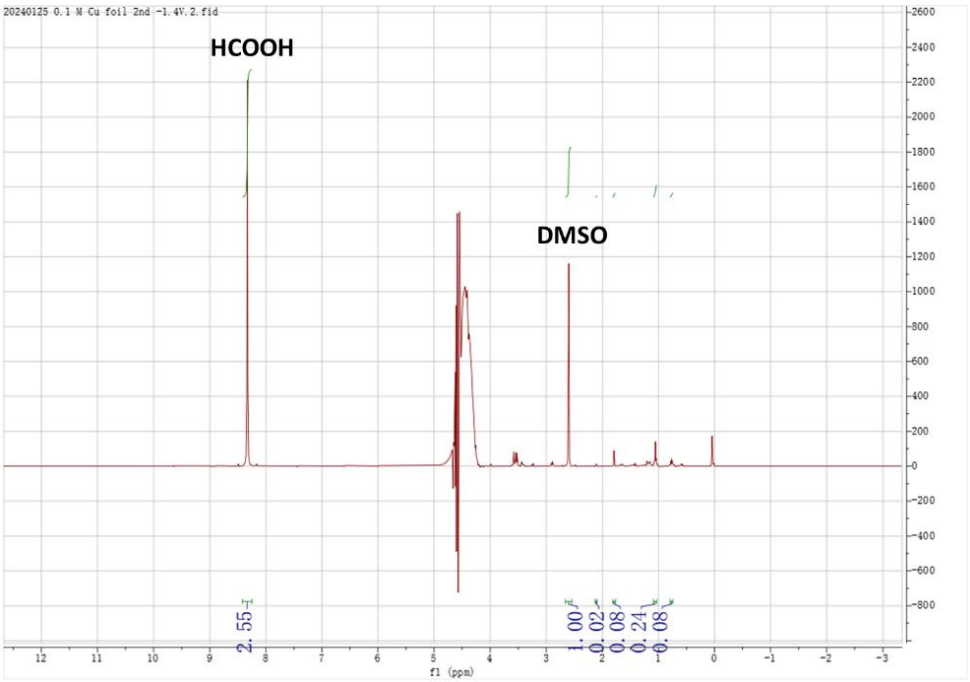

Figure A 3.27: ^{1}H NMR spectrum of liquid products on 0.1-MTS-Cu foil electrode in 0.1 M $KHCO_3$ saturated by CO_2 (at -1.4 V vs. RHE).

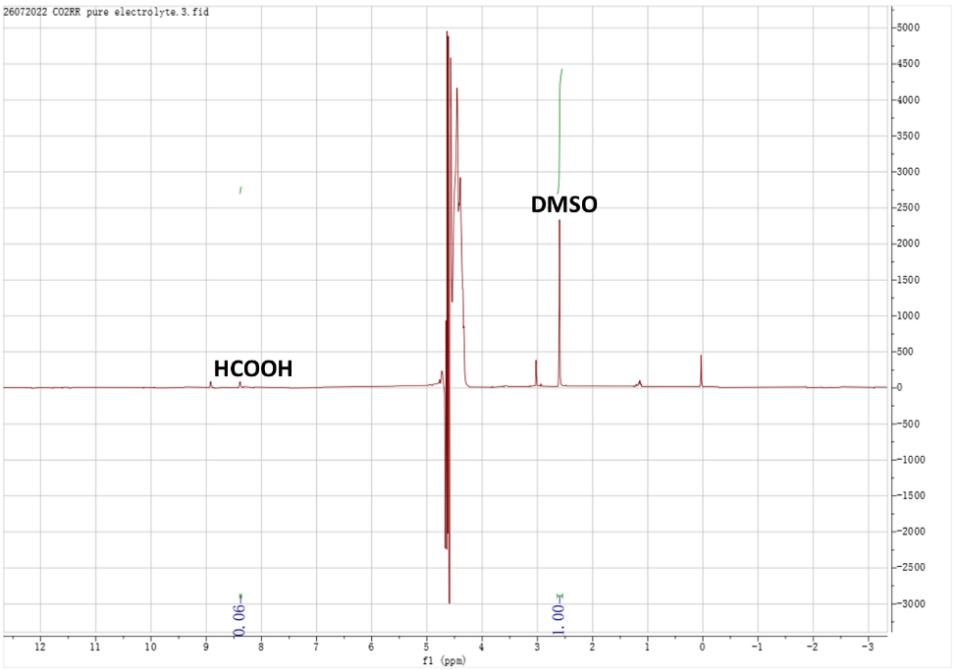

Figure A 3.28: ^{1}H NMR spectrum of liquid products on 0.1-MTS-Cu foil electrode in 0.1 M $KHCO_3$ saturated by CO_2 (at OCP)

Abbreviation list

AAO	Anodized aluminium oxide
CA	Chronoamperometry
CDU	Carbon dioxide utilization
CDS	Carbon dioxide storage
CE%	Current efficiency
CO_2RR	CO_2 reduction reaction
CuNW	Copper nanowire
CV	Cyclic Voltammetry
DMSO	Dimethyl sulfoxide
DLC	Double-layer capacitance
DTS	Dodecyltrichlorosilane
ECSA	Electrochemical surface area
EDX (EDS)	Energy-dispersive X-ray spectroscopy
EIS	Electrochemical impedance
FE%	Faradaic efficiency
FID	Flame ionization detector
GDL	Gas diffusion layer
GC	Gas chromatography
HER	Hydrogen evolution reaction
LSV	Linear Sweep Voltammetry
MTS	Methyltrichlorosilane
MV	Methylviologen
NMR	Nuclear magnetic resonance
NW	Nanowire
OCP	Open circuit potential
PCET	Proton coupled electron transfer
Rf	Roughness factor

RHE	Reversal hydrogen electrode
SEM	Scanning electron microscope
TCD	Thermal conductivity detector
TES	(3-aminopropyl) triethoxysilane
TPS	Trichloro(phenyl)silane
PXRD	Powder X-Ray powder diffraction
XPS	X-ray photoelectron spectroscopy

References

1 J. H. Montoya, L. C. Seitz, P. Chakthranont, A. Vojvodic, T. F. Jaramillo and J. K. Nørskov, *Nat. Mater.*, 2017, **16**, 70–81.

2 D. Gao, H. Zhou, F. Cai, J. Wang, G. Wang and X. Bao, *ACS Catal.*, 2018, **8**, 1510–1519.

3 B. Obama, *Science*, 2017, **355**, 126–129.

4 A. S. Varela, W. Ju and P. Strasser, *Adv. Energy Mater.*, 2018, **8**, 1703614.

5 C. Kim, F. Dionigi, V. Beermann, X. Wang, T. Möller and P. Strasser, *Adv. Mater.*, 2019, **31**, 1805617.

6 K. Wiranarongkorn, K. Eamsiri, Y. S. Chen and A. Arpornwichanop, *J. CO_2 Util.*, 2023, **71**, 102477.

7 D. Larcher and J.-M. Tarascon, *Nat. Chem.*, 2015, **7**, 19–29.

8 X. Zou and Y. Zhang, *Chem. Soc. Rev.*, 2015, **44**, 5148–5180.

9 P. Friedlingstein, et al. *Earth Syst. Sci. Data*, 2022, **14**, 4811–4900.

10 T. Güney, *Renew. Energy*, 2022, **184**, 791–798.

11 W. Wang, S. Wang, X. Ma and J. Gong, *Chem. Soc. Rev.*, 2011, **40**, 3703–3727.

12 M. Lameh, D. M. Al-Mohannadi and P. Linke, *Clean Eng. Technol.*, 2020, **1**, 100023.

13 D. Yang, S. Li, S. He and Y. Zheng, *Energy Convers. Manag.*, 2022, **273**, 116425.

14 C. Kim, C. J. Yoo, H. S. Oh, B. K. Min and U. Lee, *J. CO_2 Util.*, 2022, **65**, 102239.

15 S. Tripathi, S. Choudhary, A. Meena and K. M. Poluri, *Environ. Chem. Lett.*, 2023, **21**, 2085–2128.

16 Y. Hori, K. Kikuchi and S. Suzuki, *Chem. Lett.*, 1985, **14**, 1695–1698.

17 J. W. Wang, D. C. Zhong and T. B. Lu, *Coord. Chem. Rev.*, 2018, **377**, 225–236.

18 G. Gastelu, P. Saha, P. J. Dyson, M. Hulla and J. G. Uranga, *ChemCatChem*, 2023, **15**, e202300905.

19 C. Wang, Z. Lv, X. Feng, W. Yang and B. Wang, *Adv. Energy Mater.*, 2023, **13**, 2302382.

20 J. Zhao, S. Xue, J. Barber, Y. Zhou, J. Meng and X. Ke, *J. Mater. Chem. A Mater.*, 2020, **8**, 4700–4734.

21 R. Kortlever, J. Shen, K. J. P. Schouten, F. Calle-Vallejo and M. T. M. Koper, *J. Phys. Chem. Lett.*, 2015, **6**, 4073–4082.

22 J. Ran, M. Jaroniec and S.-Z. Qiao, *Adv. Mater.*, 2018, **30**, 1704649.

23 K. Li, B. Peng and T. Peng, *ACS Catal.*, 2016, **6**, 7485–7527.

24 R. G. Grim, Z. Huang, M. T. Guarnieri, J. R. Ferrell, L. Tao and J. A. Schaidle, *Energy Environ. Sci.*, 2020, **13**, 472–494.

25 J. Wu, Y. Huang, W. Ye and Y. Li, *Adv. Sci.*, 2017, **4**, 1700194.

26 X. Li and Q. L. Zhu, *EnergyChem.*, 2020, **2**, 100033.

27 S. N. Habisreutinger, L. Schmidt-Mende and J. K. Stolarczyk, *Angew. Chem. Int. Edit.*, 2013, **52**, 7372–7408.

28 Z. Shang, X. Feng, G. Chen, R. Qin and Y. Han, *Small*, 2023, **19**, 2304975.

29 W. Wang, L. Wang, W. Su and Y. Xing, *J. CO_2 Util.*, 2022, **61**, 102056.

30 J. Sadhukhan, J. R. Lloyd, K. Scott, G. C. Premier, E. H. Yu, T. Curtis and I. M. Head, *Renew. Sustain. Energy Rev.*, 2016, **56**, 116–132.

31 G. Mohanakrishna, K. Vanbroekhoven and D. Pant, *J. CO_2 Util.*, 2016, **15**, 57–64.

32 S. T. Huang, Y. Q. Lei, P. R. Guo, H. X. Chen, S. C. Gan and Z. H. Diao, *Chem. Eng. J.*, 2024, **484**, 149543.

33 H. Rabiee, L. Ge, S. Hu, H. Wang and Z. Yuan, *Chem. Eng. J.*, 2022, **450**, 138476.

34 M. Yuan, M. J. Kummer and S. D. Minteer, *Chem. Eur. J.*, 2019, **25**, 14258–14266.

35 B. Tan, D. P. Hickey, R. D. Milton, F. Giroud and S. D. Minteer, *J. Electrochem. Soc.*, 2015, **162**, H102–H107.

36 B. Hu, D. F. Harris, D. R. Dean, T. L. Liu, Z. Y. Yang and L. C. Seefeldt, *Bioelectrochemistry*, 2018, **120**, 104–109.

37 M. T. Noori, M. T. Vu, R. B. Ali and B. Min, *Chem. Eng. J.*, 2020, **392**, 123689.

38 E. Sapountzaki, U. Rova, P. Christakopoulos and I. Antonopoulou, *ChemSusChem*, 2023, **16**, e202202312.

39 A. B. T. Nelabhotla and C. Dinamarca, *Rev. Environ. Sci. Biotechnol.*, 2018, **17**, 531–551.

40 P. Gupta, M. T. Noori, A. E. Núñez and N. Verma, *iScience*, 2021, **24**, 102294.

41 S. Popović, M. Smiljanić, P. Jovanovič, J. Vavra, R. Buonsanti and N. Hodnik, *Angew. Chem. Int. Edit.*, 2020, **59**, 14736–14746.

42 P. Saha, S. Amanullah and A. Dey, *Acc. Chem. Res.*, 2022, **55**, 134–144.

43 M. G. Kibria, J. P. Edwards, C. M. Gabardo, C.-T. Dinh, A. Seifitokaldani, D. Sinton and E. H. Sargent, *Adv. Mater.*, 2019, **31**, 1807166.

44 G. H. Han, J. Bang, G. Park, S. Choe, Y. J. Jang, H. W. Jang, S. Y. Kim and S. H. Ahn, *Small*, 2023, **19**, 2205765.

45 T. K. Todorova, M. W. Schreiber and M. Fontecave, *ACS Catal.*, 2020, **10**, 1754–1768.

46 S. Nitopi, E. Bertheussen, S. B. Scott, X. Liu, A. K. Engstfeld, S. Horch, B. Seger, I. E. L. Stephens, K. Chan, C. Hahn, J. K. Nørskov, T. F. Jaramillo and I. Chorkendorff, *Chem. Rev.*, 2019, **119**, 7610–7672.

47 W. Zhang, Y. Hu, L. Ma, G. Zhu, Y. Wang, X. Xue, R. Chen, S. Yang and Z. Jin, *Adv. Sci.*, 2018, **5**, 1700275.

48 C. Wang, A. He, N. Zhang, H. Sui, Z. Wen, C. Xu, G. Yan and R. Xue, *J. Catal.*, 2023, **428**, 115128.

49 I. Burgers, E. Pérez-Gallent, E. Goetheer and R. Kortlever, *Energy Technol.*, 2023, **11**, 2201465.

50 R. A. Tufa, D. Chanda, M. Ma, D. Aili, T. B. Demissie, J. Vaes, Q. Li, S. Liu and D. Pant, *Appl. Energy*, 2020, **277**, 115557.

51 A. Bagger, W. Ju, A. S. Varela, P. Strasser and J. Rossmeisl, *ChemPhysChem*, 2017, **18**, 3266–3273.

52 J. Hussain, H. Jónsson and E. Skúlason, *ACS Catal.*, 2018, **8**, 5240–5249.

53 S. Rasul, A. Pugnant, H. Xiang, J. M. Fontmorin and E. H. Yu, *J. CO_2 Util.*, 2019, **32**, 1–10.

54 J. Zou, G. Liang, C. Y. Lee and G. G. Wallace, *Mater. Today Energy*, 2023, **38**, 101433.

55 T. Zheng, K. Jiang, N. Ta, Y. Hu, J. Zeng, J. Liu and H. Wang, *Joule*, 2019, **3**, 265–278.

56 Q. He, J. H. Lee, D. Liu, Y. Liu, Z. Lin, Z. Xie, S. Hwang, S. Kattel, L. Song and J. G. Chen, *Adv. Funct. Mater.*, 2020, **30**, 2000407.

57 T. Qu, J. Hu, X. Dai, Q. Tan, Y. Liu, Y. Chen, S. Guo and Y. Liu, *ACS Appl. Mater. Interfaces*, 2021, **13**, 23523–23531.

58 M. Ma, H. A. Hansen, M. Valenti, Z. Wang, A. Cao, M. Dong and W. A. Smith, *Nano Energy*, 2017, **42**, 51–57.

59 J. Tian, K. Zhong, X. Zhu, J. Yang, Z. Mo, J. Liu, J. Dai, Y. She, Y. Song, H. Li and H. Xu, *Chem. Eng. J.*, 2023, **451**, 138392.

60 Y. S. Ham, S. Choe, M. J. Kim, T. Lim, S. K. Kim and J. J. Kim, *Appl. Catal. B*, 2017, **208**, 35–43.

61 T. Chen, J. Hu, K. Wang, K. Wang, W. Zhang, G. Gan and J. Shi, *J. Phys. Chem. Solids*, 2022, **163**, 110574.

62 B. Rhimi, M. Zhou, Z. Yan, X. Cai and Z. Jiang, *Nanomicro Lett.*, 2024, **16**, 64.

63 T. Dou, J. Du, J. He, Y. Wang, X. Zhao, F. Zhang and X. Lei, *J Power Sources*, 2022, **533**, 231393.

64 H. Han, S. Lee, J. Im, M. Lee, T. Lee, S. T. Hyun, J. Hong, T. Seok and D. Choo, *Chem. Eng. J.*, 2024, **479**, 147603.

65 B. Jung, S. Park, C. Lim, W. H. Lee, Y. Lim, J. Na, C. J. Lee, H. S. Oh and U. Lee, *Chem. Eng. J.*, 2021, **424**, 130265.

66 C. Chen, J. F. Khosrowabadi Kotyk and S. W. Sheehan, *Chem.*, 2018, **4**, 2571–2586.

67 O. S. Bushuyev, P. De Luna, C. T. Dinh, L. Tao, G. Saur, J. van de Lagemaat, S. O. Kelley and E. H. Sargent, *Joule*, 2018, **2**, 825–832.

68 Z. Sun, T. Ma, H. Tao, Q. Fan and B. Han, *Chem.*, 2017, **3**, 560–587.

69 S. M. Stratton, S. Zhang and M. M. Montemore, *Surf. Sci. Rep.*, 2023, **78**, 100597.

70 A. Goyal, G. Marcandalli, V. A. Mints and M. T. M. Koper, *J. Am. Chem. Soc.*, 2020, **142**, 4154–4161.

71 J. Tamura, A. Ono, Y. Sugano, C. Huang, H. Nishizawa and S. Mikoshiba, *Phys. Chem. Chem. Phys.*, 2015, **17**, 26072–26078.

72 Y. Chen, C. W. Li and M. W. Kanan, *J. Am. Chem. Soc.*, 2012, **134**, 19969–19972.

73 D. R. Yang, L. Liu, Q. Zhang, Y. Shi, Y. Zhou, C. Liu, F. Bin Wang and X. H. Xia, *Sci. Bull. (Beijing)*, 2020, **65**, 796–802.

74 M. Yang, J. Zhang, Y. Cao, M. Wu, K. Qian, Z. Zhang, H. Liu, J. Wang, W. Chen and W. Huang, *ChemCatChem*, 2018, **10**, 5128–5134.

75 S.-Q. Liu, S.-W. Wu, M.-R. Gao, M.-S. Li, X.-Z. Fu and J.-L. Luo, *ACS Sustain. Chem. Eng.*, 2019, **7**, 14443–14450.

76 M. Ma, K. Liu, J. Shen, R. Kas and W. A. Smith, *ACS Energy. Lett.*, 2018, **3**, 1301–1306.

77 W. Yang, W. Ma, Z. Zhang and C. Zhao, *Faraday Discuss*, 2018, **210**, 289–299.

78 Y. Lu, B. Han, C. Tian, J. Wu, D. Geng and D. Wang, *Electrochem. Commun.*, 2018, **97**, 87–90.

79 F. xia Shen, J. Shi, T. you Chen, F. Shi, Q. yuan Li, J. zheng Zhen, Y. fei Li, Y. nian Dai, B. Yang and T. Qu, *J. Power Sources*, 2018, **378**, 555–561.

80 K. Liu, J. Wang, M. Shi, J. Yan and Q. Jiang, *Adv. Energy Mater.*, 2019, **9**, 1900276.

81 T. Zhang, H. Zhong, Y. Qiu, X. Li and H. Zhang, *J. Mater. Chem. A Mater.*, 2016, **4**, 16670–16676.

82 S. Y. Lee, S. Y. Chae, H. Jung, C. W. Lee, D. L. T. Nguyen, H.-S. Oh, B. K. Min and Y. J. Hwang, *J. Mater. Chem. A Mater.*, 2020, **8**, 6210–6218.

83 D. Gao, I. Sinev, F. Scholten, R. M. Arán-Ais, N. J. Divins, K. Kvashnina, J. Timoshenko and B. Roldan Cuenya, *Angew. Chem. Int. Edit.*, 2019, **58**, 17047–17053.

84 K. Jiang, R. B. Sandberg, A. J. Akey, X. Liu, D. C. Bell, J. K. Nørskov, K. Chan and H. Wang, *Nat. Catal.*, 2018, **1**, 111–119.

85 F. S. Roberts, K. P. Kuhl and A. Nilsson, *ChemCatChem*, 2016, **8**, 1119–1124.

86 J. Li, G. Chen, Y. Zhu, Z. Liang, A. Pei, C.-L. Wu, H. Wang, H. R. Lee, K. Liu, S. Chu and Y. Cui, *Nat. Catal.*, 2018, **1**, 592–600.

87 Y. C. Tan, K. B. Lee, H. Song and J. Oh, *Joule*, 2020, **4**, 1104–1120.

88 M. Ma, K. Djanashvili and W. A. Smith, *Phys. Chem. Chem. Phys.*, 2015, **17**, 20861–20867.

89 G. Ma, O. A. Syzgantseva, Y. Huang, D. Stoian, J. Zhang, S. Yang, W. Luo, M. Jiang, S. Li, C. Chen, M. A. Syzgantseva, S. Yan, N. Chen, L. Peng, J. Li and B. Han, *Nat. Commun.*, 2023, **14**, 501.

90 S. C. Perry, S. Mavrikis, M. Wegener, P. Nazarovs, L. Wang and C. Ponce de León, *Faraday Discuss*, 2021, **230**, 375–387.

91 S. D. Giri, S. M. Mahajani, A. K. Suresh and A. Sarkar, *Mater. Res. Bull.*, 2020, **123**, 110702.

92 G. Ren, T. Dai, Y. Tang, Z. Su, N. Xu, W. Du, C. Dai and X. Ma, *J. CO_2 Util.*, 2022, **65**, 102256.

93 L. Xie, Y. Jiang, W. Zhu, S. Ding, Y. Zhou and J.-J. Zhu, *Chem. Sci.*, 2023, **14**, 13629–13660.

94 M. S. Xie, B. Y. Xia, Y. Li, Y. Yan, Y. Yang, Q. Sun, S. H. Chan, A. Fisher and X. Wang, *Energy Environ. Sci.*, 2016, **9**, 1687–1695.

95 X. Liu, P. Schlexer, J. Xiao, Y. Ji, L. Wang, R. B. Sandberg, M. Tang, K. S. Brown, H. Peng, S. Ringe, C. Hahn, T. F. Jaramillo, J. K. Nørskov and K. Chan, *Nat. Commun.*, 2019, **10**, 32.

96 A. S. Varela, *Curr. Opin. Green Sustain. Chem.*, 2020, **26**, 100371.

97 R. E. Warburton, A. V Soudackov and S. Hammes-Schiffer, *Chem. Rev.*, 2022, **122**, 10599–10650.

98 S. Garg, M. Li, A. Z. Weber, L. Ge, L. Li, V. Rudolph, G. Wang and T. E. Rufford, *J. Mater. Chem. A Mater.*, 2020, **8**, 1511–1544.

99 S. Ringe, C. G. Morales-Guio, L. D. Chen, M. Fields, T. F. Jaramillo, C. Hahn and K. Chan, *Nat. Commun.*, 2020, **11**, 33.

100 B. A. Zhang, T. Ozel, J. S. Elias, C. Costentin and D. G. Nocera, *ACS Cent. Sci.*, 2019, **5**, 1097–1105.

101 D. Bohra, J. H. Chaudhry, T. Burdyny, E. A. Pidko and W. A. Smith, *Energy Environ. Sci.*, 2019, **12**, 3380–3389.

102 B. M. Ceballos and J. Y. Yang, P*NAI*, 2018, **115**, 12686–12691.

103 T. Sheng and S. G. Sun, *J. Electroanal. Chem.*, 2017, **793**, 184–187.

104 N. J. Firet and W. A. Smith, *ACS Catal.*, 2017, **7**, 606–612.

105 W. Zheng, X. Yang, Z. Li, B. Yang, Q. Zhang, L. Lei and Y. Hou, *Angew. Chem. Int. Edit.*, 2023, **62**, e202307283.

106 N. Han, P. Ding, L. He, Y. Li and Y. Li, *Adv. Energy Mater.*, 2020, **10**, 1902338.

107 M. Li, Y. Hu, T. Wu, A. Sumboja and D. Geng, *Mater. Today*, 2023, **67**, 320–343.

108 Q. Zhao, J. M. P. Martirez and E. A. Carter, *J. Am. Chem. Soc.*, 2021, **143**, 6152–6164.

109 C. Xiao and J. Zhang, *ACS Nano*, 2021, **15**, 7975–8000.

110 J. Sang, P. Wei, T. Liu, H. Lv, X. Ni, D. Gao, J. Zhang, H. Li, Y. Zang, F. Yang, Z. Liu, G. Wang and X. Bao, *Angew. Chem. Int. Edit.*, 2022, **61**, e202114238.

111 C. W. Li and M. W. Kanan, *J. Am. Chem. Soc.*, 2012, **134**, 7231–7234.

112 M. Favaro, H. Xiao, T. Cheng, W. A. Goddard, J. Yano and E. J. Crumlin, *PNAI*, 2017, **114**, 6706–6711.

113 P. Iyengar, M. J. Kolb, J. R. Pankhurst, F. Calle-Vallejo and R. Buonsanti, *ACS Catal.*, 2021, **11**, 4456–4463.

114 H. Luo, B. Li, J.-G. Ma and P. Cheng, *Angew. Chem. Int. Edit.*, 2022, **61**, e202116736.

115 C. G. Morales-Guio, E. R. Cave, S. A. Nitopi, J. T. Feaster, L. Wang, K. P. Kuhl, A. Jackson, N. C. Johnson, D. N. Abram, T. Hatsukade, C. Hahn and T. F. Jaramillo, *Nat. Catal.*, 2018, **1**, 764–771.

116 H.-Q. Liang, T. Beweries, R. Francke and M. Beller, *Angew. Chem. Int. Edit.*, 2022, **61**, e202200723.

117 C. Costentin and J. M. Savéant, *Curr. Opin. Electrochem.*, 2017, **1**, 104–109.

118 Q. Zhao, J. M. P. Martirez and E. A. Carter, *J. Phys. Chem. Lett.*, 2022, **13**, 10282–10290.

119 K. J. P. Schouten, Z. Qin, E. Pérez Gallent and M. T. M. Koper, *J. Am. Chem. Soc.*, 2012, **134**, 9864–9867.

120 T. Zhang, B. Yuan, W. Wang, J. He and X. Xiang, *Angew. Chem. Int. Edit.*, 2023, **62**, e202302096.

121 R. Reske, H. Mistry, F. Behafarid, B. Roldan Cuenya and P. Strasser, *J. Am. Chem. Soc.*, 2014, **136**, 6978–6986.

122 W. Luo, X. Nie, M. J. Janik and A. Asthagiri, *ACS Catal.*, 2016, **6**, 219–229.

123 J. H. Montoya, A. A. Peterson and J. K. Nørskov, *ChemCatChem*, 2013, **5**, 737–742.

124 K. K. Patra, Z. Liu, H. Lee, S. Hong, H. Song, H. G. Abbas, Y. Kwon, S. Ringe and J. Oh, *ACS Catal.*, 2022, **12**, 10973–10983.

125 J. Zhang, Y. Wang, Z. Li, S. Xia, R. Cai, L. Ma, T. Zhang, J. Ackley, S. Yang, Y. Wu and J. Wu, *Adv. Sci.*, 2022, **9**, 2200454.

126 T. Kim and G. T. R. Palmore, *Nat. Commun.*, 2020, **11**, 3622.

127 J. Shan, Y. Shi, H. Li, Z. Chen, C. Sun, Y. Shuai and Z. Wang, *Chem. Eng. J.*, 2022, **433**, 133769.

128 L. Ma, W. Zhao, B. Wang, L. Ling and R. Zhang, *Fuel*, 2022, **313**, 122686.

129 X. Zhang, C. Liu, Y. Zhao, L. Li, Y. Chen, F. Raziq, L. Qiao, S. X. Guo, C. Wang, G. G. Wallace, A. M. Bond and J. Zhang, *Appl. Catal. B*, 2021, **291**, 120030.

130 Z. Gu, H. Shen, Z. Chen, Y. Yang, C. Yang, Y. Ji, Y. Wang, C. Zhu, J. Liu, J. Li, T. K. Sham, X. Xu and G. Zheng, *Joule*, 2021, **5**, 429–440.

131 S. Sen, D. Liu and G. T. R. Palmore, *ACS Catal.*, 2014, **4**, 3091–3095.

132 T. Cheng, H. Xiao and W. A. Goddard, *J. Am. Chem. Soc.*, 2017, **139**, 11642–11645.

133 D. Raciti, M. Mao, J. H. Park and C. Wang, *Catal. Sci. Technol.*, 2018, **8**, 2364–2369.

134 D. Gao, I. Zegkinoglou, N. J. Divins, F. Scholten, I. Sinev, P. Grosse and B. Roldan Cuenya, *ACS Nano*, 2017, **11**, 4825–4831.

135 X. Zi, Y. Zhou, L. Zhu, Q. Chen, Y. Tan, X. Wang, M. Sayed, E. Pensa, R. A. Geioushy, K. Liu, J. Fu, E. Cortés and M. Liu, *Angew. Chem. Int. Edit.*, 2023, **62**, e202309351.

136 T. Shi, D. Liu, H. Feng, Y. Zhang and Q. Li, *Chem. Eng. J.*, 2022, **431**, 134348.

137 I.-H. Tseng, Y.-H. Yang, Y.-T. Chen and L.-C. Hsu, *ACS Appl. Mater. Interfaces*, 2023, **15**, 5038–5048.

138 M. Ma, K. Djanashvili and W. A. Smith, *Angew. Chem. Int. Edit.*, 2016, **55**, 6680–6684.

139 Z.-Z. Niu, F.-Y. Gao, X.-L. Zhang, P.-P. Yang, R. Liu, L.-P. Chi, Z.-Z. Wu, S. Qin, X. Yu and M.-R. Gao, *J. Am. Chem. Soc.*, 2021, **143**, 8011–8021.

140 F. P. García de Arquer, C.-T. Dinh, A. Ozden, J. Wicks, C. McCallum, A. R. Kirmani, D.-H. Nam, C. Gabardo, A. Seifitokaldani, X. Wang, Y. C. Li, F. Li, J. Edwards, L. J. Richter, S. J. Thorpe, D. Sinton and E. H. Sargent, *Science*, 2020, **367**, 661–666.

141 M. Zhuansun, Y. Liu, R. Lu, F. Zeng, Z. Xu, Y. Wang, Y. Yang, Z. Wang, G. Zheng and Y. Wang, *Angew. Chem. Int. Edit.*, 2023, **62**, e202309875.

142 J. Bai, W. Wang and J. Liu, *Chem. Eur. J.*, 2023, **29**, e202302461.

143 L. Li, X. Zhang, C. Liu, V. S. S. Mosali, J. Chen, A. M. Bond, Q. Gu and J. Zhang, *Appl. Catal. B*, 2023, **331**, 122597.

144 A. Senocrate, F. Bernasconi, D. Rentsch, K. Kraft, M. Trottmann, A. Wichser, D. Bleiner and C. Battaglia, *ACS Appl. Energy Mater.*, 2022, **5**, 14504–14512.

145 D. Wakerley, S. Lamaison, F. Ozanam, N. Menguy, D. Mercier, P. Marcus, M. Fontecave and V. Mougel, *Nat. Mater.*, 2019, **18**, 1222–1227.

146 Z. Han, R. Kortlever, H.-Y. Chen, J. C. Peters and T. Agapie, *ACS Cent. Sci.*, 2017, **3**, 853–859.

147 H. Liu, K. Xiang, Y. Liu, F. Zhu, M. Zou, X. Yan and L. Chai, *ChemElectroChem*, 2018, **5**, 3991–3999.

148 X. Wei, Z. Yin, K. Lyu, Z. Li, J. Gong, G. Wang, L. Xiao, J. Lu and L. Zhuang, *ACS Catal.*, 2020, **10**, 4103–4111.

149 Z. Liu, X. Lv, S. Kong, M. Liu, K. Liu, J. Zhang, B. Wu, Q. Zhang, Y. Tang, L. Qian, L. Zhang and G. Zheng, *Angew. Chem. Int. Edit.*, 2023, **62**, e202309319.

150 M. Liu, Y. Pang, B. Zhang, P. De Luna, O. Voznyy, J. Xu, X. Zheng, C. T. Dinh, F. Fan, C. Cao, F. P. G. de Arquer, T. S. Safaei, A. Mepham, A. Klinkova, E.

Kumacheva, T. Filleter, D. Sinton, S. O. Kelley and E. H. Sargent, *Nature*, 2016, **537**, 382–386.

151 M. Bevilacqua, J. Filippi, A. Lavacchi, A. Marchionni, H. A. Miller, W. Oberhauser, E. Vesselli and F. Vizza, *Energy Technol.*, 2014, **2**, 522–525.

152 D. T. Whipple, E. C. Finke and P. J. A. Kenis, *Electrochem. Solid-St. Lett.*, 2010, **13**, B109.

153 G. Kaur, A. P. Kulkarni and S. Giddey, *Int. J. Hydrogen Energy*, 2018, **43**, 21769–21776.

154 E. L. Clark, M. R. Singh, Y. Kwon and A. T. Bell, *Anal. Chem.*, 2015, **87**, 8013–8020.

155 C. Zhao and J. Wang, *Chem. Eng. J.*, 2016, **293**, 161–170.

156 K. P. Kuhl, E. R. Cave, D. N. Abram and T. F. Jaramillo, *Energy Environ. Sci.*, 2012, **5**, 7050–7059.

157 D. Ewis, M. Arsalan, M. Khaled, D. Pant, M. M. Ba-Abbad, A. Amhamed and M. H. El-Naas, *Sep. Purif. Technol.*, 2023, **316**, 123811.

158 S. A. Al-Tamreh, M. H. Ibrahim, M. H. El-Naas, J. Vaes, D. Pant, A. Benamor and A. Amhamed, *ChemElectroChem*, 2021, **8**, 3207–3220.

159 A. Löwe, C. Rieg, T. Hierlemann, N. Salas, D. Kopljar, N. Wagner and E. Klemm, *ChemElectroChem*, 2019, **6**, 4497–4506.

160 K. P. Kuhl, E. R. Cave, D. N. Abram and T. F. Jaramillo, *Energy Environ. Sci.*, 2012, **5**, 7050–7059.

161 J. Wu, F. G. Risalvato, P. P. Sharma, P. J. Pellechia, F.-S. Ke and X.-D. Zhou, *J. Electrochem. Soc.*, 2013, **160**, F953.

162 S. Ren, D. Joulié, D. Salvatore, K. Torbensen, M. Wang, M. Robert and C. P. Berlinguette, *Science*, 2019, **365**, 367–369.

163 R. Inguanta, S. Piazza and C. Sunseri, *Appl. Surf. Sci.*, 2009, **255**, 8816–8823.

164 D. Voiry, M. Chhowalla, Y. Gogotsi, N. A. Kotov, Y. Li, R. M. Penner, R. E. Schaak and P. S. Weiss, *ACS Nano*, 2018, **12**, 9635–9638.

165 P. Connor, J. Schuch, B. Kaiser and W. Jaegermann, *Zeitschrift für Physikalische Chemie*, 2020, **234**, 979–994.

166 L. Xiao, G. G. Wildgoose and R. G. Compton, *New J. Chem.*, 2008, **32**, 1628–1633.

167 Q. Lin, Q. Li, C. Batchelor-McAuley and R. G. Compton, *Phys. Chem. Chem. Phys.*, 2013, **15**, 7760–7767.

168 P. M. S. Monk, C. Turner and S. P. Akhtar, *Electrochim. Acta*, 1999, **44**, 4817–4826.

169 T. R. L. C. Paixão, *ChemElectroChem*, 2020, **7**, 3414–3415.

170 A. Sah, H. L. Castricum, A. Bliek, D. H. A. Blank and J. E. Ten Elshof, *J. Memb. Sci.*, 2004, **243**, 125–132.

171 J. Yu, S. Li, D. Hou, Z. Jin and Q. Liu, *Phys. Chem. Chem. Phys.*, 2019, **21**, 19026–19038.

172 C. Picard, A. Larbot, F. Guida-Pietrasanta, B. Boutevin and A. Ratsimihety, *Sep. Purif. Technol.*, 2001, **25**, 65–69.

173 X. Han, L. Wang, J. Li, X. Zhan, J. Chen and J. Yang, *Appl. Surf. Sci.*, 2011, **257**, 9525–9531.

174 A. Y. Fadeev, R. Helmy and S. Marcinko, *Langmuir*, 2002, **18**, 7521–7529.

175 Z. Ma, Z. Yang, W. Lai, Q. Wang, Y. Qiao, H. Tao, C. Lian, M. Liu, C. Ma, A. Pan and H. Huang, *Nat. Commun.*, 2022, **13**, 7596.

176 C. F. C. Lim, University of Canterbury, 2017.

177 Z. Han, R. Kortlever, H.-Y. Chen, J. C. Peters and T. Agapie, *ACS Cent. Sci.*, 2017, **3**, 853–859.

178 K. P. Kuhl, E. R. Cave, D. N. Abram and T. F. Jaramillo, *Energy Environ. Sci.*, 2012, **5**, 7050–7059.

179 C. S. Chen, J. H. Wan and B. S. Yeo, *J. Phys. Chem. C*, 2015, **119**, 26875–26882.

180 D. Raciti, L. Cao, K. J. T. Livi, P. F. Rottmann, X. Tang, C. Li, Z. Hicks, K. H. Bowen, K. J. Hemker, T. Mueller and C. Wang, *ACS Catal.*, 2017, **7**, 4467–4472.

181 S. Liang, N. Altaf, L. Huang, Y. Gao and Q. Wang, *J. CO_2 Util.*, 2020, **35**, 90–105.

182 C. Zhao and J. Wang, *Chem. Eng. J.*, 2016, **293**, 161–170.

183 A. Gawel, T. Jaster, D. Siegmund, J. Holzmann, H. Lohmann, E. Klemm and U. P. Apfel, *iScience*, 2022, **25**, 104011.

184 T. Burdyny and W. A. Smith, *Energy Environ. Sci.*, 2019, **12**, 1442–1453.

185 Z.-Z. Niu, L.-P. Chi, R. Liu, Z. Chen and M.-R. Gao, *Energy Environ. Sci.*, 2021, **14**, 4169–4176.

186 D. Ma, T. Jin, K. Xie and H. Huang, *J. Mater. Chem. A Mater.*, 2021, **9**, 20897–20918.

187 D. M. Weekes, D. A. Salvatore, A. Reyes, A. Huang and C. P. Berlinguette, *Acc. Chem. Res.*, 2018, **51**, 910–918.

188 B. Liu, T. Wang, S. Wang, G. Zhang, D. Zhong, T. Yuan, H. Dong, B. Wu and J. Gong, *Nat. Commun.*, 2022, **13**, 7111.

189 C. Chen, Y. Li, S. Yu, S. Louisia, J. Jin, M. Li, M. B. Ross and P. Yang, *Joule*, 2020, **4**, 1688–1699.

190 H. Yan, H. S. Choe, S. Nam, Y. Hu, S. Das, J. F. Klemic, J. C. Ellenbogen and C. M. Lieber, *Nature*, 2011, **470**, 240–244.

191 S. Khan, B. A. Primavera, J. Chiles, A. N. McCaughan, S. M. Buckley, A. N. Tait, A. Lita, J. Biesecker, A. Fox, D. Olaya, R. P. Mirin, S. W. Nam and J. M. Shainline, *Nat. Electron.*, 2022, **5**, 650–659.

192 A. Takemoto, T. Araki, K. Nishimura, M. Akiyama, T. Uemura, K. Kiriyama, J. M. Koot, Y. Kasai, N. Kurihira, S. Osaki, S. Wakida, J. M. J. den Toonder and T. Sekitani, *Adv. Sci.*, 2023, **10**, 2204746.

193 J. Meng and Z. Li, *Adv. Mater.*, 2020, **32**, 2000130.

194 Q.-L. Liao, H. Jiang, X.-W. Zhang, Q.-F. Qiu, Y. Tang, X.-K. Yang, Y.-L. Liu and W.-H. Huang, *Nanoscale*, 2019, **11**, 10702–10708.

195 X. Li, Y. Wang, C. Yin and Z. Yin, *J Mater Chem C Mater*, 2020, **8**, 849–872.

196 D. Wang, Y. Zhang, X. Lu, Z. Ma, C. Xie and Z. Zheng, *Chem. Soc. Rev.*, 2018, **47**, 4611–4641.

197 A. Ganapathi, P. Swaminathan and L. Neelakantan, *ACS Appl. Nano Mater.*, 2019, **2**, 5981–5988.

198 O. E. Cigarroa-Mayorga, S. Gallardo-Hernández and P. Talamás-Rohana, *Appl. Surf. Sci.*, 2021, **536**, 147674.

199 A. K. Singh and O. N. Srivastava, *Nanoscale Res. Lett.*, 2015, **10**, 353.

200 W. Zhu, K. Zhao, S. Liu, M. Liu, F. Peng, P. An, B. Qin, H. Zhou, H. Li and Z. He, *J. Energy Chem.*, 2019, **37**, 176–182.

201 A. Conte, M. Baron, S. Bonacchi, S. Antonello and A. Aliprandi, *Nanoscale*, 2023, **15**, 3693–3703.

202 G. Riveros, H. Gómez, A. Cortes, R. E. Marotti and E. A. Dalchiele, *Appl. Phys. A*, 2005, **81**, 17–24.

203 A. Yadav, M. Muthukumar and M. S. Bobji, *Surf. and Interfaces*, 2021, **24**, 101115.

204 J. Vanpaemel, A. M. Abd-Elnaiem, S. De Gendt and P. M. Vereecken, *J. Phys. Chem. C*, 2015, **119**, 2105–2112.

205 L. Zaraska, G. D. Sulka and M. Jaskuła, *Appl. Surf. Sci.*, 2012, **258**, 7781–7786.

206 S. M. Reddy, J. J. Park, S.-M. Na, M. M. Maqableh, A. B. Flatau and B. J. H. Stadler, *Adv. Funct. Mater.*, 2011, **21**, 4677–4683.

207 Y. H. Lee, I. C. Leu, M. T. Wu, J. H. Yen and K. Z. Fung, *J. Alloys Compd.*, 2007, **427**, 213–218.

208 L. Ji, L. Zhu, J. Wang and Z. Chen, *Electrochim. Acta*, 2017, **252**, 516–522.

209 S. Kukunuri, K. Naik and S. Sampath, *J. Mater. Chem. A Mater.*, 2017, **5**, 4660–4670.

210 X. D. Yang, X. D. Yang, T. L. Wang, B. Y. Wang, Q. Chen, Y. Q. Wang and D. L. Liu, *New J. Chem.*, 2020, **44**, 64–71.

211 R. Inguanta, S. Piazza and C. Sunseri, *Appl. Surf. Sci.*, 2009, **255**, 8816–8823.

212 Z.-C. Meng, L.-Y. Gao and Z.-Q. Liu, *J. Electron. Mater.*, 2023, **52**, 3463–3471.

213 H. S. Jeon, S. Kunze, F. Scholten and B. Roldan Cuenya, *ACS Catal.*, 2018, **8**, 531–535.

214 E. O. Barnes, X. Chen, P. Li and R. G. Compton, *J. Electroanal. Chem.*, 2014, **720–721**, 92–100.

215 K. Jangid, R. Gupta, R. P. Sahu, I. Zhitomirsky and I. K. Puri, *J. Electroanal. Chem.*, 2022, **910**, 116200.

216 Q. Feng, W. N. Yue and T. M. Cotton, *J. Phys. Chem.*, 1990, **94**, 2082–2091.

217 J. W. Zheng, X. W. Li, R. N. Gu and T. H. Lu, *J. Phys. Chem. B*, 2002, **106**, 1019–1023.

218 L. Xiao, G. G. Wildgoose and R. G. Compton, *New J. Chem.*, 2008, **32**, 1628–1633.

219 Q. Lin, Q. Li, C. Batchelor-McAuley and R. G. Compton, *Phys. Chem. Chem. Phys.*, 2013, **15**, 7760–7767.

220 S. Sen, D. Liu and G. T. R. Palmore, *ACS Catal.*, 2014, **4**, 3091–3095.

221 M. Rahaman, A. Dutta, A. Zanetti and P. Broekmann, *ACS Catal.*, 2017, **7**, 7946–7956.

222 T. R. L. C. Paixão, *ChemElectroChem*, 2020, **7**, 3414–3415.

223 M. Gu and B.-S. Kim, *Acc. Chem. Res.*, 2021, **54**, 57–69.

224 Q. Cao, Z. Shao, D. K. Hensley, N. V Lavrik and B. J. Venton, *Langmuir*, 2021, **37**, 2667–2676.

225 E. M. Akinoglu, E. Kätelhön, J. Pampel, Z. Ban, M. Antonietti, R. G. Compton and M. Giersig, *Carbon*, 2018, **130**, 768–774.

226 P. He, Y. Quan, X. Xu, M. Yan, W. Yang, Q. An, L. He and L. Mai, *Small*, 2017, **13**, 1702551.

227 P. Zhu and Y. Zhao, *Mater. Chem. Phys.*, 2019, **233**, 60–67.

228 I. I. Suni, *TrAC Trends in Anal. Chem.*, 2008, **27**, 604–611.

229 G. Barbero and I. Lelidis, *Phys. Chem. Chem. Phys.*, 2017, **19**, 24934–24944.

230 I. Roh, S. Yu, C.-K. Lin, S. Louisia, S. Cestellos-Blanco and P. Yang, *J. Am. Chem. Soc.*, 2022, **144**, 8002–8006.

231 L. Han, B. Tian, X. Gao, Y. Zhong, S. Wang, S. Song, Z. Wang, Y. Zhang, Y. Kuang and X. Sun, *SmartMat.*, 2022, **3**, 142–150.

232 F. Mattarozzi, N. van der Willige, V. Gulino, C. Keijzer, R. C. J. van de Poll, E. J. M. Hensen, P. Ngene and P. E. de Jongh, *ChemCatChem*, 2023, **15**, e202300792.

233 W. Zhu, K. Zhao, S. Liu, M. Liu, F. Peng, P. An, B. Qin, H. Zhou, H. Li and Z. He, *J. Energy Chem.*, 2019, **37**, 176–182.

234 Y. Wu, X. Deng, H. Yuan, X. Yang, J. Wang and X. Wang, *ChemElectroChem*, 2021, **8**, 2701–2707.

235 S. Mou, Y. Li, L. Yue, J. Liang, Y. Luo, Q. Liu, T. Li, S. Lu, A. M. Asiri, X. Xiong, D. Ma and X. Sun, *Nano Res.*, 2021, **14**, 2831–2836.

236 Y. Wang, C. Niu, Y. Zhu, D. He and W. Huang, *ACS Appl. Energy Mater.*, 2020, **3**, 9841–9847.

237 D. Er, B. Avcı and M. Ürgen, *ChemElectroChem*, 2023, **10**, e202300196.

238 N. Ulrich, M. Schäfer, M. Römer, S. D. Straub, S. Zhang, J. Brötz, C. Trautmann, C. Scheu, B. J. M. Etzold and M. E. Toimil-Molares, *ACS Appl. Nano Mater.*, 2023, **6**, 4190–4200.

239 Z. Lyu, S. Zhu, M. Xie, Y. Zhang, Z. Chen, R. Chen, M. Tian, M. Chi, M. Shao and Y. Xia, *Angew. Chem. Int. Edit.*, 2021, **60**, 1909–1915.

240 J. Zhang, Z. Li, S. Xia, T. Zhang, Y. Wang, Y. Wu and J. Wu, *Chem. Commun.*, 2021, **57**, 8276–8279.

241 A. Conte, M. Baron, S. Bonacchi, S. Antonello and A. Aliprandi, *Nanoscale*, 2023, **15**, 3693–3703.

242 C. Yang, Y. Wang, L. Qian, A. M. Al-Enizi, L. Zhang and G. Zheng, *ACS Appl. Energy Mater.*, 2021, **4**, 1034–1044.

243 H. Song, J. T. Song, B. Kim, Y. C. Tan and J. Oh, *Appl. Catal. B*, 2020, **272**, 119049.

244 X. Tan, W. Guo, S. Liu, S. Jia, L. Xu, J. Feng, X. Yan, C. Chen, Q. Zhu, X. Sun and B. Han, *Chem. Sci.*, 2022, **13**, 11918–11925.

245 M. Fang, M. Wang, Z. Wang, Z. Zhang, H. Zhou, L. Dai, Y. Zhu and L. Jiang, *J. Am. Chem. Soc.*, 2023, **145**, 11323–11332.

246 Z.-Z. Niu, F.-Y. Gao, X.-L. Zhang, P.-P. Yang, R. Liu, L.-P. Chi, Z.-Z. Wu, S. Qin, X. Yu and M.-R. Gao, *J. Am. Chem. Soc.*, 2021, **143**, 8011–8021.

247 J.-J. Lv, R. Yin, L. Zhou, J. Li, R. Kikas, T. Xu, Z.-J. Wang, H. Jin, X. Wang and S. Wang, *Angew. Chem. Int. Edit.*, 2022, **61**, e202207252.

248 F. P. García de Arquer, C.-T. Dinh, A. Ozden, J. Wicks, C. McCallum, A. R. Kirmani, D.-H. Nam, C. Gabardo, A. Seifitokaldani, X. Wang, Y. C. Li, F. Li, J. Edwards, L. J. Richter, S. J. Thorpe, D. Sinton and E. H. Sargent, *Science*, 2020, **367**, 661–666.

249 D. Wang, J. Mao, C. Zhang, J. Zhang, J. Li, Y. Zhang and Y. Zhu, *eScience*, 2023, **3**, 100119.

250 Y. Zhong, Y. Xu, J. Ma, C. Wang, S. Sheng, C. Cheng, M. Li, L. Han, L. Zhou, Z. Cai, Y. Kuang, Z. Liang and X. Sun, *Angew. Chem. Int. Edit.*, 2020, **59**, 19095–19101.

251 H.-Q. Liang, S. Zhao, X.-M. Hu, M. Ceccato, T. Skrydstrup and K. Daasbjerg, *ACS Catal.*, 2021, **11**, 958–966.

252 A. K. Buckley, M. Lee, T. Cheng, R. V Kazantsev, D. M. Larson, W. A. Goddard III, F. D. Toste and F. M. Toma, *J. Am. Chem. Soc.*, 2019, **141**, 7355–7364.

253 C. Ye, S. J. Raaijman, X. Chen and M. T. M. Koper, *ACS Appl. Mater. Interfaces*, 2022, **14**, 45263–45271.

254 J. Peng, B. Chen, Z. Wang, J. Guo, B. Wu, S. Hao, Q. Zhang, L. Gu, Q. Zhou, Z. Liu, S. Hong, S. You, A. Fu, Z. Shi, H. Xie, D. Cao, C.-J. Lin, G. Fu, L.-S. Zheng, Y. Jiang and N. Zheng, *Nature*, 2020, **586**, 390–394.

255 H. Sun, O. A. Zelekew, X. Chen, Y. Guo, D.-H. Kuo, Q. Lu and J. Lin, *RSC Adv.*, 2019, **9**, 31828–31839.

256 M. Sun, Z. Li, Q. Fang, S. Han, C. Cai, H. Li, W. Shen, X. Liu and Y. Fu, *J. Mater. Chem. A Mater.*, 2020, **8**, 724–734.

257 A. Kumar, A. Thomas, M. Garg, G. Perumal, H. S. Grewal and H. S. Arora, *J. Mater. Chem. A Mater.*, 2021, **9**, 9327–9336.

258 J. Jiang, X. X. Liu, J. Han, K. Hu and J. S. Chen, *Processes*, DOI:10.3390/pr9040680.

259 M. Swadźba-Kwaśny, L. Chancelier, S. Ng, H. G. Manyar, C. Hardacre and P. Nockemann, *Dalton T.*, 2012, **41**, 219–227.

260 Z. Lyu, S. Zhu, M. Xie, Y. Zhang, Z. Chen, R. Chen, M. Tian, M. Chi, M. Shao and Y. Xia, *Angew. Chem. Int. Edit.*, 2021, **60**, 1909–1915.

261 S. Jia, Q. Zhu, S. Han, J. Zhai, M. Dong, W. Xia, X. Xing, H. Wu, M. He and B. Han, *Chem. Sci.*, 2023, **14**, 11474–11480.

262 M. Rahaman, A. Dutta, A. Zanetti and P. Broekmann, *ACS Catal.*, 2017, **7**, 7946–7956.

263 D. Wakerley, S. Lamaison, F. Ozanam, N. Menguy, D. Mercier, P. Marcus, M. Fontecave and V. Mougel, *Nat. Mater.*, 2019, **18**, 1222–1227.

264 C. Kim, J. C. Bui, X. Luo, J. K. Cooper, A. Kusoglu, A. Z. Weber and A. T. Bell, *Nat. Energy*, 2021, **6**, 1026–1034.

265 E. M. Akinoglu, E. Kätelhön, J. Pampel, Z. Ban, M. Antonietti, R. G. Compton and M. Giersig, *Carbon*, 2018, **130**, 768–774.

266 K. R. Ward and R. G. Compton, *J. Electroanal. Chem.*, 2014, **724**, 43–47.

267 E. O. Barnes, X. Chen, P. Li and R. G. Compton, *J. Electroanal. Chem.*, 2014, **720–721**, 92–100.

268 H. Gerengi, K. Schaefer and H. I. Sahin, *J. Ind. Eng. Chem.*, 2012, **18**, 2204–2210.

269 B. A. Abd-El-Nabey, S. El-Housseiny and M. A. Abd-El-Fatah, *Sci. Rep.*, 2022, **12**, 15346.

270 C. Cao and Z. Wen, *J. CO_2 Util.*, 2017, **22**, 231–237.

271 W. T. Osowiecki, J. J. Nussbaum, G. A. Kamat, G. Katsoukis, M. Ledendecker, H. Frei, A. T. Bell and A. P. Alivisatos, *ACS Appl. Energy Mater.*, 2019, **2**, 7744–7749.

272 S. Min, X. Yang, A. Y. Lu, C. C. Tseng, M. N. Hedhili, L. J. Li and K. W. Huang, *Nano Energy*, 2016, **27**, 121–129.

273 H. Xie, T. Wang, J. Liang, Q. Li and S. Sun, *Nano Today*, 2018, **21**, 41–54.

274 M. Wu, C. Zhu, K. Wang, G. Li, X. Dong, Y. Song, J. Xue, W. Chen, W. Wei and Y. Sun, *ACS Appl. Mater. Interfaces*, 2020, **12**, 11562–11569.

275 Y.-J. Zhang, V. Sethuraman, R. Michalsky and A. A. Peterson, *ACS Catal.*, 2014, **4**, 3742–3748.

276 H. Wu, J. Li, K. Qi, Y. Zhang, E. Petit, W. Wang, V. Flaud, N. Onofrio, B. Rebiere, L. Huang, C. Salameh, L. Lajaunie, P. Miele and D. Voiry, *Nat. Commun.*, 2021, **12**, 7210.

277 T. Zheng, C. Liu, C. Guo, M. Zhang, X. Li, Q. Jiang, W. Xue, H. Li, A. Li, C.-W. Pao, J. Xiao, C. Xia and J. Zeng, *Nat. Nanotechnol.*, 2021, **16**, 1386–1393.

278 Y. Zhao, L. Hao, A. Ozden, S. Liu, R. K. Miao, P. Ou, T. Alkayyali, S. Zhang, J. Ning, Y. Liang, Y. Xu, M. Fan, Y. Chen, J. E. Huang, K. Xie, J. Zhang, C. P. O'Brien, F. Li, E. H. Sargent and D. Sinton, *Nat. Synth.*, 2023, **2**, 403–412.

279 C.-T. Dinh, T. Burdyny, M. G. Kibria, A. Seifitokaldani, C. M. Gabardo, F. P. García de Arquer, A. Kiani, J. P. Edwards, P. De Luna, O. S. Bushuyev, C. Zou, R. Quintero-Bermudez, Y. Pang, D. Sinton and E. H. Sargent, *Science*, 2018, **360**, 783–787.

280 G. Lee, Y. C. Li, J.-Y. Kim, T. Peng, D.-H. Nam, A. Sedighian Rasouli, F. Li, M. Luo, A. H. Ip, Y.-C. Joo and E. H. Sargent, *Nat. Energy*, 2021, **6**, 46–53.

281 N. Sreekanth, M. A. Nazrulla, T. V. Vineesh, K. Sailaja and K. L. Phani, *Chem. Commun.*, 2015, **51**, 16061–16064.

282 J. E. Huang, F. Li, A. Ozden, A. Sedighian Rasouli, F. P. García de Arquer, S. Liu, S. Zhang, M. Luo, X. Wang, Y. Lum, Y. Xu, K. Bertens, R. K. Miao, C.-T. Dinh, D. Sinton and E. H. Sargent, *Science*, 2021, **372**, 1074–1078.

283 Y. Cui, Y. Cheng, C. Yang, Y. Su, D. Yao, B. Liufu, J. Li, Y. Fang, S. Liu, Z. Zhong, X. Wang, Y. Song and Z. Li, *ACS Sustain. Chem. Eng.*, 2023, **11**, 11229–11238.

284 Y. Wen, W.-H. Cheng, Y.-R. Wang, F.-C. Shen and Y.-Q. Lan, *Small*, 2023, **n/a**, 2307467.

285 S. Mu, L. Li, R. Zhao, H. Lu, H. Dong and C. Cui, *ACS Appl. Mater. Interfaces*, 2021, **13**, 47619–47628.

286 T. Shi, D. Liu, H. Feng, Y. Zhang and Q. Li, *Chem. Eng. J.*, 2022, **431**, 134348.

287 D. Zeng, C. Li, W. Wang, L. Zhang, Y. Zhang, J. Wang, L. Zhang, X. Zhou and W. Wang, *Chem. Eng. J.*, 2023, **461**, 142133.

288 Y. Lin, T. Wang, L. Zhang, G. Zhang, L. Li, Q. Chang, Z. Pang, H. Gao, K. Huang, P. Zhang, Z.-J. Zhao, C. Pei and J. Gong, *Nat. Commun.*, 2023, **14**, 3575.

289 S. Popović, M. A. Nazrulla, P. Šket, K. M. Kamal, B. Likozar, L. Suhadolnik, L. Pavko, A. K. Surca, M. Bele and N. Hodnik, *Electrochim. Acta*, 2022, **436**, 141458.

290 A. K. Ummireddi, S. K. Sharma and R. G. S. Pala, *Catal. Sci. Technol.*, 2021, **11**, 4857–4865.

291 X. Su, Z. Jiang, J. Zhou, H. Liu, D. Zhou, H. Shang, X. Ni, Z. Peng, F. Yang, W. Chen, Z. Qi, D. Wang and Y. Wang, *Nat. Commun.*, 2022, **13**, 1322.

292 A. R. Woldu, Z. Huang, P. Zhao, L. Hu and D. Astruc, *Coord. Chem. Rev.*, 2022, **454**, 214340.

293 P. Li, J. Bi, J. Liu, Q. Zhu, C. Chen, X. Sun, J. Zhang, Z. Liu and B. Han, *Chem. Sci.*, 2023, **14**, 310–316.

294 Z. Han, D. Han, Z. Chen, J. Gao, G. Jiang, X. Wang, S. Lyu, Y. Guo, C. Geng, L. Yin, Z. Weng and Q.-H. Yang, *Nat. Commun.*, 2022, **13**, 3158.

295 J. F. Xie, Y. X. Huang, W. W. Li, X. N. Song, L. Xiong and H. Q. Yu, *Electrochim. Acta*, 2014, **139**, 137–144.

296 X. Zhang, S. X. Guo, K. A. Gandionco, A. M. Bond and J. Zhang, *Mater. Today Adv*, 2020, **7**, 100074.

297 C. Choi, S. Kwon, T. Cheng, M. Xu, P. Tieu, C. Lee, J. Cai, H. M. Lee, X. Pan, X. Duan, W. A. Goddard and Y. Huang, *Nat. Catal.*, 2020, **3**, 804–812.

298 W. He, I. Liberman, I. Rozenberg, R. Ifraemov and I. Hod, *Angew. Chem. Int. Edit.*, 2020, **59**, 8262–8269.

299 D. Ewis, M. Arsalan, M. Khaled, D. Pant, M. M. Ba-Abbad, A. Amhamed and M. H. El-Naas, *Sep. Purif. Technol.*, 2023, **316**, 123811.

300 J. T. Feaster, C. Shi, E. R. Cave, T. Hatsukade, D. N. Abram, K. P. Kuhl, C. Hahn, J. K. Nørskov and T. F. Jaramillo, *ACS Catal.*, 2017, **7**, 4822–4827.

301 P. Wang, H. Yang, C. Tang, Y. Wu, Y. Zheng, T. Cheng, K. Davey, X. Huang and S.-Z. Qiao, *Nat. Commun.*, 2022, **13**, 3754.

302 Y. Baek, H. Song, D. Hong, S. Wang, S. Lee, Y.-C. Joo, G.-D. Lee and J. Oh, *J. Mater. Chem. A Mater.*, 2022, **10**, 9393–9401.

303 H. Lee, J. Kim, I. Choi and S. H. Ahn, *Electrochim. Acta*, 2019, **323**, 133102.

304 H. Wu, J. Li, K. Qi, Y. Zhang, E. Petit, W. Wang, V. Flaud, N. Onofrio, B. Rebiere, L. Huang, C. Salameh, L. Lajaunie, P. Miele and D. Voiry, *Nat. Commun.*, 2021, **12**, 7210.

305 J. Wang, J. Zou, X. Hu, S. Ning, X. Wang, X. Kang and S. Chen, *J. Mater. Chem. A Mater.*, 2019, **7**, 27514–27521.

306 S. Asperti, R. Hendrikx, Y. Gonzalez-Garcia and R. Kortlever, *ChemCatChem*, 2022, **14**, e202200540.

307 G. Li, H. Liu, H. Yang, X. Chen, K. Ji, D. Yang, S. Zhang and X. Ma, *Chem. Eng. Sci.*, 2022, **263**, 118142.

308 A. Dutta, M. Rahaman, N. C. Luedi, M. Mohos and P. Broekmann, *ACS Catal.*, 2016, **6**, 3804–3814.

309 H. Mistry, A. S. Varela, C. S. Bonifacio, I. Zegkinoglou, I. Sinev, Y.-W. Choi, K. Kisslinger, E. A. Stach, J. C. Yang, P. Strasser and B. R. Cuenya, *Nat. Commun.*, 2016, **7**, 12123.

310 M. Ma, K. Djanashvili and W. A. Smith, *Angew. Chem. Int. Edit.*, 2016, **55**, 6680–6684.

311 N. Ulrich, M. Schäfer, M. Römer, S. D. Straub, S. Zhang, J. Brötz, C. Trautmann, C. Scheu, B. J. M. Etzold and M. E. Toimil-Molares, *ACS Appl. Nano Mater.*, 2023, **6**, 4190–4200.

312 Y. Wang, Y. Zhu and C. Niu, *J. Phys. Chem. Solids*, 2020, **144**, 109507.

313 D. Raciti, M. Mao, J. H. Park and C. Wang, *Catal. Sci. Technol.*, 2018, **8**, 2364–2369.

314 Y. Fu, Q. Xie, L. Wu and J. Luo, *Chinese J. Catal.*, 2022, **43**, 1066–1073.

315 T. Kim, A. Kargar, Y. Luo, R. Mohammed, E. Martinez-Loran, A. Ganapathi, P. Shah and D. P. Fenning, *ACS Appl. Energy Mater.*, 2018, **1**, 1965–1972.

316 Q. Zhang, D. Ren, S. Pan, M. Wang, J. Luo, Y. Zhao, M. Grätzel and X. Zhang, *Adv. Funct. Mater.*, 2021, **31**, 2103966.

317 H. Zhang, Y. Zhang, Y. Li, S. Ahn, G. T. R. Palmore, J. Fu, A. A. Peterson and S. Sun, *Nanoscale*, 2019, **11**, 12075–12079.

318 K. Manthiram, B. J. Beberwyck and A. P. Alivisatos, *J. Am. Chem. Soc.*, 2014, **136**, 13319–13325.

319 C. S. Chen, A. D. Handoko, J. H. Wan, L. Ma, D. Ren and B. S. Yeo, *Catal. Sci. Technol.*, 2015, **5**, 161–168.

320 L. Wu, K. E. Kolmeijer, Y. Zhang, H. An, S. Arnouts, S. Bals, T. Altantzis, J. P. Hofmann, M. Costa Figueiredo, E. J. M. Hensen, B. M. Weckhuysen and W. van der Stam, *Nanoscale*, 2021, **13**, 4835–4844.

321 X. Huang, D. Wang, S. Yan, P. An, J. Han, Z. Guo, X. Li, Z. Chen, L. Chang, S. Lu and Z. Tang, *Nano Res.*, 2022, **15**, 7910–7916.

322 S. Kuang, M. Li, R. Xia, L. Xing, Y. Su, Q. Fan, J. Liu, E. J. M. Hensen, X. Ma and S. Zhang, *ACS Appl. Nano Mater.*, 2020, **3**, 8328–8334.

323 J. Zeng, M. Castellino, K. Bejtka, A. Sacco, G. Di Martino, M. A. Farkhondehfal, A. Chiodoni, S. Hernández and C. F. Pirri, *J. Mater. Sci.*, 2021, **56**, 1255–1271.

324 P. Grosse, A. Yoon, C. Rettenmaier, A. Herzog, S. W. Chee and B. Roldan Cuenya, *Nat. Commun.*, 2021, **12**, 6736.

325 A. Loiudice, P. Lobaccaro, E. A. Kamali, T. Thao, B. H. Huang, J. W. Ager and R. Buonsanti, *Angew. Chem. Int. Edit.*, 2016, **55**, 5789–5792.

326 P. De Luna, R. Quintero-Bermudez, C.-T. Dinh, M. B. Ross, O. S. Bushuyev, P. Todorović, T. Regier, S. O. Kelley, P. Yang and E. H. Sargent, *Nat. Catal.*, 2018, **1**, 103–110.

327 C. Reller, R. Krause, E. Volkova, B. Schmid, S. Neubauer, A. Rucki, M. Schuster and G. Schmid, *Adv. Energy Mater.*, 2017, **7**, 1602114.

328 Z. Chen, Y. Song, Z. Zhang, Y. Cai, H. Liu, W. Xie and D. Deng, *J. Energy Chem.*, 2022, **74**, 198–202.

329 H. S. Jeon, S. Kunze, F. Scholten and B. Roldan Cuenya, *ACS Catal.*, 2018, **8**, 531–535.